Commissioning of the LHCb Inner Tracker and Measurement of V^0-Particle Production in *pp* Collisions at 0.9 TeV

PAR

Mathias Oleg KNECHT

acceptée sur proposition du jury:

Prof. G. Gremaud, président du jury
Prof. O. Schneider, directeur de thèse
Dr W. Bonivento, rapporteur
Dr A. Gallas Torreira, rapporteur
Dr T. Schietinger, rapporteur

ÉCOLE POLYTECHNIQUE
FÉDÉRALE DE LAUSANNE

Suisse
2011

Résumé

Le Grand Collisionneur de Hadrons (LHC) au CERN, près de Genève, est un accélérateur conçu pour faire entrer en collision des protons à une énergie de $\sqrt{s} = 14$ TeV dans le centre de masse. Il est en fonction depuis novembre 2009 et a fourni des collisions jusqu'à l'énergie de $\sqrt{s} = 7$ TeV en 2010. L'expérience LHCb est l'une des quatre plus grandes expériences au LHC, avec ATLAS, CMS et ALICE. Le détecteur LHCb est un spectromètre à bras unique destiné à étudier la violation de CP ainsi que les désintégrations rares dans le secteur des quarks b.

Le système de trajectographie de l'expérience LHCb est composé du Vertex Locator (VELO), du Tracker Turicensis (TT), de l'aimant dipolaire, de l'Inner Tracker (IT) et de l'Outer Tracker (OT). Le VELO, le TT et l'IT sont basés sur la technologie à micro-bandes de silicium, alors que l'OT est composé de chambres proportionnelles tubulaires à fil unique. L'IT couvre la region la plus proche de l'axe du faisceau, où la multiplicité des traces est la plus grande (20% des traces dans 1.5% de l'acceptance).

Deux sujets ont été abordés dans cette thèse de doctorat. La première partie est dédiée à la phase de mise en service de l'IT. Tout d'abord, nous décrivons le développement de la première version du "monitoring" des données en temps réel. Plusieurs histogrammes et cartes de signaux bruts ont été implémentés, afin de surveiller la bonne marche du détecteur et d'identifier rapidement les problèmes de fonctionnement. Le monitoring en temps réel a permis la détection de la présence de particules produites par les rayons cosmiques, qui ont elles-mêmes permis un premier alignement spatial de l'IT. En septembre 2008 et juin 2009, le LHC a procédé à des tests d'injection de protons à partir du SPS dans l'anneau LHC. Des paquets de $2 - 5 \times 10^9$ protons ont été stoppés dans des absorbeurs de faisceau (TED), produisant une gerbe de particules secondaires dirigée vers LHCb. Ces événements ont été enregistrés par le détecteur LHCb et ont permis la synchronisation de l'IT avec une précision de 1 ns.

La deuxième partie décrit une analyse d'un échantillon de données coorrespondant à une luminosité intégrée de 6.8 ± 1.0 μb^{-1} et enregistré en 2009 à partir de collisions proton-proton à une énergie de $\sqrt{s} = 0.9$ TeV dans le centre de masse. Les sections efficaces différentielles de production des particules V^0 (K_S, Λ et $\bar{\Lambda}$) ont été mesurées en fonction de la quantité de mouvement transverse p_T ainsi que de la rapidité y, en utilisant uniquement le système de trajectographie de l'expérience. Une sélection simple basée sur une variable géométrique *ad hoc* construite sur les paramètres d'impact des particules filles ainsi que de la particule mère a été développée. Les résultats sont comparés à quelques modèles de génération Monte Carlo (MC), et montrent que la section efficace de production de mésons K_S est sur-estimée pour $p_T < 0.4$ GeV/c, et sous-estimée pour $p_T > 1$ GeV/c par tous les modèles considérés. La section efficace de production des baryons Λ et $\bar{\Lambda}$ est sous-estimée par tous les modèles pour $p_T > 0.8$ GeV/c. De plus, les données semblent également montrer un rapport $\bar{\Lambda}/\Lambda$ plus petit que prédit par les modèles considérés.

Mots-clé : CERN, LHCb, Inner Tracker synchronization, online monitoring, strangeness production.

Abstract

The Large Hadron Collider (LHC) at CERN near Geneva is an accelerator designed to collide protons at a centre-of-mass energy of $\sqrt{s} = 14$ TeV. It is operational since November 2009 and has delivered collisions up to an energy of $\sqrt{s} = 7$ TeV in 2010. The LHCb experiment is one of the four major LHC experiments, together with ATLAS, CMS and ALICE. It is a single-arm forward spectrometer designed to study CP-violation and rare decays in the b-quark sector.

The tracking system of the LHCb experiment is composed of the silicon Vertex Locator (VELO), the silicon Tracker Turicensis (TT), the dipole magnet, the silicon Inner Tracker (IT) and the straw-tube Outer Tracker (OT). The IT is covering the innermost acceptance region close to the beam-pipe, where the track multiplicity is highest (20% of the tracks for 1.5% of the acceptance).

Two topics have been addressed in this doctoral thesis. The first part is dedicated to the IT commissioning phase. In particular the first version of the data-quality online monitoring is described. Several histograms and cluster maps have been developed, in order to watch the detector operation and ensure fast problem identification. The online monitoring allowed the identification of cosmic ray tracks which where used for a first spatial alignment. In September 2008 and June 2009, LHC injection tests from the SPS to the LHC ring were performed. Bunches of $2 - 5 \times 10^9$ protons were dumped onto a beam stopper (TED), producing a shower of secondary particles heading towards LHCb. These events were recorded by the LHCb detector and allowed a time-alignment of the IT up to a precision of 1 ns.

The second part describes an analysis of a data sample corresponding to an integrated luminosity of 6.8 ± 1.0 μb^{-1} and recorded in 2009 from proton-proton collisions at a centre-of-mass energy of $\sqrt{s} = 0.9$ TeV. The double-differential V^0 (K_{S}, Λ and $\bar{\Lambda}$) production cross-sections as a function of transverse momentum p_{T} and rapidity y have been measured using only the tracking system of the experiment. A simple selection using an *ad hoc* geometrical variable based on the impact parameters of the daughters and mother particles has been developed. The results are compared with a few Monte Carlo (MC) generator tunings. They indicate that the K_{S} production cross-section is mostly overestimated for $p_{\text{T}} < 0.4$ GeV/c and underestimated for $p_{\text{T}} > 1$ GeV/c for all considered models. For Λ and $\bar{\Lambda}$, the production cross-section is mostly underestimated by all models for $p_{\text{T}} > 0.8$ GeV/c. In addition, the data seem to indicate that the $\bar{\Lambda}/\Lambda$ ratio is smaller than predicted by the considered models.

Keywords: CERN, LHCb, Inner Tracker synchronization, online monitoring, strangeness production.

Remerciements

Ce travail de doctorat m'aura permis de découvrir tout un monde. Un monde unique où le moteur n'est pas l'argent, mais la curiosité humaine. Un monde de réflexions intellectuelles poussées, conduites par des gens extrêmement motivés qui ne laissent rien au hasard. Enfin, un monde où la patience est une qualité indispensable, étant donné l'échelle de temps sur laquelle se déroulent les expériences de physique des particules.

Même si l'on jouit d'une grande liberté en tant que doctorant, la vie n'est pas toujours facile. Il faut faire preuve d'une grande persévérance pour gérer un projet de recherche sur plusieurs années, s'adapter aux changements réguliers d'échéance pour la finalisation du détecteur, et enfin pour rédiger la thèse. Je n'aurais pu commencer, ni terminer cette recherche sans un certain nombre de personnes qui ont toutes contribué, à des degrés divers, à me permettre d'arriver au bout de mon projet.

Tout d'abord, je tiens à exprimer ma profonde gratitude à mon directeur de thèse, Olivier Schneider, pour ses conseils plus qu'avisés, sa patience illimitée, ainsi que sa passion pour tous les aspects de son travail (enseignement, recherche, supervision de doctorants). Sa disponibilité immense, doublée d'un esprit critique et précis, en font un excellent directeur de thèse et je le remercie donc chaleureusement de m'avoir suivi et aidé à mener ce projet à bien durant ces années passées au Laboratoire de Physique des Hautes Energies (LPHE) de l'EPFL.

Je tiens également à remercier mes collègues pour l'analyse des V^0, Raluca, Yasmine, Raphael et Yanxi, sans qui rien n'aurait été possible. En effet, la masse de travail liée à une première analyse dans laquelle tout est à "débugger", n'aurait pas permis à une personne seule de parvenir à une analyse complète en relativement peu de temps à partir de la prise de données. Tout était neuf, et la mise à jour permanente de l'alignement et de la calibration nécessitait de refaire l'analyse entière un nombre incalculable de fois, obligeant tout le monde à s'y mettre. Cette première réalisation avec le détecteur LHCb constitue donc, à l'instar de toutes les expériences de physique des particules, un vrai travail d'équipe.

Un grand merci aussi aux collègues avec qui j'ai travaillé les premières années pour l'Inner Tracker: Helge, Daniel, Eliseo, Pablo, Fred, Jeroen, qui m'ont guidé durant mes premiers pas au CERN; Alain et Rodolphe, avec qui j'ai beaucoup rigolé (mais aussi un peu travaillé); Matt, pour toute son aide durant la partie "software" de ma thèse, pour sa disponibilité et sa connaissance presque illimitée du software LHCb.

Gudrun, Federica et Thomas, merci pour l'excellente collaboration au sujet du travail théorique

qui m'a permis de sortir des rails habituels pour un physicien expérimentateur, Thomas pour m'avoir suivi depuis mon travail de diplôme en 2004, pour notre collaboration en 2005, ainsi que lors de la première année de ma thèse, collaboration qui s'est rapidement transformée en amitié.

L'ambiance dans le LPHE était excellente, et pour une bonne part cela tient à nos deux "mamans": Erika et Esther. En effet, non seulement nos deux secrétaires préférées savent à peu près tout sur tout, dans tous les domaines, mais elles sont en plus doublées de caractères adorables. En tant que résident au LPHE, je savais que je sortais du secrétariat moins bête et moins perdu que lorsque j'y entrais. Je vous remercie du fond du coeur de vous être occupées de moi !

Kim, Géraldine, Shirit, je ne saurais vous remercier assez pour les bons moments passés au labo et en dehors !

J'aimerais aussi remercier Aurelio, Tatsuya, et tous les autres membres du LPHE que je ne mentionne pas ici, pour rendre cette ambiance si sympathique, pour avoir une fois ou l'autre répondu à l'une de mes sottes questions, pour m'avoir accompagné lors d'un café ou tenu la porte de l'ascenseur !

Merci infiniment à mes très chers amis, Jess, Greg, Aline et Jairo, Alvaro, Gael, Hinnerk, Fabien, Marie-Emmannuelle et Jean-Philippe, Aline Amstein, Victoria, qui m'ont accompagné dans tout ce qui fait la vie en dehors du travail, chez moi, chez vous, au bord du lac, sur un bateau ou dans un chalet, et qui ont assuré mon équilibre personnel, nécessaire pour mener à bien un travail de cette ampleur. La vie est tellement plus simple lorsqu'on est bien entouré !

Merci à toute ma famille, à Grand-Père et Lalla, qui m'ont soutenu lors de mes études et dans la vie en général, à ma tante Dominique, qui m'a permis de réussir mes examens de première année de physique en m'offrant ses conseils de physicienne pendant dix jours dans sa maison du sud de la France. A Anton et Florence, qui se plaignaient continuellement d'être envahis de muons cosmiques dans leur cuisine depuis que nous les avions repérés dans l'Inner Tracker. A mes cousins Irène, Olivier, Stéphane et Solène, à Jean-Pierre, à mon tonton Jean ainsi que Willy, qui a passé de nombreuses heures à la plage avec moi à essayer de comprendre la relativité générale. A mon cher frère Yasha et toute la famille, Yael, Bat-Sheva, Anael, Hanna et Odelia, qui malgré la distance sont toujours dans nos coeurs !

Merci infiniment à mes parents, Nina et Pierre, de m'avoir soutenu totalement et permis de faire des études, de m'avoir tant offert dans la vie et aussi permis de découvrir d'autres chefs d'oeuvres, comme la musique et les voyages. Merci à ma soeur Anna et son mari Luca de m'avoir offert leur amour, le gîte à New York pendant de longues semaines, lorsque nous étions bloqués par l'Eyjafjallajökull, et surtout de m'avoir fait d'adorables petits neveux ! Merci donc aussi à Arturo et César d'être venus au monde !

Enfin, Béatrice, merci infiniment d'être à mes côtés chaque jour, et de m'avoir soutenu sans faille dans la partie la plus difficile de ma thèse, depuis ce beau mois d'août 2009 où je t'ai rencontrée !

A tous, du fond du coeur, merci !

<div style="text-align: right;">

12 mai 2011
Mathias Knecht

</div>

Contents

1

Introduction

In this chapter, I summarize the different steps of my doctoral studies, as well as the organisation of this document. After an introductory part on the aims of particle physics, I give a simplified view of the Standard Model (SM) for the elementary particles and their interactions, as well as a brief introduction on symmetry. I finally mention interesting results that I have obtained at the beginning of my doctoral studies, since these are not developed further in this thesis.

The aim of particle physicists is to provide the most complete picture of the origin of the universe, and find a unique theory containing all physics laws. Indeed, two main theories are nowadays used for the physical description of the universe: General Relativity developed by Einstein in 1915 [1, 2, 3], which describes the geometry of space-time and gravitation at large scales, and the Standard Model (see Sec. 1.2), which describes the elementary particles and their interactions at the microscopic level. The good news is that almost each of the experimentally accessible predictions of these theories have been up to now verified. However, the bad news is that this twofold description of nature suffers from an important flaw: General Relativity and the Standard Model are not compatible with each other. Indeed, the application of one of these theories in the domain of the other leads to unsolved theoretical contradictions. In mathematics, this has a terrible meaning: taking a statement as hypothesis and ending up with a contradiction is a proof *ab absurdo* that the starting hypothesis is wrong.

However in the case of Standard Model and General Relativity, the situation may not be as bad. Indeed, these contradictions happen generally at the border between these two theories, where they are overlapping, and when one tries to combine them. In fact, the correct answer is that none of them is wrong, simply they are both *almost* true. In other terms, they are an approximation: they give an account of the underlying phenomena up to a limited precision.

It is therefore reasonable to think that there must be another theory which is unique and predicts *almost* the same results, but is more accurate. In any way, the fact that these theories are limited to their application domain is not conceptually satisfactory for the physicists, who

always look for simplicity, aesthetics, and completeness.

The best scenario available today describing the origin of the universe is the "Big Bang": a brutal release of the total energy of the universe contained in a tiny portion of space, followed by a cooling and a condensation of the energy into matter. The condensation formed the hydrogen and helium of the universe (primordial nucleosynthesis), which then clustered in giant clouds and finally gravitationally collapsed to form the stars. The elements heavier than helium and lighter than iron are created continuously in the core of the stars by nuclear fusion (stellar nucleosynthesis). The other stable elements heavier than iron and up to uranium are produced by the shock waves of the exploding stars (supernovae). Planets and asteroids are later formed by the condensation of the heavy atoms which are spread out in the universe by dying stars. This overall picture is up to now very satisfactory and is confirmed by the observations, such as the expansion of the universe, discovered by E. Hubble in 1929 [4], and the remnant cosmic micro-wave radiation.

From the theoretical point of view, the Big Bang is a "scenario", not a theory, and is using a mixture of some elements of both the Standard Model and General Relativity. The most interesting part for the particle physicists is what happened from the time of the Big Bang, up to the formation of the first hydrogen atoms. At that time, the universe was an extremely hot "soup" of elementary particles and energy interacting together, via complex processes.

The precise description of what happened shortly after the Big Bang, and therefore the understanding of the current physics laws, requires to reach the extreme energy density (or temperature[1]) that was present at that time in the universe. One of the technical options available is to accelerate elementary particles close to the speed of light, allowing them to acquire kinetic energy, and smash them together in a detector. The Large Hadron Collider (LHC) at CERN (Organisation Européenne pour la Recherche Nucléaire) in Geneva is one of these accelerators. It is a proton-proton collider, designed to provide a wealth of collisions at a yet unexplored energy scale for the next years. It has been designed to answer many open questions concerning physics at the microscopic level.

The research presented in this doctoral thesis is devoted to LHCb (LHC "beauty" experiment), which is one of the four major detectors at the LHC. I had the great opportunity to start my doctoral studies right at the time when I could participate in the last steps of the construction of the detector, be involved in the commissioning phase, and finally analyse the first data recorded by the LHCb experiment. Starting earlier would have prevented me to analyse real data and forced me to concentrate on simulations, which would have been a great frustration. In contrary, starting later would have made me unaware of the difficulties and the challenges of building and operating an extremely complex device such as the LHCb detector.

The tasks I have contributed to were concentrated on the testing and commissioning of the LHCb Inner Tracker (IT) sub-detector, which measures the charged particle trajectories, and performing the first physics measurement with LHCb data. Indeed, I started with the testing of the silicon modules used to build the IT detector, performing various tasks such as stressing the modules in a temperature cycle, and testing cooling pipes in order to optimize heat exchange. Once the modules were built and fully tested, I was responsible of building an experimental setup with its associated software that allowed the commissioning of the IT boxes before installation in the LHCb cavern.

I then started to work on the site of the LHCb experiment in order to prepare the software for the data-acquisition chain. After all the IT boxes were finally installed on the LHCb site, I was responsible for the developement of the data monitoring software. This software was an important element for the observation of real-time cosmic rays in the IT. In September 2008,

---

[1]Temperature can be defined as the average energy per volume unit.

when the first particle splashes from LHC injection tests were observed in LHCb, I performed the time calibration of the IT.

In order to be prepared for the analysis of the first collisions foreseen at the end of 2009, I then developed a selection for the measurement of the production of V^0 (K_{S}, Λ and $\bar{\Lambda}$) particles, using Monte Carlo simulations. Finally, in collaboration with my colleagues, I performed the measurement of the V^0 production cross-sections[2], which was the first physics analysis achieved within LHCb. My results were partly used for the first LHCb publication [5].

This document is organized as follows: after this introductory chapter on particle physics and the Standard Model (**Chapter 1**), I describe the experimental apparatus at CERN, including the LHC accelerator and the LHCb experiment (**Chapter 2**). I continue with the description of the hardware and software work I have performed for the LHCb IT detector (**Chapter 3**), and finally present the results I have obtained for the K_{S} and Λ production measurement (**Chapter 4**).

1.1   Energy and structure of matter

The Heisenberg uncertainty principle, expounded by W. Heisenberg in 1927 [6], states that the uncertainty on the measured momentum p of an object and the uncertainty on the position x of this object cannot be infinitely small. In mathematical words

$$\Delta x \Delta p \geq \frac{\hbar}{2} \ ,$$

where $\hbar$ is Heisenberg's constant.

A key consequence of this principle is that the smaller a constituent of matter, the higher the energy needed to observe this constituent. An increase in energy allows us therefore to see more fundamental constituents and their interactions, and study physics processes which would be absolutely invisible otherwise.

As an illustration, most of the processes surrounding us are of the order of the electron-Volt (eV) energy scale[3]. Chemical reactions such as combustion of sugar in our body, photo-synthesis in the plants, and the fact that sunlight is visible for the human eye, are all different aspects of the physics at the eV scale. The chemical reactions bind or unbind atoms together to form molecules. The visible light is able to provoke chemical reactions and reversely chemical reactions sometimes emit light. This implies that the energy of the visible light is of the same order of magnitude than the binding energy of atoms together to form molecules. In other terms, physics at the eV scale is only able to see the atoms as the smaller constituents of matter, and the atom nucleus is absolutely invisible a this scale.

At the end of the 19th century, the discovery of radioactivity by H. Becquerel, P. Curie and M. Curie [7] opened the door to a new energy scale. The existence of a massive, positively charged nucleus inside the atom was discovered by Ernest Rutherford in 1911. In 1932, James Chadwick discovered the neutron and a clear picture of the atomic nucleus, formed by protons and neutrons, emerged. Between the keV (10^3 eV) and the MeV (10^6 eV) scale, the atomic nucleus started to become "visible". For instance, it was understood that the source of the sunlight in the centre of the sun is nuclear fusion, which builds heavier nuclei out of lighter nuclei. Nuclear fission, which is the break down of heavier nuclei into lighter ones, was also discovered and domesticated in various ways, for the best (medical imagery, nuclear power) and the worst (nuclear weapons). At this level of understanding, it was thought that the smallest

---

[2]In particle physics, the cross-section is similar to the probability of a given process to occur, such as producing a given particle in a proton-proton collision.

[3]The electron-Volt is a energy unit (1 eV$= 1.6 \times 10^{-19}$ Joules).

constituents of matter were the protons and neutrons forming the nucleus, and the electrons orbiting in its vicinity. Since the radiation around the MeV scale allows the breaking or the binding of atomic nuclei, it implies that the binding energy of protons and neutrons inside a nucleus is of that energy scale.

Starting with the first cyclotron in 1932, the idea to smash "elementary" particles together came up, in order to probe more deeper the structure of matter. With these new experiments, it was thought to be possible to observe new phenomena, and eventually understand the structure of the protons and neutrons. The very simple idea, which is less simple to realize, of a particle experiment implies two distinct components: firstly the accelerator itself, that accelerates electrons or protons to very high energies – formerly GeV (10^9 eV) scale, nowadays TeV (10^{12} eV) scale – and make them collide, and secondly a detector around the collision point, which detects the particles that are produced in the collisions. The conversion from kinetic energy in the initial protons or electrons into matter is driven by Einstein's famous equation $E = mc^2$. These new physics experiments allowed the discovery of a deeper structure of matter, at a higher energy scale. The quarks were discovered as the constituents of the protons and neutrons. They are the smallest visible constituents of matter at the GeV and the TeV scale, together with the leptons, such as for instance the electron. Experimentalists and theorists built together a theoretical model – the "Standard Model" – which describes the fundamental constituents of matter and the interactions between them.

1.2 The Standard Model

The Standard Model (SM) is up to now the best description of the physics at the microscopic level. It states that there are twelve building blocks of matter, six quarks (u,c,t,d,s,b) and six leptons (e,μ,τ,ν_e,ν_μ,ν_τ). All the matter we know is composed of these particles, mainly the quarks u ("up") and d ("down"), which are the constituents of the proton (uud) and the neutron (udd). For each of these particles, there is an anti-matter counterpart, with the same mass but an opposite charge.

These elementary particles interact together via four forces (the electromagnetic, strong, weak and gravitational forces) although the description of gravity is not part of the SM. The three other forces have been "unified" in the SM, which means they are described by the same formalism. In this formalism each force is described with at least one mediator, whose exchange between two particles provokes an interaction. The known mediators, called "exchange bosons" are the photon for the electromagnetic force, the W^+, W^- and Z bosons for the weak force, and the gluons for the strong force. The electromagnetism is responsible for the attraction between the positively charged nucleus and the negatively charged electrons in the atom. The strong force is responsible for the cohesion of the nucleus, and the weak force is responsible for β radioactivity. As a summary, Table 1.1 shows the fundamental particles and the bosons mediating the fundamental forces described in the SM.

The exchange bosons are all predicted to be massless. However, the $W^\pm$ and Z bosons have non-zero masses, which have been precisely measured [9]. The mass of these bosons can be explained by the "Higgs mechanism", requiring another particle, the Higgs boson [10]. The Higgs boson has not yet been observed, and its existence is even questioned by a non-negligible fraction of the scientific community [11].

The SM can be seen as a great success of particle physics, since apart from the Higgs boson which is still to be discovered, all its predicitons have been verified up to now Nevertheless, it remains puzzling for the scientific community mainly for two reasons. The first reason is, as it was previously mentioned, that the SM is not compatible with General Relativity, which describes gravity. The second reason is that the SM contains 19 free parameters, which have

Table 1.1: Elementary particles and mediators. The particles in bold are the constituents of the atom. Inspired from Ref. [8].

	Charge	Particles			
Matter	$+\frac{2}{3}$	**u**	c	t	Quarks
	$-\frac{1}{3}$	**d**	s	b	
	-1	***e***$^-$	μ^-	τ^-	Leptons
	0	ν_e	ν_μ	ν_τ	
Mediators	0	gluons			Strong
	0	photons			Electromagnetic
	$-1,0,+1$	W^-,Z^0,W^+			Weak
	0	graviton?			Gravity
Anti-Matter	0	$\bar{\nu}_e$	$\bar{\nu}_\mu$	$\bar{\nu}_\tau$	Anti-Leptons
	$+1$	e^+	μ^+	τ^+	
	$+\frac{1}{3}$	$\bar{d}$	$\bar{s}$	$\bar{b}$	Anti-Quarks
	$-\frac{2}{3}$	$\bar{u}$	$\bar{c}$	$\bar{t}$	

to be measured experimentally. The link between these parameters is not understood and their values cannot be predicted. This is quite unsatisfactory theoretically. Indeed, a very subjective point of view is that nature can be described by laws and three or four universal constants, but 19 looks rather as a simple parametrization of our ignorance.

Physicists think therefore that there must be a more general theory for which the SM is an approximation at low energies, in analogy to the Newton laws of mechanics which are an approximation of General Relativity at low velocities and in a universe with absolute time. This higher-level theory could be one of the recently developed Grand Unified Theories (GUT) [12], which are trying to include gravity in the SM. Up to now, any attempt has failed, or cannot be tested experimentally. One of the most popular theory is the Super Symmetry (SUSY) [13], which predicts for each particle a heavy super-symmetric partner. The current challenge of particle physics is therefore to discover the last SM particle, the Higgs boson, and observe the first hints of new phenomena beyond the SM, which are called in general "New Physics".

1.3   Symmetries

One of the key concepts in physics is the notion of symmetry. Physicists always look for a symmetry while trying to solve a problem. Symmetry in physics is not only a handy and aestethic consideration, it is a very strong property of invariance of a system under certain transformations, which leads to the most important physics theorems. For instance, as it was formulated by Emmy Noether in 1918 [14], the conservation of momentum is a consequence of the invariance of space by translation, equivalent to the fact that there are no privileged place in the universe (homogeneity of space). The conservation of angular momentum is a consequence of invariance of space under rotation, equivalent to the assertion that there are no privileged directions in space (isotropy). And, last but not least, the conservation of energy is a consequence of the invariance of space under time translation, equivalent to the homogeneity of time.

Apart from the above symmetries which are continuous, there are "discrete" symmetries, which are very common in particle physics. The P (Parity) symmetry, for example, is what could be called the "left-right" symmetry. It states that the laws of physics remain unchanged when one of the space coordinates is inverted, such as what happens in a mirror. The C

(Charge Conjugation) symmetry states that the laws of physics are unchanged when replacing paticles with their antiparticles, and the T (Time) symmetry states that the laws of physics are unchanged under time reversal. It is believed that when applying these three transformations simultaneously, the laws of physics are unchanged[4]. However, when applying only one or two of these transformations, the system can behave slightly differently from the original one and therefore the symmetry is broken.

One of the most important violations of these symmetries is the violation of the CP symmetry. The CP transformation corresponds to the exchange of a particle with its anti-particle and the inversion of one space coordinate. At the time of the Big-Bang, pure energy is believed to have condensed into matter and anti-matter. After cooling of the universe, the anti-matter annihilated with matter. The fact that we now live in a universe exclusively composed of matter implies that at the beginning, there was slightly more matter than anti-matter, i.e. an asymmetry. CP violation is believed to be responsible for this asymmetry, making it one of the most interesting research subjects in particle physics. The LHCb experiment is mainly dedicated to the study of this asymmetry.

1.4 Results related to New Physics searches

In the first year of my doctoral studies, I have been involved in different projects in direct relation to the search for New Physics. These projects were mainly concentrated on the "penguin" transition $b \to s\gamma$, since the Standard Model predicts that in such transitions, the polarization of the photon emitted is predominantly left-handed. It is therefore very important to test this prediction, since any deviation from the Standard Model could be an interesting hint for New Physics. I briefly summarize below the work that has been performed, as well as my personal contributions.

Probing photon helicity in $b \to s\gamma$ transitions via charmonium interference

I studied the possibility to determine the helicity of the photon emitted in $b \to s\gamma$ transitions, via the interference of the processes $B \to K^*(K\gamma)\gamma$ and $B \to K\eta_c(\gamma\gamma)$. The idea is that the interference between these two processes leading to the same final state $K\gamma\gamma$ depends on the strength of the Wilson coefficients C_7 and C_7', which determine the photon polarization in the underlying process $b \to s\gamma$. A new observable, the charge asymmetry, was proposed to determine these coefficients. My task consisted of generating the events with the full amplitude, and compute the asymmetries for different Wilson coefficients, with the help of a custom event generator [15]. This research was published [16].

Photon polarization from helicity suppression in radiative decays of polarized Λ_b baryons

The idea of this research was to compute the full $\Lambda_b \to \Lambda(1520)\gamma$ decay amplitude, and calculate the branching fraction and helicity amplitudes. After calculating the form factors associated with this amplitude, we have shown that in the Soft Collinear Effective Theory (SCET), the helicity-3/2 amplitudes vanish at lowest order. This suppression can be observed at the LHC and elsewhere, and provides a test for SCET theory. My contribution in this research, was to perform the calculations of the decay amplitude and the branching fraction, which were done analytically and solved numerically. This research resulted in a publication [17].
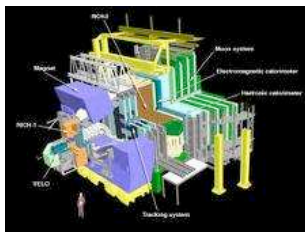
---

[4]This assertion is known as the CPT theorem.

2

The LHCb experiment

In this chapter I describe the experimental apparatus, which consists of the LHC machine and its associated detectors. I also describe the LHCb experiment in detail. The LHC and the triggering system of the LHCb experiment are described for nominal conditions. The specific conditions of the 2009 run, which is used for the V^0 analysis, are described in Chap. 4.

2.1 CERN and the LHC

CERN (Organisation Européenne pour la recherche nucléaire) was founded in 1954 by fourteen European states following a proposal by Louis de Broglie. It is the world's largest laboratory for particle physics, involving ~8'000 physicists from all over the world. Since 1954, several experiments were performed, among which the LEP experiments (1989–2000). The LEP (Large Electron Positron) was an e^+e^- collider operating at a centre-of-mass energy of $\sqrt{s} \sim 88 - 209$ GeV. The LEP experiments allowed a precise measurement of the Z and $W^{\pm}$ boson masses, after their discoveries at the Super Proton Synchrotron (SPS) in 1983. These experiments were an important milestone for the confirmation of the Standard Model.

After the success of the LEP experiments, it was decided to increase the energy to probe more deeply the structure of matter. One of the objectives was the discovery of the last missing SM brick, the Higgs boson, but also of super-symmetric particles or other new particles. It was decided to build a proton-proton collider, designed to operate at a centre-of-mass energy of $\sqrt{s} = 14$ TeV. After the first proposal in 1984, the LHC (Large Hadron Collider) project was officially started in 1994. The research and development started the same year, and the civil engeneering work started in 1998, just two years before the shutdown of the LEP experiments. The accelerator ring was installed in the 27 km LEP tunnel, under the Swiss-French border near Geneva, Switzerland. The first collisions were observed in the detectors in November 2009 at a center-of-mass energy of 0.9 TeV, and 7 TeV in March 2010. The operation at the nominal energy of 14 TeV is currently foreseen for 2014 at the earliest.

The LHC project consists of the accelerator itself – commonly called "the machine" –, and six detectors with their own physics program – called the "experiments":
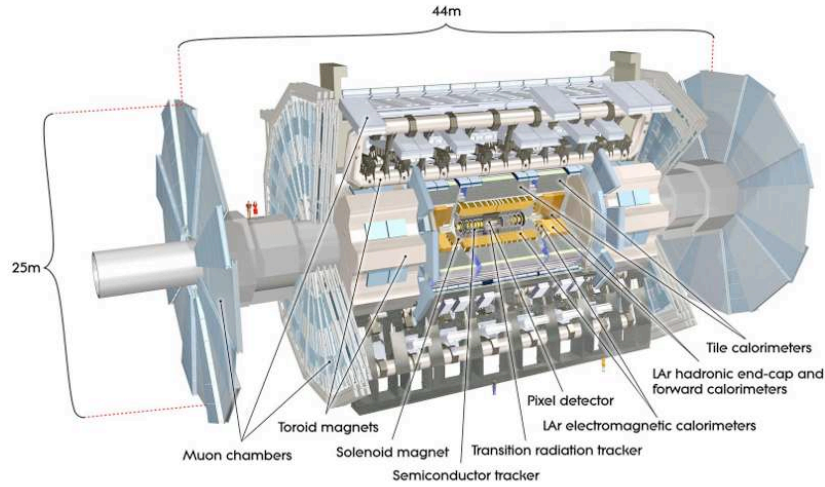
Figure 2.1: ATLAS detector.

ATLAS [20]: A Toroidal LHC Apparatus System. It is a "general purpose" detector (Fig. 2.1), designed mainly to discover the Higgs boson, but also to discover any new particle that will be produced at the unexplored TeV scale.

CMS [71]: Compact Muon Solenoid. It has the same goals as ATLAS, but with a different detector (Fig. 2.2). Any discovery made by ATLAS or CMS must be confirmed by the other experiment.

ALICE [22]: A Large Ion Collider Experiment. It is dedicated to the study of quark-gluon plasma (QGP), resulting from heavy-ions collisions at high energy. Unlike the other LHC experiments, it will operate with heavy ions collisions such as Pb-Pb (Fig. 2.3).

LHCb [23]: Large Hadron Collider beauty. It is dedicated to the physics of the b-quark sector, and aims at the study of CP asymmetries and rare decays. It is detailed in Sec. 2.2.

LHCf [24]: Large Hadron Collider forward. Its goal is the study of the particles generated in the forward collision region, to verify hadronic models related to the ultra-high energy cosmic rays. It consists of two small detectors placed at 140 m on either sides of the ATLAS experiment.

TOTEM [25]: Total Elastic and Diffractive cross section. It is designed to measure the total pp collision cross-section, as well as elastic scattering and diffraction at the LHC. It is located near the CMS detector.

MoEDAL [26]: Monopole and Exotics Detector at the LHC. It is mainly dedicated to the search of magnetic monopoles and other "exotic" particles. It is located in the same cavern as LHCb.
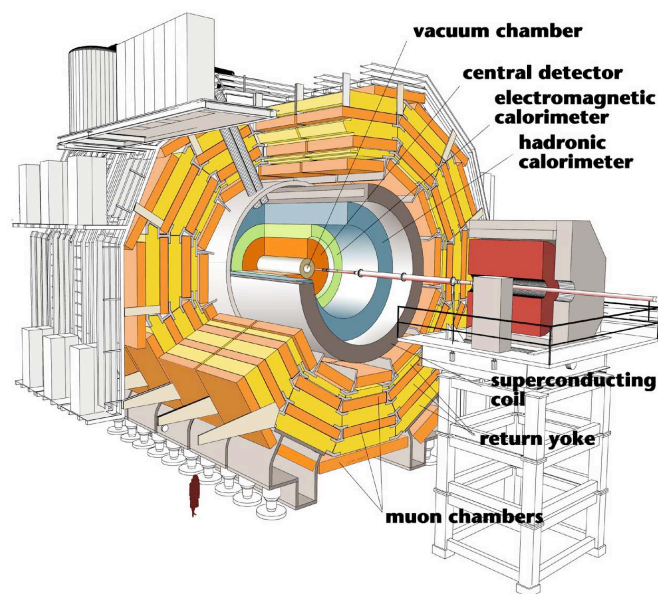
Figure 2.2: CMS detector.
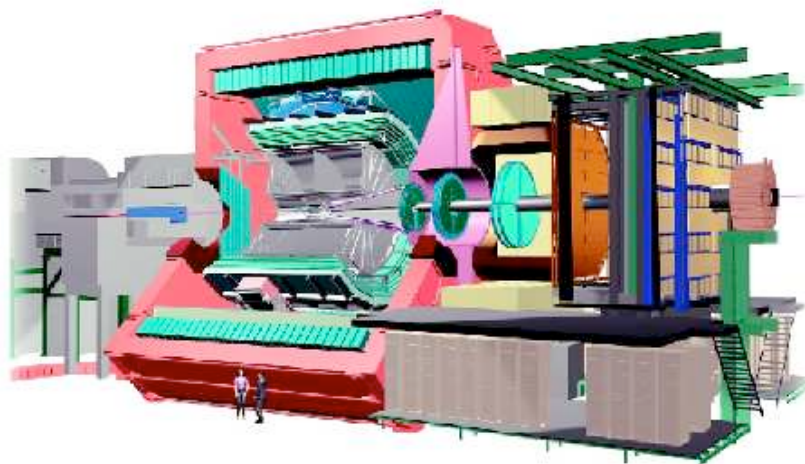
Figure 2.3: ALICE detector.
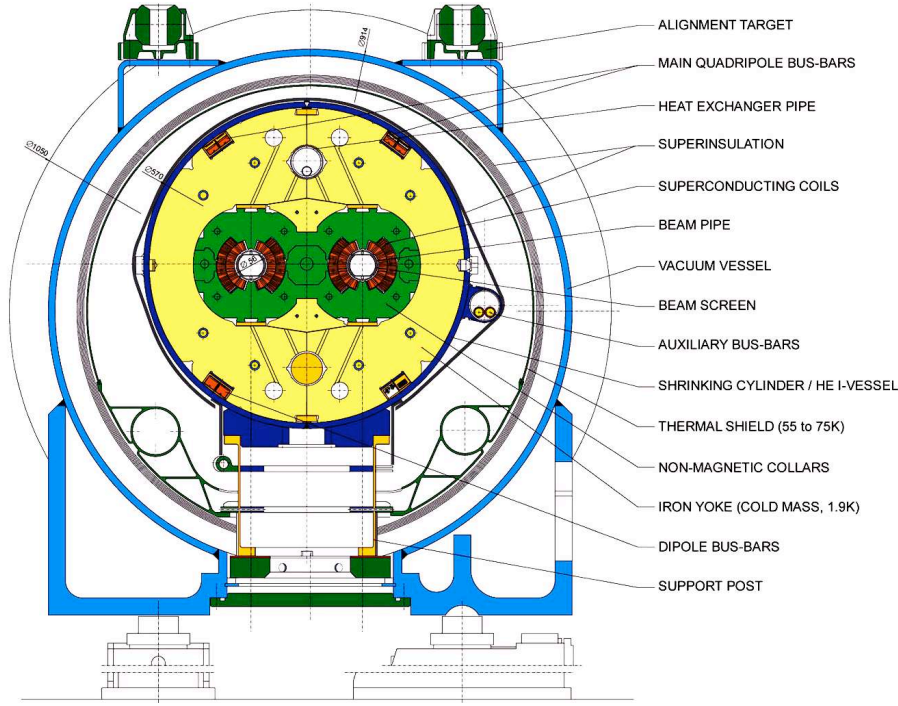
Figure 2.4: Cross section of an LHC dipole magnet [19].

2.1.1 The LHC collider

The LHC [18] is a circular proton-proton collider, whose operation relies on two basic principles: the acceleration of the protons, and the maintaining of the protons on a circular trajectory until they collide. The acceleration is achieved through an oscillating electric field and using the Coulomb force

$$\vec{F} = q\vec{E} \ ,$$

where q is the particle charge and $\vec{E}$ the electric field. The force is therefore parallel to the electric field. The circular trajectory is maintained with the help of a strong magnetic field and using the Lorentz force

$$\vec{F} = q\vec{v} \times \vec{B} \ ,$$

where $\vec{v}$ is the velocity of the particle, and $\vec{B}$ the magnetic field. The force is perpendicular to the magnetic field and to the velocity, bending the trajectory.

As in all other accelerators, the electric field needed for the acceleration in the LHC is provided by Radio-Frequency (RF) cavities. In order to maintain the circular trajectory of the particles, a magnetic field of 8.3 Tesla is provided by 1232 dipole magnets. To obtain these high magnetic fields, the magnets need to be maintained in a superconducting state, and this is achieved by cooling the inner core of the dipole magnets with liquid He at 1.9 K. A cross section of one of these magnets is shown in Fig. 2.4.

In nominal design conditions, protons are accelerated in 2808 bunches of 10^{11} protons, and the time separating two bunches is 25 ns, leading to a bunch-crossing rate of 40 MHz. Before the protons are injected in the LHC ring, they are accelerated through the linear accelerator (LINAC) up to 50 MeV, and injected into the Proton Synchrotron Booster (PBS), where they acquire an energy of 1 GeV. The Proton Synchrotron (PS) is then accelerating the protons up
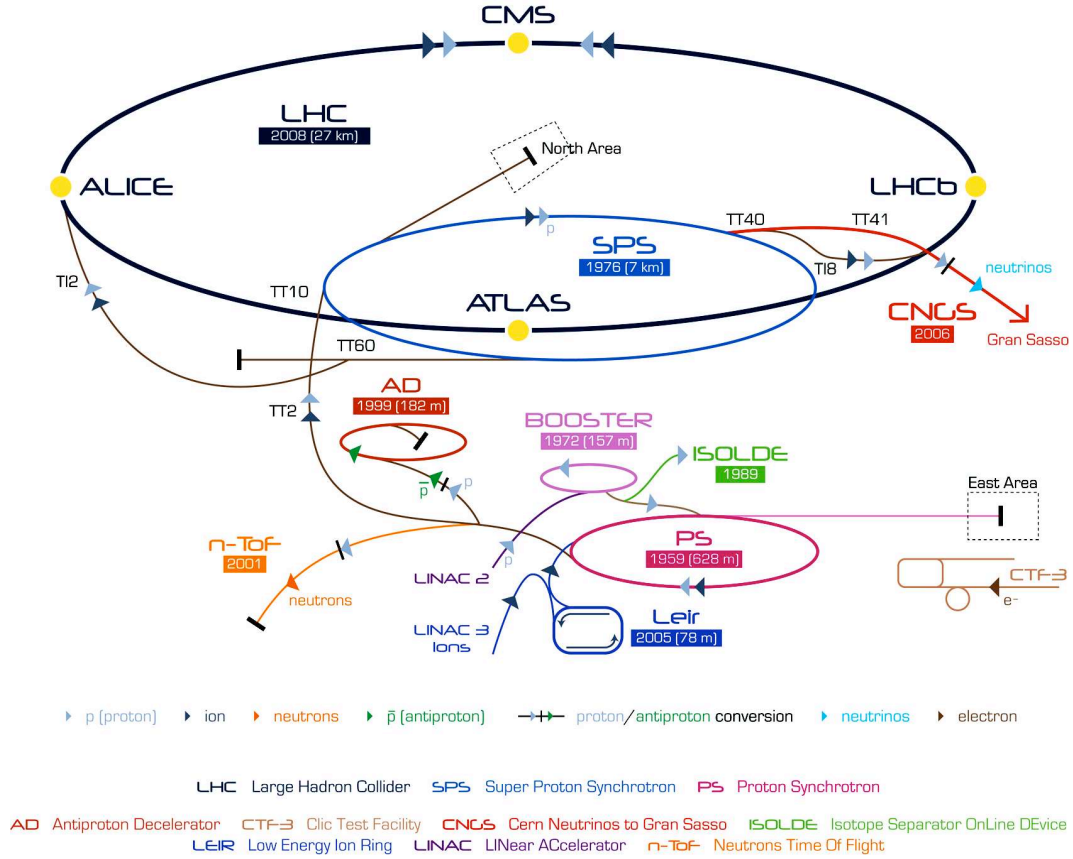
Figure 2.5: Layout of the CERN accelerators [18].

to 26 GeV before they are injected in the Super Proton Synchrotron (SPS), where they reach 450 GeV. Finally they are injected into the LHC, where they are accelerated to 7 TeV (Fig. 2.5).

The choice made between a $p\bar{p}$ collider and a pp collider was motivated by the fact that anti-protons are difficult to produce in large quantities. The disadvantage of this choice is that it requires two separate vacuum pipes with opposite magnetic fields for the simultaneous acceleration of oppositely moving protons.

At each interaction point, the two counter-rotating beams are focalized by quadrupole magnets in order to maximize the probability for a collision. The number N of collisions per second is the product of the instantaneous luminosity L, which is dependent on the machine and the beams only, with the proton-proton cross-section σ_{pp}, which depends only on the physics:

$$N = L\sigma_{pp} \ .$$

The total cross-section for proton-proton collisions at $\sqrt{s} = 14$ TeV is not well known, since it is the first time such collisions occur at a collider. However, an estimate of 100 mb (80 mb) for the total (inelastic) cross-section is generally assumed, allowing the computation of the expected collision rate in the LHC. The luminosity can be expressed as

$$L = \frac{N_b^2 n_b f_{rev}}{F} \ ,$$

where N_b is the number of particles per bunch, n_b the number bunches per beam, f_{rev} the revolution frequency of 11.245 kHz, and F a factor which depends on the geometry of the
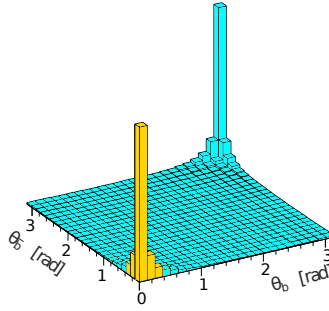
Figure 2.6: Generator-level angular distribution of $b\bar{b}$ pairs produced in pp collisions at the LHC. The yellow area indicates the LHCb acceptance.

beams. The luminosity determines the mean of the Poisson law describing the number of pp inelastic collisions per event. For ATLAS and CMS, the design luminosity is 10^{34} cm^{-2}s^{-1}, in order to obtain a rate of ~ 20 inelastic collisions per event. In LHCb, for specific physics analysis needs, the design luminosity is 2×10^{32} cm^{-2}s^{-1} in order to produce most of the time a single pp collision per event.

2.2 The LHCb detector

The LHCb detector is a single-arm forward spectrometer, mainly dedicated to the study of CP violating processes and rare decays in the b-quark sector. It covers an angle of 15–300 (15–250) mrad with respect to the beam axis in the magnet bending plane (non-bending plane), and its acceptance in pseudo-rapidity[1] is $1.8 < \eta < 4.9$. This particular layout differs from that of the other LHC experiments: it is adapted to the b-quark production scheme, which is predominantly at low angles θ with respect to the beam (Fig. 2.6). LHCb uses a right-handed cartesian coordinate system with its origin at the nominal LHC interaction point, the z axis along the beam axis in the direction of the spectrometer, the x axis horizontal and the y axis vertical, pointing upwards. The layout of the detector is shown in Fig. 2.7. The tracking system is composed of the Vertex Locator (VELO), the Tracker Turicensis (TT), the dipole magnet and the tracking stations T1–T3. The particle identification systems are composed of the Ring Imaging Cherenkov Counters (RICH I and II), the calorimeters (SPD, PS, ECAL and HCAL) and the muon chambers (M1–M5). A more detailed description of the different subdetectors is given in the next sections, and an extensive description of the detector can be found in Ref. [23].

2.2.1 Tracking system

The goal of the tracking system is to provide precise charged particle trajectory measurements for position and momentum determination. The tracking system includes the Vertex Locator (VELO), which is a silicon detector for primary vertex reconstruction surrounding the interaction region, the silicon Tracker Turicensis (TT) upstream of the dipole magnet, and three tracking stations (T1, T2, T3) downstream of the magnet. The tracking stations are composed of the silicon Inner Tracker (IT) and the straw-tube Outer Tracker (OT). A view of the tracking system is shown in Fig. 2.8. Although these sub-detectors are based on different detection technologies, they are used altogether for track reconstruction. The design has been motivated by different

---

[1]The pseudo-rapidity is defined as $\eta = \ln(\tan(\theta/2))$, where θ is the angle of emission of the particle with respect to the beam.
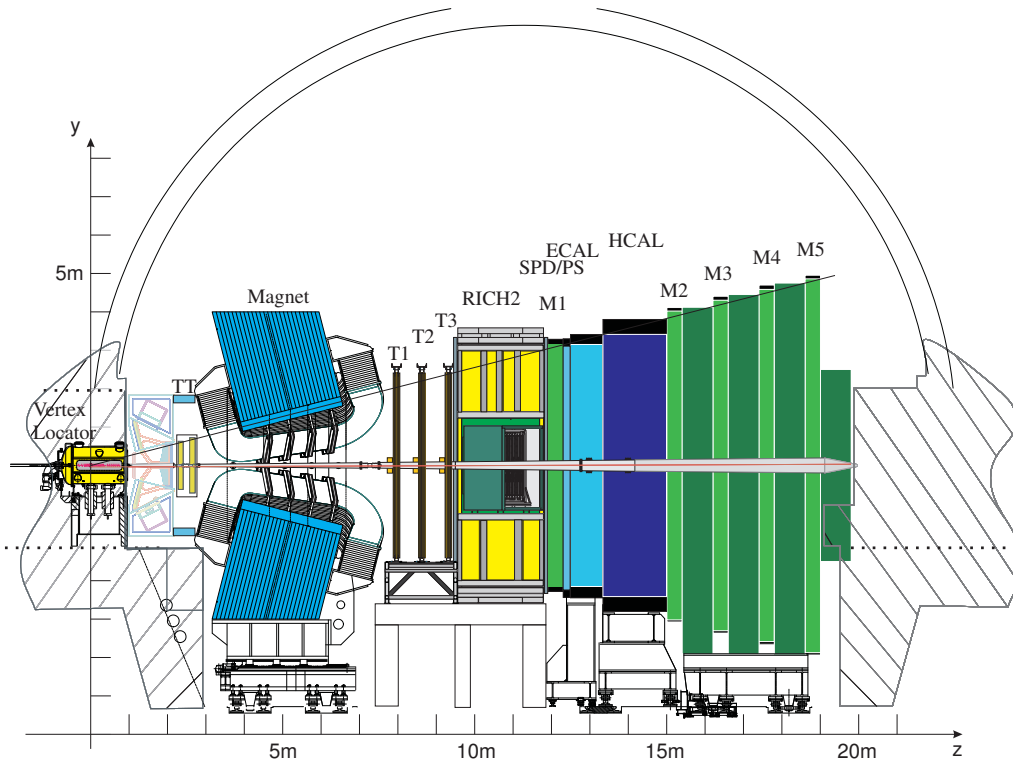
Figure 2.7: Layout of the LHCb detector in the non-bending (y,z) plane. The beam pipe traverses LHCb along the z axis and the interaction point is located at $z = 0$.

constraints. For instance, the tracking stations are made of two different types of detectors because of the inhomogenous track distribution in the x–y plane. While a silicon detector was choosen for very high particle density regions close to the beam-axis, the straw tube technology was adopted for the rest of the coverage mainly for cost reasons. I will describe all these sub-detectors separately in the next paragraphs.

Vertex Locator (VELO)

The VELO provides very precise measurements of the charged tracks originating from the interaction region. Its measurements are used for Primary Vertex (PV) reconstruction, trigger, and precise measurements of secondary vertices which are used in lifetime measurements. It is made of 21 stations along and perpendicular to the beam axis. Each station is made of two half modules, on both sides of the beam (left and right). Each half module consists of a sensor with radial strips which measures the track angle ϕ in the x-y plane (ϕ sensor), and a sensor with circular strips which measures the track radial distance r from the beam line (r sensor).

The sensors are 300 μm thick and use single-sided n-implants in n-bulk technology. The diameter of the sensors is 84 mm. The pitch of the r strips varies from 38 μm close to the beam up to 101.6 μm at the outer radius of 41.9 mm, in order to average the occupancy. The ϕ sensors are divided in two regions: the inner region, from a radius of 8.2 mm up to 17.25 mm, where the pitch varies from 35.5 μm and 78.3 μm, and the outer region, from 17.25 mm to 41.9 mm, with a pitch between 39.3 μm and 97 μm. The innermost strip distance to the beam is 8.2 mm, implying that the VELO is the detector which is the closest to the beam among all the LHC experiments.
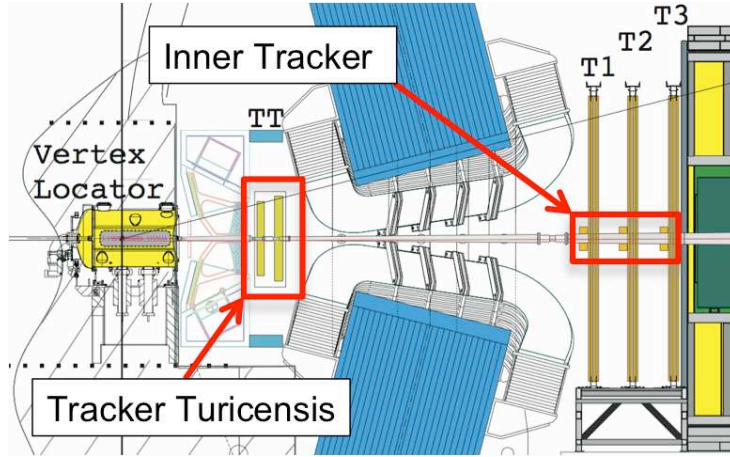
Figure 2.8: Tracking system of the LHCb experiment.
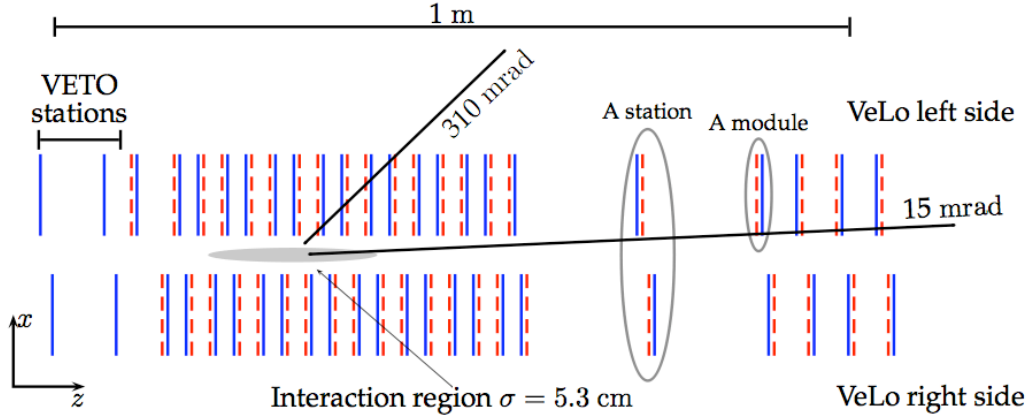
Figure 2.9: Layout of the VELO stations and the Pile-Up ("VETO") system [27]. The location of the interaction region and the angular acceptance are also shown. The blue (solid) line represents an r sensor, and the red (dashed) line represent a ϕ sensor.

Upstream of the 21 VELO stations, two additional r-sensor stations form the Pile-Up detector, which is part of the first level of the trigger system (see Sec. 2.2.3). These two stations are used to determine the number of primary interactions and the track multiplicity within one bunch crossing, to avoid recording of events which contain more than one bunch crossing.

Being so close to the beam, and to avoid material between the beam and the VELO sensors, the VELO modules are separated from the LHC vacuum by a thin aluminium foil. For the safety of the detector, the two halves of the VELO can be moved apart when the beams are not stable, typically during injection. The layout of the stations is shown in Fig. 2.9.

Inner Tracker (IT)

The IT is composed of 336 silicon micro-strip modules arranged in three stations with four boxes each, in a cross shape around the beam axis. The stations are separated by $\simeq 70$ cm in z. The boxes are located at 7 mm from the beam pipe, covering the very forward region of
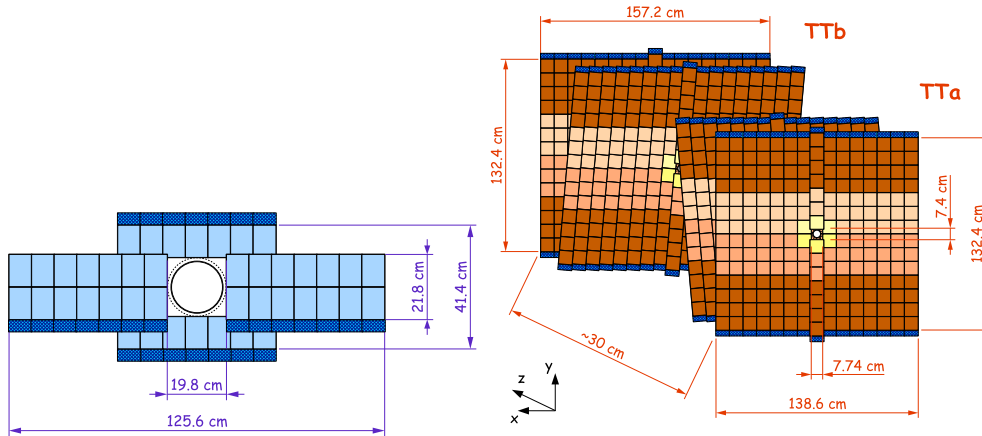
Figure 2.10: Silicon sensors arranged in x–y planes around the beam pipe (each rectangle represents one sensor). Left: one of the 12 IT detection layers. Right: the four TT layers.

the acceptance. Each box contains 28 modules arranged in four layers. Two of the four layers have vertical readout strips, while the other two have readout strips tilted by a stereo angle of $+5°$ and $-5°$. Although the IT covers only 1.5% of the LHCb acceptance, about 20% of the tracks pass through it, implying high particle densities. The readout pitch is 198 μm, and the total number of channels is 129′024. The layout of a layer is shown in Fig. 2.10 (left). The 336 modules are of two types: "Short" modules (11 cm in length), built with one 320 μm-thick silicon sensor and used in upper and lower boxes, and "Long" modules (22 cm in length), built with two 410 μm-thick silicon sensors and used in side boxes. The Signal-over-Noise ratio (S/N) of the IT modules is about 15. A detailed explanation of the Inner Tracker readout chain and electronics will be given in Chapter 3, dedicated to the commissioning of the Inner Tracker.

Tracker Turicensis (TT)

The TT (Fig. 2.10, right), located between the RICH1 and the magnet, is composed of 128 half-modules arranged in four layers. The four layers have the same orientation as in the IT: two layers are vertical, and the other two are tilted by $+5°$ and $-5°$. In contrast to the IT it covers the full LHCb acceptance. The half-modules are made of seven 500 μm-thick sensors (each sensor is 9.4 cm long). The readout pitch is 183 μm, and the total number of channels is 143′360. The S/N ratio of the TT modules is about 12.

Outer Tracker (OT)

The Outer Tracker covers most of the 6×5 m^2 area of the T stations, with a small overlap with the IT acceptance. The boundaries between the IT and the OT have been chosen such as to limit the expected occupancy in the OT to 10%. A sketch of the T stations is shown in Fig. 2.11. The OT is composed of 4.9 mm diameter drift cells (straw tubes) arranged in four layers. The orientation of the layers is the same as in the IT and the TT. The cells are filled with a mixture of Ar, CF_4 and CO_2 gases, which has a drift time of less than 50 ns. The hit resolution is about 200 μm. In total, the OT consists of 168 long and 96 short modules, for a total of 55'000 readout channels.
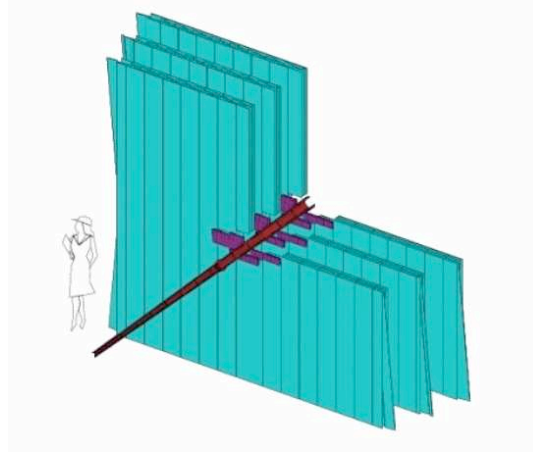
Figure 2.11: Sketch of the three T stations. The OT (blue) surrounds the IT (purple). The beam pipe (red) is also shown.

Magnet

In order to bend the charged particle trajectories and determine their momentum, a magnetic field is applied. It is provided by a dipole magnet, whose main field component is along the vertical y axis. The total integrated field is 3.7 Tm on average. The momentum resolution is $\delta p/p < 0.4\%$ for 40 GeV/c tracks. The warm magnet has a short ramping time, and its polarity is regularly flipped to reduce the systematic uncertainty associated to the P (parity) transformation. This is very important since P bias can alter the measurements of the CP asymmetries, which are one of the main goals of the experiment.

2.2.2   Particle identification systems

The particle identification consists in the discrimination between different particle hypotheses, such as K, π or μ. It is of great importance for LHCb, since it allows the separation of decays of the type $B \rightarrow hh$ where $h = \pi, K, p$ or $B_s \rightarrow D_s K$ and $B_s \rightarrow D_s \pi$, and allows the flavour tagging needed for CP asymmetry measurements in the b-quark sector. The particle identification system for LHCb consists of two RICH (Ring Imaging Cherenkov) detectors, the calorimeters, and the muon chambers.

RICH (Ring Imaging Cherenkov detectors)

RICH1 is located between the VELO and the TT, and RICH2 is located between the last T station and the calorimeters. They are based on the Cherenkov effect: when a charged particle traverses a medium with a velocity higher than the speed of light in this medium, an electromagnetic radiation is emitted at an angle θ with respect to the particle direction, given by

$$\cos\theta = \frac{1}{n\beta} \ ,$$

where $\beta = v/c$ is the velocity of the particle n the refraction index of the medium. The radiators are composed of silica aerogel ($n = 1.03$) and C_4F_{10} gas ($n = 1.0014$) for RICH1, and CF_4 ($n = 1.0005$) for RICH2.
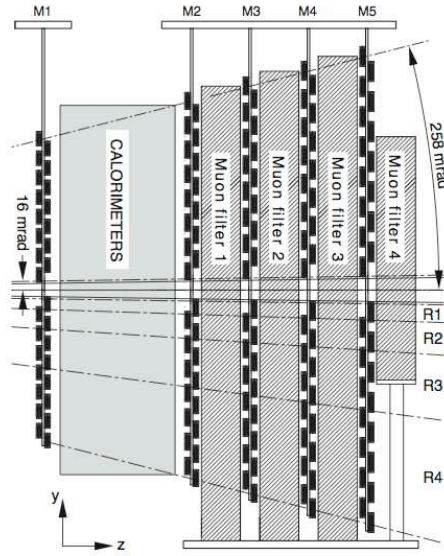
Figure 2.12: The muon stations.

Calorimeters

The calorimeters are located between the first and second muon stations M1 and M2. Apart from neutrinos and muons, they are stopping all particles and measure their energy. The calorimeter system is composed of the following items:

Scintillating Pad detector (SPD) and Pre-Shower detector (PS): The SPD and PS are made of 15 mm-thick scintillating pads on either side of a 12 mm-thick lead wall. The SPD is used to separate photons and electrons. This separation is used in the early stage of the trigger to reject high-E_T π^0 background. The PS converts incoming electrons in an electromagnetic shower, allowing the separation between electrons and charged pions. The SPD/PS system allows 99.6% $\pi^{\pm}$ rejection.

Electromagnetic Calorimeter (ECAL): This calorimeter is made of Shashlik-type modules, which consist of alternating 4 mm-thick scintillating tiles with 2 mm-thick lead slices. Unlike the SPD/PS, it contains the full electromagnetic showers created by photons and electrons.

Hadronic Calorimeter (HCAL): This calorimeter detects hadrons via their showers. It is made of 16 mm-thick iron plates alternated with 4 mm-thick scintillating tiles.

Muon chambers

The muon sub-detector is composed of five stations, M1–M5 (Fig. 2.12). The muons are the only charged particles that are able to traverse all the LHCb sub-detectors; all the other particles, except the neutrinos, are absorbed earlier. The muon stations are placed right after the calorimeters, except M1 which is before the SPD. They are of great importance for the trigger, since muons from b-hadron decays provide a clearly identifiable signature. Apart the inner region of the M1 station which is made of gaseous triple-GEM electron multipliers, the muon chambers

are made of multi-wire proportional chambers. Each station is divided into four regions with different pad granularity, to ensure uniform p_T resolution over the whole detector. The muon reconstruction needed for the trigger is achieved with fast matching between a T track (a track segment from the IT/OT stations) and a muon track.

2.2.3 Trigger

For nominal beam parameters and luminosity, the interaction rate in LHCb is expected to be about 16 MHz. A more interesting number is the "visible" rate, meaning the interactions that can be seen by the detector. This rate is expected to be about 10 MHz. Given the enormous amount of data that each sub-detector is producing, recording and analysing the full detector data for every interaction would be technically impossible. Moreover, not every interaction is interesting for physics analysis according to the LHCb physics program. It is therefore needed to have a real time ("online") selection, which decides which pp collisions are worth being recorded. This system, called "trigger", must reduce the nominal 10 MHz collision rate to a much smaller acceptable rate of 2 kHz – which will probably evolve over the years – while keeping the interesting decays for LHCb. In order to accomplish this task, two levels of triggers have been developed, the Level 0 (L0) trigger and the High-Level Trigger (HLT) [28].

The L0 trigger is a hardware trigger reducing the rate to 1 MHz, based on the calorimeter, muon and the Pile-Up veto, with a latency of 4.2 μs. A central decision unit (L0DU) combines the information of these subdetectors and takes a decision. The three components of the L0 trigger are:

Calorimeter trigger: it uses the fact that heavy b hadrons decay to low-mass particles with large p_T and E_T. The calorimeter is looking for either a hadron with $E_T > 3.5$ GeV, or a photon/electron with $E_T > 2.5$ GeV. Moreover, there is a veto if the total energy is below 5 GeV or if the SPD multiplicity is above 280.

Muon trigger: after having selected the two muons with the largest p_T, it requires that either at least one of them has $p_T > 1.2$ GeV/c, or that the sum of the p_T ot the two muons is above 1.5 GeV/c. In that case, the event is accepted anyway, even with a veto of another L0 sub-system.

Pile-Up: It is using two planes of VELO-like r-sensors, located upstream of the VELO. It detects events with more than one primary vertex. Since tracks cannot be reconstructed at 10 MHz, it is measuring the radial positions of the hits in the sensors, and gives an estimate of the z position of the origin of these tracks. The event is rejected if the pile-up system detects more than 112 particles or if more than one peak is found in the histogram of the origin z position.

The HLT is a software program running on an Event Filter Farm consisting of $\sim$ 2000 CPUs, and operating at the L0 output rate of 1 MHz. It is reducing the rate to the acceptable rate of 2 kHz. HLT is divided into two sub-levels: HLT1, which performs a selection on tracks with partial information from the sub-detectors, and HLT2 which runs specific inclusive or exclusive selections using the complete detector information. A schematic view of the trigger system is depicted in Fig. 2.13.

2.2.4 Software

Any physics analysis requires preliminary simulations, in order to determine the selection cuts, quantify the detector response or simply test the software. The simulations are using Monte
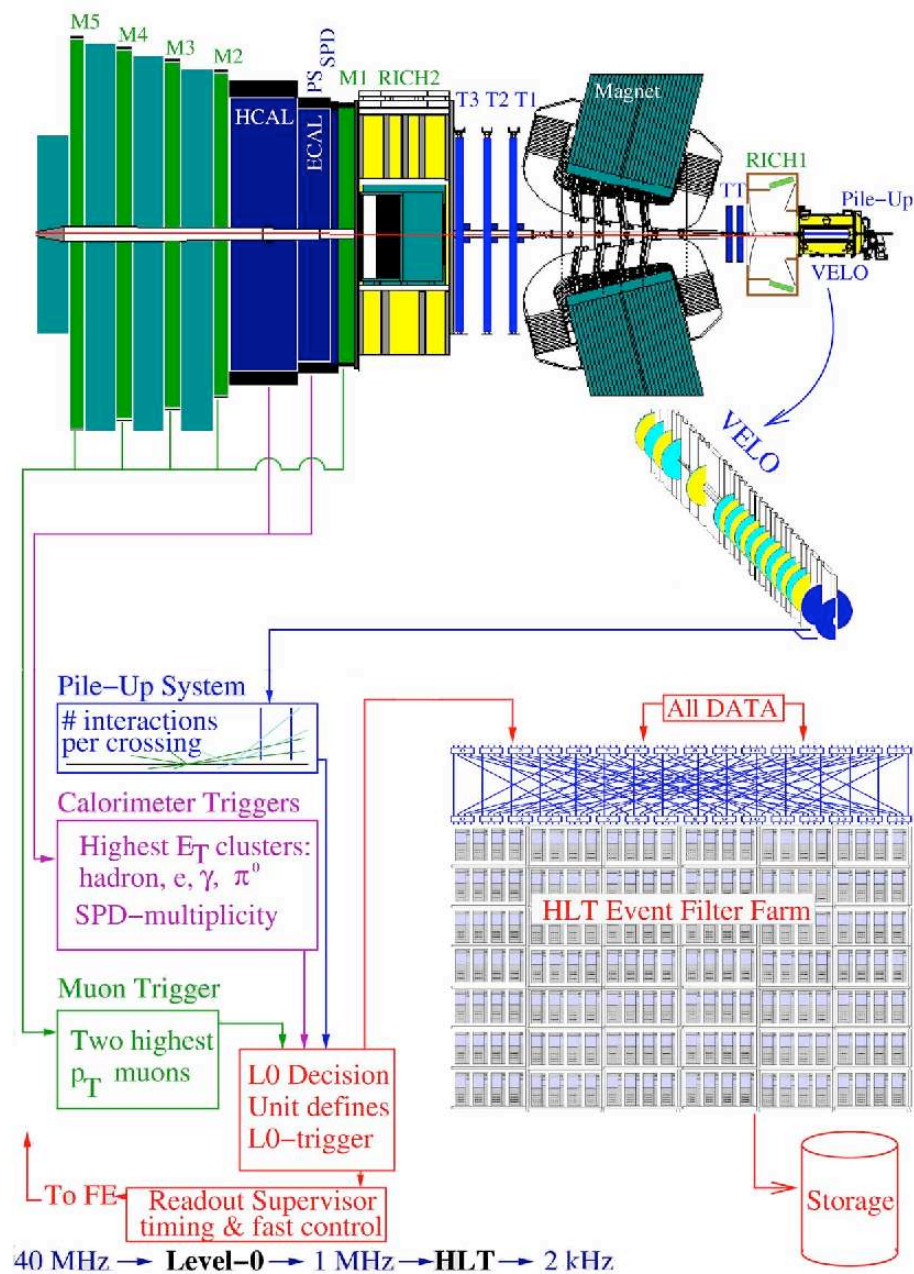
Figure 2.13: The trigger system.
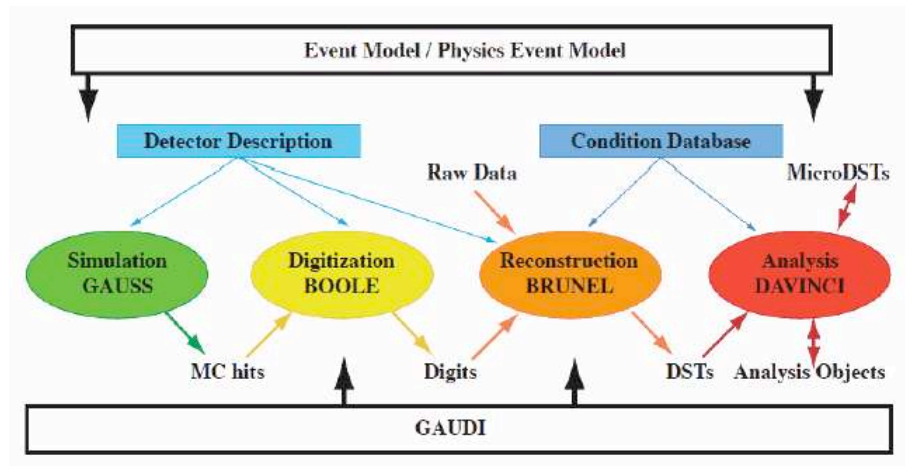
Figure 2.14: The LHCb software chain.

Carlo (MC) numerical techniques, based on randomly generated numbers. The LHCb software is subdivided in several applications, which are each perfoming a particular task. These programs are all running under the GAUDI framework [29], which serializes the algorithms from the different applications. These applications are the following (Fig. 2.14):

GAUSS [30]: This application generates the pp collisions according to known or expected physical processes using the PYTHIA package [31] and the decay of the generated particles is performed by the EVTGEN package [32]. The radiative corrections are handled by the PHOTOS package [33]. The particles are then passed through a detector simulation, during which the magnetic field effect and the physics interactions in the detector material are simulated using the GEANT4 package [34].

BOOLE [35]: This application simulates the detector output due to the passage of GAUSS-generated particles through the detection layers. It simulates the behavior of the readout electronics and the L0-trigger hardware, and produces an output with the same format as the output of the real detector.

BRUNEL [36]: This application is also used for real data, as it reconstructs the tracks from either simulated hits from BOOLE in the case of MC simulation, or real hits from real particles. It provides a Data Summary Tape (DST) as output.

DAVINCI [37]: This application allows the user to perform any physics analysis, based on tracks or particles (track+identification) coming from BRUNEL. Any user algorithm can be integrated for custom analyses.

Commissioning of the Inner Tracker

The Inner Tracker is one of the key detectors of LHCb. It measures the particle passage points in the area close to the beam-pipe, where the track multiplicity is highest. I have worked on various development stages of the project, from the initial testing of the silicon modules, to the commissioning with the first LHC injection tests. The concepts and abbreviations already introduced in Sec. 2.2 are not redefined here, I invite therefore the reader to refer to this section whenever needed.

Since the beginning of my Ph.D. studies I have been involved in various tasks related to the building and commissioning of the Inner Tracker. I had the opportunity to work for the Inner Tracker at the most exciting stage of the project, when the R&D was mainly finished and the installation started. After my participation in the module testing, installation in the pit, and data acquisiton and monitoring software development, I have performed the analysis of the first calibration data produced by cosmic rays. Initially, a commissioning with cosmic rays was never thought possible due to the horizontal orientation of LHCb and the small coverage of the Inner Tracker. However, it was clear that some cosmic rays were crossing the IT, though at a quite low rate ($\simeq 1$ every two minutes). It was therefore an interesting challenge to reconstruct their trajectories. The search was successful, and allowed a preliminary synchronization (time alignment) and space alignment.

After the commissioning with cosmics, the first "beam data", consisting of secondary particles produced in beam dumps during LHC injection tests, allowed a very precise time alignment. The spatial alignment could also be performed, though only at a rough level, due to the high track multiplicity.

In the next sections, I will summarize my personal contributions to the commissioning, after a description of the Inner Tracker readout chain in terms of hardware and software. I will start from a general view of the readout, and further give some more detailed description of the main building blocks of the chain: the Beetle readout chip, the Digitzer Boards and the TELL1 readout board.
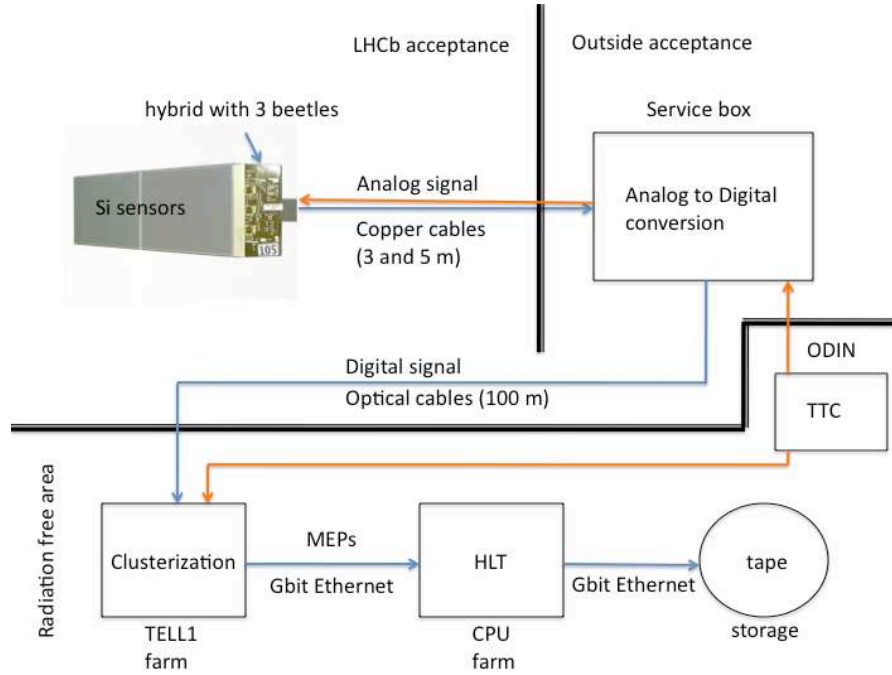
Figure 3.1: Simplified block diagram of the IT readout.

3.1 Inner Tracker readout chain

The readout chain is pictured in a simplified block diagram in Fig. 3.1. Each Inner Tracker box is filled with 28 modules of 384 readout channels each. The silicon sensors – one on "short" modules and two on "long" modules – are mounted on a carbon fibre structure, called "ladder", providing mechanical resistance, heat dissipation and allowing assembly with the front-end (FE) electronics (Fig. 3.2). The FE electronics consists mainly of three integrated circuits called "Beetles", soldered on a printed circuit board (PCB) called "hybrid". Each of these Beetle chips handles 128 readout channels. A charged particle passing through the bulk silicon of a sensor produces an electrical signal that is propagated to the Beetle. The two main functions of the Beetle are the amplification and shaping of the electric signal, and the storage of the data in an analogue pipeline while waiting for a trigger. The pipeline stores the values of the signal for each channel and each slice of 25 ns. A number is associated to each of the positions in the pipline, called the "Pipe Column Number" (PCN). Whenever a trigger signal is received by the Beetle, the corresponding event is picked up. There are 160 pipeline positions in the Beetle, corresponding to the L0 trigger latency of 4 μs. See Ref. [38] for details.

The Beetle serializes the amplified signal for all the 128 channels into 4 streams of 32 channels. This allows the transfer of the information through 4 parallel communication ports per Beetle, increasing the transmission speed. Since each module contains three Beetles, the output of a full module consists therefore of 12 analog ports. The 12-fold signal is then propagated through the PCB of the box cover into copper cables. The copper cables carry the signals outside of the LHCb acceptance, into the digitizer boards inside the "Service Boxes". These boards are converting the analog signal into a digital signal (ADC, "Analog-Digital Converter", 8-bit value). Each analog value for a given channel corresponds therefore to an ADC value between 0 and 255. The digital signals are then transferred via 100 m optical fibres into a radiation free area, where they enter the TELL1 readout boards.
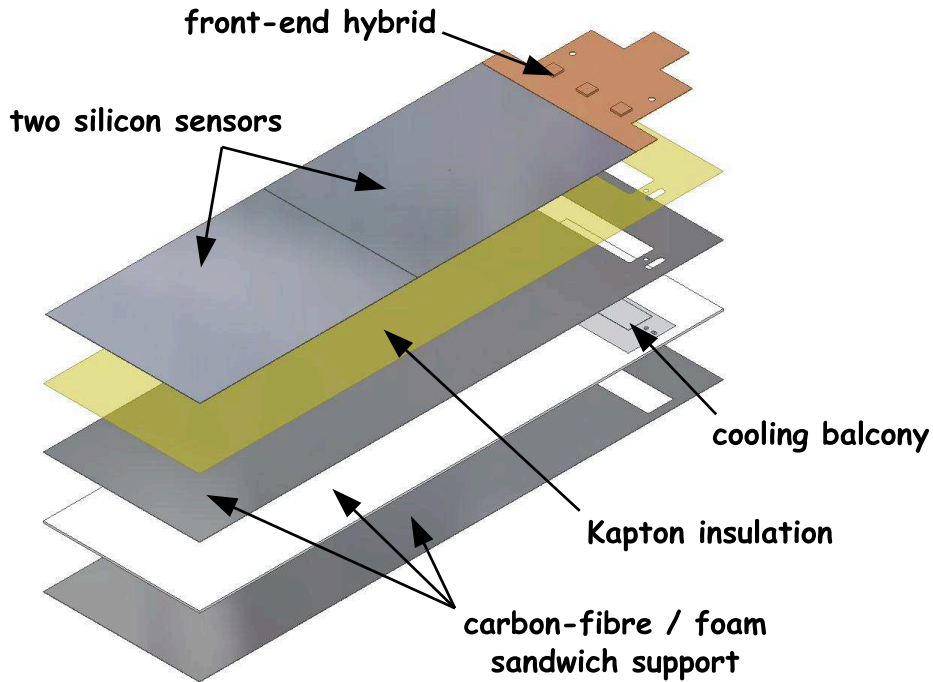
Figure 3.2: Exploded view of an IT module.

The TELL1 board, described in detail in Sec. 3.1.3, is executing various algorithms on the data, and provides compressed information in the form of a list of hit positions and charges. It is sending the data via Gigabit Ethernet cables directly into the High-Level Trigger CPU farm, where the data are merged with the other sub-detector data. After analysis by the HLT, the selected data are finally recorded on tape for offline analysis.

The L0 hardware trigger signal, generated from the observed signals in other sub-detectors such as the ECAL and SPD, is sent by another board called "Readout Supervisor" [39], which also provides the synchronisation with the LHC machine. The ODIN is responsible for Timing and Fast Control (TFC), sending a TTC (Time Trigger Control) signal to both the TELL1 and the Digitizer Boards, where the signal is propagated into the FE electronics. The fast control (trigger, clock, IP-protocol addressing) is named so by opposition with the slow control (programming and monitoring of the various electronics).

3.1.1 Beetle chip and signal pulse-shape

The Beetle chip is a radiation-hard integrated circuit bonded to the channels on the hybrid. It allows fast amplification, shaping and storage in an analogue pipeline. The shape of the pulse can be fine-tuned to comply with the LHC/LHCb requirements. The peaking time has to be 25 ns, and the remainder (fraction of the signal 25 ns after the peak) has to be lower than 30% to avoid spill-over[1]. The shape of the pulse is a semi-Gaussian[2] and can be characterized by three parameters (Fig. 3.4, left):

- peaking time t_p $(0\% - 100\%$ of the signal) or rise-time t_r $(10\% - 90\%)$;

---

[1]The "spill-over" is a ghost hit that remains from the previous bunch crossing.

[2]A semi-Gaussian is a function of the form $f(t) = g(t^n)e^{-t/\tau}$ where $g(t^n)$ is a polynom. These functions describe well the output of a CR-RC shaper.
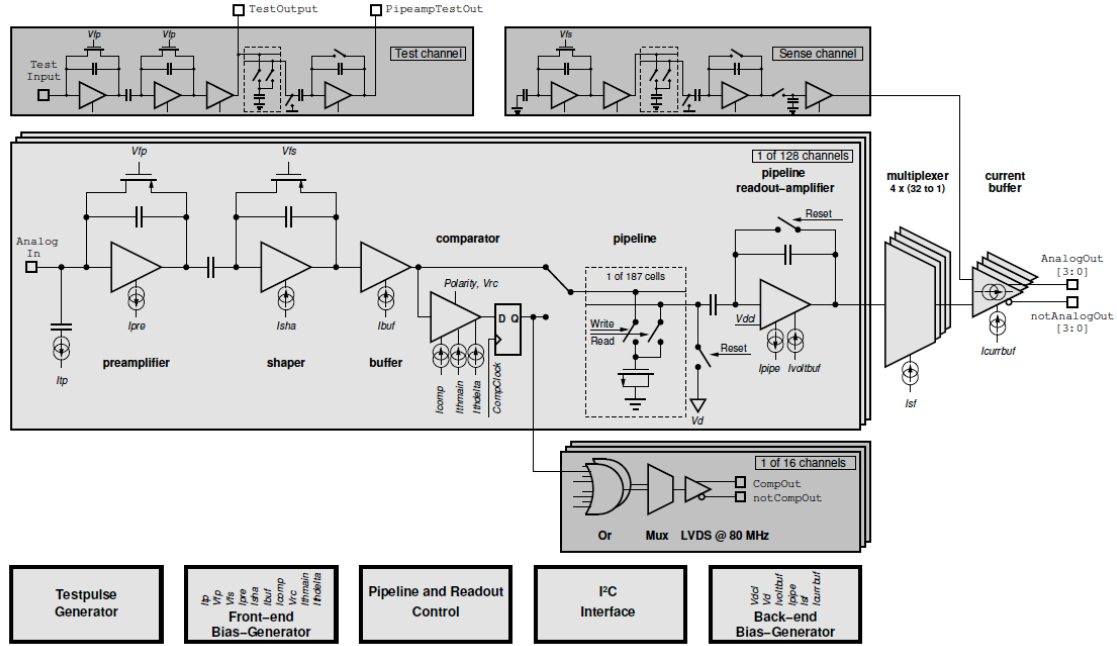
Figure 3.3: Block diagram of the Beetle readout chip [38].

- peaking voltage V_p;

- remainder $R = \frac{V(t_{\max}+25 \text{ ns})}{V(t_{\max})}$, where $t_{\max}$ is the time of the maximum of the pulse.

Five parameters allow the tuning of the shape of the pulse (Fig. 3.3): the pre-amplifier bias current (I_{pre}), the shaper bias current (I_{sha}), the buffer bias current (I_{buf}), the pre-amplifier feedback voltage (V_{fp}) and the shaper feedback voltage (V_{fs}). These parameters allow for instance to increase the signal, with the drawback that the remainder will also be larger. Examples of pulse-shape obtained with different parameters are shown in Fig. 3.4 (right).

3.1.2 Service Boxes

The Service Box (SB) (Fig. 3.5) consists of a Control Board (CB) and up to 16 Digitizer Boards (DB). Each DB treats the data of a single detector module (384 channels). It is located outside the LHCb acceptance, but still in a high radiation area. The DB are responsible for digitization of the data, and for their optical transmission to the TELL1s via the CERN GOL (Gigabit Optical Link). The CB is responsible for carrying the slow control (SPECS protocol), and the fast control (TTC signal) to the FE electronics and the DBs. The output of the DB is carried via 100 m optical-fiber cables into the TELL1s, in the radiation protected area.

3.1.3 TELL1 boards

The TELL1 readout board [40], also used by several other sub-detectors, is the last piece of hardware handling the data before software processing. Its purpose is to read the digital signals for each port of 32 channels, and to execute various algorithms on the data.

The first algorithm run by the TELL1 board is the pedestal subtraction. The pedestal of a channel is obtained as the average of the ADC count over a large number of events, and regularly
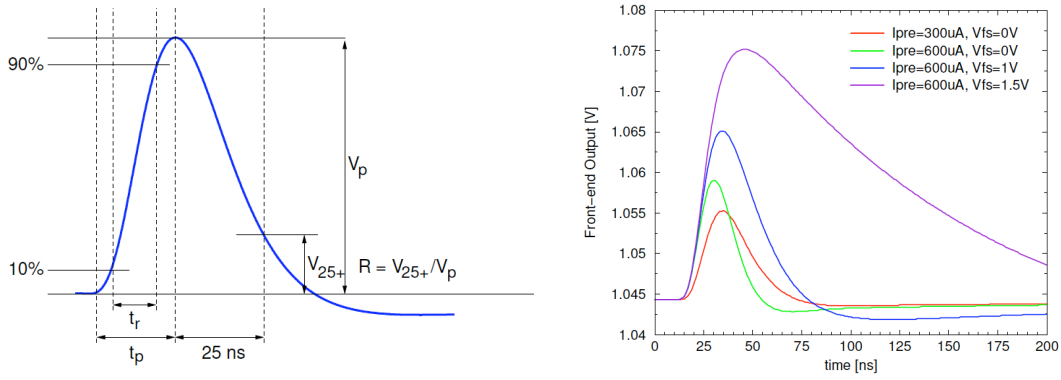
Figure 3.4: Left: Shape of the pulse after the shaper. Right: pulse-shapes obtained with various shaping parameters. Taken from Ref. [38].
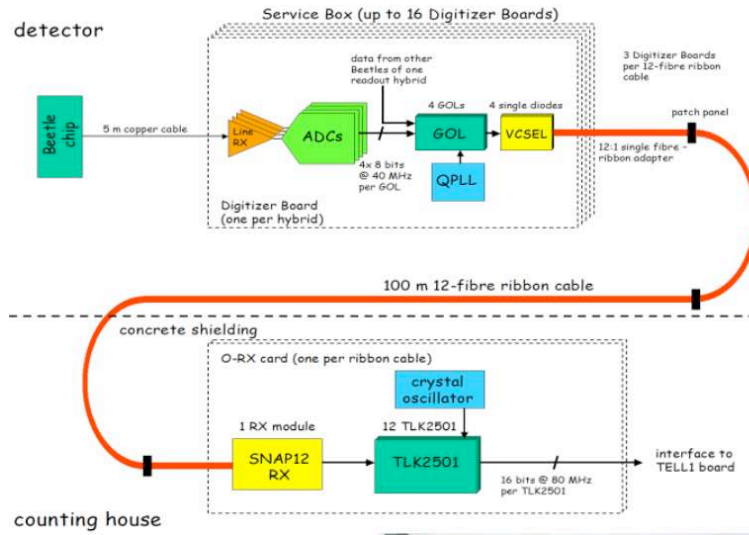
Figure 3.5: Diagram of the digitizer boards and TELL1 optical receiver card (O-Rx).

updated and monitored. The next algorithm is the linear common-mode noise suppression (LCMS), which removes the component of the noise which is correlated between the channels of a given port. In addition, the first channel of each port has to be corrected as it suffers from header cross-talk, since it is the first channel to be sent in the serial transmission, just after the header bits.

Finally the clustering algorithm is executed. Firstly, a threshold cut is applied on the signal of the channels, based on their noise level which has been previously measured. The ADC values of the channels that are below threshold are set to zero. Secondly, the sharing of the signal between the different channels[3] allows the finding of the "centre of gravity" of the particle passage point, in terms of a fraction of the channel pitch. The information of the centre of gravity and the total energy is called a "cluster". The output data from the TELL1 board is therefore a list of clusters with their sizes, total charges and positions.

---

[3]A particle traversing a silicon channel induces a signal in the neighbouring channels. A cluster can therefore be formed of 1, 2, 3 or 4 channels, depending on the energy loss.

The TELL1 board is mainly composed of a mother board, on which several daughter boards are integrated. The main elements are (Fig. 3.6):

Receiver cards: There are two types of receiver cards, analog (A-Rx) and optical (O-Rx). Most of the sub-detectors are using the optical transmission system from the FE to the TELL1, apart from the VELO which is using analog transmission[4].

4 PP-FPGA (Pre-Processing Field Programmable Gate Arrays): These programmable chips are performing the pedestal subtraction, LCMS and clustering algorithms. Each PP-FPGA handles the output of 6 Beetle chips (768 channels).

SyncLink-FPGA: This FPGA distributes the TTC signals and synchronizes the data coming out of the four PP-FPGA. It also encodes the data and produces Multi-Events Packages (MEP) that are sent via the IP protocol to a Gigabit Ethernet network.

Gigabit Ethernet (GBE) card: The MEP packets are distributed to the network via four Gbit ethernet ports to the HLT[5] farm.

TTCRx: This card is an optical receiver for the TTC signal. The main information are the trigger, reset information, clock, and main IP destination address.

Throttle: The size of an event is variable, since it depends on the detector occupancy. Whenever the TELL1 is saturated with triggers and the output rate is lower than the trigger rate, a "throttle" signal is sent to the Readout Supervisor which slows down the trigger rate until the TELL1 is below saturation again.

Experiment Control System (ECS): This slow control allows the programmation and monitoring of the TELL1. It mainly consists of a "Credit Card PC" (CCPC), a small PC operating under Linux.

The TELL1 board is designed to send various data banks, depending on the running conditions. In nominal running conditions, the TELL1 sends a list of clusters with their positions and total charges, called "Zero-Suppressed" (ZS) data bank. In addition, there are several other possible data banks. For instance, for analysis of the raw data, the TELL1 can send the "Non-Zero Suppressed" (NZS) bank, consisting of the ADC values for all the channels. The pedestal, defined by the mean of the ADC value without signal for a given channel, is also calculated and can be sent via the "Pedestal" bank. Whenever an error is detected in one of the optical links or one of the PP-FPGAs, an "Error" bank is sent. The data formats and information contained in the banks are given in Refs. [43, 44, 45, 46].

3.2 Personal contributions to the Inner Tracker commissioning

The building, testing and commissioning of a complex device such as the Inner tracker required many stages performed by a wide team for several years. Since a complete description of all these stages would be outside the scope of this document, I will describe only my personal contributions. I summarize the main topics I have contributed to in the list below.

---

[4]The digitization of the data for the VELO is done inside the TELL1. Indeed, very hard radiation environment and tight space around the VELO prevented to setup a digitization device close to the VELO.

[5]High Level Trigger, see Sec. 2.2.3.
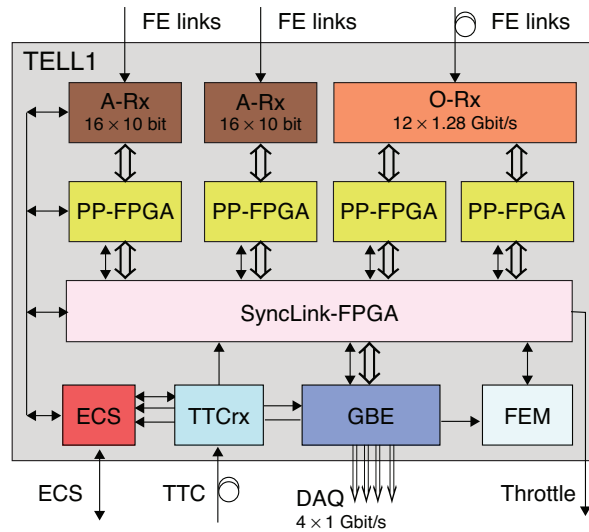
Figure 3.6: Simplified block diagram of the TELL1 board.

Gluing tests for the cooling rods: the cooling pipes of the Inner Tracker, which are carrying the refrigerant C_6F_{14} for power dissipation, are glued on the "cooling rods", small aluminium bars on which the silicon sensor modules are screwed. The heat transfer was not optimal, and I was given the task of improving it while maintaining mechanical resistance. I have performed heat transfer and mechanical resistance measurements. My results showed that the gluing procedure had to be changed, and the new method I proposed was used for the final gluing [41].

Building of a readout setup for laboratory testing: before the Inner Tracker boxes could be brought down in the LHCb cavern, they needed to be extensively tested using the same hardware and software as in the LHCb experiment. I have built a setup designed to work as closely as possible to the LHCb running conditions. This setup was used for all the final testings of the boxes before they were installed.

Silicon modules testing: in order to test and stress the silicon sensors together with their electronics before they were installed in the boxes, an artificial ageing was simulated by a temperature cycle between -5 and $+40$ degrees Celsius, once every hour and a half over a span of 48 hours. I have participated in the testing of the 336 Inner Tracker modules, which consisted in operating the system, introducing the discovered faults in the database and running the corresponding software [42]. In addition, I have participated to the measurements of the leakage currents of each sensor when the high voltage is applied. I have also participated in the metrology survey of the sensors, measuring optically the offsets observed between the actual position of the sensor on the module and their nominal position.

Noise source searches: An excess of noise was detected in the data coming from the IT modules. A series of tests have been performed to find the cause by studying the modules, the cables, the electronics and the IT boxes [42]. I was part of the working group that was created for identification of the noise source. The problem was finally solved by addition of a filter on the digitizer boards.

Installation: I have participated in some steps of the installation process in the LHCb UX85 cavern in Ferney-Voltaire. These included plugging and mapping of the readout cables, isolation of the cooling pipes, and installation of various hardware elements.

DAQ software: I have integrated the testing setup described above inside the LHCb framework, written the decoding of several data banks, and installed and tested the software in the LHCb control room.

Monitoring: My experience in the DAQ software naturally brought me to the data monitoring, for which I have developed the software.

Cosmics searches: The monitoring and data analysis software I have developed allowed the identification of the first cosmic ray tracks in the Inner Tracker, which was challenging since the rate of triggered cosmics that are passing through the IT is quite small. The cosmic analyses that were done later provided a first estimate of the time settings of the Inner Tracker, and a first approximate space alignment.

Time alignment with the LHC injection tests: The LHC injection tests ("TED runs") allowed the measurement of the charge distribution of the hits in the modules, and precisely determine the time delays that needed to be set in order to synchronize the readout electronics components of the detector ("time-alignment"). It was the very first in-situ test with "beam data".

The last three items are described in more details in the next sections, respectively in Sec. 3.2.1, Sec. 3.2.2 and Sec. 3.2.3.

3.2.1 Monitoring

The data-quality monitoring is providing immediate observation of the output data from the sub-detectors. It has to be distinguished from the ECS (Experiment Control System) monitoring, which monitors the proper operation of the detector in terms of low-voltage, high-voltage and cooling. The output data from the TELL1 boards are decoded and stored in a temporary memory (Transient Event Store, TES), and custom algorithms can be created to publish histograms of the data.

The produced histograms can be displayed in quasi-realtime, depending on the data taking rate. At low trigger rates, the refreshing rate of the display of the histograms corresponds to almost real-time. However at higher rates, the display is only refreshed after a fixed number of events.

I have written the monitoring algorithms for the IT as well as TT, and integrated them in the existing LHCb online software framework. The histograms can be displayed and analysed online via an interface, and saved into a database [47]. The algorithms I have created were an initial version of the monitoring software, that was used for cosmics and LHC injection tests. The list of histograms implemented is given in Table 3.1. The items in bold, ADC values and noise, will be presented in more detail in the next sections.

The histograms mentioned in Table 3.1 are a preliminary version of the current monitoring tools mainly used in 2008, which continued to evolve during the 2009 and 2010 data-taking. The choice of histograms were based on several requirements relevant at the time of the commissioning. For instance, the "Live" cluster map was especially dedicated to the cosmics. The monitoring histograms were used mainly by the shift team. All the information contained in these histograms are still available for offline analysis.

Table 3.1: Histograms implemented in the monitoring. In the table, x_i = raw ADC value, x_{CMS} = pedestal and LCMS-subtracted ADC value, n = number of events used for the average. "PCN" stands for "Pipe Column Number", a 8-bit number assigned to every position in the analogue pipe-line.

Bank	Name	Value (if not clear from the name)	Histogram type	Histogram multiplicity
NZS	**Raw noise**	$\sqrt{\frac{1}{n}\Sigma_i^n (x_i - \bar{x})^2}$ vs. channel	graph	1 per module
NZS	**CMS noise**	$\sqrt{\frac{1}{n}\Sigma_i^n (x_{\mathrm{CMS},i} - \bar{x}_{\mathrm{CMS}})^2}$ vs. channel	graph	1 per module
NZS	**Raw ADC**	x_i	1D hist.	1 per module
NZS	**CMS ADC**	$x_{\mathrm{CMS},i}$ vs. channel	2D hist.	1 per module
NZS	Headers		1D hist.	1 per module
NZS	PCN	PCN vs. Beetle	2D hist.	1 per module
ZS	Num. of clusters		1D histo	1 per station
ZS	Cluster charge		1D histo	1 for IT +1 per station
ZS	Cluster size		1D histo	1 for IT +1 per station
ZS	Neighbour sum		1D histo	1 for IT +1 per station
ZS	Rel. neigh. sum		1D histo	1 for IT +1 per station
ZS	**Cluster map**	x vs.z cluster position	2D histo	1 for IT
ZS	**"Live" cluster map**	x vs.z cluster position	2D histo	1 for IT
Error	PCN Error	0 or 1	1D histo	1 per PP-FPGA
Error	Sync RAM Full	0 or 1 vs. Opt Link	2D histo	1 per PP-FPGA
Error	TLK Link Loss	0 or 1 vs. Opt Link	2D histo	1 per PP-FPGA
Error	Sync Event Size Error	0 or 1 vs. Opt Link	2D histo	1 per PP-FPGA
Error	Opt. Link No Event	0 or 1 vs. Opt Link	2D histo	1 per PP-FPGA

Raw and CMS ADC

The raw ADC histogram (Fig. 3.7, left) shows the raw information from the detector. The ADC values of all channels of a module are filled in a single histogram, before any pedestal or CMS subtraction.

The CMS ADC histogram (Fig. 3.7, right) allows all the information to be kept on the ADC counts after pedestal and CMS noise subtraction, without any averaging. It gives a visual representation of the noise (given by the r.m.s in y), and deviations from the pedestals. For instance, when real particles are traversing the IT, few data points at higher signals are visible. This histogram has the disadvantage of requiring lots of CPU power and memory, it can therefore be de-activated on demand.
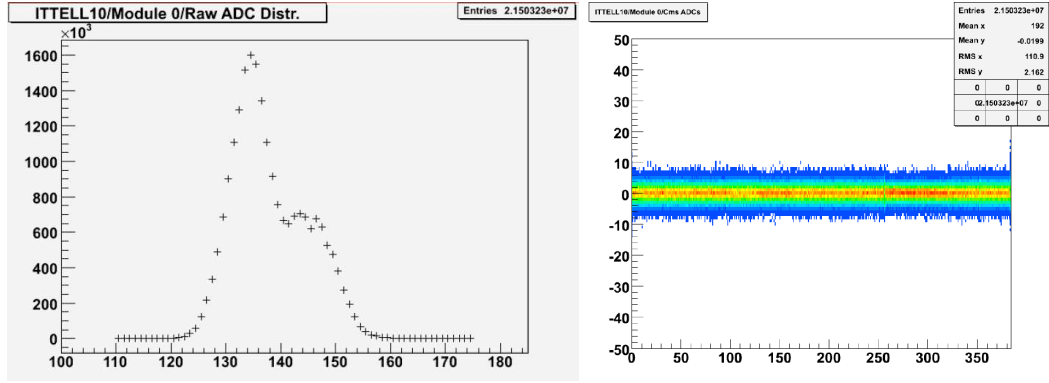
Figure 3.7: Left: Raw ADC distribution for one module. Right: 2D-distribution of CMS ADC counts versus channel number for a particular module. The RMS in y corresponds to the noise, and the mean compatible with zero in y is due to the fact that the data used for this plot does not contain any signal.
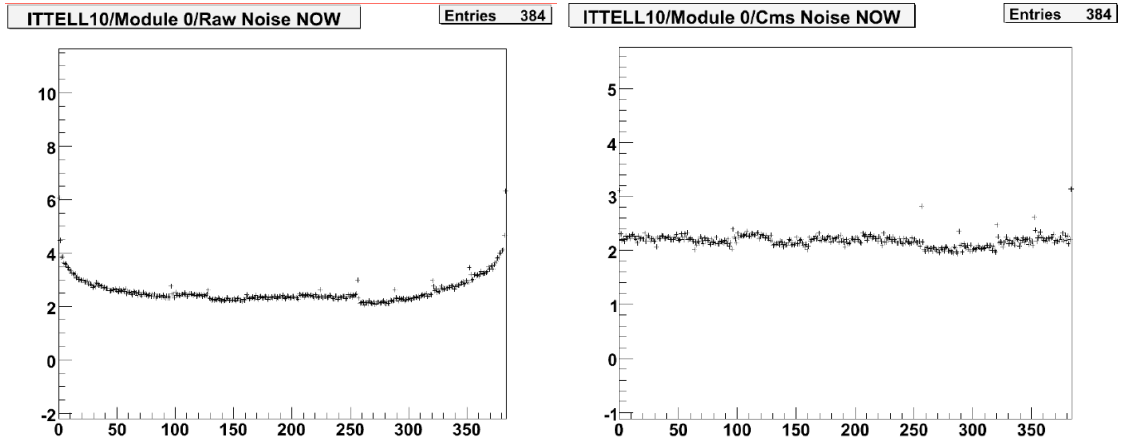
Figure 3.8: Left: Raw noise for a particular module, calculated over the last 2000 events. The U-shape of the noise is typical for most of the modules. Right: Common-Mode Subtracted (CMS) noise for the same module. The U-shape, which disappeared, corresponds to the noise correlated between the channels.

Noise distributions per module

The raw and CMS noise plots per module allow a monitoring of the noise calculated over a certain number of events. This number depends on the trigger rate, and can be set manually. An option is also provided, allowing the calculation of the noise over all the previous events. The raw noise is calculated using the raw ADC counts per channel, and the CMS noise based on CMS-subtracted ADC per channel. Figure 3.8 shows the raw and CMS noise for a particular module. The typical U-shape of the raw noise comes mainly from edge-effects along the module. After CMS subtraction, by definition the common component to all the channels disappears and the individual component remains – ~ 2 ADC counts for most of the modules. There are also spikes visible every 32nd channel, corresponding to the first channel of each port which suffers from header cross-talk[6].

---

[6]Before the analog serialized transmission of the data from a Beetle port (32 channels), three "headers" are sent to start the transmission. The last header bit influences the level of the signal of the first channel of each
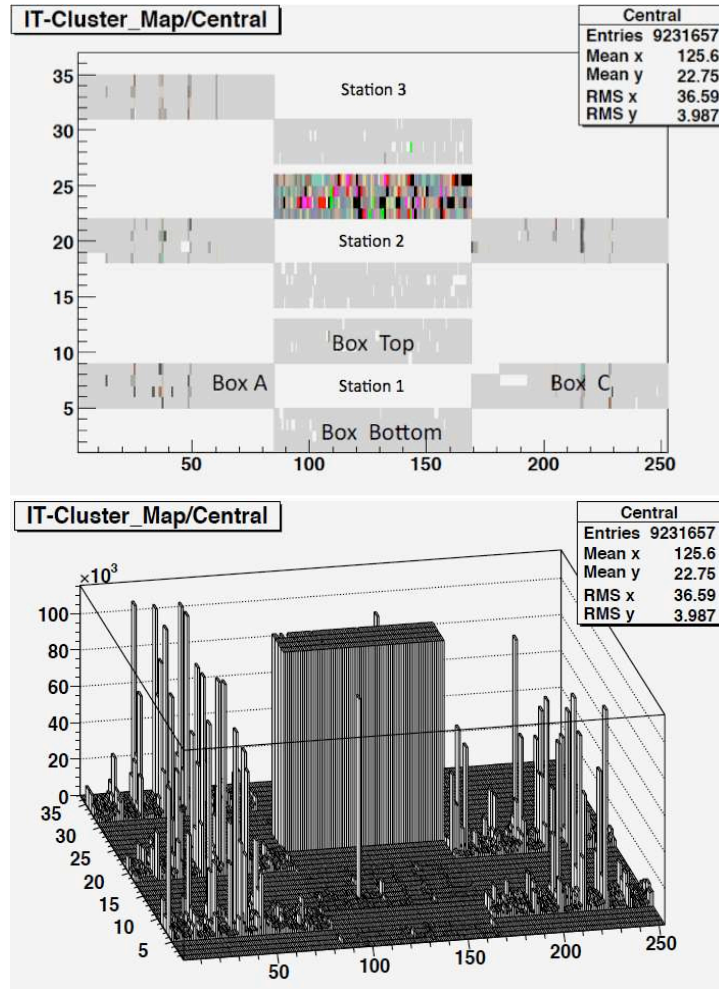
Figure 3.9: Top: Cluster map in 2D display. Bottom: Same plot in 3D. Side boxes, made of long modules, are usually more noisy.

Cluster maps

The cluster map gives information on the location of clusters. Cluster positions are displayed on the x-z plane. In order to simplify the display, the x-binning has been chosen to correspond to a port (32 channels), and the z binning to a layer. The three stations are plotted on the same 2D histogram, and for simplicity the 4 boxes of each station are drawn as a cross, with top box on top, bottom box on bottom, and side boxes in each side. The cluster map is depicted in Fig. 3.9.

This representation doesn't correspond exactly to the x-z position of the clusters, but allows a very quick representation and immediate problem identification. For instance, Fig. 3.9 shows clearly that, due to the absence of clusters, no data are available for the top and C boxes of Station 3. One can spot also that there is an excess of clusters in the top box of Station 2, which was identified as an excess of noise due to a malfunction. One can also see deactivated beetle ports, beetles or modules, materialized by white blocks inside a particular box. For instance, two modules in the C box of Station 2 were not operating at the time of the measurement.

---

port, being sent right after the last header. This effect is called "header cross-talk".

Noisy ports can also be spotted easily. This map can be compared immediately to the known problems, to check whether the problem is new or not. By default, all the clusters are summed up on this plot, but the refreshing or reset option can be changed.

The "live" cluster map is a variant of the cluster map, showing the clusters from a single event, rather than an accumulation of all the clusters from a certain number of past events. The display of a single event requires a set of conditions to be fulfilled. For instance, the "cosmic" condition (see Sec. 3.2.2) allows the display of events containing tracks from cosmic rays. Historically, this histogram was dedicated to cosmics, although it can be used for a different purpose. Examples of these "live" cluster maps are given in the next section.

3.2.2   Cosmic muons

Due to the LHCb geometry, cosmic muons were initially not thought to be usable for the commissionning of the Silicon Tracker. However, they were used for the commissioning and time-alignment of the calorimeters. A trigger based on the coincidence ECAL+HCAL provided a rate of ~ 11 Hz in the calorimeters, most of the events being cosmic muons.

Since no other data were available at that moment for time and space alignment, it was finally attempted to use cosmic muon hits for the IT and OT. The cluster map, together with the charge distribution, allowed easy finding of cosmic muons hits in the IT. A cosmic candidate was defined as an event with at least one cluster of charge larger than 17 ADC counts in each layer of a given box, after masking the noisy ports[7], mainly consisting of the first two channels of each port due to header cross-talk. Whenever this condition was fulfilled, the cluster map for this particular event was displayed. This very simple algorithm gave immediate results. Some of the observed cosmics are shown in Fig. 3.10. The proximity of the clusters and their alignment gives confidence that they originate from a real track. Later, the extrapolation of the tracks to ECAL/HCAL hits confirmed the cosmic nature of these events.

In total, about 1000 good quality cosmic tracks were found in at least one IT box, in a sample of 2.6 million CALO-triggered events, and three of them were passing through all three IT boxes ("golden cosmics", Fig. 3.11). Such tracks were of great help since they were the only way to obtain a first estimate of the time and space alignment.

3.2.3   Time-alignment during TED runs

In September 2008 and June 2009, injection tests were performed with the LHC machine. These tests consisted of injecting 450 GeV protons in the transfer line from the SPS to the LHC. Bunches of 2–5×10^9 protons were dumped onto a beam stopper (TED), located in the transfer line. Since LHCb is located 350 m downstream of the cone of secondary particles produced by the beam dump, it was possible to observe these particles, about 1000 to 2000 per event in the LHCb acceptance. The data were collected without magnetic field. The analysis of the TED events was challenging, since particle densities in the Inner Tracker were about ten times larger than expected in a typical $b\bar{b}$ event from a pp collision, leading to strip occupancies up to 8%.

The goal of the time alignment was to synchronize the maximum of the signal amplitude from the output of the front-end electronics with the sampling time given by the LHC clock at 40 MHz. Different timings had to be set for each specific part of the IT or TT. The timings depend on three parameters: the time of flight between the tracking stations, the signal cable lengths which are different for various parts of the detector, and the different capacitances between the detector modules due to the different readout strip lengths.

---

[7]At that stage of the commissioning, no database with the thresholds for each channel was available.
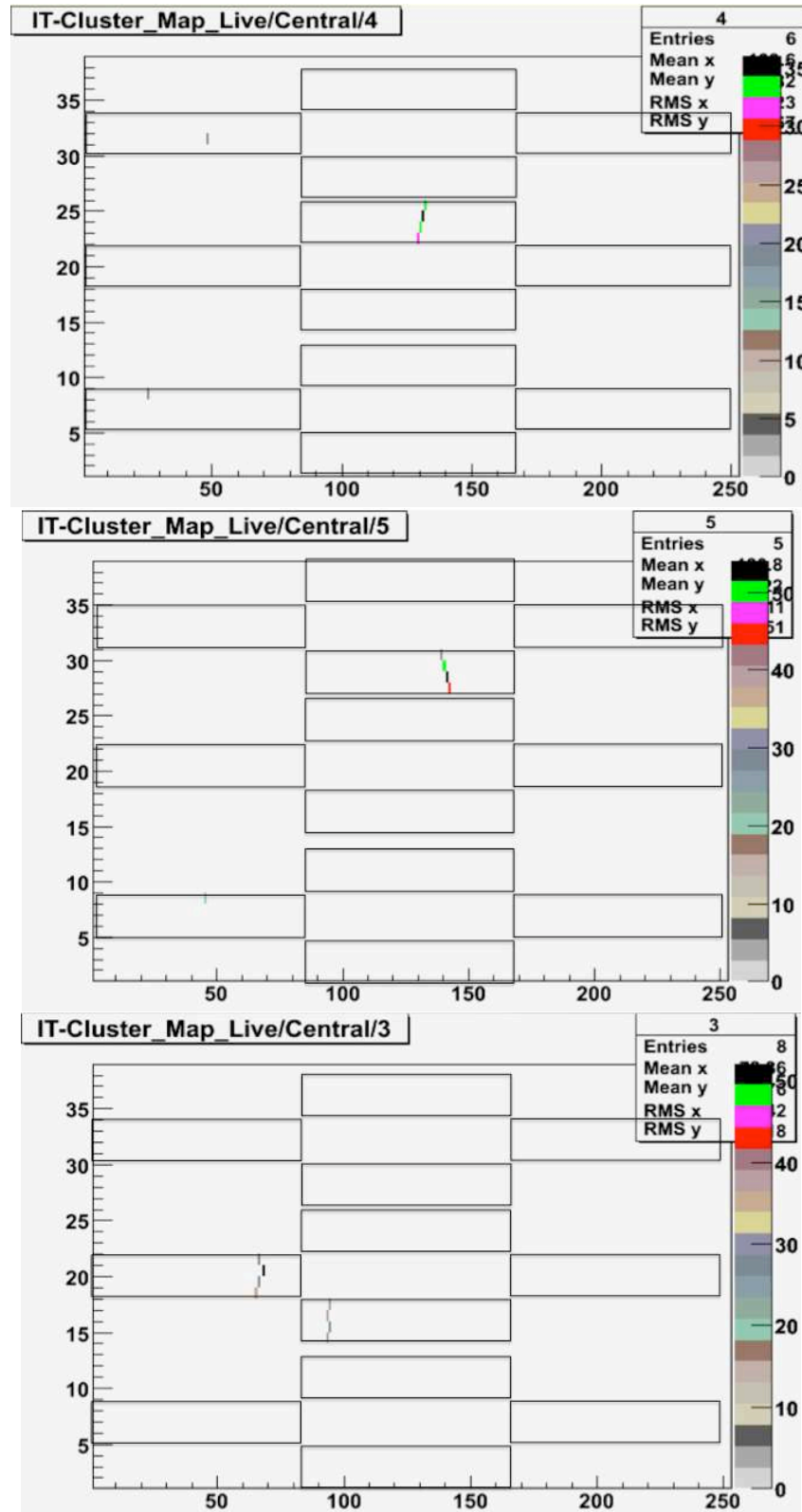
Figure 3.10: Three "live" cluster maps showing cosmic tracks. On the bottom, the two muons are coming from a probable cosmic-initiated secondary shower. These arise when a cosmic triggers a hadronic shower after hitting a nucleus of, for instance, the HCAL.
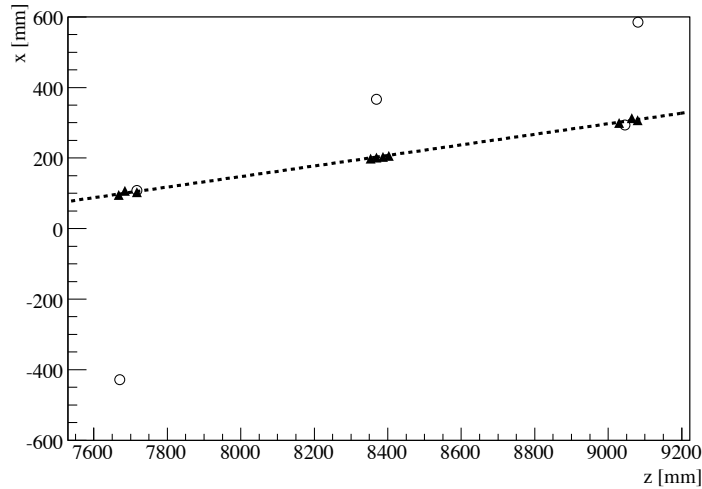
Figure 3.11: Position of the hits in an event with a cosmic particle traversing all three IT boxes, shown in the x-z view (z coordinate of the sensor, x coordinate of the mid-point of the sensor). There are three groups of four aligned hits, corresponding to the four layers of one box in each of the three stations. Triangles are hits associated to the track while circles are other hits in the event. Figure by Matthew Needham.

The method used to find the time of the maximum signal was to reconstruct the pulse shape as a function of time, by taking several data points with different time delays between the LHC clock and the signal sampling time. The signal amplitude for each delay was determined from the measured charge distribution of all the clusters (not only the ones associated to a track) as described below. Although we show figures only for IT, the TT was time-aligned using the same technique.

The charge distribution of $\simeq 10$ GeV/c muons passing through a given thickness of silicon can be described by the convolution of a Landau distribution with a Gaussian function. The Gaussian width takes into account the effect of detector noise and atomic binding. A typical distribution is shown in Fig. 3.12 (left). The region around the maximum of the distribution is well described by the fitting function. The small peak just above $\simeq 10$ ADC counts is the tail of the noise distribution. There is a knee in the tail of the curve around 80 ADC, which is due to merged clusters coming from two distinct particles[8]. The quantity used to measure the signal from the charge distribution is the most probable value (MPV).

Several sets of data were taken with different delays between the trigger and signal sampling time, in steps of 6.25 ns[9]. For each delay, the Landau distribution was fitted to the charge distribution and the MPV was extracted. The MPV was then plotted against the different delays, allowing the reconstruction of the pulse shape in steps of 6.25 ns over more than 50 ns (Fig. 3.12, right).

The measured pulse shape was then fitted with a function describing the expected behaviour of the front-end amplifier, in order to extract parameters such as the time of the maximum and the signal amplitude at the maximum of the pulse. The function is

$$f = Ae^{-x}(x^2/2 - x^3/6) \ ,$$

---

[8]This structure is smaller during normal data taking due to the lower occupancy.

[9]This corresponds to a quarter of the time between two bunch crossings at 40 MHz.
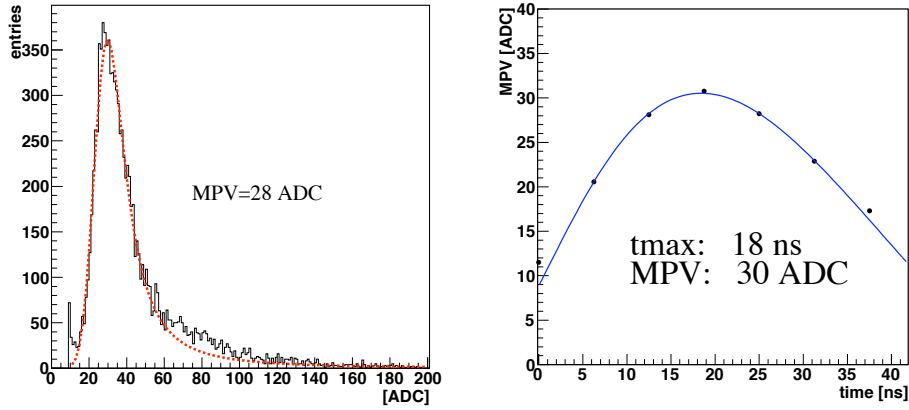
Figure 3.12: Left: Charge distribution fitted with the convolution of a Landau distribution and a Gaussian function. The Most Probable Value (MPV) is given by the fit, which was performed between 15 and 50 ADC counts. Right: Pulse-shape scan. The MPV of the charge distribution is plotted versus delay time, and fitted by a function describing well the expected signal pulse shape.

where $x = (t - t_0)/t_{\text{rise}}$, A is the scale, t_{rise} the rising time, and t_0 the starting time of the pulse. The time of the maximum is defined by

$$t_{\text{max}} = (3 - \sqrt{3})t_{\text{rise}} + t_0 \ .$$

This analysis was performed per detector module. As an example, Fig. 3.13 shows all the fits obtained for a particular box (IT1C). However, time settings cannot be set per module, but only per Service Box. A check has been performed to verify that the timing for each module of a particular SB is the same as the timing obtain on the full SB. The difference between the time of the maximum of a particular module and the time of the maximum of its associated SB has been plotted (Fig. 3.14). The plot shows that there are no big variations inside a box – which was expected – and that the timing can be set globally per SB. The distributions of the fitted parameters per module and errors on t_{max} are shown in Fig. 3.15.

The distribution of the time of the maximum shows several peaks corresponding to different data cable lengths. The distribution of the error on the time of the maximum shows that the average precision is about 1 ns. The errors are larger for short (single-sensor) modules due to their lower signal amplitude, as seen on the third plot of the figure. A few of the short modules have a larger signal than the rest (the cluster around 37 ADC), due to the fact that these special modules have been built with 410 μm sensors, instead of 320 μm for the other short modules. The larger signal observed on these modules compared to the long modules of the same thickness is consistent with the expected higher gain of the front-end amplifier for the lower capacitance in this case.

The timings have been set in accordance with the observed offsets, and a final check was performed. The signal from a given SB after the timing change was compared with the maximum signal achievable with the same SB, obtained previously by the fits. Plotting the difference allows a check of the timing (Fig. 3.16). The correspondance is perfect, since the error is dominated by the error from the fit. The IT has been time-aligned with a precision of $\simeq 1$ ns.
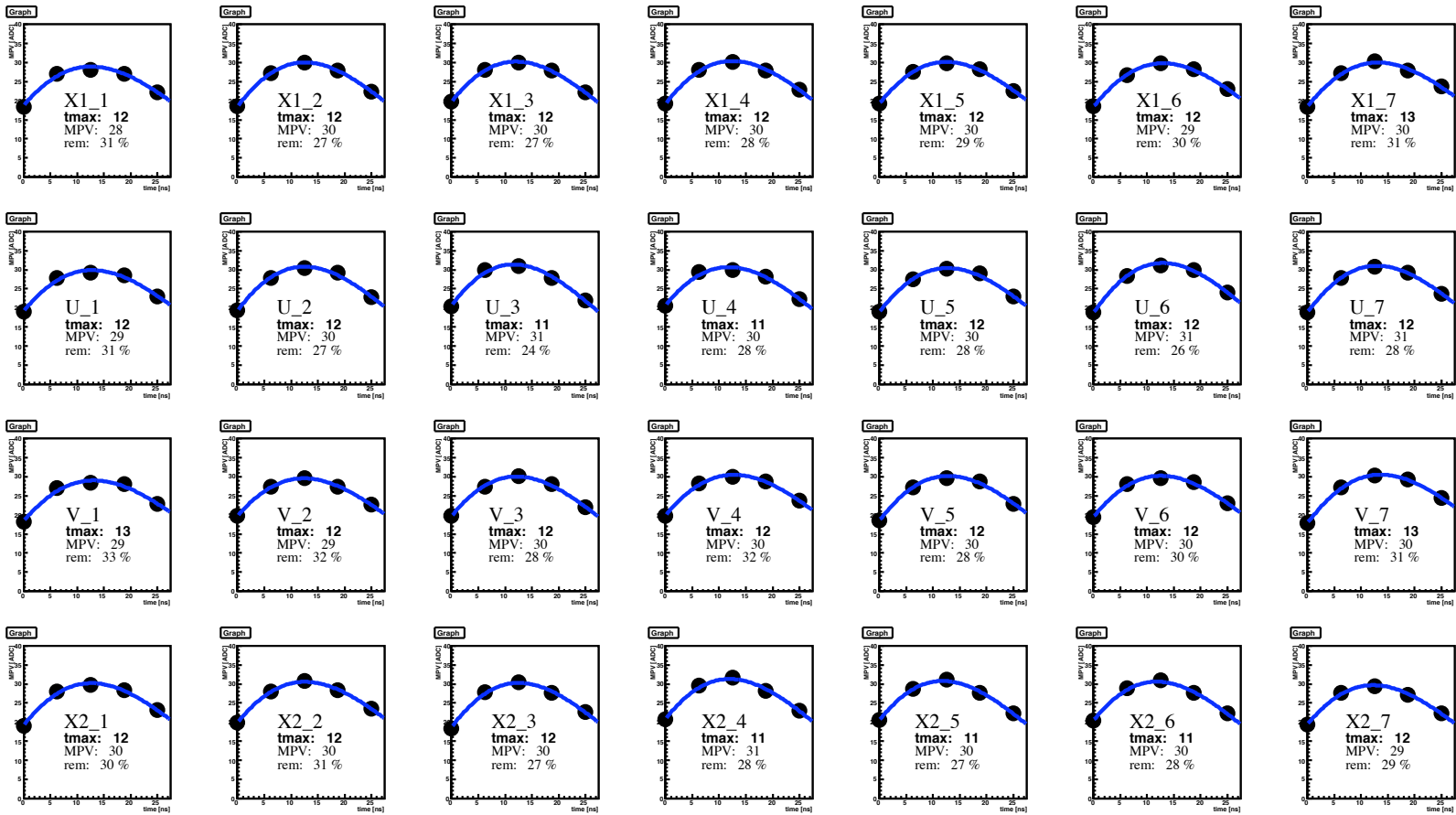
Figure 3.13: Fits performed for all the modules for box IT1C.
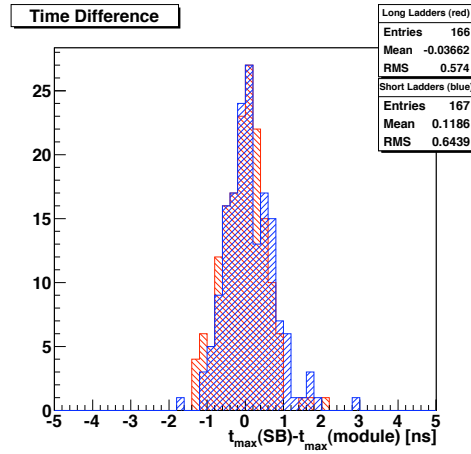
Figure 3.14: Time difference between the timing found for a Service Box and the timing found for each of its modules, for short (blue/dark grey) and long (red/light grey) IT modules.
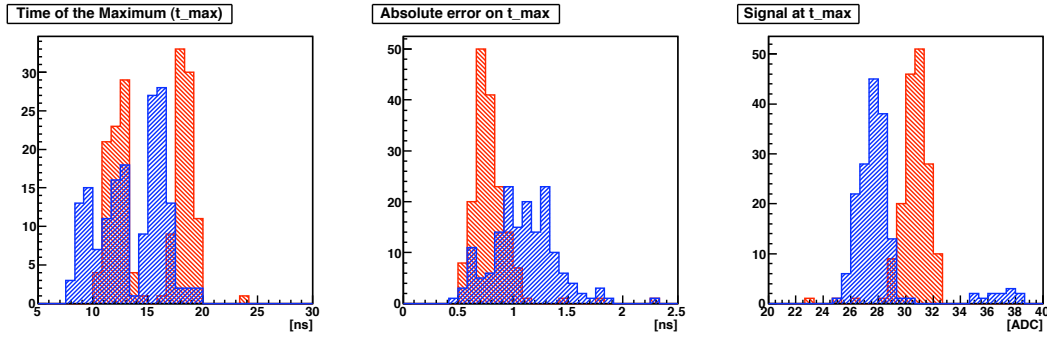
Figure 3.15: Parameters extracted by the pulse-shape fits per IT module, for the short IT modules (blue/dark grey) and the long IT modules (red/light grey). Left: Time of the maximum. Middle: Error on the time of the maximum. Right: Signal amplitude in the maximum.
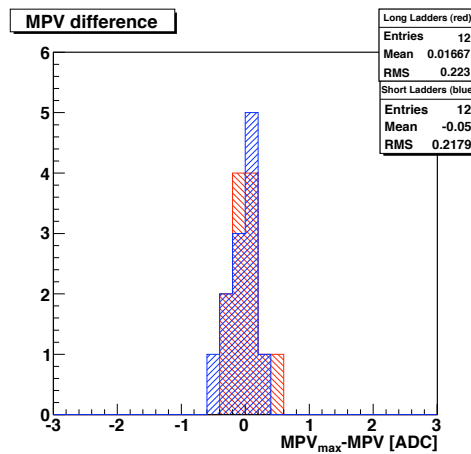
Figure 3.16: Difference between the maximum of the Most Probable Value of the signal obtained by the fit before the time setting, with the MPV of the signal after the time setting. The agreement demonstrate the perfect time-alignment of the IT.

4

Measurement of the prompt V^0 production cross-section at 0.9 TeV

The study of the prompt V^0 ($K_{\rm S}$ mesons and $\Lambda/\bar{\Lambda}$ baryons) production is important for the understanding of the hadronization processes and necessary for the tuning of the Monte Carlo generators. I will present the physics motivations, and describe in detail the analysis of the $K_{\rm S}$, Λ and $\bar{\Lambda}$ production cross-sections with the first 6.8±1.0 $\mu{\rm b}^{-1}$ of pp-collision data recorded with the LHCb detector at $\sqrt{s} = 0.9$ TeV in 2009.

4.1   Introduction

Strangeness production provides a very useful probe for the study of hadronization and fragmentation processes that occur in any kind of high energy collision. These processes are not yet fully understood, and the available phenomenological models need to be tuned. In addition to being a valuable input for the theoretical models, the knowledge of these processes is necessary for the tuning of the Monte Carlo generators. The most easily accessible strange particles are $K_{\rm S}$ and Λ, commonly called V^0 due to their neutral charge and their V-shaped decay, for two reasons: firstly, they are produced abundantly, and are among the first decaying particles to be seen in high-energy pp collisions; secondly, due to their typical decay shape, they can be selected with the sole use of a tracking system. For these reasons, the $K_{\rm S}$ and Λ production cross-section became naturally one of the first physics measurements to be performed at LHCb.

   At the beginning of 2009, I started to study minimum bias[1] Monte Carlo samples, in order

---

[1] "Minimum bias" denotes a sample of events wich is almost randomly selected, without introducing specific biases due to a trigger or a pre-selection. However, in particle physics a very basic trigger is always required and

to prepare the analysis of the first collisions that were foreseen by the end of that year. As a requirement it was necessary to develop a custom selection which would depend as little as possible on a good calibration and proper operation of the LHCb detector. For instance, it was foreseen that the RICH detectors would not yet be calibrated at that time, nor the calorimeters. The selection was therefore designed to be especially simple and minimal.

My studies were focused on the choice of selection criteria, using Monte Carlo candidates. The selection was tested, and an estimate of the sensitivity was obtained. My simulations were performed on the basis of a *pp*-collision centre-of-mass energy of 10 (5+5) TeV, since at that time it was the foreseen energy at the LHC startup.

The first collisions were observed in the four LHC experiments on November 23, 2009, and data was taken at the injection energy of 900 (450+450) GeV for several days at the beginning of December 2009. I started to undertake the measurement of the V^0-production cross-sections at this energy. Following the progress of the tracking and the alignment, a clean K_S peak, followed by a clear Λ signal emerged from the background level, and confirmed therefore that the analysis could be achieved with the very first data set.

Since the analysis was performed at an energy lower than the one assumed in my simulations, I will not describe in this document the Monte Carlo studies that were performed at 10 TeV. Whenever a conclusion was drawn from these studies, it will be clearly stated.

I will describe in detail in this chapter the analysis of the first data set of 6.8 ± 1.0 $\mu\mathrm{b}^{-1}$ integrated luminosity of *pp* collisions at $\sqrt{s} = 900$ GeV. The production cross-sections of K_S, Λ and $\bar{\Lambda}$ particles were measured as a function of rapidity and transverse momentum. As we will see, other observables of great interest can be measured, such as the asymmetry between Λ and $\bar{\Lambda}$ production rates.

The analysis is based on a single geometrical cut using the impact parameters of the mother and daughter particles with respect to the primary vertex, proposed for the occasion. Two different sets of track types were used, providing an independent cross-check. In total six analyses were therefore performed in parallel: one for each of the three V^0 types (K_S, Λ and $\bar{\Lambda}$) and for each track type.

After a review of the physics motivations for the study of V^0 particle production in Sec. 4.2, I describe the data sample used for the analysis in Sec. 4.3. The strategy of the analysis is discussed in Sec. 4.4, and the selection procedure in Sec. 4.5. The efficiency estimation is described in Sec. 4.7. The study of systematic uncertainties is described in Sec. 4.8, and the final results are given in Sec. 4.9.

4.2   Physics motivations

The physics processes taking place in an interaction at high energy between two bunches of protons are extremely complex. The complete description of all these phenomena are not relevant for this document, but some of them are of great interest for the V^0 physics. These processes can be separated into three categories, and the probability of occurence of each of them depends on the respective cross-sections and the densities of the proton bunches:

- **Elastic scattering**: Due to their relative small density, the bunches can cross each other without anything happening[2], or two protons can scatter each other. In the latter case, the collision is elastic since all the kinetic energy is conserved. These events are not triggered

---

the bias can never be totally avoided.

[2]In nominal LHCb conditions, the bunches are filled with 10^{11} protons, and the interaction region size is about ~ 1 cm^3. This is equivalent to a density of 1.7×10^{-10} kg/m^3, about a tenth of a trillionth of water's density.

in general, even with the simplest trigger, since most of the time the scattered protons remain in the beam pipe.

- **Inelastic diffractive interaction**: A proton interacting with another proton might break into several parts, leading to a cascade that can be detected. This process is called single diffraction in the case where just one proton is fragmented, or double diffraction if the two protons are fragmented. In these processes, no quantum numbers are exchanged and the particle exchanged is called "pomeron". The particular topology of these events allows most experiments to distinguish them from the non-diffractive processes. However it is more complex for LHCb, since the differences in topology arise in regions of geometrical acceptance that are not covered by LHCb, mainly lower pseudo-rapidity regions.

- **Inelastic non-diffractive interaction**: Quarks or gluons from each of the two protons interact together via the strong force, and through complex processes part of the energy of the centre-of-mass can be converted into matter. The processes that can occur in such collision are dominated by quantum chromodynamics (QCD) and can only be described by phenomenological models. The inelastic non-diffractive process is responsible for heavy particle production.

The research on all the aspects of a *pp* collision at high energy ("minimum bias" physics) is strongly related to the development of the Monte Carlo generators[3]. While all these aspects are often seen as a "background" for most particle physics analyses, their understanding is crucial for any analysis dependent on the proper description of the event by the Monte Carlo generators.

The "inelastic non-diffractive" category is typically the most interesting for the collider experiments in general. It is also the most complex one, and I will try in the next section to give a glance of which processes are taking place in such cases.

4.2.1   Inelastic non-diffractive events

First of all[4], the initial state before the collision – two protons heading towards each other – has to be mentally split into the constituents of the protons, the three quarks *uud*, with a momentum associated to each of these quarks. At high energy, the proton is not seen as a whole, but rather as three quarks sharing energy and bound together by the strong force, described by a sea of gluons interacting with the three quarks. The constituents, the quarks and the gluons, are called the partons. The distributions of the flavour and energy between the partons are described by the parton density functions.

When the two protons are passing close to each other, a quark from one proton might interact with a quark from the other proton, via the exchange of gluons. The process of gluon emission by a quark $q \rightarrow qg$ can be called "initial state showering". The outcoming partons from each of the two beams start the hard process[5], out of which partons and gluons are emitted ("final state showering"). The partons from the shower cannot be seen separately due to the quark confinement. When the distance between two quarks increase, the binding energy increases up to the level where the energy is sufficient to create a new pair of quarks (fragmentation). The coloured partons are transformed into colourless hadrons that may then decay. The process of fragmentation together with the subsequent decays of hadrons is called the hadronization process. The part of the proton which is left behind is called a "beam remnant".

---

[3]It is interesting to note that most of the articles on minimum bias physics are written by the people working on the event generators.

[4]This section and the next one are inspired by the physics introduction of T. Sjöstrand's PHYTHIA manual [31].

[5]A QCD interaction between quarks and gluons, for instance $qg \rightarrow qg$.

The process described above is not exhaustive at all, as several other processes may occur, such as resonance production (for instance $Z^0/W^{\pm}$ gauge bosons decaying further into quarks), initial or final state radiation (photons) and multiple parton interactions (MPI).

4.2.2   Fragmentation and strange quark production

Fragmentation is not yet understood fully from the QCD Lagrangian, and is so far only described by phenomenological models. The most important of them, which is used by the main event generation programs [31], is String Fragmentation (SF) [48, 49, 50, 51].

This model is based on an iterative procedure calculating the branching fractions of each elementary process, and the sharing of energy, momentum and flavour between the final state products. The main idea of the model is that the potential between two quarks moving apart can be represented by a cylindrical tube ("string") with a radius of about 1 fm, mathematically described by a single dimension corresponding to the axis of the tube. This representation leads to a linearly rising binding energy. As the quark distance increases, the string is breaking up, condensing the potential energy into a new pair of quarks $q\bar{q}$.

The breaking of the string via the creation of a $q\bar{q}$ pair is driven by quantum mechanical tunneling. The probability of breaking the string and creating a pair of quarks of mass m_q with a transverse momentum p_{T} with respect to the string is proportional to a term inspired from the tunnel effect [51],

$$P(m_q, p_{\mathrm{T}}) \simeq e^{-(m_q^2 + p_{\mathrm{T}}^2)/\kappa} \; , \tag{4.1}$$

where κ is the typical energy per unit length in the string, of the order of ~ 1 GeV/fm.

An important consequence is that the tunneling effect implies a suppression factor for the creation of $u{:}d{:}s{:}c$ quarks of $1{:}1{:}0.3{:}10^{-11}$. Strange quarks are therefore suppressed with respect to the up and down quarks, and charm quarks are almost impossible to create via the hadronization process.

Strange quarks in the final state, such as in V^0 particles, are therefore of great interest for understanding the fragmentation process and validate the models. Moreover, Λ hyperon production allows another aspect of the hadronization to be probed: the production of baryons. Indeed, the simple model for hadronization predicts the production of mesons created by the $q\bar{q}$ pair after the string breaking, but the outcome of a baryon from such processes is even more complicated.

Three different mechanisms can be invoked to describe baryon production: diquark, simple popcorn [52], and advanced popcorn [53]. In the diquark picture, the baryon and anti-baryon are both at the endpoints of the same $q - \bar{q}$ string, and the same framework is used as in the meson case. In the popcorn models, one (simple popcorn) or more (advanced popcorn) intermediate mesons are created between the baryon and anti-baryon.

I will discuss in the next section several observables of interest for the validation of the phenomenological models, that need to be experimentally determined. The results of the measurement of these observables is used for Monte Carlo generator tuning.

4.2.3   Observables

Models try to predict the amount of strangeness, for instance strange particle multiplicity, and also the location of strangeness in the two-dimensional p_{T} and η (pseudo-rapidity, defined by $\eta = -\ln(\tan(\theta/2))$) or y (rapidity, defined by $y = \frac{1}{2}\ln((E + p_z)/(E - p_z))$) phase space. The production cross-sections for K_{S} and Λ are therefore observables allowing the testing of such models. Figure 4.1 (top) shows the K_{S} and Λ multiplicities for the pseudo-rapidity region covered by CDF ($|\eta| < 1.0$), for different fragmentation models, as well as the CDF measurements in

$p\bar{p}$ collisions at 1800 GeV [54] . The same model predictions for LHC pp collisions at 900 GeV are shown in Fig. 4.2 (top), in the pseudo-rapidity region covered by LHCb ($1.8 < \eta < 4.9$). Production cross-sections for K_S and Λ particles in the same cases as above are shown in Figs. 4.1 (middle) and 4.2 (middle).

Another key feature of the fragmentation is the baryon number transport, which determines the location of the baryon number versus pseudo-rapidity, given the fact that the total baryon number is conserved and positive in the case of pp collisions. The corresponding observable is the anti-baryon/baryon ratio as a function of pseudo-rapidity, applicable to any type of strange or multi-strange hyperon. Among them, one of the most experimentally accessible is the $\bar{\Lambda}/\Lambda$ ratio, since these baryons are abundantly produced. Figure 4.1 (bottom) shows this ratio for different models for the full phase space, as well as in the CDF pseudo-rapidity region, for $p\bar{p}$ collisions at 1800 GeV. Figure 4.2 (bottom) shows the same ratio for the full phase space for pp collisions at 900 GeV, as well as in the LHCb pseudo-rapidity region.

The fragmentation models have been tuned on the observations made at SPS, RHIC, LEP and Tevatron. Therefore, as can be seen on the figures, the models agree mostly with each other in the region at small pseudo-rapidity covered by the Tevatron, which is roughly the same as for ATLAS and CMS. No particular surprises are therefore to be expected for ATLAS and CMS.

In contrary, the high pseudo-rapidity region exhibits many more differences between the models, which were never really tuned with observations in this region. It is especially clear for the $\bar{\Lambda}/\Lambda$ ratio (Fig. 4.2, bottom), where the difference between the models in the central pseudo-rapidity region $|\eta| < 1$ is about 1%, while it is about 5% in the forward pseudo-rapidity region $2 < \eta < 5$.

LHCb is therefore in an excellent position to provide an extremely valuable input for the fragmentation models. Moreover, the measurements performed at CDF do not cover the very low p_T bins, but only the hard tail of the distribution. This prevents sensitivity to the mass effect of the strange quark suppression by the tunneling effect, as parametrized in Eq. 4.1. Due to its ability to cover by design low p_T and high η/y, LHCb is the right detector to provide answers to unresolved hardonization features.

4.3   Data sample

The analysis is using minimum-bias data recorded during the pilot run in December 2009. The pp-collision centre-of-mass energy was 900 (450+450) GeV, corresponding to the injection energy of the LHC machine. The data sample is composed of thirteen runs, that have been carefully selected[6] on the basis of various criteria such as stable LHC running conditions, stability of the detector, properly working tracking detectors, and availability of a luminosity measurement. These runs correspond to several LHC fills with two sets of beam conditions:

- four bunches per beam separated by more than 8 μs, among which two were colliding, and a maximum peak intensity of 1.8×10^{10} protons per bunch;

- 16 bunches per beam separated by more than 2 μs, among which eight were colliding, and a maximum peak intensity of 1.3×10^{10} protons per bunch.

The total integrated luminosity of the data sample is 6.8 ± 1.0 μb^{-1} [5].

Due to the low energy and the dipole magnetic field, the two beams were colliding with a crossing angle leading to a moving centre-of-mass in the $-x$ direction. Since the crossing

---

[6]The selection was done by the LHCb Flavor Physics Working Group (FWG), in charge of the first physics measurements.
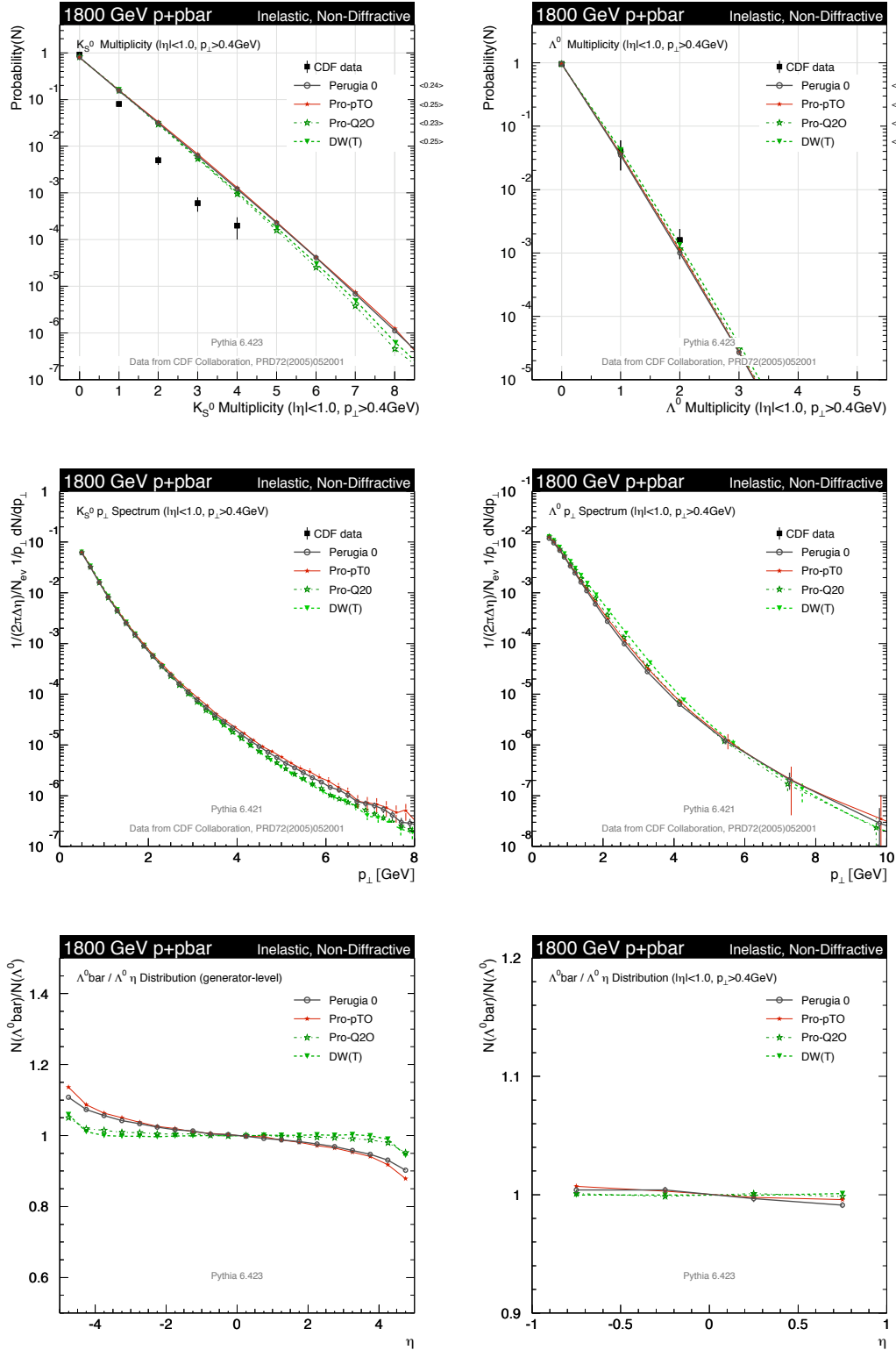
Figure 4.1: Top: K_S and Λ multiplicities in the CDF pseudo-rapidity region ($|\eta| < 1.0$) for different MC models, and CDF measurements with Tevatron $p\bar{p}$ data at 1800 GeV [54]. Middle: K_S and Λ differential production cross-sections vs p_T in the CDF pseudo-rapidity region for different MC models, and CDF measurements with Tevatron $p\bar{p}$ data at 1800 GeV [54]. Bottom: $\bar{\Lambda}/\Lambda$ ratio in the full phase space (left) and in the CDF pseudo-rapidity region (right) as a function of pseudo-rapidity for different MC models for $p\bar{p}$ data at 1800 GeV. These distributions and the meaning of the different MC tunings can be found in Ref. [55].
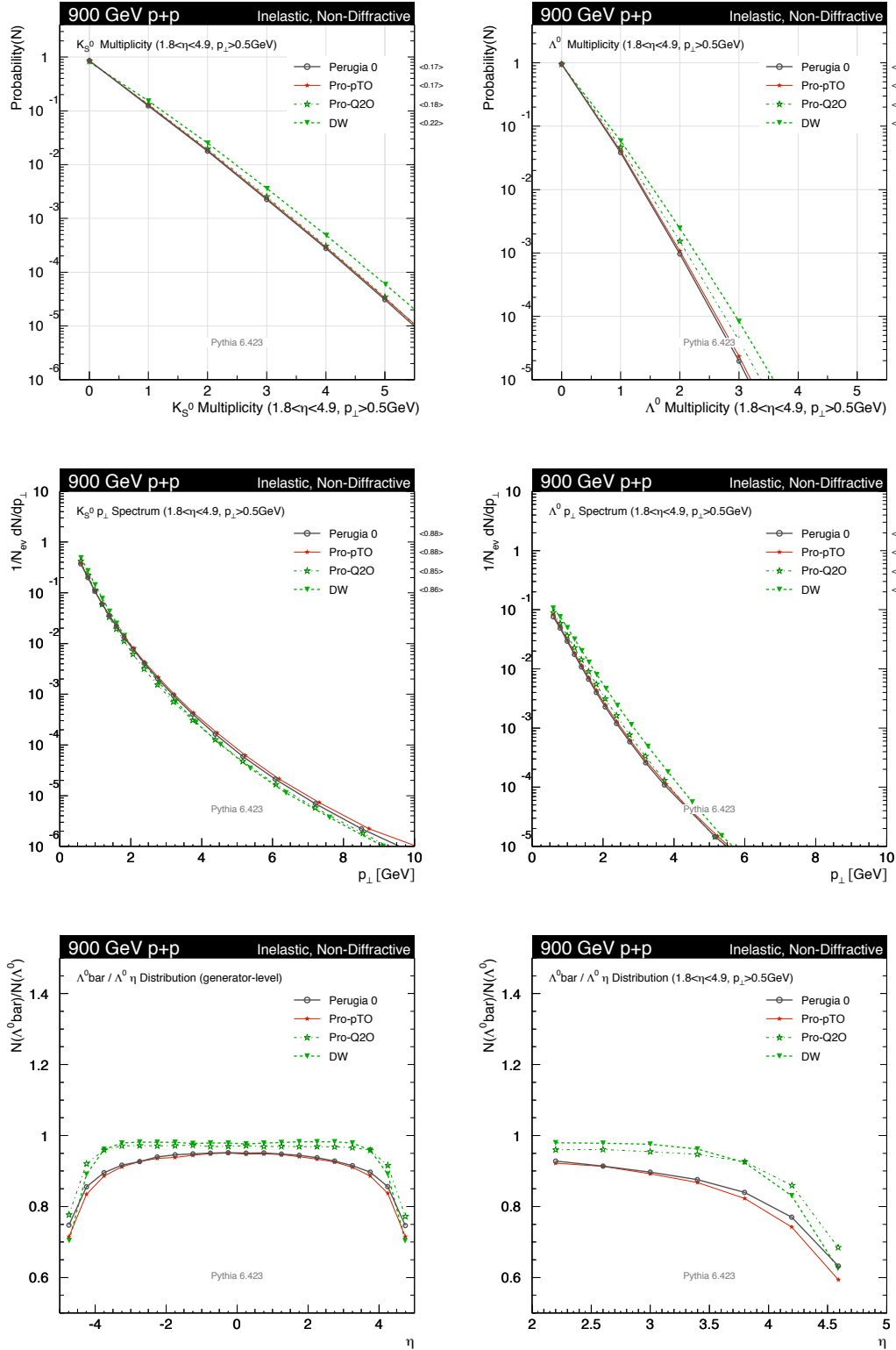
Figure 4.2: Top: K_S and Λ multiplicities in the LHCb pseudo-rapidity region ($1.8 < \eta < 4.9$) for different MC models simulated for pp collisions at 900 GeV. Middle: K_S and Λ differential production cross-sections vs p_T in the LHCb pseudo-rapidity regions for different MC models simulated for pp collisions at 900 GeV. Bottom: $\bar{\Lambda}/\Lambda$ ratio in the full phase space (left) and in the LHCb pseudo-rapidity region (right) as a function of pseudo-rapidity for different MC models for pp collisions at 900 GeV. These distributions and the meaning of the different MC tunings can be found in Ref. [55].

angle and the beam size were larger than the design running conditions, the safety of the VELO modules forbade the full closing of the two VELO halves. The VELO modules were therefore fixed at a distance of 15 mm from their nominal position for data-taking, reducing the acceptance.

To collect this "minimum bias" sample, an L0 trigger was applied. Indeed, we need a way to detect if a pp interaction has taken place in the event. However, since this is the only requirement, no High Level Trigger (HLT, see Sec. 2.2.3) was used. Two very similar L0 trigger settings were used to record the selected runs, defined in the following way:

- "1209": more than two hits in the SPD, and at least one cluster with $E_T > 240$ MeV in the hadronic calorimeter; in addition, events containing a muon with $p_{\mathrm{T}} > 480$ MeV were also triggered;

- "1309": Same as 1209, adding events containing a hit multiplicity larger than seven in the Pile-Up detector.

The list of runs is given in Table 4.6 (Sec. 4.6.1), together with the trigger settings used and the total number of triggered events.

The vacuum inside the beam-pipe is not perfect. Some protons from one of the two beams may therefore interact with residual gas in the beam pipe, leading to a pp or a pn collision at $\sqrt{s} \simeq 30$ GeV[7]. These interactions are a key ingredient for the luminosity measurement, and for this purpose three categories of events depending on the bunch crossing type were recorded: two colliding bunches (bb), beam-1 bunch only ($b1$) and beam-2 bunch only ($b2$). The crossing type is known for each event and recorded with the data.

The interactions of beam 1 with residual gas, which can occur in both bb and $b1$ crossings, constitute a background for the 900 GeV pp collisions, and they need to be subtracted from any observed interactions. A subtraction procedure has been set-up and is described in Sec. 4.6.1.

4.4   Analysis strategy

The analysis is driven by several requirements. Firstly, it has to be adapted to the early stage of the experiment, meaning that the detector is not *a priori* very well described by the Monte Carlo simulations. For this purpose, the number of selection criteria is kept as small as possible and the efficiency as high as possible, but still maintaining reasonable signal purity. It was also decided to use the actual values of the measurements and not the error estimates on these measurements, since this could increase the systematic uncertainties associated with a Monte Carlo which does not well describe the detector. As an example, the impact parameter (IP) of tracks with respect to the interaction vertex is preferred over the impact parameter significance $IP/\sigma(IP)$.

Secondly, the selection is based only on tracking measurements, since the RICH and the calorimeters were not calibrated at that time. Moreover, the K_{S} and Λ samples, providing very clean pion and proton samples, are precisely the data samples used for the calibration of the RICH particle identification.

The K_{S} mesons and Λ hyperons are weakly-decaying strange particles, whose properties are summarized in Table 4.1 and main decay channels are given in Table 4.2. The branching fractions of the two-body decay channels add up to 99.9% (99.7%) for K_{S} (Λ and $\bar{\Lambda}$). The remaining fraction is dominated by radiative decays. Since the neutral modes are more difficult

---

[7]At 30 GeV, the collision of a proton with a gas nucleus is at first approximation equivalent to a pp or a pn collision. The rest of the nucleus, whose binding energy is around a few MeV, is not "seen" by the incoming proton.

Table 4.1: Properties of the V^0 particles [56]. S is the strangeness, and B the baryon number.

particle	Composition	Mass [MeV/c^2]	$c\tau$ [cm]	$I(J^P)$	S	B
K_S	$\frac{1}{\sqrt{2}}(d\bar{s} - s\bar{d})$	497.614 ± 0.024	2.6842	$\frac{1}{2}(0^-)$	mixture	0
Λ ($\bar{\Lambda}$)	uds ($\bar{u}\bar{d}\bar{s}$)	1115.683 ± 0.006	7.89	$0(\frac{1}{2}^+)$	$+1$ (-1)	-1 $(+1)$

Table 4.2: Main decay modes of the V^0 particles. For the K_S case, the radiative mode includes only photons with energy over 50 MeV, while lower energy cases are included in the charged mode. For details, see Ref. [56].

	K_S	$\Lambda(\bar{\Lambda})$
Charged mode	$\pi^+\pi^-$: $(69.2 \pm 0.05) \times 10^{-2}$	$p^{+(-)}\pi^{-(+)}$: $(63.9 \pm 0.5) \times 10^{-2}$
Neutral mode	$\pi^0\pi^0$: $(30.69 \pm 0.05) \times 10^{-2}$	$n(\bar{n})\pi^0$: $(35.8 \pm 0.5) \times 10^{-2}$
Radiative mode	$\pi^+\pi^-\gamma$: $(1.79 \pm 0.05) \times 10^{-3}$	$n(\bar{n})\gamma$: $(1.75 \pm 0.15) \times 10^{-3}$

to observe in the detector and since the radiative modes have a very small probability, the detection channels that we use are $K_S \to \pi^+\pi^-$, $\Lambda \to p^+\pi^-$ and $\bar{\Lambda} \to p^-\pi^+$. Throughout this document I will always assume these decay modes.

The fact that the VELO was only partially closed has the disadvantage of drastically lowering the VELO acceptance and introduces a strong azimuthal dependence. In addition, due to the relatively long lifetime of V^0 particles (see Table 4.1), many of these particles decay outside of the VELO. It is therefore decided to use two sets of tracks: a set of tracks having hits in the VELO, more precise and providing cleaner signal samples but with less statistics, and a set of tracks having no hit in the VELO, with much more statistics but worse resolution. These two sets of tracks are used together for the final results.

Access to the hadronization processes requires that the observed V^0 be prompt, i.e. that it comes either from the primary interaction, or from a strongly or electromagnetically decaying particle produced at the interaction point. These two cases cannot be distinguished experimentally. The operational definition of "prompt" which is needed for the analysis is given in Sec. 4.4.2. Other sources of V^0 particles, such as secondary interactions or decay of long-lived particles are suppressed by the selection which requires the V^0 particles to point back to the pp interaction region. In this analysis, no attempt is made to exclude V^0 from diffractive events.

4.4.1 Track types

Five types of tracks are defined in LHCb (Fig. 4.3):

- **Long**: tracks having hits in the VELO, in the OT/IT stations and optionally in the TT. These tracks are the most precise, exhibit the best momentum resolution, and are used by most analyses.

- **Downstream**: tracks having hits only in the TT and OT/IT stations. Although they are less precise than the Long tracks, they are of great help for long-lived particles decaying outside the VELO.

- **VELO**: tracks made of VELO hits only. They are mainly used for the primary vertex reconstruction.
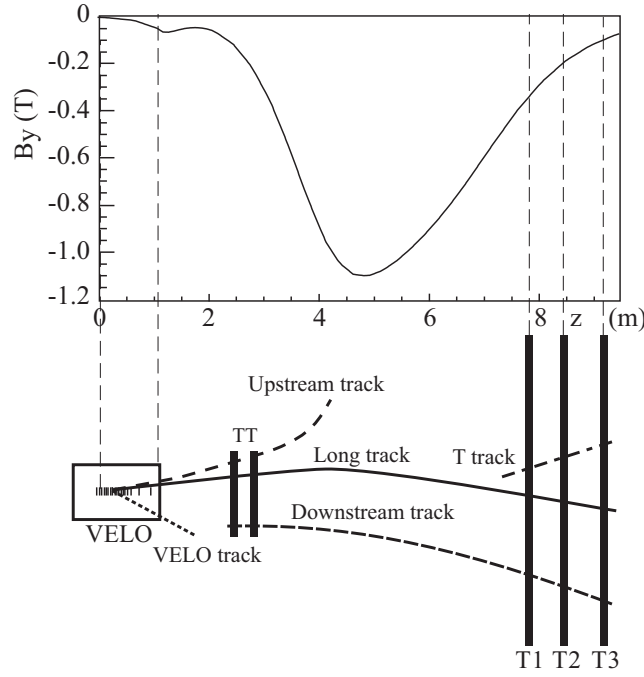
Figure 4.3: Top: y component of the magnetic field as a function of z. Bottom: sketch of the various LHCb track types.

- **Upstream**: tracks using only hits in the VELO and the TT station.

- **T**: tracks using only hits from the IT and OT stations.

In this analysis, only the first two types of tracks are used to reconstruct V^0 candidates. Indeed, Long tracks are used for their high resolution, however due to the partially closed VELO and the long lifetime of V^0-particles leading to most V^0s decaying outside the VELO, the statistics for Long tracks is limited with respect to Downstream tracks. Therefore to increase the statistics, both LL (Long-Long) – meaning that both daughter tracks are "long" –, and DD (Downstream-Downstream) combinations are used. These two samples provide an excellent cross-check, since they are totally independent.

4.4.2 Prompt-V^0 Monte Carlo definition

We are interested in probing the hadronization processes taking place at the core of the pp collision, and not in long-distance effects or secondary interactions which are not related with the primary interaction. Therefore, we need to select only V^0s which have been produced either directly in the pp collision, or from a strongly or electromagnetically decaying particle which has been produced at the primary interaction. The former type is named "direct prompt", while the latter is named naturally "indirect prompt". Both cases are "prompt", contrary to a V^0 produced by a weakly-decaying particle. The motivation for this definition is that the indirect prompt component cannot be experimentally distinguished from the direct prompt component, since a strongly-decaying particle has a lifetime well below the spatial resolution of the LHCb tracking system. On the other hand, weakly-decaying particles have a longer lifetime, and can clearly be experimentally disentangled. The operational definition, needed for and used in MC simulations, is that a K_S or Λ is prompt whenever its longest living ancestor has $c\tau < 10^{-11}$ m, where τ is the mean lifetime of the ancestor.

Table 4.3: Analysis ranges in transverse momentum p_{T} and rapidity y.

	K_{S} LL	K_{S} DD	$\Lambda/\bar{\Lambda}$ LL	$\Lambda/\bar{\Lambda}$ DD
p_{T} [GeV/c]	$0.0 - 2.0$ (10 bins)	$0.0 - 2.0$ (8 bins)	$0.4 - 1.6$ (3 bins)	$0.4 - 2.0$ (4 bins)
y	$2.5 - 4.0$ (3 bins)	$2.5 - 4.0$ (3 bins)	$2.5 - 4.0$ (3 bins)	$2.5 - 4.0$ (3 bins)

Since it is a Monte Carlo definition, it cannot be applied to the observed particles. The non-prompt component will be considered as a background to the prompt component and will be estimated at the end of the analysis.

4.4.3 Analysis range definition

The production cross-section is measured in bins of rapidity $y = \frac{1}{2}\ln((E + p_z)/(E - p_z))$ and transverse momentum $p_{\mathrm{T}} = \sqrt{p_x^2 + p_y^2}$, where (E, p) is the four-momentum vector of the V^0 particle in the pp collision centre-of-mass frame. A boost has been applied to the values of the four-momentum in the laboratory frame, to correct for the moving centre-of-mass of the pp collision due to the crossing angle of the beams.

The choice of the kinematic variables is rather arbitrary, and one could have chosen instead bins of pseudo-rapidity $\eta = -\ln(\tan(\theta/2))$ and transverse momentum p_{T}. Pseudo-rapidity has the advantage of being related to the angle with respect to the beam, while rapidity is often used due to the uniformity of particle density emission with respect to y. The analysis ranges are given in Table 4.3.

The choice of the binning and range is motivated by the balance between a sufficient number of signal events in each bin, and a sufficient resolution to establish the shapes. The smaller number of p_{T} bins for Λ and $\bar{\Lambda}$ is due to the smaller statistics. Due to large uncertainties in the signal extraction procedure in several bins (see Sec. 4.8.1), some of them will be ignored for the measurement.

4.5 Reconstruction and selection

Only the events that have been triggered by the calorimeters are selected, ignoring the muon trigger condition. The tracks are reconstructed from hits in the sub-detectors using the standard LHCb tracking algorithms [57].

The selection strategy is to use a single main cut, based on the Impact Parameters (IP) of the mother and daughter particles with respect to the Primary Vertex (PV). This analysis requires therefore at least one PV to be reconstructed. The choice of a single cut simplifies the systematic uncertainty studies since all the efficiency information is contained in one variable, avoiding the study of the correlations between the cuts. All the other cuts are chosen to be 100% efficient or very close.

The PV is reconstructed using a procedure that has been adapted to the early stage of the data-taking, with less stringent track quality requirements than for nominal conditions. The standard "Very Loose" algorithm [58] uses all types of tracks: VELO, Long, Downstream, Upstream and T. At least three tracks of any type are needed in the acceptance, which corresponds approximately to the pseudo-rapidity range $[-4, -1.5]\bigcup[+1.5, +5]$. Figure 4.4 shows the pseudo-rapidity distribution of the tracks used in the PV reconstruction.

Each pair of oppositely-charged LL or DD tracks in the event is then selected. For the K_{S} selection, the mass of the pion is assigned to each of the two tracks. For the Λ candidates, the
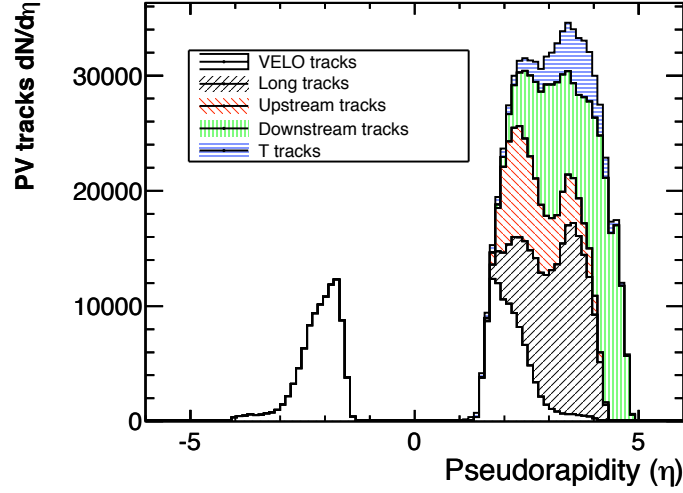
Figure 4.4: Distribution of the pseudo-rapidity of the tracks used in the PV reconstruction, per track type, by Raphael Maerki.
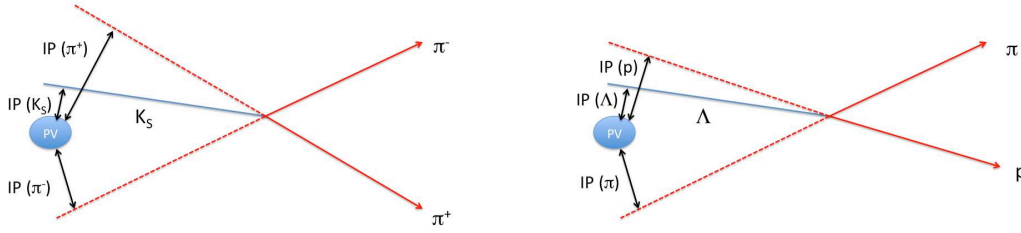
Figure 4.5: Sketch of the IP of the mother and the daughters for the K_S decay (left) and Λ decay (right).

mass of the proton is assigned to one of the tracks, and the mass of the pion to the other. This generates two combinations, among which only one is kinematically possible. Indeed, the proton being heavier has to take always much more momentum than the pion in the laboratory frame[8].

The pair of tracks is then subject to a few individual requirements on the tracks and one main requirement acting on the combination of the impact parameters (IP) of the daughter and the mother. The four-momentum of the pair is then computed, and the invariant mass calculated.

4.5.1   Selection requirements

Due to the decay geometry, and to reject background from the primary particles, daughter momenta are requested to have a large IP with respect to the PV. In contrast, the IP of the mother particle has to be small in order to select promptly-produced V^0 (Fig. 4.5). Combining

---

[8]This can be proven using the Armenteros-Podolanski plot [59]
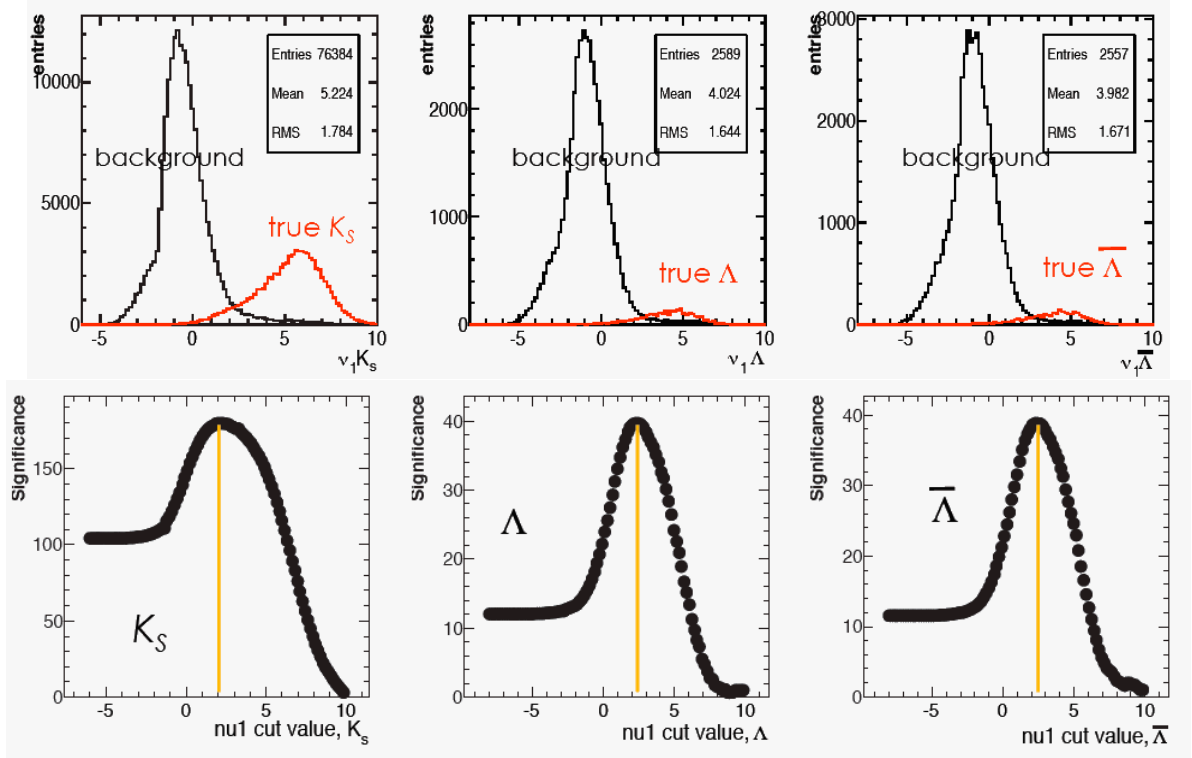
Figure 4.6: Top: MC signal and background distributions of the ν_1 variable for the three V^0 cases, with LL tracks. The signal component has been multiplied by a factor of 5 for better visibility. Bottom: Significance as a function of the ν_1 cut, for the three V^0 cases, with LL tracks. Simulations at 10 TeV.

these requirements into one single variable, and taking the logarithm[9], we obtain

$$\nu_1 = \ln\left(\frac{\mathrm{IP}_{\mathrm{d}^+} \times \mathrm{IP}_{\mathrm{d}^-}}{\mathrm{IP}_{V^0} \times 1\ \mathrm{mm}}\right) ,$$

where d^+, d^- are the daughter particles of the V^0 candidate. The IP of a track is always computed with respect to the closest PV. This ensures that the daughter tracks are the further away from any PV, and hence are not primary particles, and that the mother origin point is the closest from the closest PV.

The ν_1 variable provides excellent separation between signal and background, and the cut value can be optimized for significance. Figure 4.6 shows the ν_1 distributions for Monte Carlo signal and background in the three cases K_{S}, Λ and $\bar{\Lambda}$, together with the expected signal significance as a function of the ν_1 cut value. The corresponding plots obtained[10] with real data are displayed in Fig. 4.7 for the K_{S} case. It is interesting to note that the optimized cut values are extremely close to those obtained with MC (2 for the LL case and 4.5 for the DD case), and therefore we use these values for the analysis. Similar figures can be obtained for Λ, with the same optimized cut values.

In addition to the main geometrical cut ν_1, other cuts were applied mainly for background rejection, without removing signal. They are listed together with ν_1 in Table 4.4. The cuts on

---

[9]The logarithm of a sharply peaking function allows its transformation into a smooth function, keeping a constant binning at the same time.

[10]See Sec. 4.6 for details on the extraction of the signal.
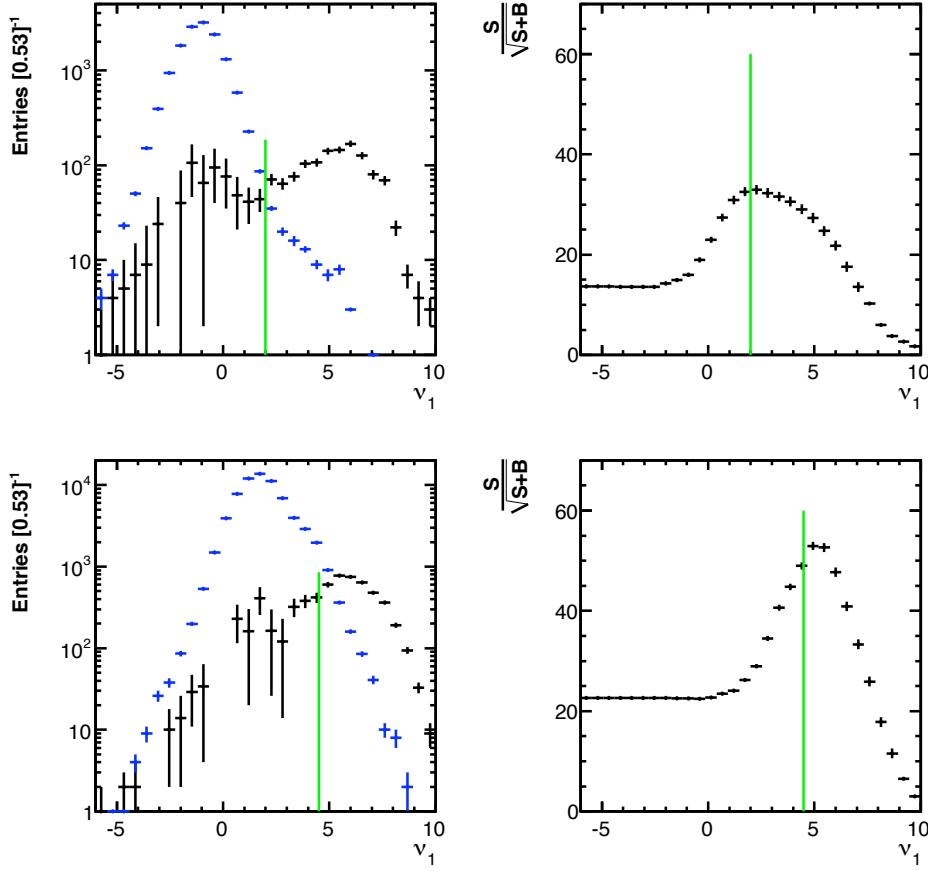
Figure 4.7: Left: ν_1 distributions for K_S signal (black) and background (blue) reconstructed with long tracks (top) or downstream tracks (bottom) in 2009 data. The background component is estimated from the side-bands. Right: corresponding signal significance $S/\sqrt{S+B}$ as a function of the ν_1 cut. The green line corresponds to the chosen cut. These plots have been obtained after cuts on the V^0 vertex χ^2/DOF, on the z flight distance and on the position of the primary vertex. Since these cuts have a signal efficiency close to 100% (as will be shown later in this document), they do not alter the ν_1 distribution of the signal in this figure.

track quality are intended to remove badly reconstructed tracks. The decay vertex quality cut allows a preliminary separation of signal and background, requiring that the two daughter tracks are intersecting. The cut on the z position of the primary vertex has been chosen such that all pp interactions primary vertices are contained in the window. It keeps therefore all the signal, allowing at the same time the rejection of beam-gas background. The cut on the z coordinate of the decay vertex can be called "positive lifetime", it is almost equivalent to requiring that the scalar product of the mother momentum and its flight path is larger than zero. The latter cut removes a lot of background, while keeping almost all the signal. The efficiency of all these cuts is studied in Sec. 4.8.5.

4.5.2 Mass distributions

Figure 4.8 shows the invariant mass distributions obtained after all selection cuts, for the bb crossings, for the full p_T and y ranges. As an example, Fig. 4.9 shows the same distributions for
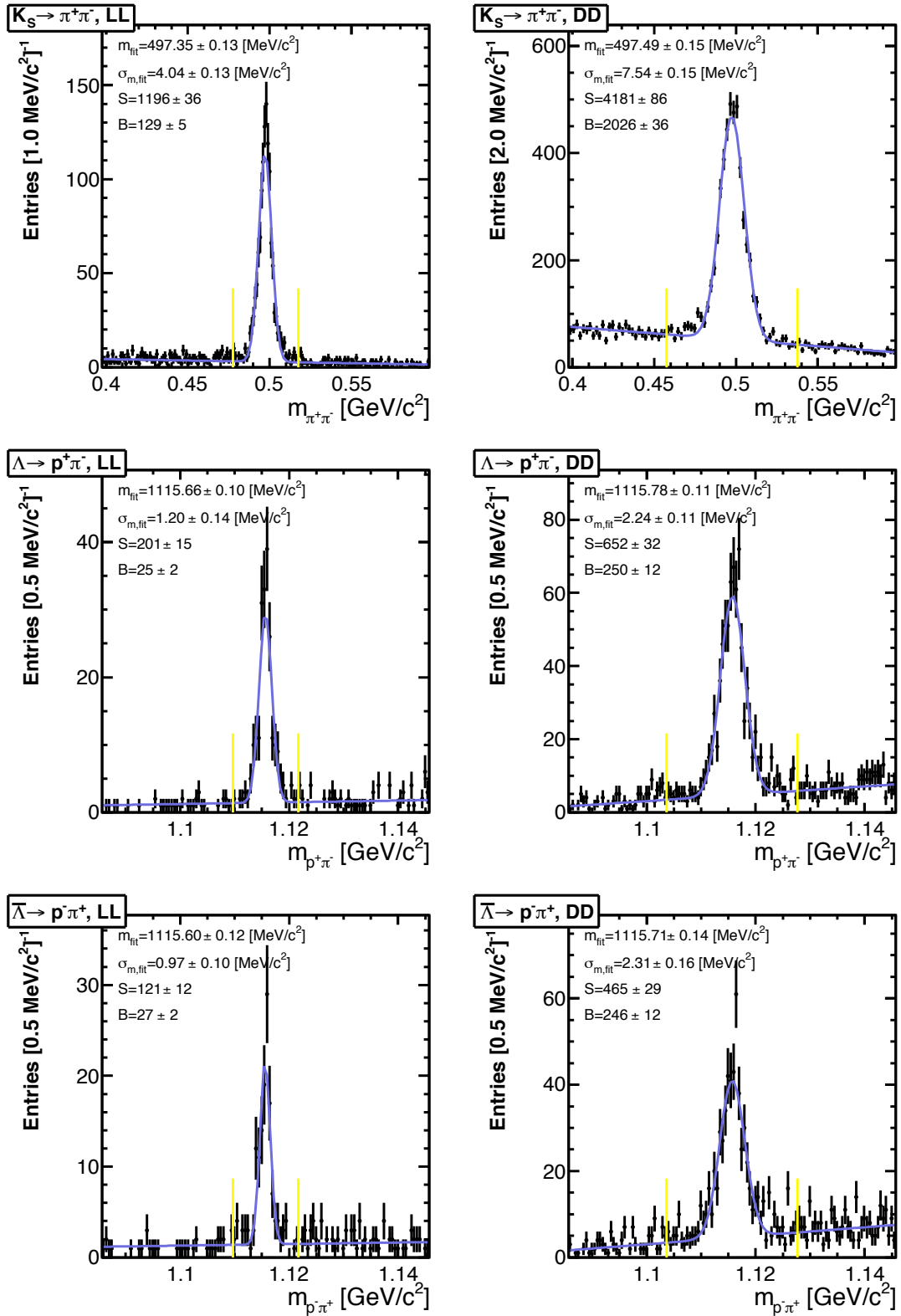
Figure 4.8: Invariant mass distributions for two oppositely-charged tracks under the $\pi\pi$ hypothesis (top), the $p\pi$ hypothesis with proton mass assigned to the positive track (middle), and the $p\pi$ hypothesis with the proton mass assigned to the negative track (bottom) for LL (left) and DD (right) cases in bb crossings.

Table 4.4: Cuts applied for the V^0 selections. Apart from the mass cuts, they are common for the K_S, Λ and $\bar{\Lambda}$ selections. The mass cut is applied on $|\Delta m| = |m - m_{PDG}|$, where m is the reconstructed V^0 mass and m_{PDG} is the known mass of the K_S (497.614 MeV/c^2) or the Λ (1115.683 MeV/c^2) [56].

Quantity	Requirement (LL)	Requirement (DD)
track quality χ^2/DOF	< 25	< 25
V^0 vertex χ^2/DOF	< 100	< 100
$z_{V^0} - z_{PV}$ [mm]	> 0	> 0
$|z_{PV}|$ [mm]	< 200	< 200
ν_1	> 2	> 4.5
$|\Delta m|$ [MeV/c^2]	K_S:< 100, Λ:< 30	K_S:< 100, Λ:< 30
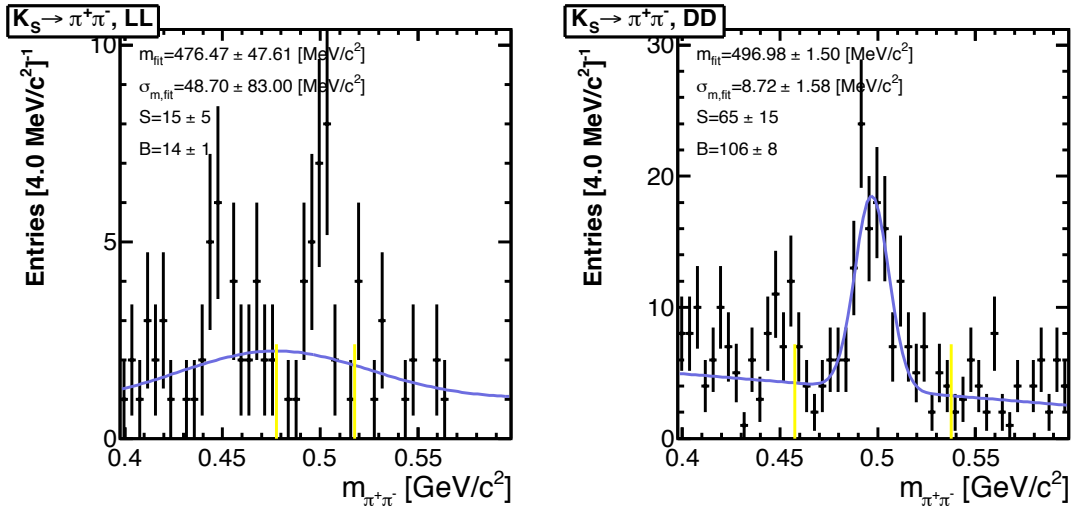
Figure 4.9: Invariant mass distributions for the two oppositely-charged tracks under the $\pi\pi$ hypothesis, for the LL (left) and DD (right) cases in $b1$ crossings.

$b1$ crossings in the case of K_S. The fits are performed with a single Gaussian function, in order to estimate the widths and measured masses, which are summarized in Table 4.5. The yellow lines on these plots indicate the tight mass windows used in the signal extraction described in Sec. 4.6.

The values obtained for the masses are compatible with the known V^0 masses, although a slight shift is observed for K_S particles, due to the fact that, at the time of the analysis, the calibration of the detector and magnetic field was not perfect. The measured widths are showing that the mass resolution of the LL case is better by a factor of two compared to the DD case, demonstrating the importance of the VELO for mass measurements. The much larger statistics for the DD case justifies the addition of this set of tracks in the analysis.

The V^0 mass distributions for the bb crossings in each bin of p_T and y are shown in Figs. A.1–A.6 (K_S), A.7–A.12 (Λ), and A.13–A.18 ($\bar{\Lambda}$) in Appendix A.3. From these figures it is obvious that the LL case gives in general very clean peaks, but with less statistics, while on the other hand the DD case exhibits more background, wider mass peaks but more statistics than the LL case.

Table 4.5: Masses and widths obtained from single Gaussian fits. The yields are estimated using a side-band subtraction algorithm that assumes a linear background.

Case	Mass [MeV/c^2]	Width [MeV/c^2]	Signal yield
K_S, LL	497.35 ± 0.13	4.04 ± 0.13	1196 ± 36
K_S, DD	497.49 ± 0.15	7.54 ± 0.15	4181 ± 86
Λ, LL	1115.66 ± 0.10	1.20 ± 0.14	201 ± 15
Λ, DD	1115.78 ± 0.11	2.24 ± 0.11	652 ± 32
$\bar{\Lambda}$, LL	1115.60 ± 0.12	0.97 ± 0.10	121 ± 12
$\bar{\Lambda}$, DD	1115.71 ± 0.14	2.31 ± 0.16	465 ± 29
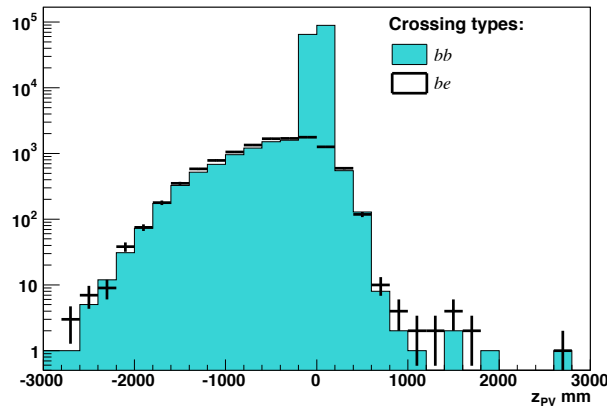
Figure 4.10: z position of reconstructed primary vertices in bb and $b1$ crossings (labelled "be" on the figure), by Yasmine Amhis.

4.6 Signal extraction

4.6.1 Beam-gas subtraction

V^0 particles can be produced in the interaction of the beams with the residual gas in the beam pipe. These are referred to as beam-gas events and are a background to V^0 particles produced in beam-beam collisions.

The beam-gas events can be subtracted from the total number of events on a statistical basis, after normalization to the ratio between the integrated luminosities of bb and $b1$ crossings. From simple bunch counting, the ratio between the total numbers of bb and $b1$ crossings is equal to unity, but using this ratio as a normalization factor would be correct only if all bunches had the same charge. Therefore we choose to measure the normalization directly on the data, normalizing the distributions of the z position of the primary vertices outside of the luminous region in $b1$ crossings to that seen in bb crossings. This method is justified by the fact that, unless there are some variations in the gas density between events, the distributions of the beam-gas interactions in $b1$ and bb crossings should be exactly the same. The similar shapes of the two distributions support this argument, as seen in Fig. 4.10.

The distribution of primary vertices in $b1$ and bb events can be normalized, with a normalization factor β, defined as:

Table 4.6: Normalization factors with statistical errors for each run, by Yasmine Amhis. The trigger settings are defined in Sec. 4.3.

Run	Trigger	# Events	β
63949	1309	64179	1.16 ± 0.05
63815	1309	11668	0.99 ± 0.11
63814	1309	4629	0.95 ± 0.17
63813	1309	71429	1.01 ± 0.05
63809	1309	23465	0.81 ± 0.05
63807	1309	75285	0.75 ± 0.03
63801	1309	94112	0.76 ± 0.07
63691	1309	2074	1.22 ± 0.27
63713	1209	14295	1.28 ± 0.10
63690	1209	20855	1.02 ± 0.07
63688	1209	2169	1.02 ± 0.20
63687	1209	15642	0.99 ± 0.08
63686	1209	24391	0.92 ± 0.05
All	-	424193	0.9075 ± 0.0148

$$\beta = \frac{N^{bb}_{\text{outside}}}{N^{b1}_{\text{outside}}} \; , \tag{4.2}$$

where $N^{bb,b1}_{\text{outside}}$ are respectively the number of reconstructed and selected primary vertices in the bb and the $b1$ crossing types outside of the luminous region ($z_{PV} < -200$ mm). Only vertices containing at least 3 VELO tracks or at least 2 long tracks are counted. Once the normalization factor is determined, the subtraction of the beam-gas background in bb crossings is performed using

$$N = N^{bb} - \beta N^{b1} \; . \tag{4.3}$$

The results of the normalization measurement for each run are shown in Table 4.6. It is important to note the run-by-run variation of the normalization factor. The average normalization is $\beta = 0.9075 \pm 0.0148$ and can be used for any selection.

4.6.2 Combinatorial background subtraction

In each bin of transverse momentum p_{T} and rapidity y, the signal is extracted from the invariant mass distribution using a side-band subtraction algorithm, assuming that the background distribution is linear in the K_{S} (Λ) mass window of ± 100 MeV/c^2 (± 30 MeV/c^2) around m_{PDG} (see Table 4.4), and that there is no signal outside the signal windows. This hypothesis is quite well supported looking at the total invariant mass distributions. The signal is extracted as

$$S = N_S - \alpha N_B \; , \tag{4.4}$$

where N_S is the number of V^0 candidates in the signal window, N_B the number of V^0 candidates in the side-bands, and α the ratio between the size of the signal window and the total size of the side-band windows. The signal and side-band windows are defined in Table 4.7, which also gives the values of α. Technically, the beam-gas subtraction (Eq. 4.3) and the side-band subtraction (Eq. 4.4) are performed in one go using

Table 4.7: Definition of the signal and side-band mass windows around m_{PDG}, and values of α.

Case	Signal mass window [MeV/c^2]	Side-bands [MeV/c^2]	α
K_{S}, LL	± 20	$[-100,-20],[+20,+100]$	1/4
K_{S}, DD	± 40	$[-100,-40],[+40,+100]$	2/3
$\Lambda/\bar{\Lambda}$, LL	± 6	$[-30,-6],[+6,+30]$	1/4
$\Lambda/\bar{\Lambda}$, DD	± 12	$[-30,-12],[+12,+30]$	2/3

$$S = N_S^{bb} - \beta N_S^{b1} - \alpha N_B^{bb} + \alpha\beta N_B^{b1} \; , \tag{4.5}$$

where $N_S^{bb,b1}$ and $N_B^{bb,b1}$ are the number of V^0 candidates in the signal mass window and the number of V^0 candidates in the side-band mass window for bb and $b1$ crossings respectively.

In order to obtain the statistical error on the signal yield S, a toy Monte Carlo is used. The number of entries in the signal window and in the side-bands are fluctuated with a Poisson law, with means set to the observed values. The statistical error is given by the r.m.s. of the distribution of S for 10k toy experiments[11]. The beam-gas subtracted yields measured in each (p_{T},y) bin are quoted in the column labelled "S" in Tables A.26–A.27 (K_{S}), A.28–A.29 (Λ) and A.30–A.31 ($\bar{\Lambda}$). The systematic uncertainty associated with the linear background hypothesis is studied in Sec. 4.8.1. Several bins are excluded from the analysis due to a large systematic uncertainty and are represented by a "$-$" in the tables. All the tables are located in Appendix A.4.

4.7 Efficiency estimation

Once the yield S in a (p_{T},y) bin has been extracted from the data, the efficiency-corrected yield in this bin is computed as

$$N^{\mathrm{prompt}} = \frac{S}{\epsilon_{\mathrm{tot}}} \; , \tag{4.6}$$

with

$$\epsilon_{\mathrm{tot}} = \epsilon_{\mathrm{reco+sel}} \times \epsilon_{\mathrm{trig}} \; , \tag{4.7}$$

where ϵ_{tot} is the total signal efficiency for prompt V^0, $\epsilon_{\mathrm{reco+sel}}$ the efficiency of the selection and reconstruction obtained without applying the trigger, and ϵ_{trig} the efficiency of the trigger on selected and reconstructed events.

We compute the efficiencies using a Monte Carlo sample of 10 million fully simulated pp collisions. The preparation of this sample is described in Ref. [60]. The hit finding efficiencies in the tracking layers have been tuned to reproduce the apparent inefficiencies in the data, mainly due to residual misalignments which are not included in the Monte Carlo. The tuning is then checked by comparing the number of hits per track in data and MC.

The yields are extracted in the MC in the same way as in the data (side-band subtraction) except that no beam-gas subtraction is necessary. This way of estimating the efficiency-corrected yields has the following advantages:

(a) No MC matching (association) is used, in order to stay safe of the inefficiencies of the MC associator, which are of the order of 1–5%.

---

[11]Thanks to Yasmine Amhis for the development of the toy.

Table 4.8: Coefficients of the weights $w(m) = a + bm + cm^2$ given by the polynomial fits for all V^0 cases.

Case	a	b	c
K_S, LL	0.92 ± 0.15	-0.07 ± 0.03	0.006 ± 0.001
K_S, DD	0.55 ± 0.09	-0.01 ± 0.02	0.005 ± 0.001
$\Lambda + \bar{\Lambda}$, LL	0.56 ± 0.28	0.00 ± 0.05	0.003 ± 0.002
$\Lambda + \bar{\Lambda}$, DD	0.33 ± 0.16	0.02 ± 0.03	0.004 ± 0.002

(b) As a consequence of (a), the non-prompt component cannot be identified in the MC, but the non-prompt component is corrected for by using as denominator all true promptly-produced V^0. This is valid under the assumption that the MC correctly simulates the sources of non-prompt V^0.

(c) Possible bin migration effects are automatically corrected for by taking the selected yields in the measured bins and the generated yields in the true bins. However this is valid under the assumption that the bin migration is correctly simulated in the MC.

The efficiency factors ϵ_{trig} and $\epsilon_{\text{reco+sel}}$, together with their systematic uncertainties, are discussed in detail in the next sections.

4.7.1 Trigger efficiency

The trigger efficiency ϵ_{trig} can in principle be measured with data (see Sec. 4.8.2), but in this analysis the available statistics are not sufficient in every bin. The trigger efficiency is therefore measured with Monte Carlo, using a L0-trigger emulation. However, the trigger efficiency depends on the overall track multiplicity of the event. Since the track multiplicity is higher in the data than in the MC, the trigger efficiency is computed after reweighting the Monte Carlo sample with the observed track multiplicity, defined by the total number of Long and Downstream tracks in the event. Thus we use

$$\epsilon_{\text{trig}} = \frac{S_{\text{w}}^{\text{L0}}}{S_{\text{w}}} \ , \tag{4.8}$$

where S_{w}^{L0} is the signal yield in the reweighted MC sample after trigger, reconstruction and selection, and S_{w} is the signal yield in the same reweighted MC sample after reconstruction and selection, without applying the L0 trigger.

The weighting is done by comparing the data and MC distributions of the total L+D multiplicity m for each type of selected and triggered V^0 signal, after side-band and beam-gas subtraction (see Fig. 4.11 left for K_S). The ratio of these distributions is fitted with a second-order polynomial function $w(m) = a + bm + cm^2$ (Fig. 4.11 right). The trigger efficiency is then computed by weighting each MC event with its value of $w(m)$.

Very similar multiplicity distributions for Λ and $\bar{\Lambda}$, not shown here, give slightly different weighting factors. Table 4.8 summarizes the results of the parabolic fits for the four cases. The results for the trigger efficiency are summarized in Tables A.2–A.3 (K_S), A.4–A.5 (Λ) and A.6–A.7 ($\bar{\Lambda}$). The results are showing that the trigger efficiency is generally very high. The trigger efficiency before the reweighting is also given for comparison, confirming the expectation that the trigger efficiency increases with track multiplicity.
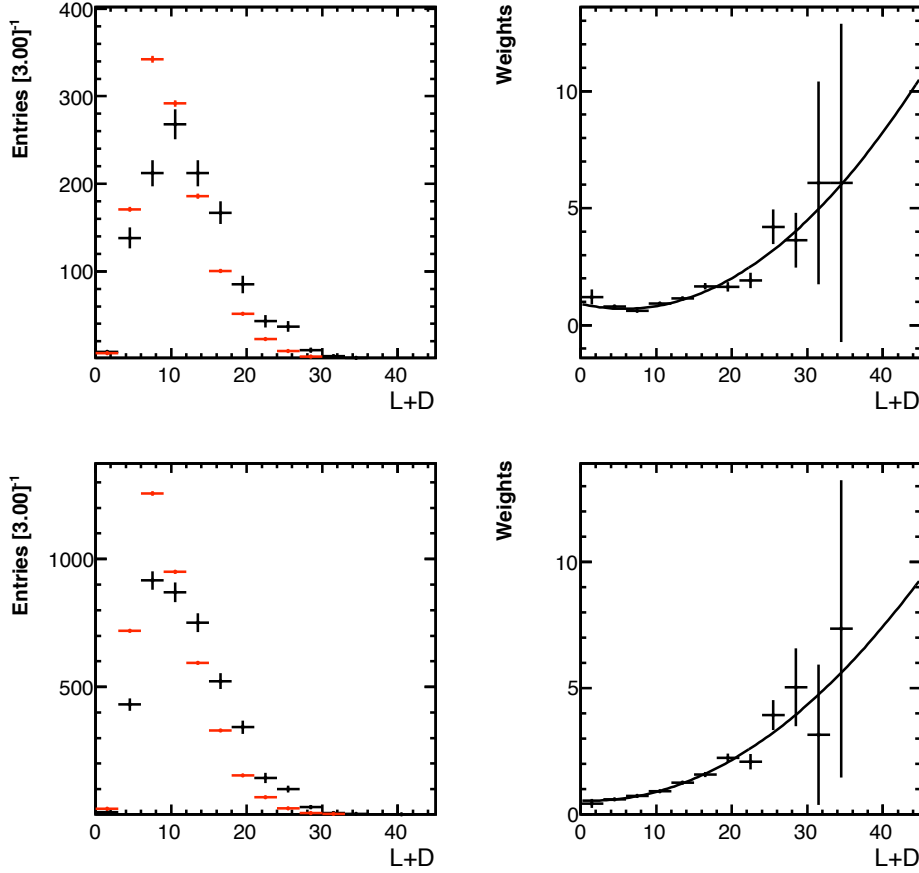
Figure 4.11: Left: L+D multiplicity distributions in the data (black) and in the MC (red), for beam-gas and side-band subtracted K_S in the LL (top) and DD (bottom) cases. Right: weights for each multiplicity bin after normalization of the MC, and second order polynomial fit.

4.7.2 Reconstruction and selection efficiency

Since the reconstruction and selection $\epsilon_{\mathrm{reco+sel}}$ does not depend strongly on the overall multiplicity, the reconstruction and selection efficiency are determined from the MC sample without reweighting. Therefore we have

$$\epsilon_{\mathrm{reco+sel}} = \frac{S_{\mathrm{nw}}}{N_{\mathrm{Gen}}^{\mathrm{prompt}}} \ , \tag{4.9}$$

where the numerator S_{nw} is the reconstructed and selected yield obtained in a given bin on the non-reweighted MC sample without applying the trigger, and the denominator $N_{\mathrm{Gen}}^{\mathrm{prompt}}$ is the number of true promptly-produced V^0 in that bin. It is important to note here that S_{nw} is taken in the "measured" (p_{T},y) bin, while $N_{\mathrm{Gen}}^{\mathrm{prompt}}$ is taken in the true (p_{T},y) bin.

The results are summarized in Tables A.8–A.9 (K_S), A.10–A.11 (Λ) and A.12–A.13 ($\bar{\Lambda}$). As we will see, the selection efficiency is relatively high ($\sim 70-80\%$), implying that the poor overall efficiency is dominated by geometrical acceptance and reconstruction. In fact, most of the loss is due to the geometrical acceptance of the detector.

It is also interesting to note that the efficiency is in general higher for the DD case, which is expected due to the reduced VELO acceptance. In general, the efficiency is increasing with p_{T}

and reaching a maximum in the middle y bin.

4.7.3   Total efficiency

The total efficiency ϵ_{tot} is computed with Eq. 4.7, and is quoted in Tables A.26–A.27 (K_{S}), A.28–A.29 (Λ) and A.30–A.31 ($\bar{\Lambda}$), with statistical and systematic errors. The systematic errors are derived in Sec. 4.8. Apart from some exceptions, the results are generally showing an increasing total efficiency with p_{T} for a given y bin, a maximum efficiency in the middle y bin for a given p_{T} bin, and that the efficiency is generally higher for the DD cases. This latter effect is due to the open VELO configuration, which reduces drastically the acceptance for LL cases.

4.8   Systematic uncertainties

4.8.1   Signal extraction

In order to estimate the systematic uncertainty associated with the linear background hypothesis, several other methods have been applied for the signal extraction. The list of all the methods, including the nominal one, is the following:

- Nominal side-band subtraction (CL).

- Side-band subtraction with a counting method assuming a quadratic background (CQ); this method is described in detail in Appendix A.1.

- Side-band subtraction with fit of the background only in the side-bands, assuming a quadratic shape (FQ).

- Fit of the mass distribution with the sum of a linear function for the background and a Gaussian function for the signal (FLG).

- Fit of the mass distribution with the sum of a quadratic function for the background and a Gaussian function for the signal (FQG).

For all these methods, the beam-gas subtraction is performed prior to any fit or side-band subtraction. For the DD case, the CQ method has been applied with two different signal windows, the nominal ± 40 MeV/c^2 mass window as well as a reduced signal window of ± 30 MeV/c^2. The sizes of the side-band windows are modified accordingly.

Tables A.14–A.15 (K_{S}), A.16–A.17 (Λ) and A.18–A.19 ($\bar{\Lambda}$) in Appendix A.4.3 summarize the results of the different methods for the LL and DD cases[12]. When the fit fails, no fitting is performed and no yield extraction is done with this particular method (represented by a "–" in the tables).

The systematic error Δ_S on the signal yield in each bin is then calculated using the signal yields S_i obtained with the n methods (other than CL) that gave results

$$\Delta_S = \sqrt{\frac{1}{n} \sum_{i=1}^{n} (S_i - S_{\text{CL}})^2} \, ,$$

where S_{CL} is the value measured with the nominal method (linear side-band subtraction). The Δ_S values as well as the relative uncertainties $\Delta_S/|S_{\text{CL}}|$ are quoted in the tables.

---

[12]Thanks to Yanxi Zhang for developing the corresponding software.

Since several bins exhibit very large uncertainties associated with the extraction of the signal or very poor signal, we decide therefore to drop them for the analysis. These bins are shown in parentheses in the tables. Apart from these dramatic exceptions which cannot be included in a measurement, the systematic uncertainties associated with the signal extraction is mostly located between 2% and 20% (3% and 30%) for the K_S (Λ and $\bar{\Lambda}$) case.

4.8.2 Trigger efficiency

The trigger efficiency can in principle be determined in the data, with the TIS-TOS method described hereafter. However, this method requires sufficient signal events in each bin. Since our available statistics are rather small, we will use this method only for the determination of a systematic error on the trigger efficiency. The trigger efficiency is measured in the data only in bands of p_T and in bands of y. We then compare the efficiency in these bands with the efficiency computed in the reweighted MC.

As mentioned in Sec. 4.3, only events triggered by the calorimeters are used in the analysis, as they represent more than 98% of the whole data sample. Starting from the number of beam-gas and background subtracted events, S, the number of signal events before trigger $N_{\mathrm{BeforeTrigger}}$ can be extracted using the TIS-TOS method, fully documented in Ref. [61]. For a given signal definition, in our case the two tracks from the V^0, this method gives

$$N_{\mathrm{BeforeTrigger}} = \frac{S_{\mathrm{TIS}} \times S_{\mathrm{TOS}}}{S_{\mathrm{TIS\&TOS}}} \text{ and } \epsilon_{\mathrm{trig}} = \frac{S}{N_{\mathrm{BeforeTrigger}}} \ , \tag{4.10}$$

where

- S_{TIS} is the number of events Triggered Independently of the Signal (TIS);

- S_{TOS} is the number of events Triggered On the Signal (TOS);

- $S_{\mathrm{TIS\&TOS}}$ is the number of events that are both TIS and TOS.

The quantities S_{TIS}, S_{TOS} and $S_{\mathrm{TIS\&TOS}}$, measured in data, are by construction correlated. To compute the number of events before trigger with its statistical error, we can rewrite Eq. 4.10 as a function of statistically independent terms

$$N_{\mathrm{BeforeTrigger}} = \frac{(S_{\mathrm{Excl.TIS}} + S_{\mathrm{TIS\&TOS}}) \times (S_{\mathrm{Excl.TOS}} + S_{\mathrm{TIS\&TOS}})}{S_{\mathrm{TIS\&TOS}}} \ , \tag{4.11}$$

where

- $S_{\mathrm{Excl.TIS}}$ is the number of events that are TIS but not TOS;

- $S_{\mathrm{Excl.TOS}}$ is the number of events that are TOS but not TIS.

From Eq. 4.11, it is trivial that if $S_{\mathrm{Excl.TIS}}$ or $S_{\mathrm{Excl.TOS}}$ is zero, the number of events before trigger equals the signal in the data, and the trigger efficiency is equal to unity. In general, the number of exclusive TOS events lies around a few percents of the number of TIS events, which in our case produces many empty bins for exclusive TOS events, preventing a correct estimate of the trigger efficiency with the TIS-TOS method.

Thanks to Eq. 4.11, the statistical error on the number of events can be calculated easily. Since $S_{\mathrm{Excl.TIS}}$ is relatively small in the data, it is not possible to make the Gaussian statistical error hypothesis when propagating the errors on $N_{\mathrm{BeforeTrigger}}$ and ϵ_{trig}.

All the quantities in Eq. 4.11 can be extracted from data after subtracting both combinatorial background and beam-gas background, using Eq. 4.5, but applying it separately for exclusive

Table 4.9: Mean and r.m.s. of the difference $\epsilon_{\text{trig}} - \epsilon_{\text{trig,DATA}}$.

Case	mean [%]	r.m.s. [%]
K_{S}, LL	+0.3	1.5
K_{S}, DD	+0.0	1.0
Λ, LL	−0.4	1.2
Λ, DD	−0.2	1.1
$\bar{\Lambda}$, LL	−0.2	1.7
$\bar{\Lambda}$, DD	−0.7	0.6

TIS, exclusive TOS, and TIS & TOS events. The errors have also been determined with the toy MC mentioned earlier. For each toy experiment i, the number of events before trigger $N^i_{\text{BeforeTrigger}}$ is extracted, and the r.m.s. of the distribution gives the error on the number of events before trigger.

To estimate the systematic uncertainty related to the trigger efficiency, we compare the trigger efficiencies obtained on V^0 particles in the data using the above described method with the MC efficiencies, but in bands of p_{T} and y. As shown in Tables A.20 (K_{S}), A.21 (Λ) and A.22 ($\bar{\Lambda}$), the results are broadly consistent. A systematic error has been obtained by calculating the r.m.s. of the differences between the two efficiencies, $\epsilon_{\text{trig}} - \epsilon_{\text{trig,DATA}}$, averaged over all p_{T} and y bins for each case. As a consequence, this systematic uncertainty is not given per bin, but per category of V^0 and track type only. The results are summarized in Table 4.9. Based on the numbers from the table, an overall absolute systematic uncertainty of 1.5% (1.0%) is assigned to the LL (DD) analyses.

4.8.3   Track reconstruction

Two methods have been used, which are called "old method" and "new method". As the names explain, a method was initially used for the estimation, which later was superseded by a new method. Intentionally, I keep here the results of the two methods, mainly to show that the average uncertainty is quite similar.

Old method

The method is based on the differences between three MC samples: a nominal sample, a sample undercorrected for the hit-finding efficiency, and a sample overcorrected for the hit-finding efficiency. The nominal sample takes into account the observed apparent inefficiencies due to the misalignments, while the two others have been tuned to vary the inefficiency in each tracking layer by $\pm 1\sigma$ from the nominal correction. Details on the preparation of these three MC samples are given in Ref. [60].

The nominal MC is used for the calculations of the central values of the efficiencies. The selection and reconstruction efficiencies estimated with the three MC samples are quoted per bin in Tables A.8–A.9 (K_{S}), A.10–A.11 (Λ) and A.12–A.13 ($\bar{\Lambda}$), in the third, second and fourth columns respectively. The tracking systematic uncertainties Δ_{hit} are calculated as

$$\Delta_{\text{hit}} = \frac{1}{\sqrt{2}} \sqrt{(\epsilon_+ - \epsilon_0)^2 + (\epsilon_- - \epsilon_0)^2} \ , \tag{4.12}$$

where ϵ_0 is the nominal efficiency, and ϵ_+ (ϵ_-) the efficiency obtained from the overcorrected (undercorrected) sample.

Table 4.10: Efficiency correction factors used for the estimation of the tracking systematics.

Track p_{T}	LL	DD
< 200 MeV/c	0.83	0.85
$\in[200 - 400]$ MeV/c	0.94	0.99
> 400 MeV/c	0.98	1.01

New method

In this method [62], the single-track finding efficiencies are measured in the data and in the MC, and compared. Tracks from the T stations are extrapolated to the VELO, and a VELO segment is searched for to match the track, providing the VELO track finding efficiency. Inversely, track segments from the VELO are extrapolated and matched in the T stations, providing the T tracking efficiency.

The comparison of these tracking efficiencies in data and MC provides correction factors on the MC tracking efficiencies for the daughter particles, as a function of their transverse momentum and type (L or D). Table 4.10 shows these correction factors, defined by $\epsilon(\text{data})/\epsilon(\text{MC})$, were ϵ is the total efficiency for reconstructing a track. When filling the mass histograms, each V^0 candidate is given a weight corresponding to the inverse of the product of these factors, depending on the daughter transverse momenta. The signal yield S_{w} extracted in a particular (p_{T},y) bin after this reweighting is compared to the original yield S, and the relative systematic error defined as $\Delta_{\mathrm{track}} = (S_{\mathrm{w}} - S)/S$. The last column in Tables A.8–A.13 contains the tracking systematics computed as described above. It is noticeable that the two methods give similar uncertainties, and that the new method actually covers the results of the old method.

4.8.4 PV reconstruction efficiency

In order to estimate the systematic uncertainty associated with the reconstruction of the PV, we study hereafter several distributions related to it. Unless specified otherwise, we study all the reconstructed PV, not only the ones associated with a V^0.

Figure 4.12 shows the distributions of the coordinates of the reconstructed PV in the data and in the Monte Carlo. Offsets of -0.5107 ± 0.0007 mm in x, $+0.32 \pm 0.0007$ mm in y and -6.21 ± 0.08 mm in z are observed in the MC compared to the data. Since the selection is based only on a variable depending on the impact parameters, these offsets can be ignored for the analysis.

The widths of the PV distributions are also different, especially in y and z. The main part of these differences can be attributed to the fact that the MC badly reproduces the distribution of the PV, rather than to large discrepancies in the vertex resolutions. To check this assumption, we show in Fig. 4.13 the distributions of the IP of the mother and the pions, in the data and in the MC for selected and side-band subtracted K_{S} (LL). The agreement is reasonable and shows that the differences observed in the PV reconstruction does not affect much the selection.

In order to estimate the PV reconstruction efficiency, under the hypothesis that any triggered event contains at least one PV, we compute the fraction of triggered events having at least one recontructed PV, per bin of total track multiplicity, in the data after beam-gas subtraction and in the Monte Carlo (Fig. 4.14, left). Tracks of all types are counted, since all track types are used for the PV reconstruction. These distributions are first multiplied by the distribution of the number of tracks observed in the data, shown in Fig. 4.14 (right), and then integrated. The integration gives the total number of events with at least one reconstructed primary vertex for the data, and
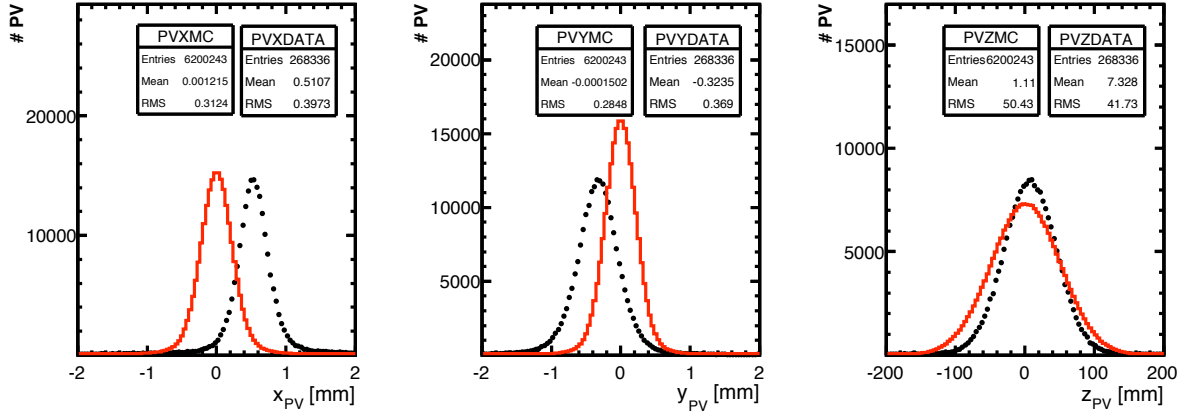
Figure 4.12: x, y and z coordinates of the reconstructed PV in all events, for the data (black points) and for the MC (red histograms).
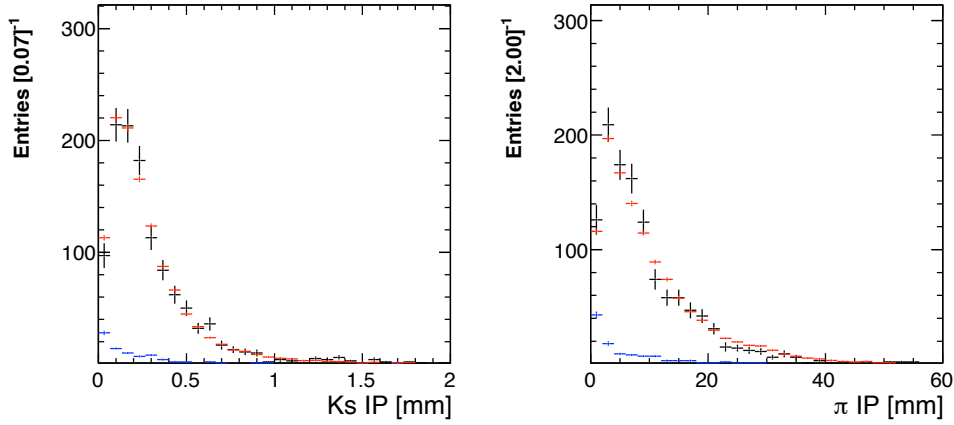
Figure 4.13: Impact parameters of the K_S (left) and one of the pions (right) for the LL case. Black: Signal (data), Blue: Background (data), Red: Signal (MC).

the number of events which would have a reconstructed PV in the MC if the track multiplicities were the same. After division by the total number of events in the sample, these numbers can be taken as the PV reconstruction efficiency. The computed values[13] are $\epsilon(\text{DATA}) = 90.44 \pm 0.57$ % and $\epsilon(\text{reweighted MC}) = 91.04 \pm 0.60$ %. The overall fraction of not reweighted MC events containing at least one reconstructed PV is equal to $\epsilon(\text{MC}) = 89.22 \pm 0.10$ %. The worst relative difference to data, found to be between data and not reweighted MC, has a value of $(1.35 \pm 0.01)\%$. Hence we assign a 1.5% systematic uncertainty on the PV reconstruction efficiency.

4.8.5   Selection efficiency

In order to estimate the systematic uncertainties associated with discrepancies between the selection efficiency in data and MC, a global selection efficiency is estimated for the full (p_T,y) range, for the data and the MC, and then compared. The result obtained will be applied to the individual (p_T,y) bins. The global selection efficiency is obtained by fully releasing the cuts, and then applying them one-by-one, in the data and the MC, each time computing the new selection

---

[13]Thanks to Raphael Maerki for providing these values.
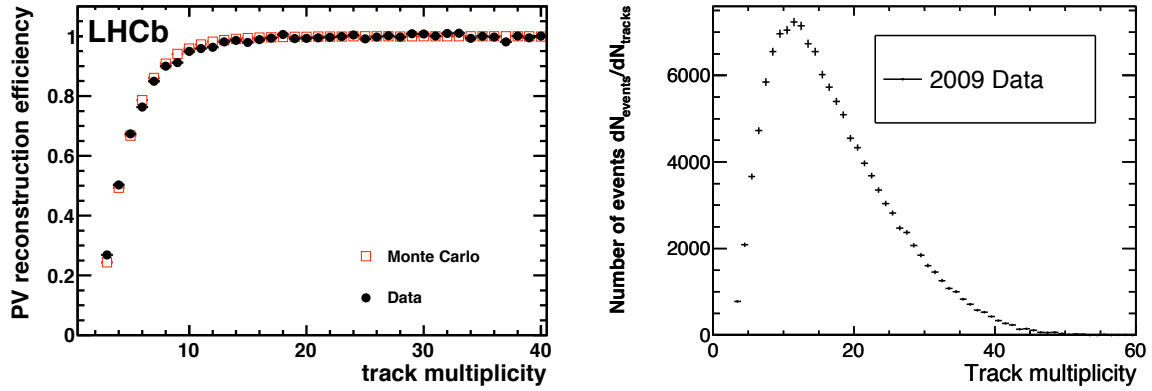
Figure 4.14: Left: Fraction of all events containing at least one reconstructed primary vertex, in the data after beam-gas subtraction and in the Monte Carlo, as a function of the total track multiplicity in the event. Right: Distribution of total track multiplicity in the data. By Raphael Maerki.

efficiency.

The only selection cut that affects significantly the signal efficiency is ν_1, all other cuts are fully efficient or close. There are three cuts that we cannot release completely. the first one is the cut on the V^0 vertex χ^2/DOF, which has been chosen to be close to 100% efficient on the signal, apart for the Λ DD case. Without this cut, it wouldn't be possible to study properly the other cuts because the signal would be completely flooded by the background; therefore it is applied in all the distributions below. Secondly, by definition it is impossible to study data events that have not been triggered, therefore all the MC distributions that will follow will be shown for triggered events. Thirdly, due to the nature of the main selection requirement ν_1, it is impossible to perform the analysis without a PV requirement.

In order to estimate the systematics related to the selection efficiency, we start with a sample on which no cut has been applied, apart from those mentioned above, and apply the cuts one by one, always keeping the previous cut, and each time estimating the systematics on the efficiency of the new cut. All the plots shown in this section are beam-gas subtracted for the data, and side-band subtracted for the data and the MC. All distributions are normalized to the total number of signal events in the data.

V^0 vertex χ^2/DOF cut

The distributions of the χ^2/DOF of the V^0 vertex are shown in Fig. 4.15 for K_S and Fig. 4.16 for $\Lambda + \bar{\Lambda}$, without applying any other cut[14] (top), and applying all the other cuts (bottom). The MC distributions are very similar to the data distributions, especially for the LL case. For the DD case, the χ^2/DOF in the MC seems in general a bit smaller than in the data. In all cases except $\Lambda + \bar{\Lambda}$ DD, the distribution before other cuts sharply falls before 100 ($\log_{10}(100) = 2$), and therefore the efficiency of the cut at 100 is very close to 100%. It is obvious that this cut rejects only background for the LL cases. Since in addition the shapes are very close in all the cases, it is reasonable to consider that the MC reproduces well the data. Since we have no means to compute the efficiency differences of that cut, we arbitrarily assign a 2% systematics on the efficiency of that cut. For the reasons mentioned above, this can be considered as a conservative estimate.

---

[14]Except those mentioned in the previous paragraph.
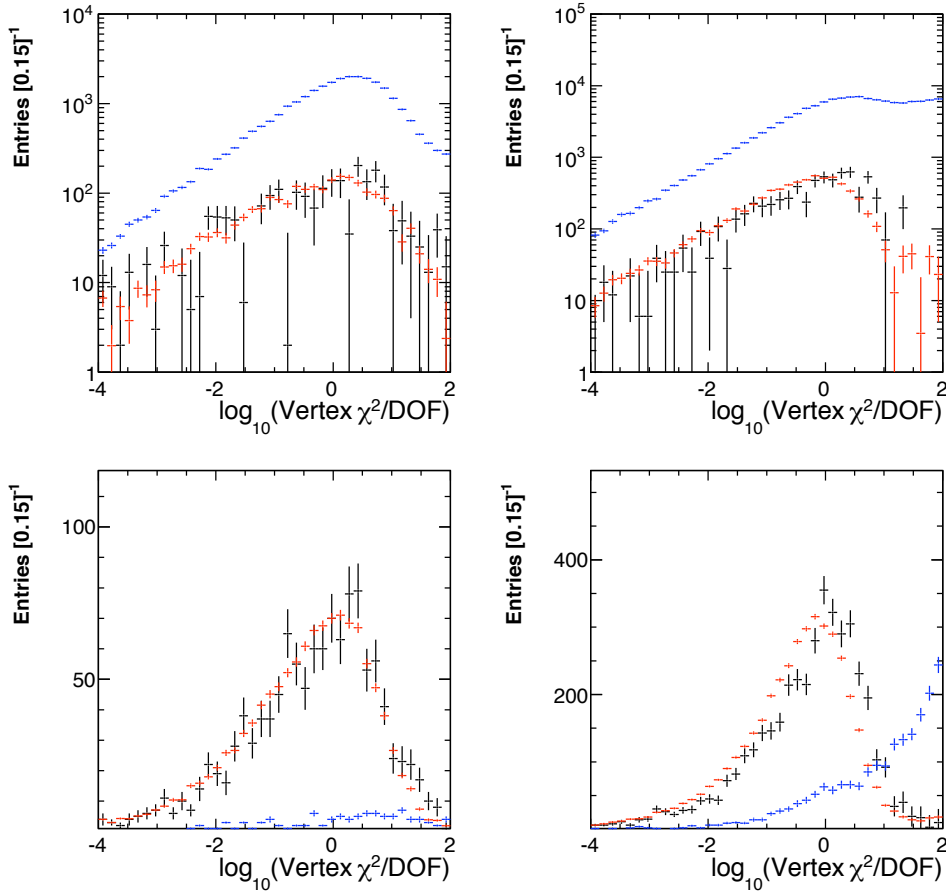
Figure 4.15: Vertex χ^2/DOF for K_S LL (left) and DD (right), without other cuts (top) and with all the other cuts (bottom) applied. Black: Signal (data), Red: Signal (MC), Blue: Background (data).

Luminous region cut

In order to reject most of the beam-gas events, we require the z coordinate of the PV to satisfy $-200 < z_{\mathrm{PV}} < 200$ mm, i.e. the z coordinate of the PV to be in the luminous region. The distributions are shown in Fig. 4.17 for K_S. This cut is found to be 100% efficient on the data and the Monte Carlo, after beam-gas subtraction. There are some statistical fluctuations outside of the window, which are disappearing when taking 200 mm bins. These statistical fluctuations are coming from the beam-gas subtraction.

Since the z distribution of the PV is independent of the presence of a V^0 in the event, we show only the distributions of the PV associated with a K_S in the event, and assume the conclusions to be valid for Λ. The reason for doing this is that it is easier to measure the efficiency of that cut on the K_S sample, because of the larger statistics with respect to Λ. Since the cut is safely far from the luminous region limits, we decide to assign no systematic uncertainty.

"Positive lifetime" cut

In order to reject combinatorial background, we require the z coordinate of the V^0 vertex to be larger than the z coordinate of its associated PV ($z_{V^0} - z_{\mathrm{PV}} > 0$). This cut is very powerful for background rejection without affecting the signal (apart for Λ DD). Indeed, the combinatorial
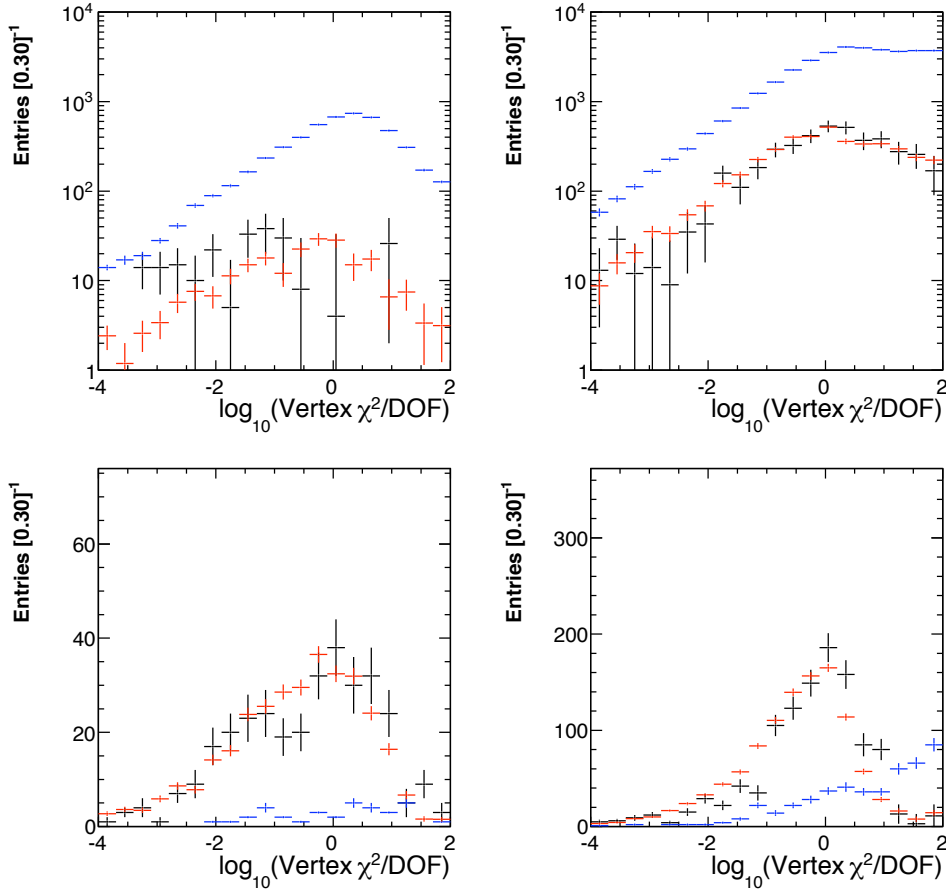
Figure 4.16: Vertex χ^2/DOF for $\Lambda + \bar{\Lambda}$ for LL (left) and DD (right), without other cuts (top) and with all the other cuts (bottom) applied. Black: Signal (data), Red: Signal (MC), Blue: Background (data).

background, formed mainly by primary particles, has a reconstructed vertex located near the PV, while the signal from a primary V^0 can only have its decay vertex downstream of the PV. It is quite obvious from Figs. 4.18 (K_S) and 4.19 (Λ) that the effect of the cut is very similar in the data and in the MC, even if the DD case for Λ exhibits a different shape, which is very well described in the MC. In order to estimate the systematics, we measure the efficiencies in the data and in the MC using only two bins, avoiding large statistical fluctuations in individual bins. We obtain exactly 100% for the K_S LL, K_S DD and Λ LL cases, for both data and MC. However for the Λ DD case, the efficiency computed from the data is $73 \pm 4\%$, while it is $71 \pm 1\%$ in the MC. We decide therefore to assign no systematics for the K_S LL, K_S DD and Λ LL cases, and assign a 3% systematics for the Λ DD case.

The tail at $z_{V^0} - z_{\rm PV} < 0$ for the Λ DD case is understood to be due to a resolution effect: since the proton (anti-proton) daughter of the Λ ($\bar{\Lambda}$) is pointing towards the PV due to its larger mass compared to the π^- (π^+), the position of the decay vertex is consequently less precisely determined for this case than for K_S DD case. In any case, this is not important for the evaluation of the systematic uncertainty, since the effect is perfectly described in the MC.
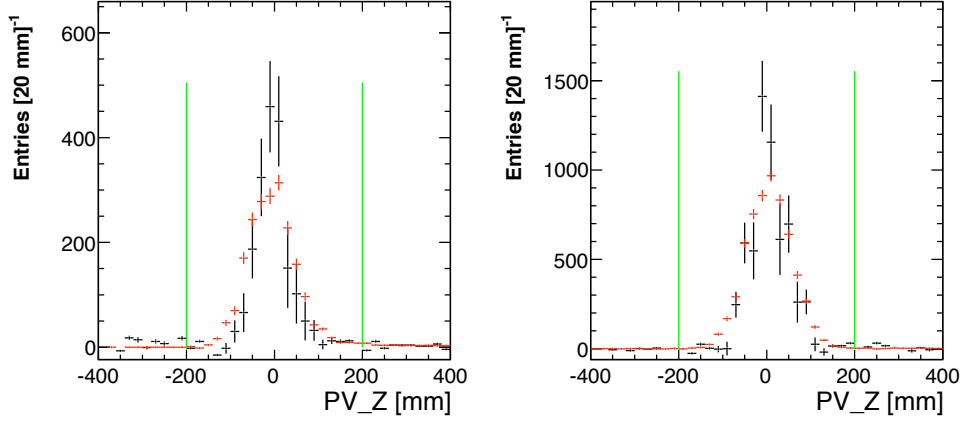
Figure 4.17: z coordinate of the PV for K_S LL (left) and DD (right). Black: Signal (data), Red: Signal (MC), Green line: cut.
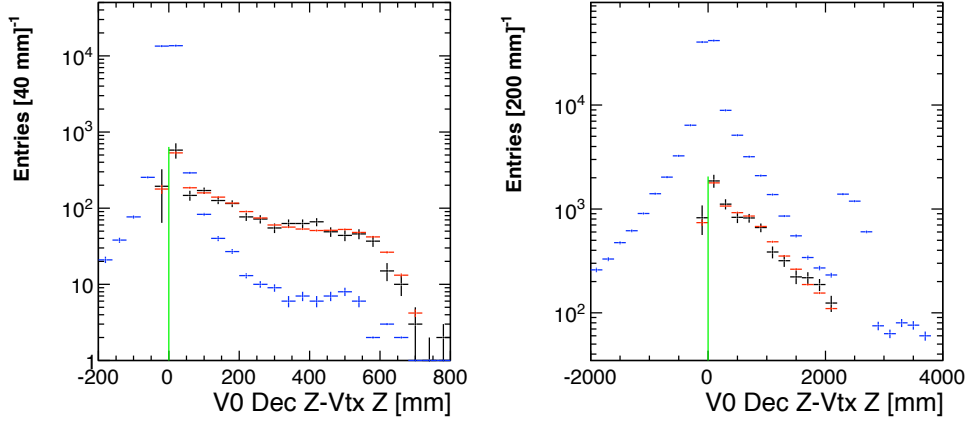
Figure 4.18: z flight distance distribution for K_S LL (left) and DD (right). Black: Signal (data), Red: Signal (MC), Blue: Background (data), Green line: cut. The background peak around 2.5 m for the DD case is due to particles coming from material interactions in the TT.

Figure 4.19: z flight distance distribution for Λ LL (left) and DD (right). Black: Signal (data), Red: Signal (MC), Blue: Background (data), Green line: cut. The background peak around 2.5 m for the DD case is due to particles coming from material interactions in the TT.

Figure 4.20: ν_1 distributions for K_S LL (left) and DD (right). Black: Signal (data), Red: Signal (MC), Blue: Background (data), Green line: cut.

Figure 4.21: ν_1 distributions for Λ LL (left) and DD (right). Black: Signal (data), Red: Signal (MC), Blue: Background (data), Green line: cut.

ν_1 cut

The distributions of the ν_1 variable in the MC are slightly different than in the data. These distributions are shown in Figs. 4.20 (K_S) and 4.21 (Λ). The calculation of the efficiencies for K_S show good agreement between data and MC: $\epsilon_{\mathrm{data}} = 68.7 \pm 2.0\%$ vs. $\epsilon_{\mathrm{MC}} = 71.5 \pm 0.5\%$ for LL, and $\epsilon_{\mathrm{data}} = 66.7 \pm 1.3\%$ vs. $\epsilon_{\mathrm{MC}} = 66.3 \pm 0.2\%$ for DD. The same calculations for Λ is very difficult, due to the lower statistics. However, since the ν_1 variable depends on IP calculations which are dominated by detector and reconstruction features, we can be confident, based on the K_S results which do not suffer from the lack of statistics, that the systematic uncertainties of the ν_1 variable is not very different for Λ than for K_S. As a consequence, we assign a 4% systematic error on the ν_1 cut efficiency.

Track quality cuts

The track quality requirement on the daughter tracks used in this analysis is $\chi^2/\mathrm{DOF} < 25$. It was agreed by the LHCb Flavour Working Group, although it does not have a strong effect, neither on the signal, nor on the background (see Figs. 4.22 and 4.23). The idea is to apply a

Table 4.11: Efficiency (in %) of the cut on the track χ^2/DOF, in Monte Carlo and in data.

Case	K_S LL	K_S DD	$\Lambda\,\pi$ LL	$\Lambda\,\pi$ DD	Λ p LL	Λ p DD
Data 2009	99.8 ± 3.0	99.7 ± 2.0	100 ± 6	100 ± 4	100 ± 6	99.5 ± 4
MC	99.7 ± 0.6	99.9 ± 0.4	99.9 ± 1.7	99.9 ± 1.1	99.8 ± 1.7	99.8 ± 1.1

loose cut, since the χ^2/DOF distributions do not look similar in the Monte Carlo and in the data, as seen on the figures. This cut is applied after all the other cuts. The efficiency of the cut on the signal for the different cases are quoted in Table 4.11. Based on these results, we assign a systematic uncertainty of 1% on the efficiency of this cut, which clearly covers the differences computed for all the cases.

4.8.6 MC modelling of the production spectra

In bins where the efficiency is varying steeply, the efficiency-corrected yields can be affected by small discrepancies in the p_T and y distributions between the data and the Monte Carlo. In order to take this effect into account, an analysis in finer bins is performed. Yields are extracted in bins of 0.1 GeV/c instead of 0.2 GeV/c in p_T, and in bins of 0.25 instead of 0.5 in y. The efficiency is extracted in the MC in the same binning, and the efficiency corrections are applied in each sub-bin. The sum of the efficiency-corrected yields from the four sub-bins is then compared to the nominal efficiency-corrected yields, which are given in Sec. 4.9. The difference is used as a systematic uncertainty on the final corrected yields. The results are quoted for K_S in Tables A.23 (LL) and A.24 (DD). This analysis is only done for K_S, since the low Λ statistics do not allow a splitting in finer bins. The tables are in general showing, among the same p_T bin, an efficiency rapidly increasing with y in the range $2.5 < y < 3.5$, and rapidly decreasing in the range $3.5 < y < 4.0$.

4.8.7 Diffraction modelling

No attempt is made to exclude the V^0 produced in diffractive events, however it is known that they are present at a yet unknown level. The measurement presented here quotes the cross-section for the sum of diffractive events (DE) and non-diffractive (NDE) events, in other terms all inelastic collisions. A possible discrepancy in the relative numbers of V^0 from DE and NDE between the MC and the data may introduce a bias which is model dependent. Indeed, if the efficiency is different for DE and NDE, the average MC efficiency used in the analysis may be wrong.

Studies have been performed[15] [63] to estimate the efficiency function for DE and NDE, using MC samples produced with two different generators: PYTHIA 8.130 [64], which is advertized as having the most accurate diffraction model on the market, and PYTHIA 6.421 [31], which is the model used by default in this analysis and takes only soft-diffraction into account. The results quoted in Table A.25 for K_S show that the relative differences in efficiency fall in the range $0.7 - 3.9\%$ for LL and $0.0 - 3.1\%$ for DD. These are taken as systematic errors on the K_S efficiencies. For Λ, for simplicity we assign a constant average systematic uncertainty of 3% on the Λ efficiencies.

---

[15]Thanks to Raluca Muresan for performing this study.
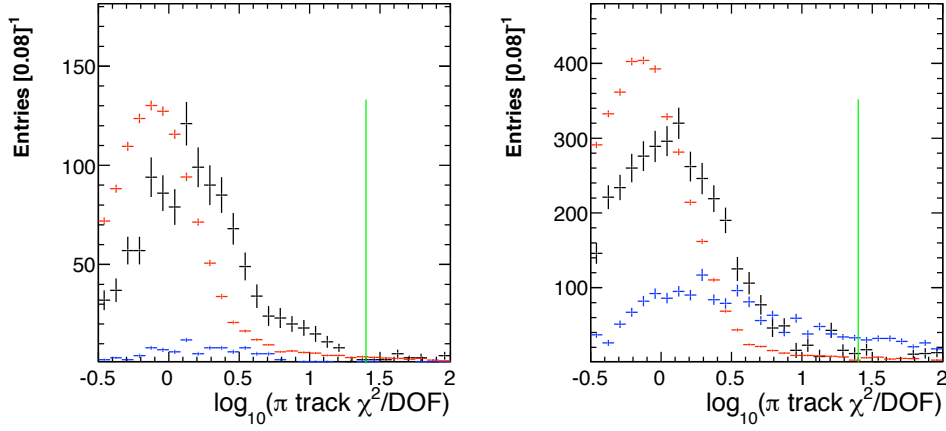
Figure 4.22: χ^2/DOF of the daughters of the K_S for LL (left) and DD (right). Black: Signal (data), Red: Signal (MC), Blue: Background (data), Green line: cut.
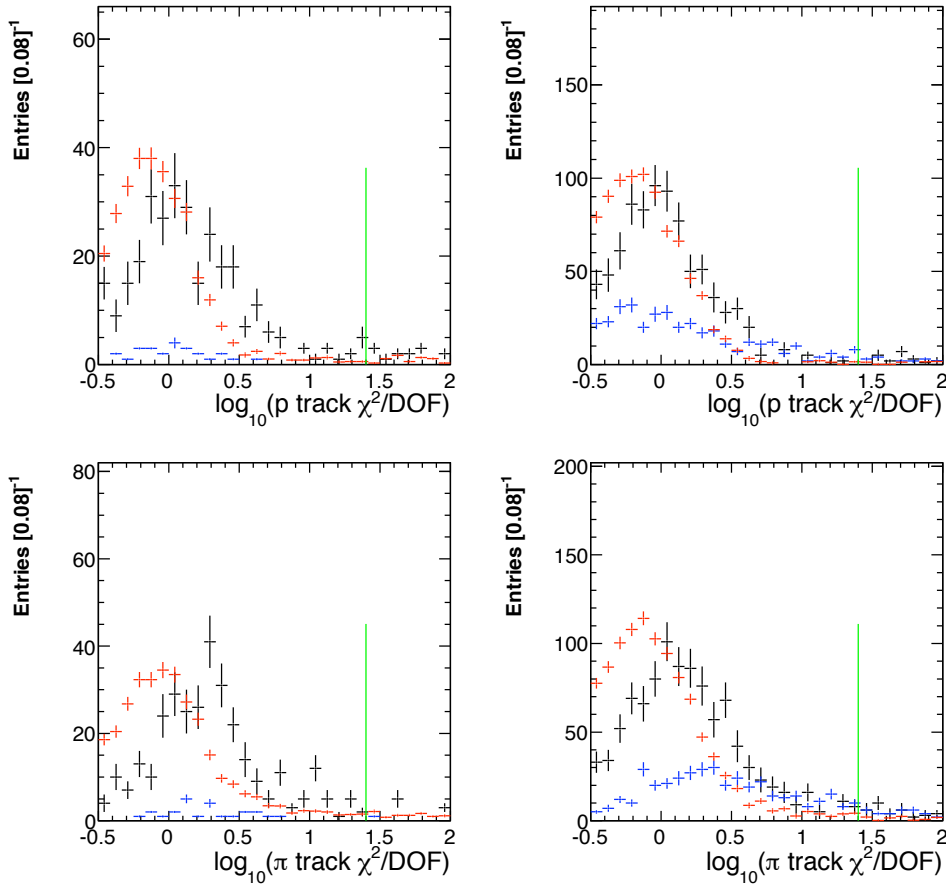
Figure 4.23: χ^2/DOF of the proton (top) and pion (bottom) of the Λ and $\bar{\Lambda}$ for LL (left) and DD (right). Black: Signal (data), Red: Signal (MC), Blue: Background (data), Green line: cut.

Table 4.12: Contamination of the selected V^0 from long-lived components and from V^0 produced in material interactions, in percents of the signal yield.

Case	decays from long-lived [%]	material interactions [%]
K_S LL	0.7	0.07
Λ LL	5	0.2
$\bar{\Lambda}$ LL	4	0.5
K_S DD	1.25	0.5
Λ DD	9	0.5
$\bar{\Lambda}$ DD	8	0.1

4.8.8   Non-prompt contamination

We estimate from the MC the contamination of the signal coming from the decays of long-lived particles and from V^0 produced in interactions with the material. These two contributions, summarized in Table 4.12, are forming together the non-prompt component. The contribution from V^0 produced in interactions in the material is negligible, even if the material simulated in the MC were underestimated by a factor two. However, since it seems that the decay from long-lived component is sizeable especially for Λ DD and $\bar{\Lambda}$ DD (of the order of 10%), it has been decided to take a 50% relative uncertainty on the long-lived component. A 2% systematic error for Λ LL and $\bar{\Lambda}$ LL, a 4% systematic error for Λ DD and $\bar{\Lambda}$ DD, and a 0.5% systematic error for K_S are therefore added.

4.8.9   Cross-checks

The lifetime distributions are an important cross-check, since they involve several observables measured by the detector, such as decay length and momentum. They are shown in Fig. 4.24, where it can be checked that data signal and MC signal are in very good agreement. Since these uncorrected distributions depend strongly on the momentum distributions (via the momentum-dependent efficiency), which are not exactly the same in the data and in the MC, the figures shown here are an approximation integrated over all momentum bins.

The geometrical acceptance of the detector as a function of the azimuthal angle is another important cross-check. We can verify that the open-VELO geometry is well reproduced in the Monte Carlo. Figure 4.25 is showing for both the LL and DD cases the distribution of the azimuthal angle ϕ of the K_S momentum in the xy plane, taken in the centre-of-mass of the pp collision. Because of the good ageement between data and MC, no additional systematic uncertainty on the geometrical acceptance is considered. Similar figures were obtained for Λ, however because of the smaller statistics they are not shown here.

4.9   Final results

The uncertainties are summarized for all V^0 categories in Table 4.13. They are considered either as correlated or uncorrelated across the bins, and are combined in quadrature. The dominant ones arise from the data statistics, the signal extraction procedure and the track finding algorithms. The total efficiency-corrected yields are quoted in the last column of Tables A.26–A.27 (K_S), A.28–A.29 (Λ) and A.30–A.31 ($\bar{\Lambda}$). The tables contain the statistical errors,
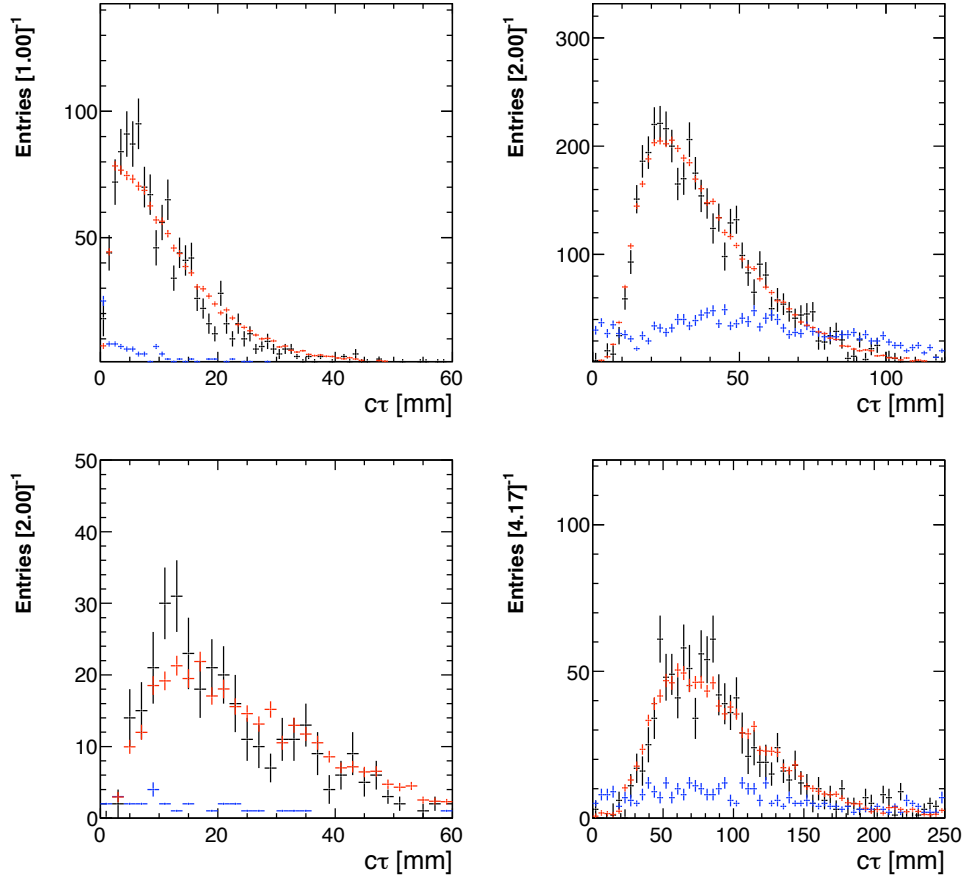
Figure 4.24: Lifetime distributions for K_S (top), and $\Lambda + \bar{\Lambda}$ (bottom), for LL (left) and DD (right). Black: Signal (data), Red: Signal (MC), Blue: Background (data).
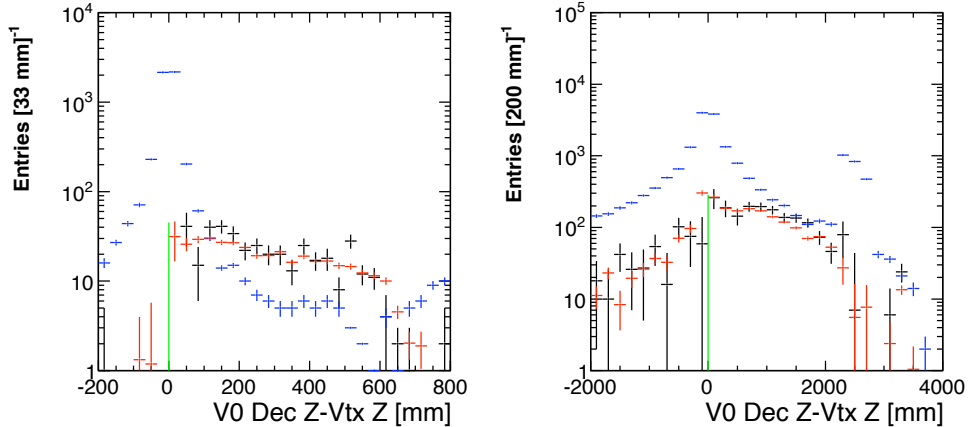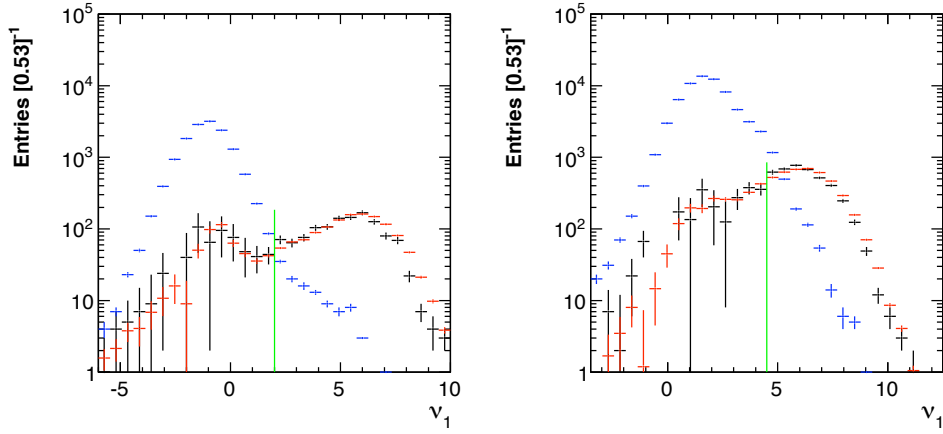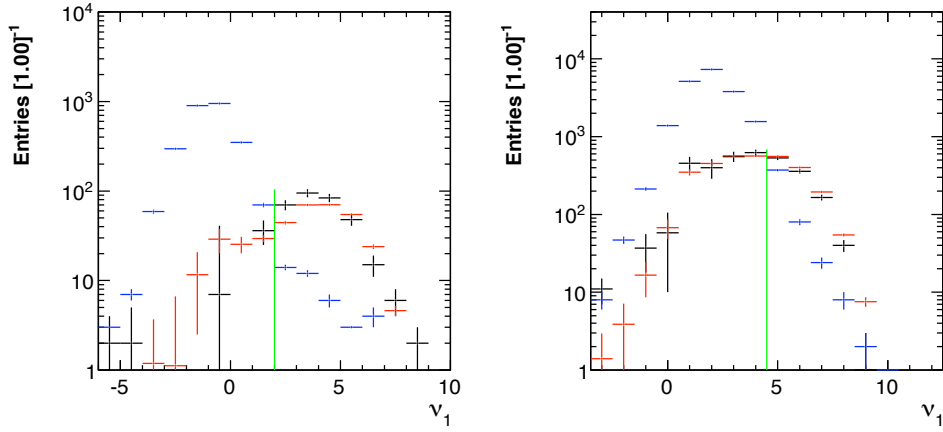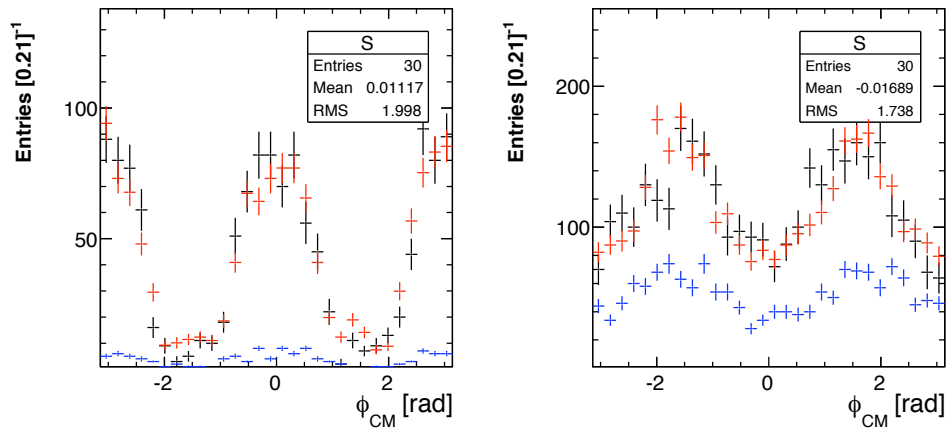

Figure 4.25: ϕ distributions for K_S, LL (left) and DD (right). Black: Signal (data), Red: Signal (MC), Blue: Background (data).

Table 4.13: Summary of uncertainties for all V^0 analyses, in percents. A range means that the corresponding uncertainty has been assigned on a bin-by-bin basis.

Analysis	K_S LL		K_S DD		$\Lambda/\bar{\Lambda}$ LL		$\Lambda/\bar{\Lambda}$ DD	
Source of uncert.	Uncorr.	Corr.	Uncorr.	Corr.	Uncorr.	Corr.	Uncorr.	Corr.
Yields								
Data statistics	$9-38$		$7-15$		$15-30$		$10-20$	
Signal extraction	$0-21$		$3-20$		$3-40$		$4-30$	
Efficiency								
MC statistics	$1-5$		$1-5$		$1-5$		$1-5$	
Track finding		$4-27$		$1-11$		$0-20$		$0-17$
MC prod. model	$0-25$		$0-8$		$-$		$-$	
ν_1 cut		4		4		4		4
V^0 vertex χ^2 cut		2		2		2		2
Track quality cut		1		1		1		1
Pos. lifetime cut		0		0		0		3
PV reconstruction		1.5		1.5		1.5		1.5
Trigger		1.5		1		1.5		1
Non-prompt model		0.5		0.5		2		4
Diffraction model		$1-4$		$1-3$		3		3
Quadratic sum	$9-50$	$6-27$	$8-27$	$5-12$	$15-50$	$6-21$	$15-40$	$8-21$

the uncorrelated systematic errors, as well as the correlated systematic errors. The latter are split in two parts, one bin-dependent part (syst$_c$) and one overall systematic uncertainty (syst$_{c2}$).

The efficiency-corrected yields for all bins are shown in Figs. 4.26 (K_S), 4.27 (Λ) and 4.28 ($\bar{\Lambda}$) with all the errors summed in quadrature, in the two cases LL and DD. As seen from the figures, the two independent LL and DD analyses give consistent results.

In order to check this assumption quantitatively, the "pull" plots are also shown in the figures. The pull is defined as the difference between the DD and the LL measurements divided by the error on this difference, where only statistical and uncorrelated systematical errors are considered. The pull distribution is then fitted with a Gaussian using the binned maximum log-likelihood method. For consistent results, the mean of the pull distribution should be compatible with zero, and the width compatible with unity. The results for the mean of the pulls obtained by the fits indicate that the agreement between LL and DD analyses is good for K_S (0.10 ± 0.16) and Λ (-0.19 ± 0.19), slightly marginal for the $\bar{\Lambda}$ (0.56 ± 0.31). The widths of the pulls (K_S: 0.77 ± 0.11, Λ: 0.53 ± 0.13, $\bar{\Lambda}$: 0.86 ± 0.21) suggest that some uncertainties which are assumed to be uncorrelated may be partially correlated.

Since the agreement between LL and DD measurements is satisfactory, we can compute the weighted average of the LL and DD efficiency-corrected yields in each bin, and use this value for the cross-section measurement. The calculation of the weighted average is described in detail in Appendix A.2. Tables A.32–A.34 quote the weighted averages and the cross-section results, using the measured luminosity value of 6.8 ± 1.0 μb^{-1} [5]. The cross-section results are shown in Fig. 4.29, together with the $\bar{\Lambda}/\Lambda$ ratio. In the latter case, only the statistical and uncorrelated systematic errors are taken into account, assuming that the correlated systematic errors cancel in the ratio.

Due to the unique coverage of the LL analysis down to very low p_T bins, the results from the first two bins for the lowest y bin have been used for the K_S analysis that was published in
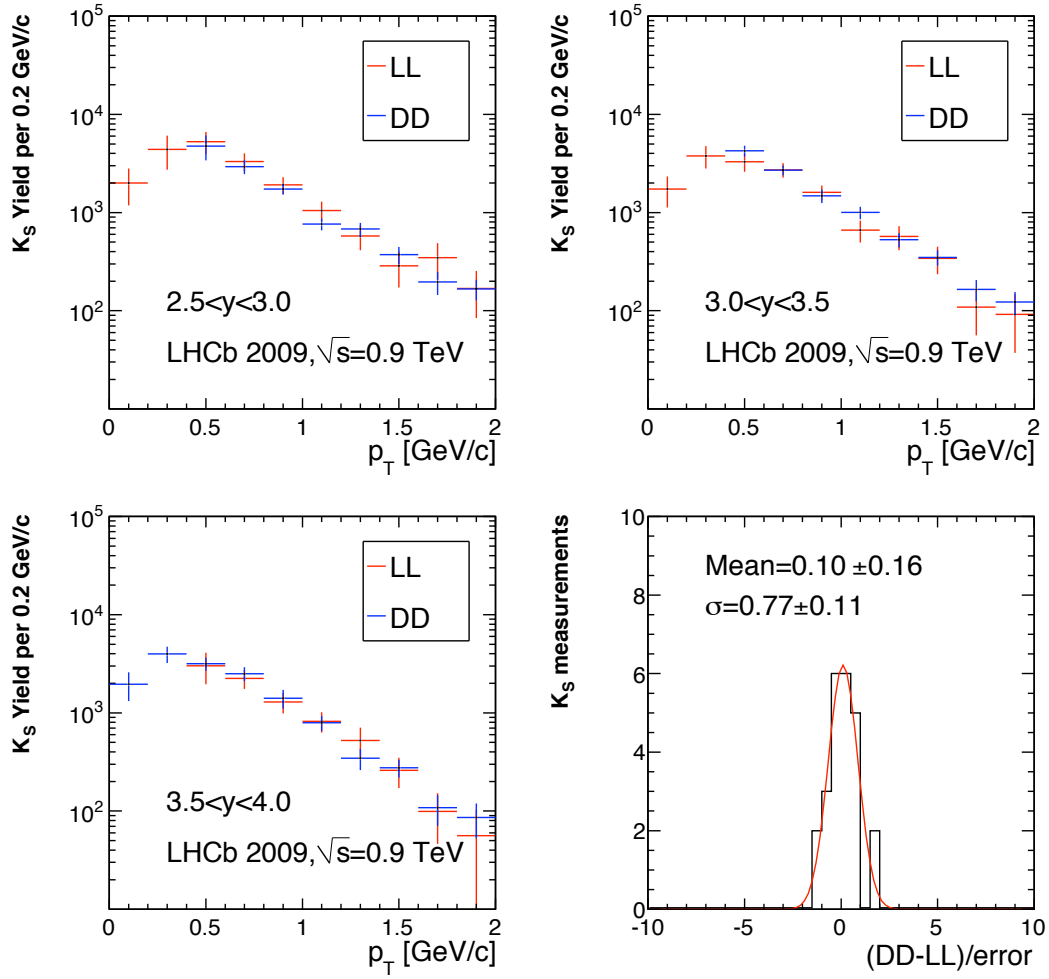
Figure 4.26: Top and bottom left: Efficiency-corrected K_S yields for LL and DD analyses, for the three rapidity bins. All errors are summed in quadrature. Bottom right: "Pull" plot of the LL and DD measurements with one entry per (p_T,y) bin. Only statistical and uncorrelated systematic errors are included in the pull calculation.

the first LHCb publication [5].

4.9.1   Data-MC comparisons

The double differential prompt V^0 production cross-sections are shown together with several MC models in Figs. 4.30 (K_S) and 4.31 (Λ and $\bar{\Lambda}$), as well as the ratio between the models and our measurements. The comparison of the $\bar{\Lambda}/\Lambda$ production ratio with the same models is shown in Fig. 4.32. The MC simulations we compare our results to are all obtained with the PYTHIA 6.4 [31] generator, with different tunings:

- The standard LHCb tuning [65], which includes only soft diffraction as described by PYTHIA 6.4;

- The LHCb tuning where diffractive processes have been switched off;

- The "Perugia 0" tuning [66], which excludes diffraction.
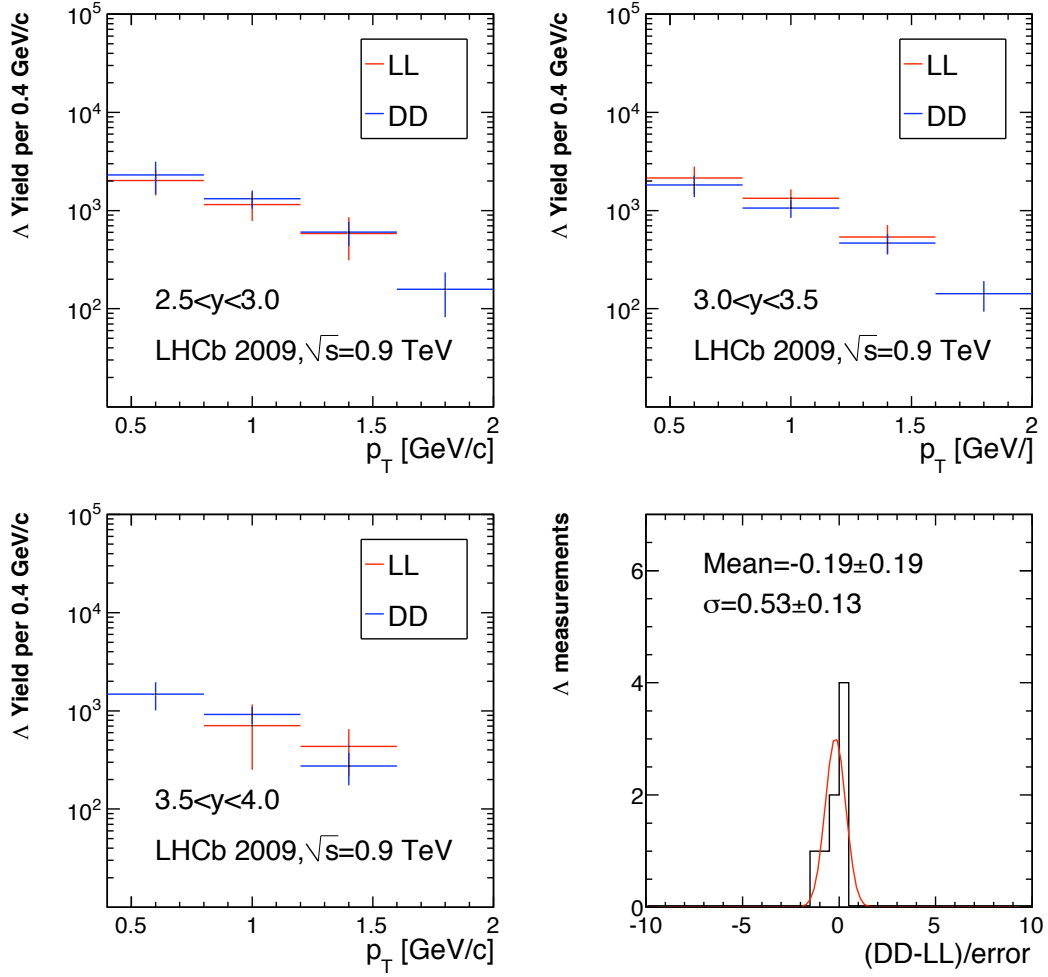
Figure 4.27: Top and bottom left: Efficiency-corrected Λ yields for LL and DD analyses, for the three rapidity bins. All errors are summed in quadrature. Bottom right: "Pull" plot of the LL and DD measurements with one entry per (p_T,y) bin. Only statistical and uncorrelated systematic errors are included in the pull calculation.

The decays and radiative corrections are handled by EvtGen [32] and PHOTOS [33] respectively.

These figures show that the K_S production cross-section is mostly overestimated for $p_T < 0.4$ GeV/c and underestimated for $p_T > 1$ GeV/c for all considered models. The Λ and $\bar{\Lambda}$ production cross-section is mostly underestimated by all models, especially for $p_T > 0.8$ GeV/c, by a factor of $\sim 2 - 3$.

In addition, the data indicate that the $\bar{\Lambda}/\Lambda$ ratio is lower than in all considered models. By looking at the comparisons of the Λ and $\bar{\Lambda}$ cross-sections with the models, it seems that the badly modelled ratio is mostly due to the underestimation of Λ production, rather than overestimation of $\bar{\Lambda}$ production, even if the two are underestimated. However due to large uncertainties, no clear interpretation can be given yet. Moreover, the Λ and $\bar{\Lambda}$ cases distinguish themselves from the K_S case, since the decays are highly asymmetric between the proton and the pion. For instance, due to the magnetic field and the configuration of the detector, LHCb detects more Λ emitted at an azimuthal angle $\phi \simeq 0$, while it detects more $\bar{\Lambda}$ emitted at an azimuthal angle $\phi \simeq \pi$. Therefore one should check that the efficiency as a function of the azimutal angle is well described in the MC. In addition, the MC modelling of the hadronic interactions of p or $\bar{p}$ with
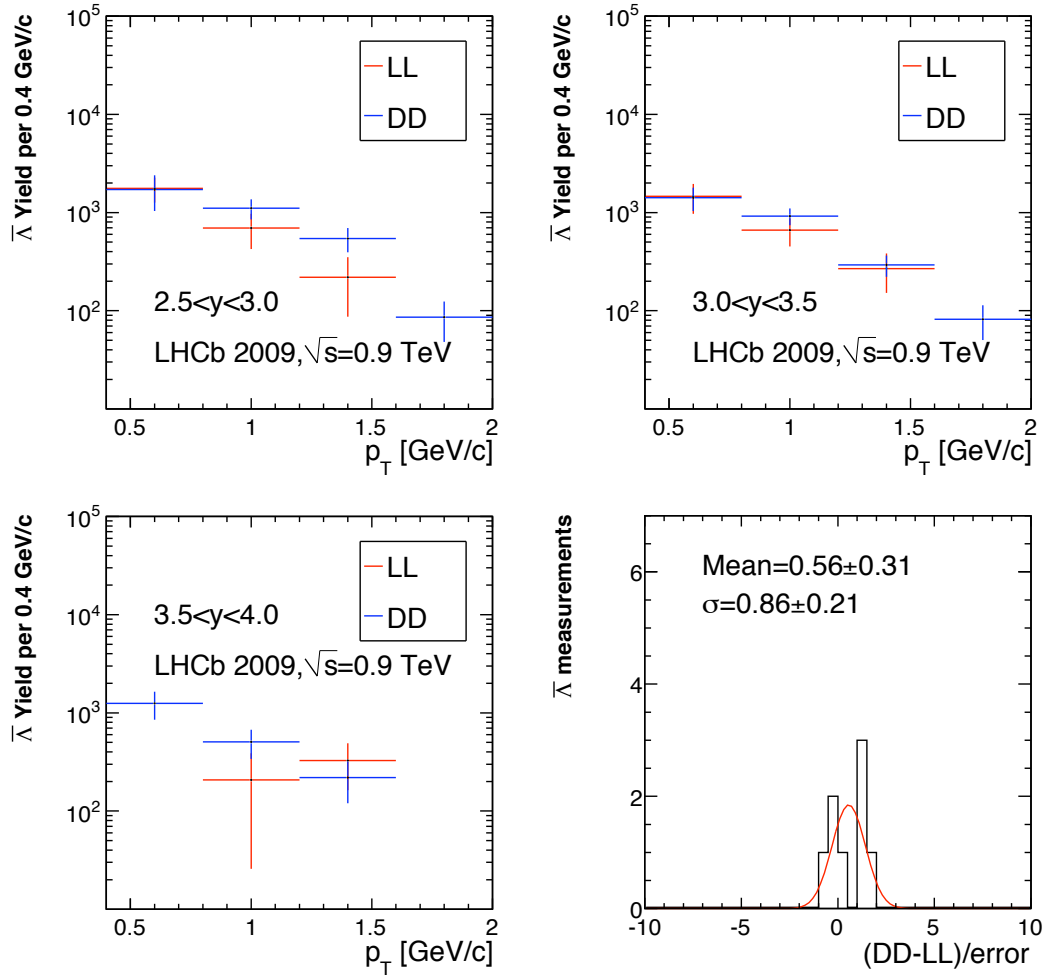
Figure 4.28: Top and bottom left: Efficiency-corrected $\bar{\Lambda}$ yields for LL and DD analyses, for the three rapidity bins. All errors are summed in quadrature. Bottom right: "Pull" plot of the LL and DD measurements with one entry per (p_T,y) bin. Only statistical and uncorrelated systematic errors are included in the pull calculation.

the detector material needs to be checked as well. Further studies are therefore needed before one can give an interpretation of the ratio. They are left for the analysis of the 2010 data, where larger statistics were recorded with each of the two magnetic field polarities.

4.9.2 Comparison with other results

The ALICE experiment has recently measured the production of strange mesons (K_S and ϕ) and both single and double strange baryons (Λ, $\bar{\Lambda}$ and $\Xi^- + \bar{\Xi}^+$) in pp collisions at $\sqrt{s} = 0.9$ TeV [70]. The results are given in terms of p_T spectra $1/N_{\text{evts}} \times d^2N/dp_T dy$ rather than cross-sections, and shown in Fig. 4.34 for K_S (top) and Λ (bottom). The measurement cannot be directly compared to our measurement since it has been performed for central values of rapidity ($|y| < 0.75$). However, it is worthwhile noting that the measured spectra for ALICE are also showing that the models for the K_S production cross-section are overestimated for low-p_T bins, and underestimated for high-p_T bins, in the y range considered. For the Λ case, the ALICE results are also showing a clear underestimation of the production cross-section.
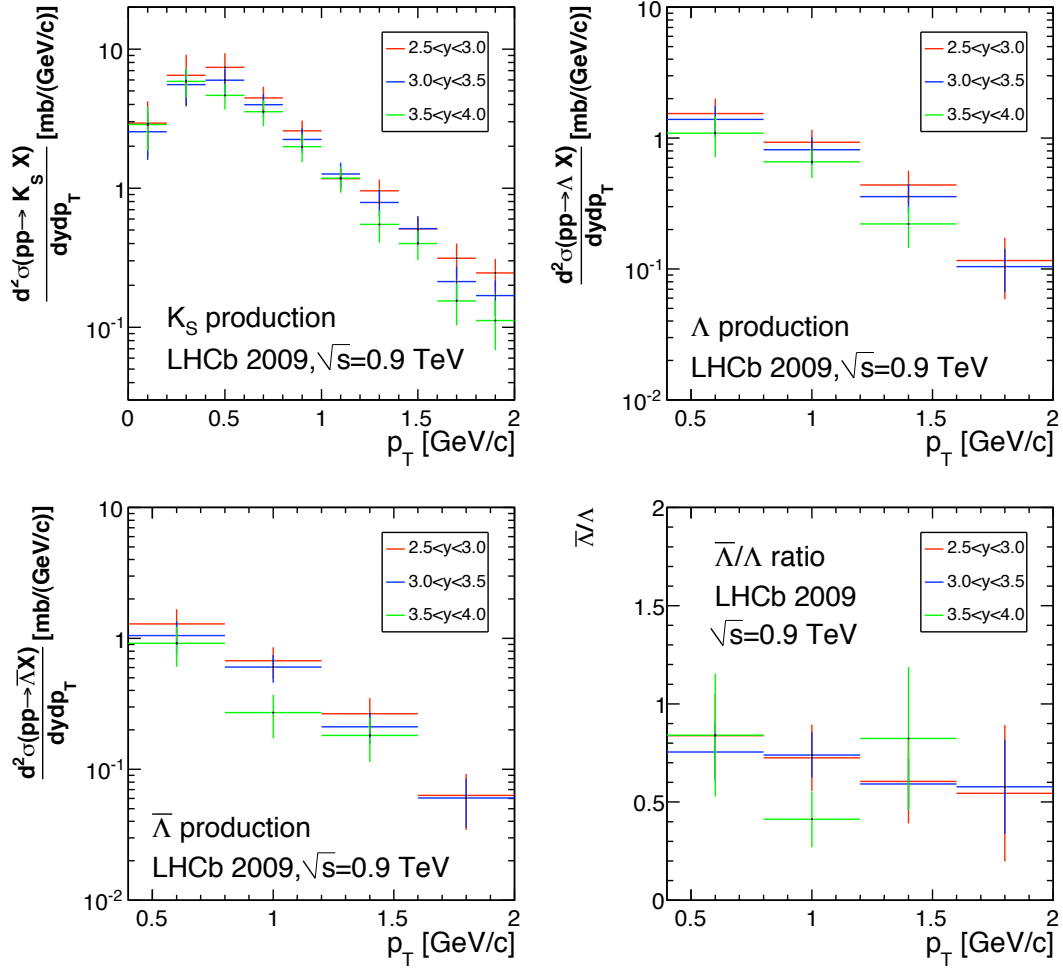
Figure 4.29: Prompt K_S (top left), Λ (top right), $\bar{\Lambda}$ (bottom left) double differential production cross-sections using combined results for LL and DD, as a function of p_T, for the three rapidity bins. All errors are summed in quadrature, including the error on the luminosity measurement. Bottom right: $\bar{\Lambda}/\Lambda$ production ratio as a function of p_T for the three rapidity bins.

The CMS experiment has also recently measured the strange particle production in pp collisions at $\sqrt{s} = 0.9$ TeV and $\sqrt{s} = 7$ TeV [71]. Their results also cover very low and very high p_T bins, though in the rapidity range $|y| < 2$. They are fully compatible with ALICE results and hence also confirm the overestimation of the K_S and Λ production cross-section in the models, especially in the p_T range covered by LHCb.

We show also in Fig. 4.33 our final results, together with several measurements from other experiments: UA1 [67], CDF [68], UA5 [69], for $p\bar{p}$ collisions, at different energies and rapidity or pseudo-rapidity ranges[16]. These measurements, published in the form of invariant differential cross-sections $E d^3\sigma/d^3p$ as a function of p_T, have been converted into values of $d^2\sigma/(dp_T dy)$ by multiplication with $2\pi p_T$. Figure 4.33 shows the uniqueness of the LHCb measurement at high rapidity and very low p_T.

---

[16]Thanks to Raluca Muresan for compiling and preparing the other experiments' data for the comparison.
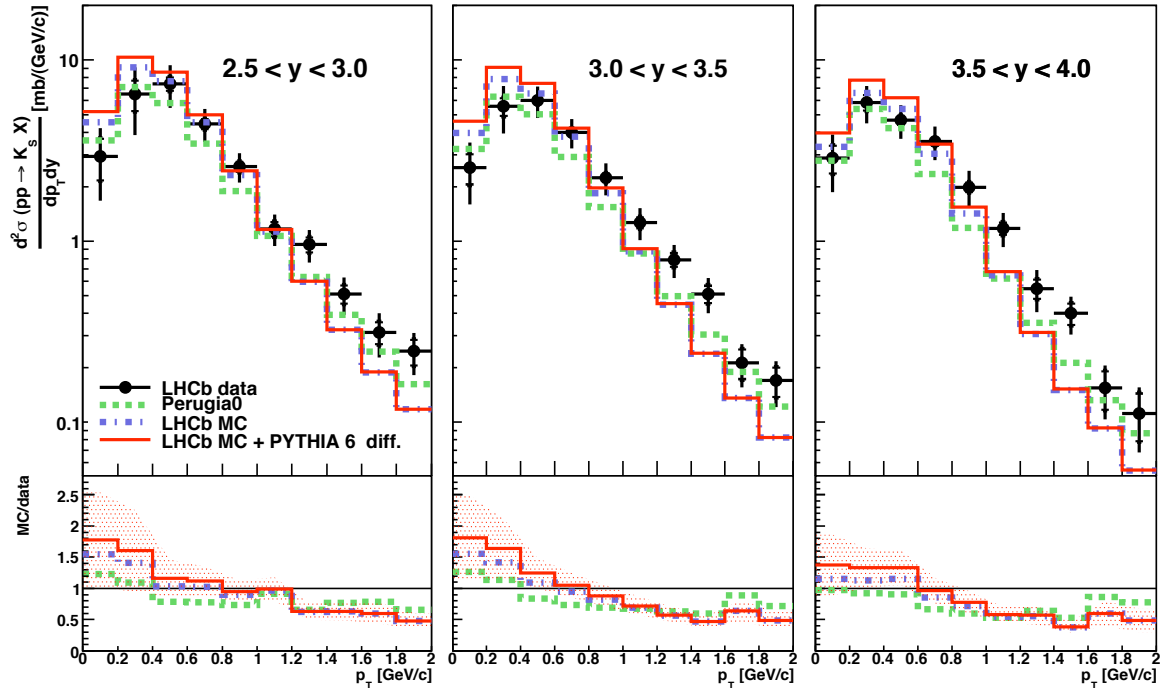
Figure 4.30: Prompt K_S double differential production cross-section as a function of transverse momentum for the three rapidity bins, superimposed with different MC models based on PYTHIA. The errors are statistical (tick marks) and total (bars). On the bottom of each figure is shown the corresponding MC/data ratio. The shaded region represents the uncertainties on one of the ratios, which are similar for all models, and dominated by the uncertainties on the measurement. The meaning of the different models is explained in the text.
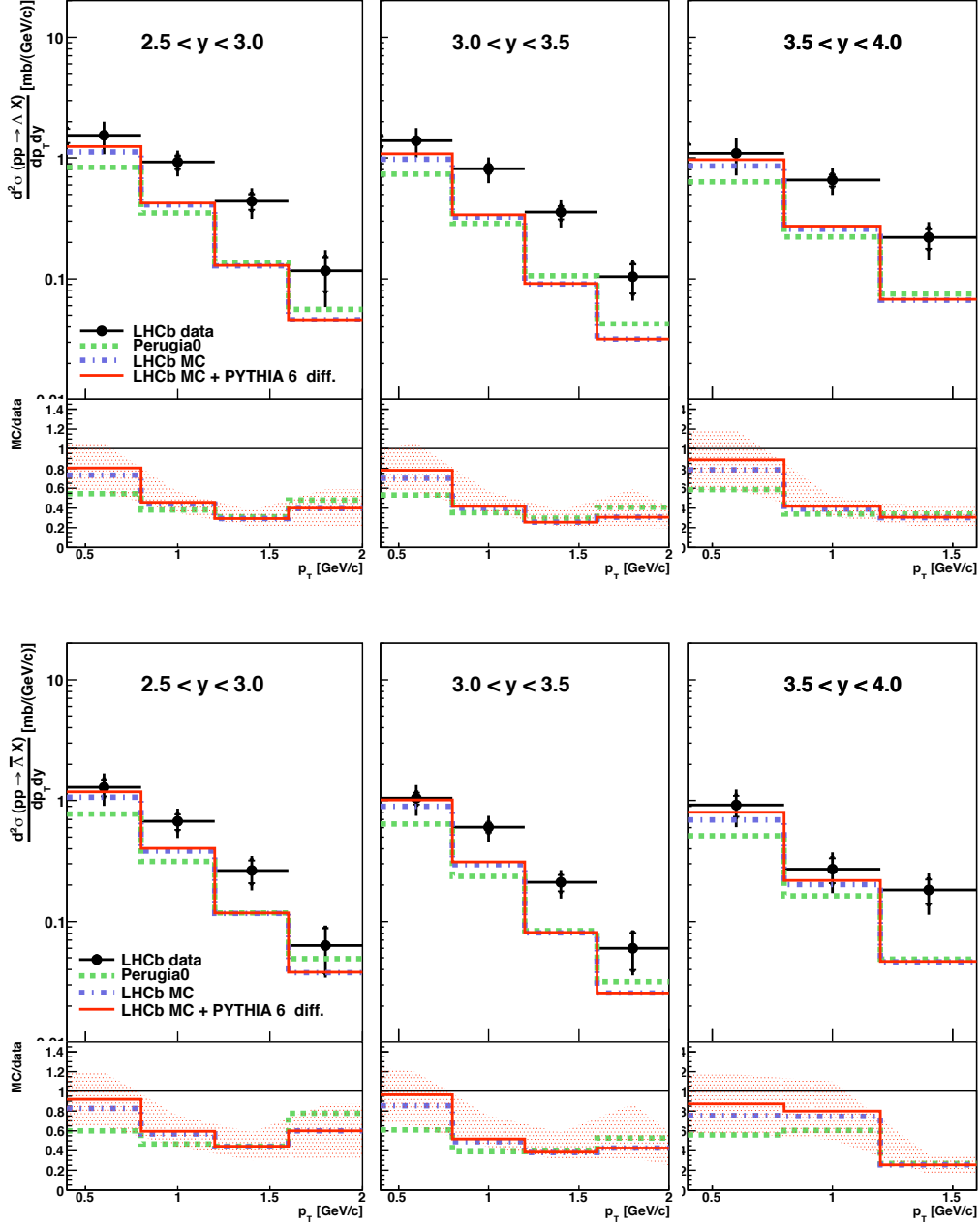
Figure 4.31: Prompt Λ (top) and $\bar{\Lambda}$ (bottom) double differential production cross-section as a function of transverse momentum for the three rapidity bins, superimposed with different MC models based on PYTHIA. The errors are statistical (tick marks) and total (bars). On the bottom of each figure is shown the corresponding MC/data ratio. The shaded region represents the uncertainties on one of the ratios, which are similar for all models, and dominated by the uncertainties on the measurement. The meaning of the different models is explained in the text.
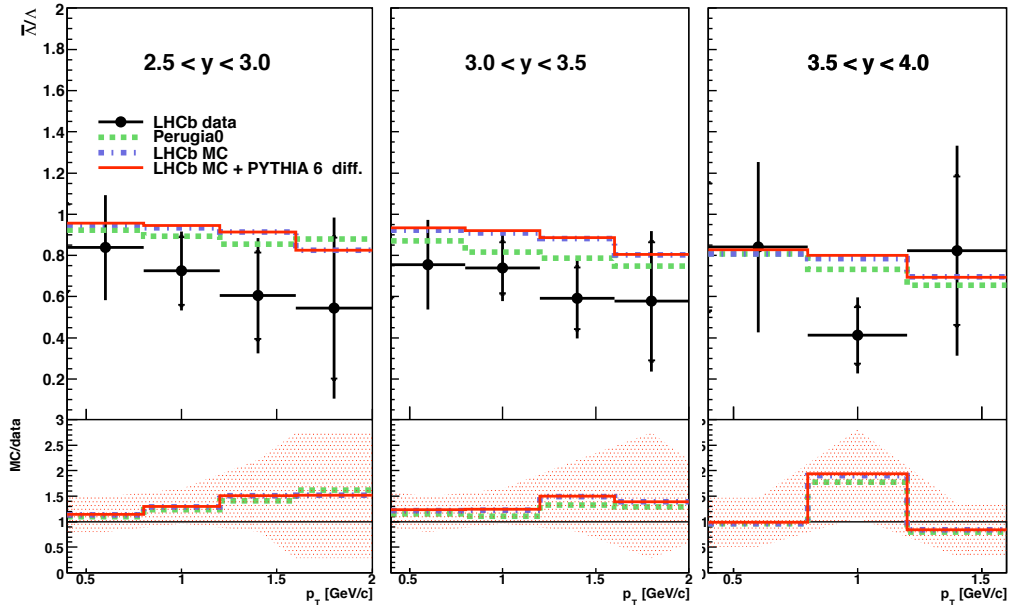
Figure 4.32: $\bar{\Lambda}/\Lambda$ production ratio as a function of transverse momentum for the three rapidity bins, superimposed with different MC models based on PYTHIA. The errors are statistical (tick marks) and total (bars), excluding the correlated sources. On the bottom of each figure is shown the corresponding MC/data ratio. The shaded region represents the uncertainties on one of the ratios, which are similar for all models, and dominated by the uncertainties on the measurement. The meaning of the different models is explained in the text.
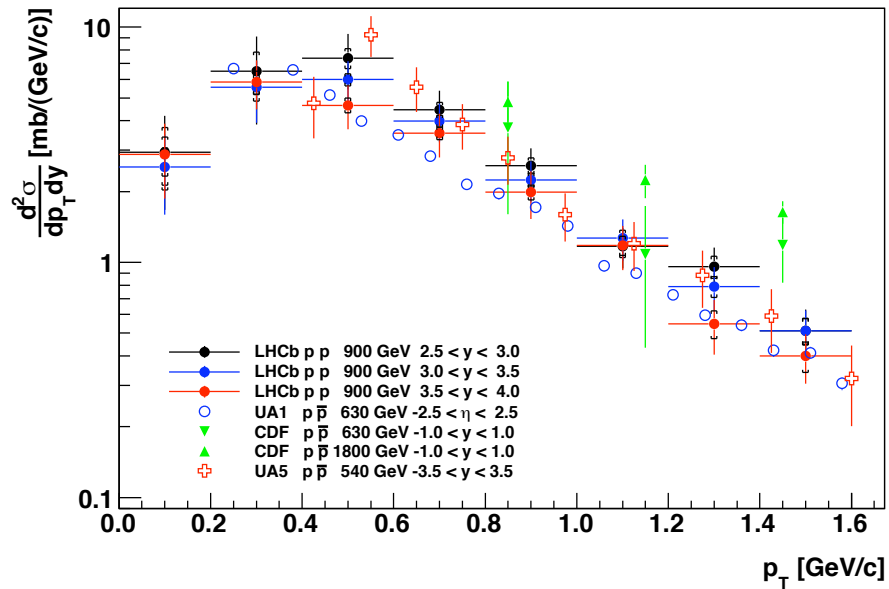
Figure 4.33: Prompt K_S double differential production cross-section measurements by different experiments, in different hadronic collisions, in various rapidity (y) or pseudo-rapidity (η) regions. LHCb provides the only measurement at high rapidity and low p_T.
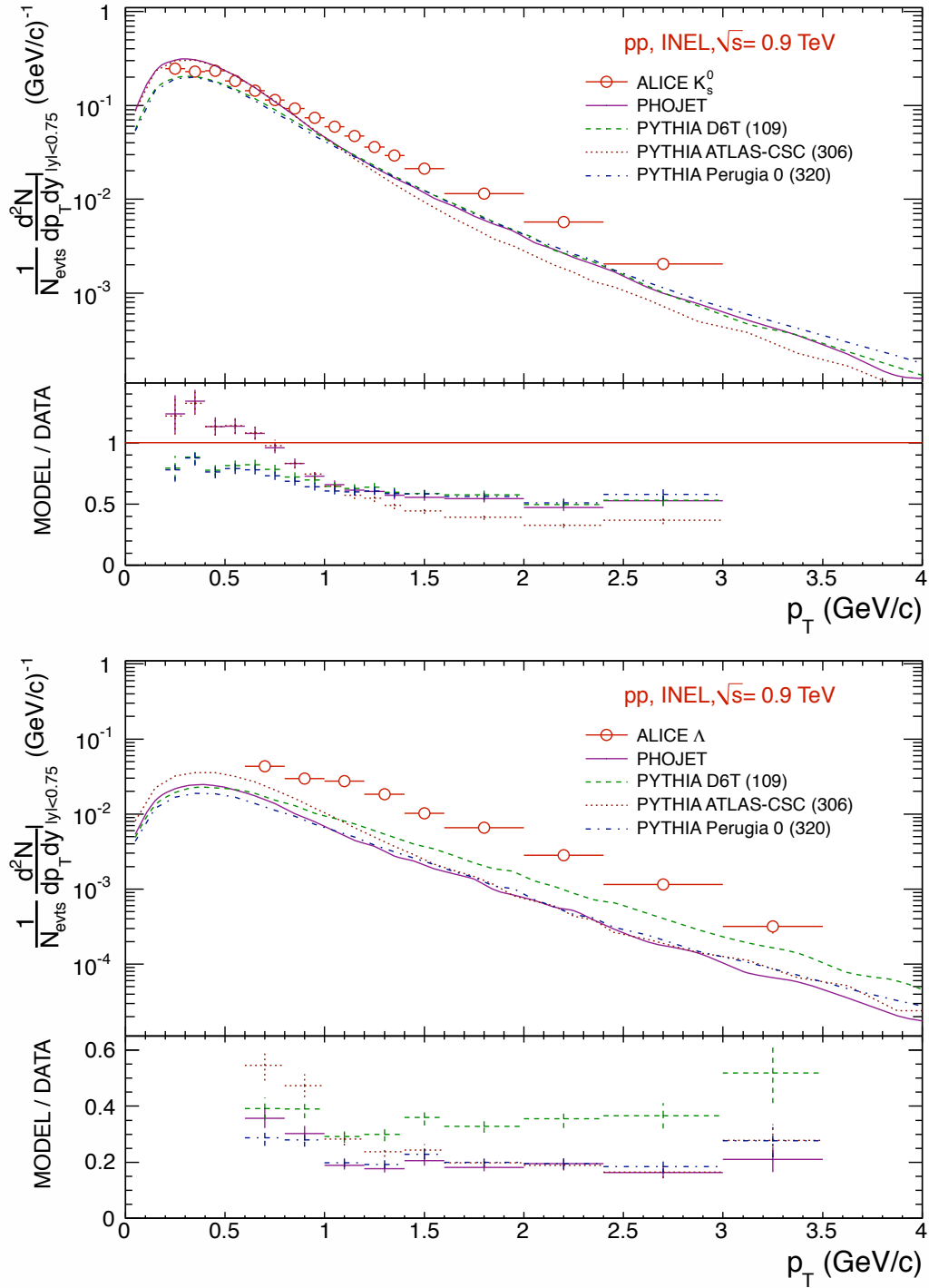
Figure 4.34: K_S (top) and Λ (bottom) production spectra measured by ALICE for $|y| < 0.75$ [70], compared with several MC tunings, and ratio between the results and the models.

5

Conclusion

The studies presented in this doctoral thesis cover different aspects of the LHCb experiment. The first part is dedicated to the Inner Tracker detector. It is one of the most important detectors since it provides particle tracking in the very forward pseudo-rapidity region, where the track multiplicity is the highest (20% of the tracks in 1.5% of the acceptance). In addition, these tracks are the most interesting for LHCb, since b hadrons, which are the experiment's main topic of study, are predominantly produced in the high pseudo-rapidity region. The main contributions presented were the development of the first version of the monitoring, and the time-alignment of the Inner Tracker using the data from the LHC injection tests in September 2008 and June 2009.

The second topic addressed in this thesis is the measurement of the double differential p_{T} and y spectra of prompt K_{S}, Λ and $\bar{\Lambda}$ particles with 6.8 ± 1.0 $\mu\mathrm{b}^{-1}$ of pp collision data at $\sqrt{s} = 0.9$ TeV recorded by the LHCb detector. The results showed that the considered Monte Carlo models, based on the PYTHIA generator, tend to overestimate (underestimate) the K_{S} production cross-section for $p_{\mathrm{T}} < 0.4$ GeV/c ($p_{\mathrm{T}} > 1$ GeV/c). The Λ and $\bar{\Lambda}$ production cross-sections are underestimated by the models for $p_{\mathrm{T}} > 0.8$ GeV/c. In addition, the $\bar{\Lambda}/\Lambda$ ratio, which provides an interesting probe for baryon transport, seems to be largely overestimated in all considered models. Although the uncertainties are still large, it is already in itself an interesting result which provides an input to the Monte Carlo models. In addition, the LHCb measurement provides the only available measurement at very low p_{T} in the rapidity range considered.

The tracking efficiency has been identified as one of the largest sources of uncertainties, apart from the data statistics. This is due to the fact that the analysis was perfomed at the same time as the calibration of the tracking system and reconstruction, and therefore this aspect of the detector was not fully understood at that time. However, given the fact that this sample was recorded very early after the first collisions and that the VELO was partially open, this measurement is a success and showed that the LHCb detector is perfectly operational.

New V^0 analyses are ongoing and will soon be published with larger data samples at $\sqrt{s} = 0.9$ and 7 TeV taken in 2010, and will reduce drastically the statistical uncertainties. Moreover, the tracking efficiencies are now better understood, and the associated systematic uncertainties have already been reduced to $\sim 4\%$ per long track, as compared to $6 - 15\%$ per long track for most bins in the the present analysis.

In the early stages of my doctoral studies, I also had the opportunity to study another interesting field, the "penguin" $b \rightarrow s\gamma$ through $\Lambda_b \rightarrow \Lambda(1520)\gamma$ decays. I have contributed to

the theoretical calculations of the amplitude, which led to the prediction of the suppression of helicity-3/2 amplitudes in the Soft Collinear Effective Theory (SCET) framework. This result should provide, once it can be tested at LHCb or elsewhere, an interesting benchmark for SCET.

I personally enjoyed very much contributing to one of the greatest physics experiments of our times, and having the opportunity to analyse the first data. Indeed, unlike several Ph.D. students on LHC before me, I was lucky to see the very first collisions before the end of my thesis. I am eager to discover what will be the next discoveries at the LHC using the wealth of data taken in 2010 and looking forward to the data from 2011 and beyond.

A
Appendix

A.1 Side-band subtraction assuming quadratic background

The method described here, referred to as the CCQ method in Sec. 4.8.1, is used for the estimation of the systematic uncertainties on the signal yields. The technique is similar to the side-band subtraction used in the linear background assumption, but using three side-band regions instead of two, reproducing the effect of a parabolic background.

In the quadratic case, the background can be described by the density function $f(x) = ax^2 + bx + c$ of $x = m - m_{\mathrm{PDG}}$, where m is the reconstructed mass, and a, b, c are background parameters. The number of background events falling in the region $[x_1, x_2]$ is the integral of $f(x)$ between x_1 and x_2. We choose three different side-band regions: $[x_0, x_1]$, $[x_1, x_2]$, $[x_3, x_4]$, and one signal region $[x_2, x_3]$.

Let N_0, N_1, N_3 be the number of events counted in the three side-band regions, and N_b be the number of background events in the signal region. We have:

$$
\begin{aligned}
N_0 &= \int_{x_0}^{x_1} f(x) = \frac{a}{3}(x_1^3 - x_0^3) + \frac{b}{2}(x_1^2 - x_0^2) + c(x_1 - x_0) \ , \\
N_1 &= \int_{x_1}^{x_2} f(x) = \frac{a}{3}(x_2^3 - x_1^3) + \frac{b}{2}(x_2^2 - x_1^2) + c(x_2 - x_1) \ , \\
N_b &= \int_{x_2}^{x_3} f(x) = \frac{a}{3}(x_3^3 - x_2^3) + \frac{b}{2}(x_3^2 - x_2^2) + c(x_3 - x_2) \ , \\
N_3 &= \int_{x_3}^{x_4} f(x) = \frac{a}{3}(x_4^3 - x_3^3) + \frac{b}{2}(x_4^2 - x_3^2) + c(x_4 - x_3) \ .
\end{aligned}
$$

Using $x_{i,j}^n = \frac{x_i^n - x_j^n}{n}$, the above equations can be rewritten in a matrix form:

$$
\mathbf{N} \equiv \begin{pmatrix} N_0 \\ N_1 \\ N_3 \end{pmatrix} = \begin{pmatrix} x_{1,0}^3 & x_{1,0}^2 & x_{1,0}^1 \\ x_{2,1}^3 & x_{2,1}^2 & x_{2,1}^1 \\ x_{4,3}^3 & x_{4,3}^2 & x_{4,3}^1 \end{pmatrix} \begin{pmatrix} a \\ b \\ c \end{pmatrix} \equiv \mathbf{U} \begin{pmatrix} a \\ b \\ c \end{pmatrix} \ ,
$$

$$
N_b = \begin{pmatrix} x_{3,2}^3 & x_{3,2}^2 & x_{3,2}^1 \end{pmatrix} \begin{pmatrix} a \\ b \\ c \end{pmatrix} \equiv \mathbf{V} \begin{pmatrix} a \\ b \\ c \end{pmatrix} \ .
$$

Table A.1: Values of x_i (in MeV/c^2) and p, q, r, for the CQ method.

case	x_0	x_1	x_2	x_3	x_4	p	q	r
$K_S \pm 30$ MeV/c^2	-100	-70	-30	$+30$	$+100$	-1.21	2.04	0.21
$K_S \pm 40$ MeV/c^2	-100	-70	-40	$+40$	$+100$	-1.98	3.94	0.35
$\Lambda(\bar{\Lambda}) \pm 6$ MeV/c^2	-30	-6	$+6$	$+20$	$+30$	0.12	1.07	-0.58
$\Lambda(\bar{\Lambda}) \pm 12$ MeV/c^2	-30	-12	$+12$	$+20$	$+30$	0.34	4.37	-1.72

Combining the above two equations, we obtain the number of background events in the signal region N_b,

$$N_b = \mathbf{V}\mathbf{U}^{-1}\mathbf{N} \equiv pN_0 + qN_1 + rN_3 \;, \tag{A.1}$$

where the constants p, q, r are known functions of x_0, x_1, x_2, x_3 and x_4. We obtain therefore the number of signal events in the signal region by subtracting the number of background events N_b from the total number of events N_2 counted in the signal region,

$$S = N_2 - N_b = N_2 - pN_0 - qN_1 - rN_3 \;, \tag{A.2}$$

and the statistical uncertainty on S is computed using

$$\sigma_S = \sqrt{N_2 + p^2 N_0 + q^2 N_1 + r^2 N_3} \;. \tag{A.3}$$

The chosen values of the region boundaries and the corresponding values of p, q, r are listed in Table A.1.

A.2   Weighted average of LL and DD measurements

The LL and DD samples are combined by using the weighted average of the two measurements. Let

- Y_{LL} and Y_{DD} be the efficiency-corrected yields measured in the LL and DD samples respectively,

- $\Delta Y_{stat,LL}$ and $\Delta Y_{stat,DD}$ be the statistical errors on Y_{LL} and Y_{DD} respectively,

- $\Delta Y_{unc,LL}$ and $\Delta Y_{unc,DD}$ be the quadratic sum of all the uncorrelated systematic errors on Y_{LL} and Y_{DD} respectively,

- $\Delta Y_{cor,LL}$ and $\Delta Y_{cor,DD}$ be the quadratic sum of all the correlated errors, $syst_c$ and $syst_{c2}$, on Y_{LL} and Y_{DD} respectively,

- $\Delta Y_{tot,LL}$ and $\Delta Y_{tot,DD}$ be the above terms summed in quadrature on Y_{LL} and Y_{DD} respectively.

We can compute the weighted average yield Y of LL and DD measurements using

$$Y = w_{LL}Y_{LL} + w_{DD}Y_{DD} \;,$$

where

$$w_{LL} = \frac{(\Delta Y_{tot,DD})^2 - \Delta Y_{cor,LL}\Delta Y_{cor,DD}}{(\Delta Y_{tot,LL})^2 + (\Delta Y_{tot,DD})^2 - 2\Delta Y_{cor,LL}\Delta Y_{cor,DD}} \;,$$

$$w_{DD} = \frac{(\Delta Y_{tot,LL})^2 - \Delta Y_{cor,LL}\Delta Y_{cor,DD}}{(\Delta Y_{tot,LL})^2 + (\Delta Y_{tot,DD})^2 - 2\Delta Y_{cor,LL}\Delta Y_{cor,DD}} \;,$$

are the respective weights for LL and DD measurements that minimize the total error on Y_{LL} and Y_{DD} under the constraint $w_{\mathrm{DD}} + w_{\mathrm{LL}} = 1$. The statistical error ΔY_{stat} on the yield Y is calculated using

$$\Delta Y_{\mathrm{stat}} \quad = \quad \frac{\Delta Y_{\mathrm{stat,LL}} \Delta Y_{\mathrm{stat,DD}}}{\sqrt{(\Delta Y_{\mathrm{stat,LL}})^2 + (\Delta Y_{\mathrm{stat,DD}})^2}} \ ,$$

The uncorrelated systematic error ΔY_{unc} on the yield Y is calculated using

$$\Delta Y_{\mathrm{unc}} \quad = \quad \sqrt{(\Delta Y_{\mathrm{unc+stat}})^2 - (\Delta Y_{\mathrm{stat}})^2} \ ,$$

where $\Delta Y_{\mathrm{unc+stat}}$ is the quadratic sum of statistical and uncorrelated systematic errors, calculated using

$$\Delta Y_{\mathrm{unc+stat}} \quad = \quad \sqrt{\frac{((\Delta Y_{\mathrm{stat,LL}})^2 + (\Delta Y_{\mathrm{unc,LL}})^2)((\Delta Y_{\mathrm{stat,DD}})^2 + (\Delta Y_{\mathrm{unc,DD}})^2)}{(\Delta Y_{\mathrm{stat,LL}})^2 + (\Delta Y_{\mathrm{unc,LL}})^2 + (\Delta Y_{\mathrm{stat,DD}})^2 + (\Delta Y_{\mathrm{unc,DD}})^2}} \ .$$

The correlated systematic error ΔY_{cor} on the yield Y is calculated using

$$\Delta Y_{\mathrm{cor}} \quad = \quad \sqrt{(\Delta Y_{\mathrm{tot}})^2 - (\Delta Y_{\mathrm{unc+stat}})^2} \ ,$$

where ΔY_{tot} is the quadratic sum of all errors, calculated using

$$\Delta Y_{\mathrm{tot}} \quad = \quad \sqrt{\frac{(\Delta Y_{\mathrm{tot,LL}})^2 (\Delta Y_{\mathrm{tot,DD}})^2 - (\Delta Y_{\mathrm{cor,LL}})^2 (\Delta Y_{\mathrm{cor,DD}})^2}{(\Delta Y_{\mathrm{tot,LL}})^2 + (\Delta Y_{\mathrm{tot,DD}})^2 - 2(\Delta Y_{\mathrm{cor,LL}})^2 (\Delta Y_{\mathrm{cor,DD}})^2}} \ .$$

A.3   Mass distributions in bins of p_T and y

A.3.1 K_S
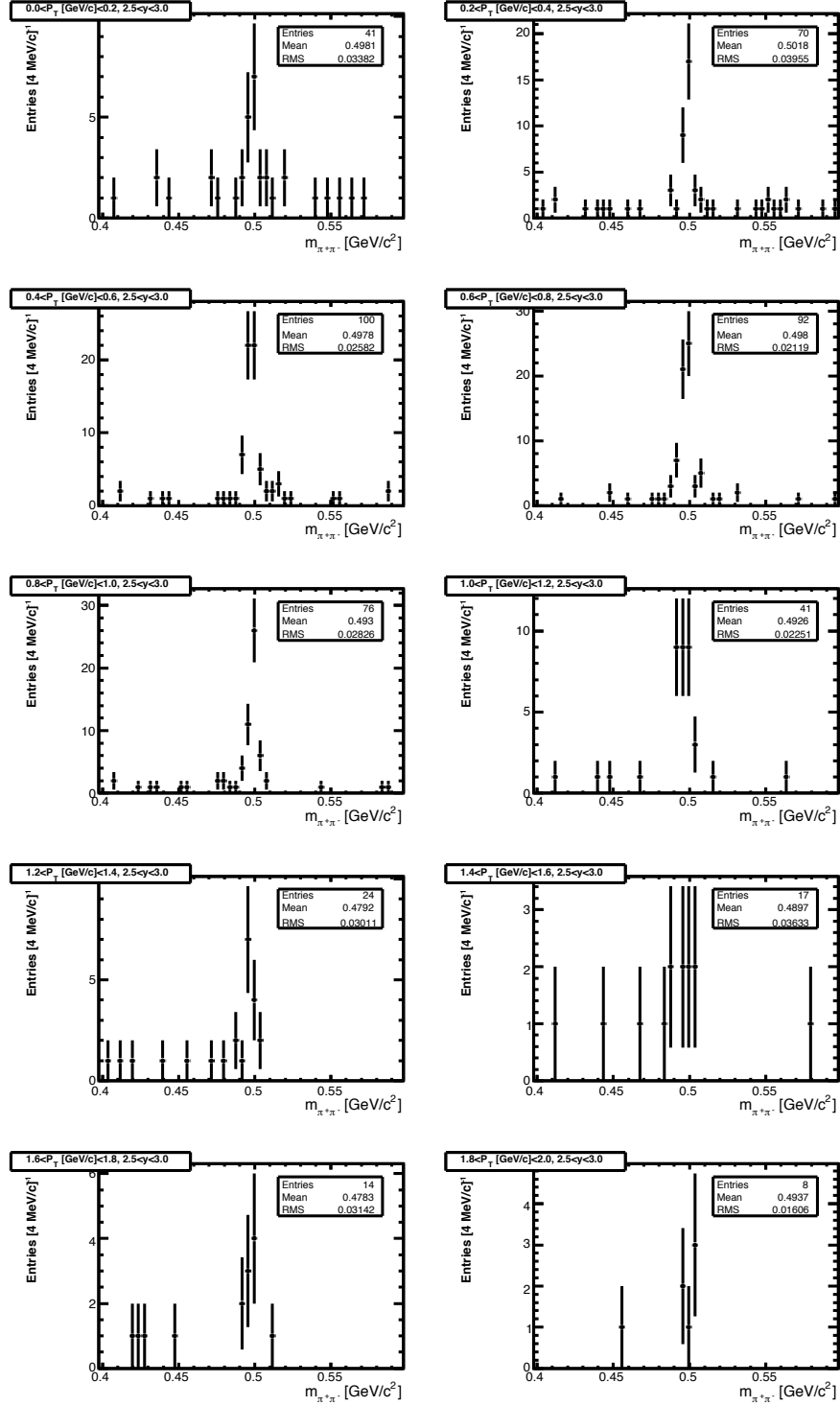
Figure A.1: Mass distributions per bin of p_T, in the rapidity range 2.5–3.0, for the K_S LL case.
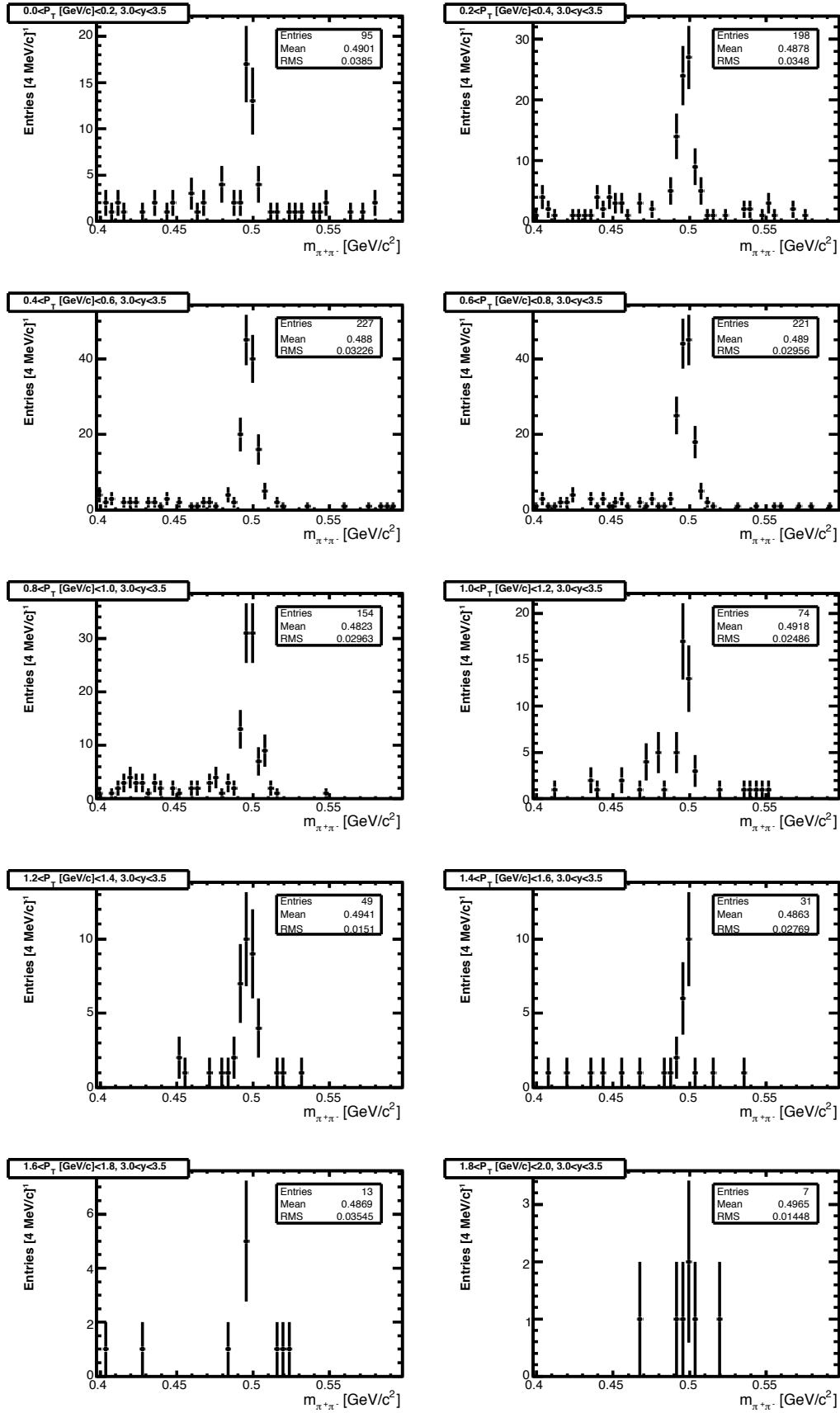
Figure A.2: Mass distributions per bin of p_T, in the rapidity range 3.0–3.5, for the K_S LL case.
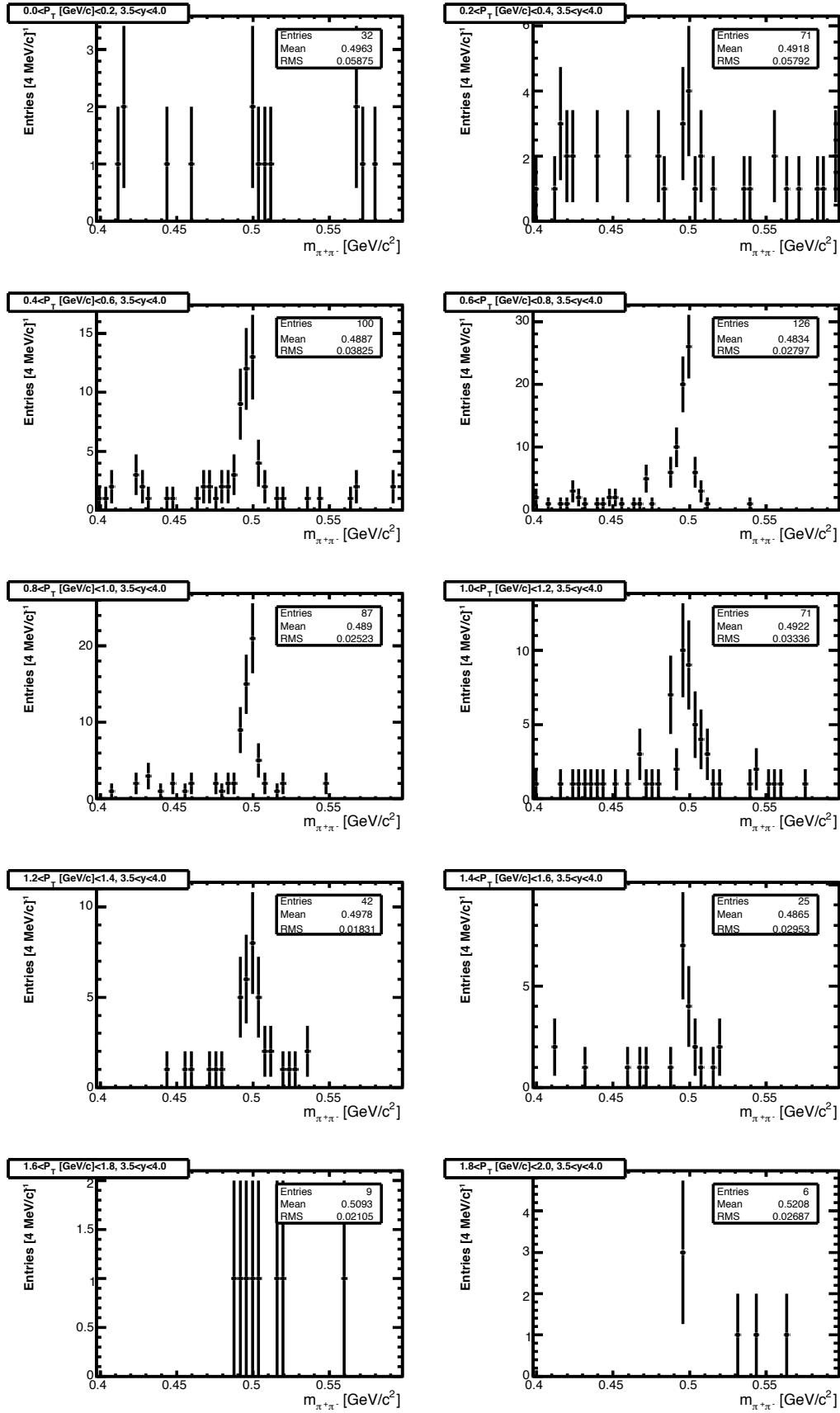
Figure A.3: Mass distributions per bin of p_{T}, in the rapidity range 3.5–4.0, for the K_{S} LL case.
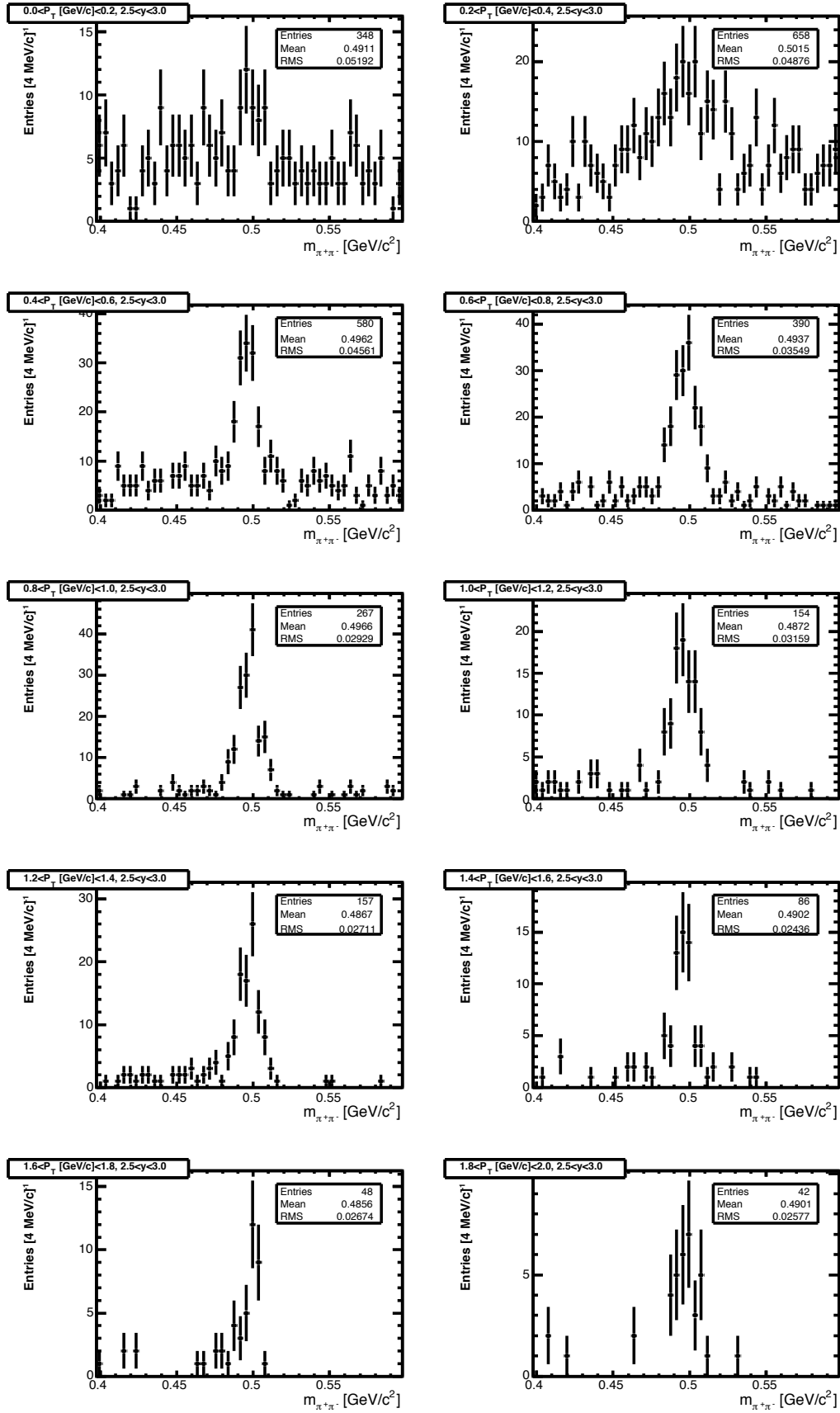
Figure A.4: Mass distributions per bin of p_T, in the rapidity range 2.5–3.0, for the K_S DD case.
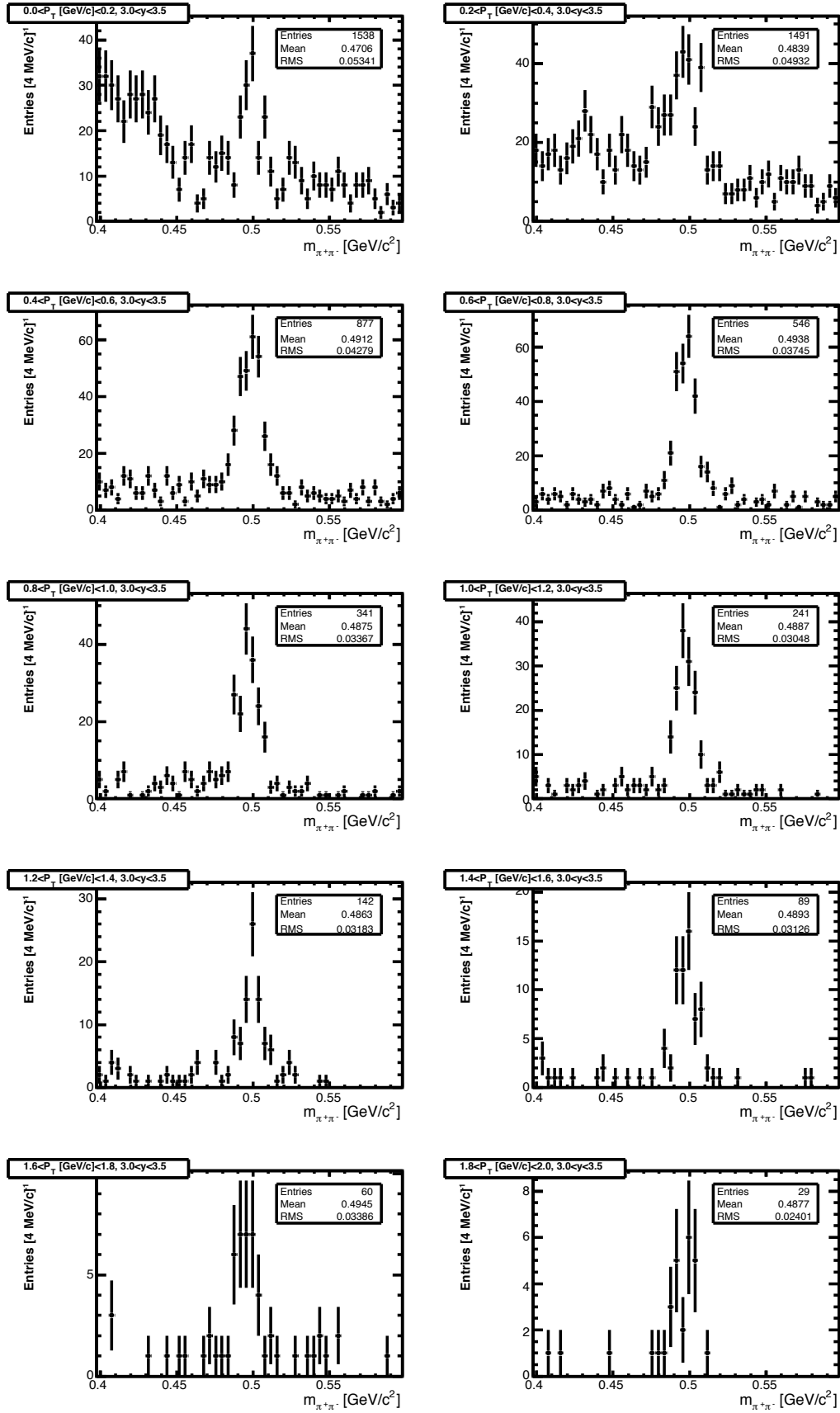
Figure A.5: Mass distributions per bin of p_T, in the rapidity range 3.0–3.5, for the K_S DD case.
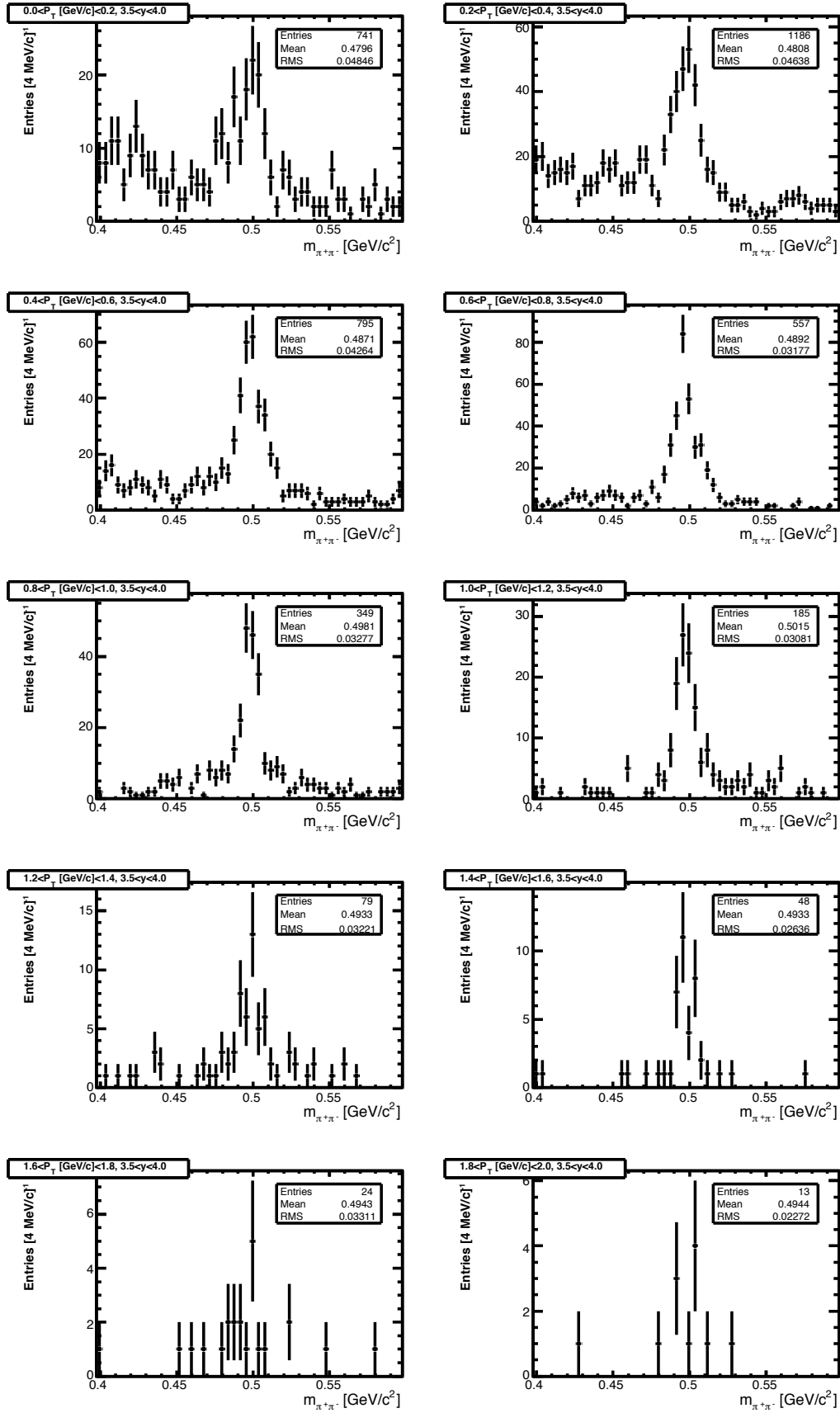
Figure A.6: Mass distributions per bin of p_T, in the rapidity range 3.5–4.0, for the K_S DD case.

A.3.2 Λ
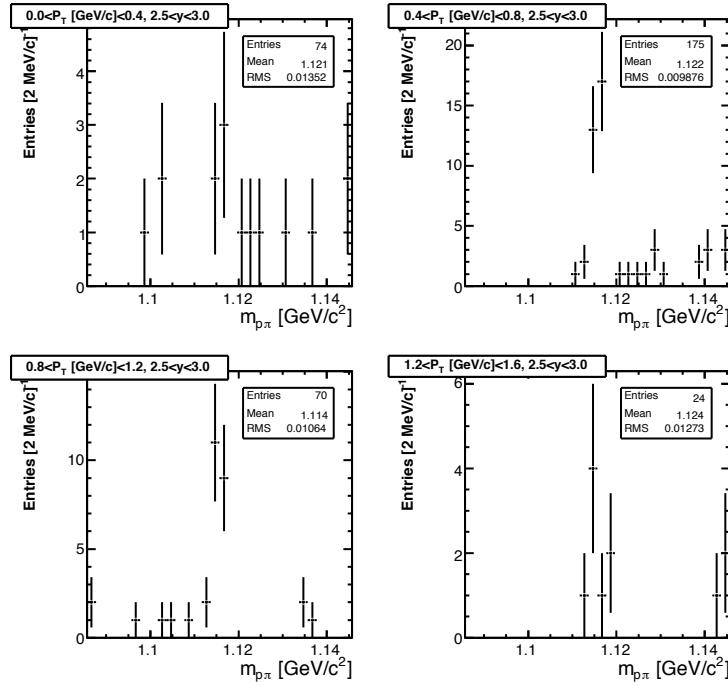
Figure A.7: Mass distributions per bin of p_T, for the rapidity bin 2.5–3.0, for the Λ LL case.
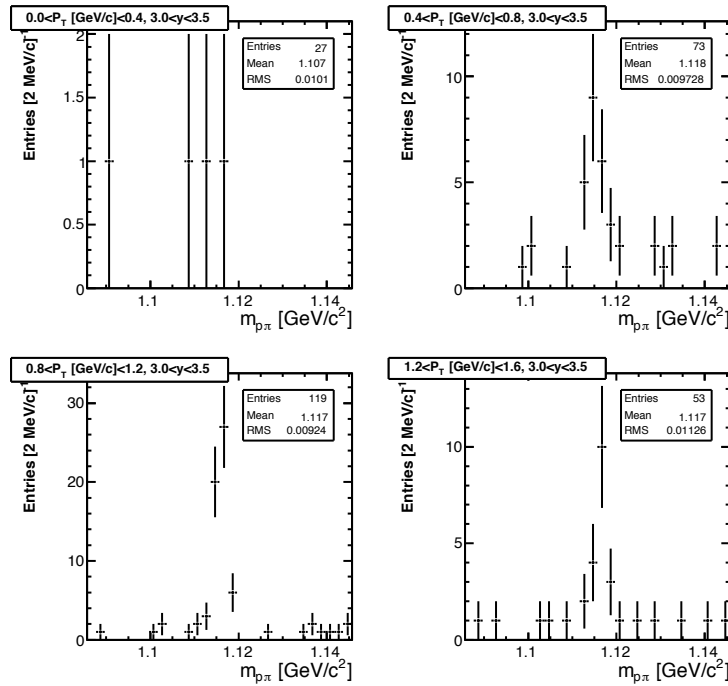
Figure A.8: Mass distributions per bin of p_T, in the rapidity range 3.0–3.5, for the Λ LL case.

Figure A.9: Mass distributions per bin of p_T, in the rapidity range 3.5–4.0, for the Λ LL case.

Figure A.10: Mass distributions per bin of p_T, in the rapidity range 2.5–3.0, for the Λ DD case.

Figure A.11: Mass distributions per bin of p_T, in the rapidity range 3.0–3.5, for the Λ DD case.

Figure A.12: Mass distributions per bin of p_T, in the rapidity range 3.5–4.0, for the Λ DD case.

A.3.3 $\bar{\Lambda}$

Figure A.13: Mass distributions per bin of p_T, in the rapidity range 2.5–3.0, for the $\bar{\Lambda}$ LL case.
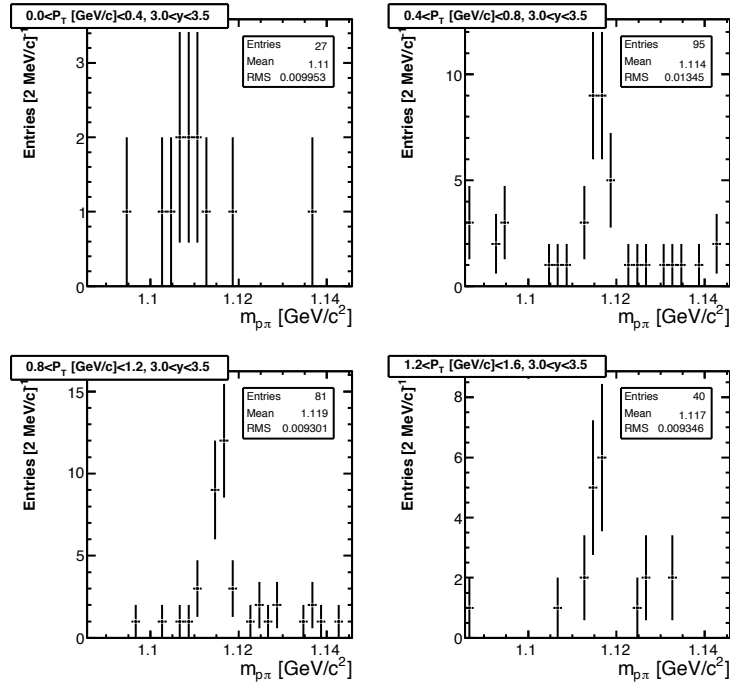
Figure A.14: Mass distributions per bin of p_T, in the rapidity range 3.0–3.5, for the $\bar{\Lambda}$ LL case.
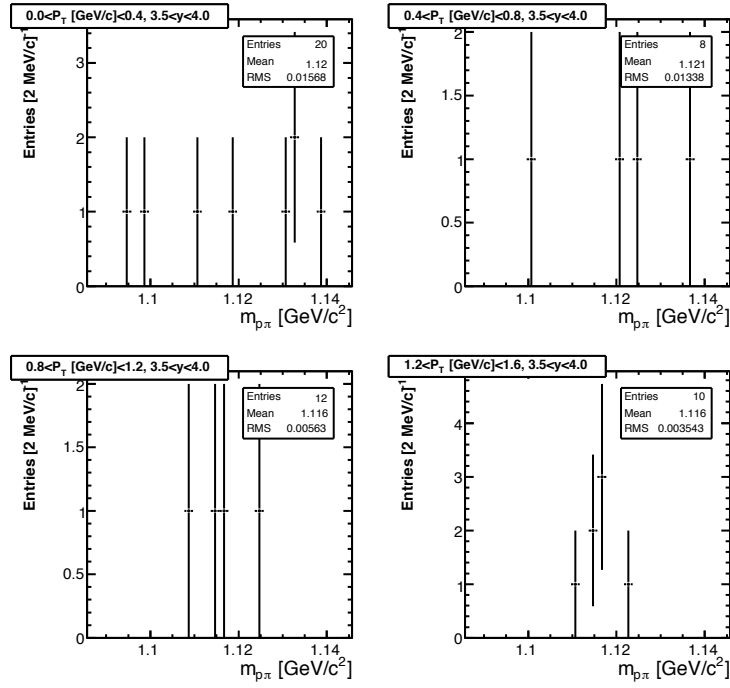
Figure A.15: Mass distributions per bin of p_T, in the rapidity range 3.5–4.0, for the $\bar{\Lambda}$ LL case.
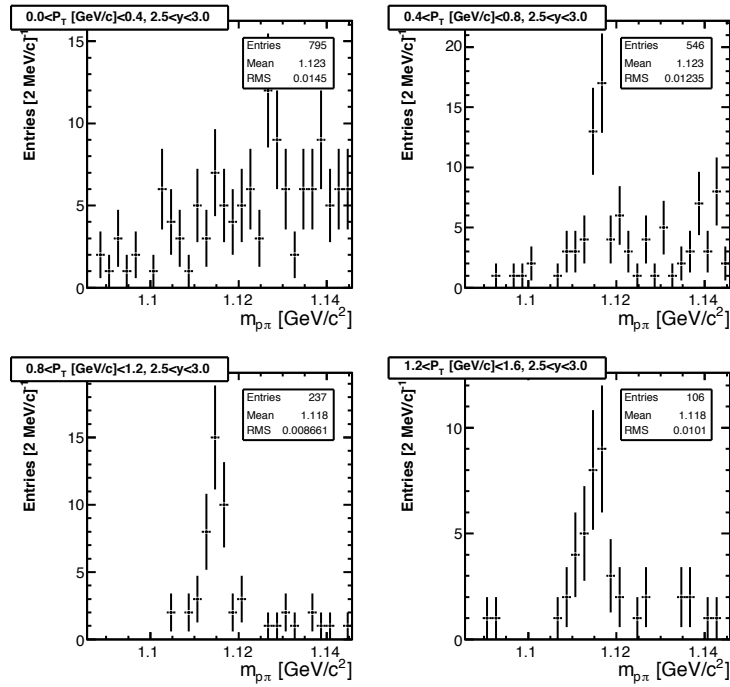
Figure A.16: Mass distributions per bin of p_T, in the rapidity range 2.5–3.0, for the $\bar{\Lambda}$ DD case.
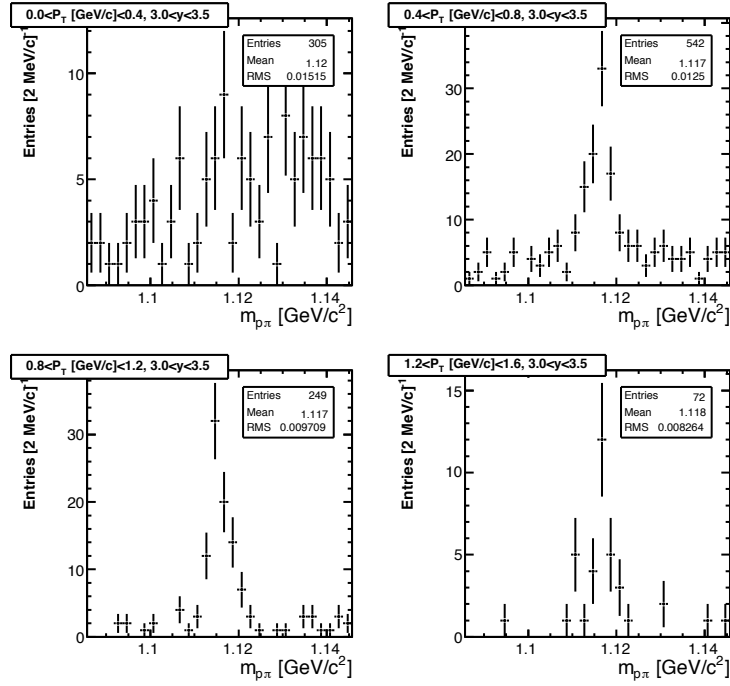
Figure A.17: Mass distributions per bin of p_T, in the rapidity range 3.0–3.5, for the $\bar{\Lambda}$ DD case.
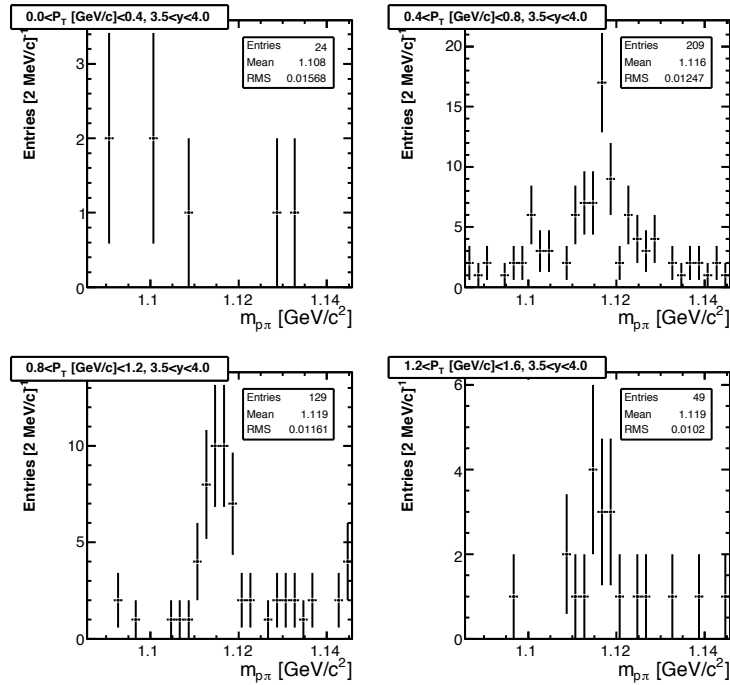
Figure A.18: Mass distributions per bin of p_T, in the rapidity range 3.5–4.0, for the $\bar{\Lambda}$ DD case.

A.4   Tables

A.4.1   Trigger efficiency

Table A.2: Monte Carlo trigger efficiencies (in percents) before ($\epsilon_{\text{trig,MC}}$) and after reweighting (ϵ_{trig}) for the K_{S} LL case. The quoted uncertainty is statistical.

$p_{\text{T}}[\text{GeV}/c]$	y	$\epsilon_{\text{trig,MC}}$	ϵ_{trig}
0.0-0.2	2.5-3.0	95.9 ± 0.8	96.8 ± 0.7
	3.0-3.5	96.4 ± 0.5	97.1 ± 0.5
	3.5-4.0	—	—
0.2-0.4	2.5-3.0	95.2 ± 0.6	96.0 ± 0.6
	3.0-3.5	97.2 ± 0.3	97.7 ± 0.3
	3.5-4.0	—	—
0.4-0.6	2.5-3.0	96.6 ± 0.5	97.3 ± 0.4
	3.0-3.5	97.4 ± 0.2	97.9 ± 0.2
	3.5-4.0	97.6 ± 0.5	98.1 ± 0.4
0.6-0.8	2.5-3.0	96.8 ± 0.5	97.4 ± 0.4
	3.0-3.5	97.4 ± 0.3	98.0 ± 0.3
	3.5-4.0	97.6 ± 0.4	98.1 ± 0.4
0.8-1.0	2.5-3.0	97.4 ± 0.5	98.0 ± 0.4
	3.0-3.5	97.2 ± 0.4	97.7 ± 0.4
	3.5-4.0	97.9 ± 0.5	98.4 ± 0.4
1.0-1.2	2.5-3.0	97.5 ± 0.7	98.1 ± 0.6
	3.0-3.5	98.6 ± 0.4	99.0 ± 0.4
	3.5-4.0	98.7 ± 0.5	99.1 ± 0.4
1.2-1.4	2.5-3.0	98.4 ± 0.8	98.9 ± 0.7
	3.0-3.5	99.0 ± 0.6	99.2 ± 0.5
	3.5-4.0	98.6 ± 0.8	98.9 ± 0.7
1.4-1.6	2.5-3.0	95.5 ± 1.7	96.6 ± 1.5
	3.0-3.5	95.4 ± 1.4	96.6 ± 1.2
	3.5-4.0	98.6 ± 1.0	99.3 ± 0.7
1.6-1.8	2.5-3.0	96.9 ± 2.1	98.1 ± 1.8
	3.0-3.5	99.2 ± 0.8	99.2 ± 0.8
	3.5-4.0	100.0 ± 0.0	100.0 ± 0.0
1.8-2.0	2.5-3.0	100.0 ± 0.0	100.0 ± 0.0
	3.0-3.5	100.0 ± 0.0	100.0 ± 0.0
	3.5-4.0	97.2 ± 2.8	96.8 ± 3.1

Table A.3: Monte Carlo trigger efficiencies (in percents) before ($\epsilon_{\text{trig,MC}}$) and after reweighting (ϵ_{trig}) for the K_S DD case. The quoted uncertainty is statistical.

$p_T[\text{GeV}/c]$	y	$\epsilon_{\text{trig,MC}}$	ϵ_{trig}
0.0-0.2	2.5-3.0	—	—
	3.0-3.5	—	—
	3.5-4.0	96.5 ± 0.4	97.6 ± 0.4
0.2-0.4	2.5-3.0	—	—
	3.0-3.5	—	—
	3.5-4.0	96.8 ± 0.3	97.8 ± 0.2
0.4-0.6	2.5-3.0	96.1 ± 0.4	97.3 ± 0.3
	3.0-3.5	97.2 ± 0.2	98.1 ± 0.2
	3.5-4.0	97.6 ± 0.2	98.3 ± 0.2
0.6-0.8	2.5-3.0	96.8 ± 0.3	97.9 ± 0.2
	3.0-3.5	97.1 ± 0.2	98.1 ± 0.2
	3.5-4.0	97.6 ± 0.2	98.4 ± 0.2
0.8-1.0	2.5-3.0	97.7 ± 0.3	98.5 ± 0.2
	3.0-3.5	97.7 ± 0.3	98.5 ± 0.2
	3.5-4.0	97.8 ± 0.3	98.4 ± 0.2
1.0-1.2	2.5-3.0	98.0 ± 0.3	98.8 ± 0.2
	3.0-3.5	98.3 ± 0.3	99.0 ± 0.2
	3.5-4.0	98.7 ± 0.3	99.3 ± 0.3
1.2-1.4	2.5-3.0	98.9 ± 0.3	99.2 ± 0.2
	3.0-3.5	98.6 ± 0.4	99.2 ± 0.3
	3.5-4.0	98.6 ± 0.4	99.1 ± 0.3
1.4-1.6	2.5-3.0	99.2 ± 0.3	99.5 ± 0.2
	3.0-3.5	98.4 ± 0.5	98.8 ± 0.4
	3.5-4.0	99.2 ± 0.6	99.6 ± 0.5
1.6-1.8	2.5-3.0	98.7 ± 0.5	99.1 ± 0.4
	3.0-3.5	99.0 ± 0.5	99.7 ± 0.4
	3.5-4.0	100.0 ± 0.0	100.0 ± 0.0
1.8-2.0	2.5-3.0	99.4 ± 0.4	99.5 ± 0.3
	3.0-3.5	99.6 ± 0.4	100.0 ± 0.0
	3.5-4.0	100.0 ± 0.0	100.0 ± 0.0

Table A.4: Monte Carlo trigger efficiencies (in percents) before ($\epsilon_{\mathrm{trig,MC}}$) and after reweighting (ϵ_{trig}) for the Λ LL case. The quoted uncertainty is statistical.

$p_{\mathrm{T}}[\mathrm{GeV}/c]$	y	$\epsilon_{\mathrm{trig,MC}}$	ϵ_{trig}
0.4-0.8	2.5-3.0	96.2 ± 0.9	96.8 ± 0.8
	3.0-3.5	97.8 ± 0.8	98.4 ± 0.8
	3.5-4.0	$-$	$-$
0.8-1.2	2.5-3.0	98.9 ± 0.8	99.9 ± 0.5
	3.0-3.5	96.7 ± 0.9	97.9 ± 0.7
	3.5-4.0	100.0 ± 0.0	100.0 ± 0.0
1.2-1.6	2.5-3.0	94.7 ± 3.3	96.0 ± 2.8
	3.0-3.5	100.3 ± 0.3	100.2 ± 0.2
	3.5-4.0	97.3 ± 2.7	97.2 ± 2.7

Table A.5: Monte Carlo trigger efficiencies (in percents) before ($\epsilon_{\mathrm{trig,MC}}$) and after reweighting (ϵ_{trig}) for the Λ DD case. The quoted uncertainty is statistical.

$p_{\mathrm{T}}[\mathrm{GeV}/c]$	y	$\epsilon_{\mathrm{trig,MC}}$	ϵ_{trig}
0.4-0.8	2.5-3.0	98.3 ± 0.8	99.1 ± 0.7
	3.0-3.5	97.0 ± 0.5	98.3 ± 0.4
	3.5-4.0	97.3 ± 0.6	97.8 ± 0.6
0.8-1.2	2.5-3.0	95.9 ± 0.9	97.2 ± 0.7
	3.0-3.5	98.0 ± 0.5	98.8 ± 0.4
	3.5-4.0	97.9 ± 0.7	98.4 ± 0.6
1.2-1.6	2.5-3.0	98.5 ± 0.8	98.9 ± 0.6
	3.0-3.5	98.5 ± 0.8	98.9 ± 0.7
	3.5-4.0	99.3 ± 0.7	99.4 ± 0.6
1.6-2.0	2.5-3.0	100.0 ± 0.0	100.0 ± 0.0
	3.0-3.5	100.7 ± 0.7	100.7 ± 0.7
	3.5-4.0	$-$	$-$

Table A.6: Monte Carlo trigger efficiencies (in percents) before ($\epsilon_{\text{trig,MC}}$) and after reweighting (ϵ_{trig}) for the $\bar{\Lambda}$ LL case. The quoted uncertainty is statistical.

$p_{\text{T}}[\text{GeV}/c]$	y	$\epsilon_{\text{trig,MC}}$	ϵ_{trig}
0.4-0.8	2.5-3.0	97.0 ± 0.8	97.7 ± 0.8
	3.0-3.5	96.9 ± 1.0	97.5 ± 0.9
	3.5-4.0	$-$	$-$
0.8-1.2	2.5-3.0	96.5 ± 1.3	97.8 ± 1.1
	3.0-3.5	98.8 ± 0.7	99.0 ± 0.7
	3.5-4.0	96.5 ± 2.4	96.2 ± 2.7
1.2-1.6	2.5-3.0	94.4 ± 3.1	96.2 ± 2.7
	3.0-3.5	99.8 ± 1.0	99.5 ± 1.0
	3.5-4.0	100.0 ± 0.0	100.0 ± 0.0

Table A.7: Monte Carlo trigger efficiencies (in percents) before ($\epsilon_{\text{trig,MC}}$) and after reweighting (ϵ_{trig}) for the $\bar{\Lambda}$ DD case. The quoted uncertainty is statistical.

$p_{\text{T}}[\text{GeV}/c]$	y	$\epsilon_{\text{trig,MC}}$	ϵ_{trig}
0.4-0.8	2.5-3.0	95.5 ± 1.0	97.1 ± 0.9
	3.0-3.5	96.8 ± 0.5	97.9 ± 0.4
	3.5-4.0	98.2 ± 0.7	98.5 ± 0.6
0.8-1.2	2.5-3.0	97.3 ± 0.9	98.4 ± 0.7
	3.0-3.5	97.5 ± 0.6	98.5 ± 0.5
	3.5-4.0	99.4 ± 0.5	99.5 ± 0.4
1.2-1.6	2.5-3.0	97.6 ± 1.1	99.1 ± 0.7
	3.0-3.5	99.1 ± 1.0	99.6 ± 0.7
	3.5-4.0	99.0 ± 1.0	100.0 ± 0.0
1.6-2.0	2.5-3.0	95.7 ± 1.9	96.4 ± 1.6
	3.0-3.5	98.8 ± 1.2	98.8 ± 1.2
	3.5-4.0	$-$	$-$

A.4.2   Reconstruction and selection efficiency

Table A.8: K_S LL reconstruction and selection efficiencies ($\epsilon_{\text{rec+sel}}$, in percents) in three different Monte Carlo samples, nominal (ϵ_0), undercorrected (ϵ_-) and overcorrected (ϵ_+), and their statistical errors. The systematic error on the hit finding efficiency Δ_{hit} is derived. The relative errors associated with the tracking Δ_{tracking} are quoted in the last column.

$p_T[\text{GeV}/c]$	y	ϵ_-	ϵ_0	ϵ_+	Δ_{hit}	$\Delta_{\text{hit}}/\epsilon_0$ [%]	Δ_{track} [%]
0.0-0.2	2.5-3.0	0.81 ± 0.05	0.85 ± 0.03	0.87 ± 0.04	0.03	3.6	26.7
	3.0-3.5	1.95 ± 0.08	2.05 ± 0.06	2.01 ± 0.06	0.08	3.9	25.5
	3.5-4.0	—	—	—	—	—	—
0.2-0.4	2.5-3.0	0.72 ± 0.03	0.73 ± 0.02	0.74 ± 0.02	0.01	1.6	23.8
	3.0-3.5	1.98 ± 0.06	2.03 ± 0.04	2.03 ± 0.04	0.03	1.5	20.8
	3.5-4.0	—	—	—	—	—	—
0.4-0.6	2.5-3.0	1.21 ± 0.05	1.22 ± 0.03	1.27 ± 0.04	0.04	2.9	18.8
	3.0-3.5	3.73 ± 0.09	3.75 ± 0.06	3.77 ± 0.07	0.02	0.5	17.2
	3.5-4.0	1.36 ± 0.06	1.38 ± 0.04	1.39 ± 0.05	0.01	1.0	16.4
0.6-0.8	2.5-3.0	1.87 ± 0.07	1.97 ± 0.05	2.04 ± 0.06	0.09	4.3	14.5
	3.0-3.5	4.84 ± 0.13	5.02 ± 0.09	5.07 ± 0.10	0.13	2.7	12.7
	3.5-4.0	2.72 ± 0.11	2.94 ± 0.08	2.86 ± 0.09	0.16	5.5	13.5
0.8-1.0	2.5-3.0	2.69 ± 0.13	2.67 ± 0.09	2.64 ± 0.09	0.03	1.1	11.3
	3.0-3.5	5.39 ± 0.20	5.77 ± 0.14	5.76 ± 0.16	0.27	4.6	11.5
	3.5-4.0	3.77 ± 0.19	4.15 ± 0.14	4.15 ± 0.15	0.27	6.5	11.3
1.0-1.2	2.5-3.0	3.00 ± 0.19	2.89 ± 0.13	2.94 ± 0.14	0.09	3.0	10.4
	3.0-3.5	5.61 ± 0.30	6.14 ± 0.21	6.07 ± 0.24	0.38	6.2	10.3
	3.5-4.0	4.53 ± 0.32	4.34 ± 0.22	4.72 ± 0.25	0.30	7.0	9.2
1.2-1.4	2.5-3.0	2.39 ± 0.24	2.71 ± 0.18	2.55 ± 0.19	0.26	9.5	4.9
	3.0-3.5	5.68 ± 0.43	5.76 ± 0.29	5.83 ± 0.33	0.08	1.4	8.6
	3.5-4.0	5.10 ± 0.49	5.11 ± 0.33	5.16 ± 0.37	0.04	0.7	11.9
1.4-1.6	2.5-3.0	3.27 ± 0.37	2.89 ± 0.24	2.95 ± 0.27	0.27	9.3	7.2
	3.0-3.5	6.09 ± 0.59	5.85 ± 0.40	6.02 ± 0.45	0.21	3.6	6.9
	3.5-4.0	5.43 ± 0.70	5.43 ± 0.49	5.37 ± 0.54	0.04	0.8	9.5
1.6-1.8	2.5-3.0	2.59 ± 0.45	2.63 ± 0.31	2.60 ± 0.34	0.04	1.5	8.3
	3.0-3.5	5.22 ± 0.73	5.57 ± 0.51	5.46 ± 0.57	0.26	4.6	7.5
	3.5-4.0	5.23 ± 0.90	5.56 ± 0.64	4.94 ± 0.68	0.49	8.9	9.7
1.8-2.0	2.5-3.0	3.60 ± 0.65	3.41 ± 0.43	2.79 ± 0.44	0.46	13.5	5.5
	3.0-3.5	4.11 ± 0.88	5.13 ± 0.66	5.48 ± 0.75	0.77	14.9	4.6
	3.5-4.0	3.67 ± 1.02	4.13 ± 0.71	3.90 ± 0.78	0.37	8.9	3.4

Table A.9: K_S DD reconstruction and selection efficiencies ($\epsilon_{\text{rec+sel}}$, in percents) in three different Monte Carlo samples, nominal (ϵ_0), undercorrected (ϵ_-) and overcorrected (ϵ_+), and their statistical errors. The systematic error on the hit finding efficiency Δ_{hit} is derived. The relative errors associated with the tracking Δ_{tracking} are quoted in the last column.

$p_{\text{T}}[\text{GeV}/c]$	y	ϵ_-	ϵ_0	ϵ_+	Δ_{hit}	$\Delta_{\text{hit}}/\epsilon_0$ [%]	Δ_{track} [%]
0.0-0.2	2.5-3.0	—	—	—	—	—	—
	3.0-3.5	—	—	—	—	—	—
	3.5-4.0	4.08 ± 0.16	4.48 ± 0.11	4.75 ± 0.13	0.34	7.6	10.2
0.2-0.4	2.5-3.0	—	—	—	—	—	—
	3.0-3.5	—	—	—	—	—	—
	3.5-4.0	4.75 ± 0.12	5.38 ± 0.08	5.72 ± 0.10	0.51	9.4	11.4
0.4-0.6	2.5-3.0	2.42 ± 0.08	2.61 ± 0.05	2.65 ± 0.06	0.13	5.1	11.7
	3.0-3.5	5.70 ± 0.12	6.28 ± 0.09	6.41 ± 0.10	0.42	6.7	7.7
	3.5-4.0	7.73 ± 0.16	8.82 ± 0.11	9.26 ± 0.13	0.83	9.5	9.1
0.6-0.8	2.5-3.0	5.36 ± 0.13	5.71 ± 0.09	5.85 ± 0.11	0.26	4.6	6.1
	3.0-3.5	8.64 ± 0.19	9.41 ± 0.13	9.82 ± 0.15	0.62	6.6	6.0
	3.5-4.0	10.82 ± 0.24	12.39 ± 0.17	13.11 ± 0.20	1.23	9.9	7.6
0.8-1.0	2.5-3.0	8.55 ± 0.23	8.94 ± 0.16	9.30 ± 0.18	0.37	4.2	2.4
	3.0-3.5	11.57 ± 0.31	12.71 ± 0.22	12.99 ± 0.25	0.83	6.5	5.5
	3.5-4.0	12.77 ± 0.38	14.91 ± 0.27	15.78 ± 0.32	1.63	11.0	6.0
1.0-1.2	2.5-3.0	11.64 ± 0.39	11.92 ± 0.26	12.35 ± 0.30	0.36	3.0	0.1
	3.0-3.5	14.84 ± 0.51	15.33 ± 0.36	16.24 ± 0.40	0.73	4.8	3.8
	3.5-4.0	13.76 ± 0.58	14.72 ± 0.41	16.01 ± 0.48	1.14	7.8	5.3
1.2-1.4	2.5-3.0	13.55 ± 0.60	14.17 ± 0.41	14.27 ± 0.46	0.45	3.1	0.7
	3.0-3.5	16.99 ± 0.78	17.13 ± 0.53	17.96 ± 0.61	0.59	3.5	3.1
	3.5-4.0	13.44 ± 0.83	14.40 ± 0.60	15.95 ± 0.69	1.29	9.0	5.0
1.4-1.6	2.5-3.0	16.37 ± 0.86	17.48 ± 0.61	17.87 ± 0.68	0.83	4.8	0.8
	3.0-3.5	14.99 ± 1.00	17.54 ± 0.74	17.83 ± 0.82	1.81	10.3	3.1
	3.5-4.0	11.78 ± 1.09	13.57 ± 0.81	14.11 ± 0.91	1.32	9.7	4.4
1.6-1.8	2.5-3.0	20.06 ± 1.24	19.29 ± 0.84	19.93 ± 0.94	0.71	3.7	0.9
	3.0-3.5	19.09 ± 1.42	19.86 ± 1.01	19.59 ± 1.13	0.58	2.9	0.9
	3.5-4.0	13.01 ± 1.46	14.21 ± 1.06	16.14 ± 1.25	1.60	11.3	3.4
1.8-2.0	2.5-3.0	16.69 ± 1.45	18.68 ± 1.05	19.33 ± 1.21	1.48	7.9	1.1
	3.0-3.5	14.76 ± 1.76	18.66 ± 1.30	19.00 ± 1.47	2.76	14.8	2.3
	3.5-4.0	10.05 ± 1.82	11.95 ± 1.30	12.91 ± 1.49	1.50	12.6	1.7

Table A.10: Λ LL reconstruction and selection efficiencies ($\epsilon_{\text{rec+sel}}$, in percents) in three different Monte Carlo samples, nominal (ϵ_0), undercorrected (ϵ_-) and over corrected (ϵ_+), and their statistical errors. The systematic error on the hit finding efficiency Δ_{hit} is derived. The relative errors associated with the tracking Δ_{tracking} are quoted in the last column.

$p_{\text{T}}[\text{GeV}/c]$	y	ϵ_-	ϵ_0	ϵ_+	Δ_{hit}	$\Delta_{\text{hit}}/\epsilon_0$ [%]	Δ_{track} [%]
0.4-0.8	2.5-3.0	1.40 ± 0.10	1.52 ± 0.07	1.52 ± 0.08	0.09	6.0	20.3
	3.0-3.5	1.04 ± 0.09	1.08 ± 0.06	1.15 ± 0.07	0.05	5.0	16.1
	3.5-4.0	—	—	—	—	—	—
0.8-1.2	2.5-3.0	1.49 ± 0.16	1.64 ± 0.12	1.64 ± 0.13	0.10	6.2	13.2
	3.0-3.5	4.14 ± 0.30	4.17 ± 0.21	4.07 ± 0.23	0.07	1.8	15.6
	3.5-4.0	0.76 ± 0.15	0.83 ± 0.10	0.79 ± 0.12	0.05	6.4	9.7
1.2-1.6	2.5-3.0	1.83 ± 0.33	1.30 ± 0.19	1.47 ± 0.22	0.40	30.8	0.0
	3.0-3.5	3.21 ± 0.56	3.12 ± 0.36	3.36 ± 0.43	0.18	5.9	8.2
	3.5-4.0	1.53 ± 0.40	1.84 ± 0.32	1.68 ± 0.34	0.25	13.4	12.9

Table A.11: Λ DD reconstruction and selection efficiencies ($\epsilon_{\text{rec+sel}}$, in percents) in three different Monte Carlo samples, nominal (ϵ_0), undercorrected (ϵ_-) and overcorrected (ϵ_+), and their statistical errors. The systematic error on the hit finding efficiency Δ_{hit} is derived. The relative errors associated with the tracking Δ_{tracking} are quoted in the last column.

$p_{\text{T}}[\text{GeV}/c]$	y	ϵ_-	ϵ_0	ϵ_+	Δ_{hit}	$\Delta_{\text{hit}}/\epsilon_0$ [%]	Δ_{track} [%]
0.4-0.8	2.5-3.0	2.03 ± 0.14	2.06 ± 0.10	2.11 ± 0.11	0.04	2.0	15.4
	3.0-3.5	5.31 ± 0.24	6.26 ± 0.18	6.56 ± 0.20	0.71	11.3	14.7
	3.5-4.0	2.39 ± 0.17	3.10 ± 0.13	3.24 ± 0.15	0.52	16.6	15.0
0.8-1.2	2.5-3.0	4.00 ± 0.30	3.99 ± 0.20	4.17 ± 0.23	0.13	3.3	6.9
	3.0-3.5	8.07 ± 0.47	9.23 ± 0.35	9.78 ± 0.39	0.91	9.9	11.5
	3.5-4.0	6.10 ± 0.46	7.42 ± 0.35	7.87 ± 0.40	0.99	13.3	10.6
1.2-1.6	2.5-3.0	4.73 ± 0.65	6.44 ± 0.48	6.30 ± 0.53	1.22	18.9	2.5
	3.0-3.5	7.60 ± 0.91	9.49 ± 0.65	10.61 ± 0.75	1.55	16.4	6.3
	3.5-4.0	7.32 ± 1.00	7.45 ± 0.72	9.06 ± 0.87	1.14	15.3	4.9
1.6-2.0	2.5-3.0	7.78 ± 1.27	8.29 ± 0.91	8.90 ± 1.05	0.57	6.8	4.4
	3.0-3.5	9.78 ± 1.67	10.10 ± 1.20	10.42 ± 1.39	0.32	3.2	0.0
	3.5-4.0	—	—	—	—	—	—

Table A.12: $\bar{\Lambda}$ LL reconstruction and selection efficiencies ($\epsilon_{\text{rec+sel}}$, in percents) in three different Monte Carlo samples, nominal (ϵ_0), undercorrected (ϵ_-) and overcorrected (ϵ_+), and their statistical errors. The systematic error on the hit finding efficiency Δ_{hit} is derived. The relative errors associated with the tracking Δ_{tracking} are quoted in the last column.

$p_{\text{T}}[\text{GeV}/c]$	y	ϵ_-	ϵ_0	ϵ_+	Δ_{hit}	$\Delta_{\text{hit}}/\epsilon_0$ [%]	Δ_{track} [%]
0.4-0.8	2.5-3.0	1.51 ± 0.10	1.48 ± 0.07	1.47 ± 0.08	0.02	1.7	16.7
	3.0-3.5	1.32 ± 0.11	1.44 ± 0.08	1.46 ± 0.08	0.08	5.8	18.6
	3.5-4.0	—	—	—	—	—	—
0.8-1.2	2.5-3.0	1.55 ± 0.17	1.66 ± 0.12	1.72 ± 0.14	0.09	5.6	15.1
	3.0-3.5	3.44 ± 0.31	3.55 ± 0.21	3.73 ± 0.24	0.14	4.1	15.0
	3.5-4.0	0.82 ± 0.18	0.87 ± 0.13	0.88 ± 0.14	0.04	4.3	0.0
1.2-1.6	2.5-3.0	1.19 ± 0.28	1.42 ± 0.21	1.23 ± 0.22	0.21	14.9	0.0
	3.0-3.5	4.65 ± 0.67	4.22 ± 0.44	4.07 ± 0.49	0.32	7.6	6.7
	3.5-4.0	1.53 ± 0.53	1.76 ± 0.38	2.02 ± 0.45	0.25	14.0	0.0

Table A.13: $\bar{\Lambda}$ DD reconstruction and selection efficiencies ($\epsilon_{\text{rec+sel}}$, in percents) in three different Monte Carlo samples, nominal (ϵ_0), undercorrected (ϵ_-) and overcorrected (ϵ_+), and their statistical errors. The systematic error on the hit finding efficiency Δ_{hit} is derived. The relative errors associated with the tracking Δ_{tracking} are quoted in the last column.

$p_{\text{T}}[\text{GeV}/c]$	y	ϵ_-	ϵ_0	ϵ_+	Δ_{hit}	$\Delta_{\text{hit}}/\epsilon_0$ [%]	Δ_{track} [%]
0.4-0.8	2.5-3.0	1.72 ± 0.14	1.85 ± 0.10	1.83 ± 0.11	0.10	5.3	16.7
	3.0-3.5	5.18 ± 0.24	6.24 ± 0.18	6.39 ± 0.20	0.76	12.1	16.9
	3.5-4.0	2.90 ± 0.21	3.45 ± 0.15	3.72 ± 0.18	0.43	12.6	16.5
0.8-1.2	2.5-3.0	3.31 ± 0.29	3.72 ± 0.21	3.79 ± 0.24	0.29	7.9	10.2
	3.0-3.5	8.82 ± 0.52	9.07 ± 0.36	9.19 ± 0.41	0.19	2.1	9.3
	3.5-4.0	4.87 ± 0.49	6.88 ± 0.38	6.93 ± 0.43	1.42	20.7	12.2
1.2-1.6	2.5-3.0	5.67 ± 0.67	5.86 ± 0.49	6.01 ± 0.54	0.17	2.9	3.2
	3.0-3.5	8.79 ± 1.01	9.82 ± 0.73	9.83 ± 0.82	0.73	7.5	7.0
	3.5-4.0	3.88 ± 1.09	6.54 ± 0.82	7.45 ± 0.98	1.99	30.4	7.0
1.6-2.0	2.5-3.0	9.59 ± 1.51	9.63 ± 1.04	9.32 ± 1.15	0.21	2.2	0.0
	3.0-3.5	6.92 ± 1.84	9.88 ± 1.26	8.14 ± 1.36	2.43	24.6	0.0
	3.5-4.0	—	—	—	—	—	—

A.4.3 Signal extraction systematics

Table A.14: Signal yields extracted with different methods for the K_S LL case and their systematic uncertainties Δ_S. The bins that are not used for a measurement are quoted in parentheses.

$p_T[GeV/c]$	y	CL	CQ	FQ	FLG	FQG	Δ_S	$\frac{\Delta_S}{\overline{CL}}$[%]
0.0-0.2	2.5-3.0	17	15	13	15	13	1.9	12
	3.0-3.5	34	31	33	31	39	2.9	8
	(3.5-4.0)	3	5	–	–	–	1.6	(51)
0.2-0.4	2.5-3.0	31	32	31	29	34	1.9	6
	3.0-3.5	75	68	70	77	75	3.8	5
	(3.5-4.0)	8	14	12	–	–	4.4	(53)
0.4-0.6	2.5-3.0	63	66	62	55	53	5.6	9
	3.0-3.5	121	123	125	118	120	2.5	2
	3.5-4.0	41	39	40	39	39	1.2	3
0.6-0.8	2.5-3.0	64	60	62	61	60	2.1	3
	3.0-3.5	134	129	136	133	135	2.5	2
	3.5-4.0	65	54	61	67	67	5.0	8
0.8-1.0	2.5-3.0	50	48	50	47	47	1.6	3
	3.0-3.5	91	85	91	90	88	2.2	2
	3.5-4.0	53	48	47	51	47	3.8	7
1.0-1.2	2.5-3.0	30	28	–	29	29	0.6	2
	3.0-3.5	40	34	35	35	32	5.0	12
	3.5-4.0	35	32	31	36	37	2.2	6
1.2-1.4	2.5-3.0	16	15	–	15	15	0.2	1
	3.0-3.5	33	27	–	38	27	4.8	15
	3.5-4.0	27	23	17	34	22	5.7	22
1.4-1.6	2.5-3.0	8	7	–	–	–	0.0	1
	3.0-3.5	19	18	–	17	14	2.9	15
	3.5-4.0	14	11	–	–	–	1.5	11
1.6-1.8	2.5-3.0	9	9	–	–	–	0.5	5
	3.0-3.5	6	7	–	–	–	0.9	15
	3.5-4.0	6	5	–	–	–	0.1	2
1.8-2.0	2.5-3.0	6	4	–	–	–	0.9	16
	3.0-3.5	5	3	–	–	–	0.9	19
	3.5-4.0	2	2	–	–	–	0.3	14

Table A.15: Signal yields extracted with different methods for the K_S DD case and their systematic uncertainties Δ_S. The bins that are not used for a measurement are quoted in parentheses.

p_T GeV/c	y	CL (30)	CL (40)	CQ (30)	CQ (40)	FQ (30)	FQ (40)	FLG	FQG	Δ_S	$\frac{\Delta_S}{|CL(40)|}$ [%]
0.0-0.2	(2.5-3.0)	33	34	15	1	20	13	24	19	17.2	(50)
	(3.0-3.5)	28	−15	134	112	68	30	60	75	89.1	(595)
	3.5-4.0	85	85	109	122	99	114	84	96	19.8	23
0.2-0.4	(2.5-3.0)	99	113	56	68	72	75	125	79	34.9	(31)
	(3.0-3.5)	159	151	84	21	152	126	173	177	53.7	(36)
	3.5-4.0	212	209	211	207	237	249	203	218	17.9	9
0.4-0.6	2.5-3.0	123	121	97	73	103	81	115	105	24.6	20
	3.0-3.5	258	263	255	260	260	270	253	252	6.4	2
	3.5-4.0	262	275	270	307	274	312	251	258	20.8	8
0.6-0.8	2.5-3.0	162	164	147	137	149	142	156	145	16.1	10
	3.0-3.5	254	250	254	243	255	252	239	237	6.9	3
	3.5-4.0	301	305	257	225	288	290	294	280	35.4	12
0.8-1.0	2.5-3.0	151	153	142	144	147	145	152	150	5.6	4
	3.0-3.5	176	185	154	151	176	193	166	164	19.6	11
	3.5-4.0	191	207	156	154	167	178	174	151	38.4	19
1.0-1.2	2.5-3.0	86	90	84	84	83	87	89	89	3.7	4
	3.0-3.5	146	152	133	137	138	143	137	131	13.5	9
	3.5-4.0	107	116	99	110	98	107	102	93	13.3	12
1.2-1.4	2.5-3.0	95	96	82	77	94	92	90	90	8.3	9
	3.0-3.5	86	90	86	102	84	90	80	74	8.2	9
	3.5-4.0	46	49	42	42	38	41	43	35	8.1	16
1.4-1.6	2.5-3.0	58	65	55	69	52	−	56	52	8.6	13
	3.0-3.5	60	61	65	69	63	68	60	62	4.8	8
	3.5-4.0	37	37	36	39	−	−	33	33	2.5	7
1.6-1.8	2.5-3.0	37	38	44	50	−	−	34	32	6.4	17
	3.0-3.5	33	33	33	30	30	27	31	28	2.7	8
	3.5-4.0	15	15	13	15	−	−	12	11	2.0	13
1.8-2.0	2.5-3.0	29	31	32	38	−	−	29	−	3.8	12
	3.0-3.5	24	23	25	25	−	−	27	−	2.3	10
	3.5-4.0	11	10	8	7	−	−	−	−	1.8	18

Table A.16: Signal yields extracted with different methods for the Λ LL case and their systematic uncertainties Δ_S. The bins that are not used for a measurement are quoted in parentheses.

$p_{\mathrm{T}}[\mathrm{GeV}/c]$	y	CL	CQ	FQ	FLG	FQG	Δ_S	$\frac{\Delta_S}{|\mathrm{CL}|}[\%]$
0.4-0.8	2.5-3.0	30	28	29	29	29	0.8	3
	3.0-3.5	23	18	18	21	21	2.7	12
	(3.5-4.0)	−1	0	–	–	–	0.1	(38)
0.8-1.2	2.5-3.0	19	22	17	19	19	1.6	9
	3.0-3.5	55	58	53	52	52	2.5	5
	3.5-4.0	6	6	2	–	–	1.8	30
1.2-1.6	2.5-3.0	7	9	–	–	–	1.4	19
	3.0-3.5	17	19	14	17	17	1.5	9
	3.5-4.0	8	4	–	–	–	2.0	26

Table A.17: Signal yields extracted with different methods for the Λ DD case and their systematic uncertainties Δ_S. The bins that are not used for a measurement are quoted in parentheses.

$p_{\mathrm{T}}[\mathrm{GeV}/c]$	y	CL	CQ	FQ	FLG	FQG	Δ_S	$\frac{\Delta_S}{|\mathrm{CL}|}[\%]$
0.4-0.8	2.5-3.0	47	70	53	49	50	11.1	23
	3.0-3.5	112	84	99	107	108	13.8	12
	3.5-4.0	45	53	51	36	35	7.5	17
0.8-1.2	2.5-3.0	51	49	53	49	49	1.7	3
	3.0-3.5	97	103	90	91	84	7.4	8
	3.5-4.0	67	66	64	60	64	3.5	5
1.2-1.6	2.5-3.0	38	53	42	39	40	6.9	18
	3.0-3.5	44	39	35	39	39	5.0	12
	3.5-4.0	20	10	–	21	20	4.8	23
1.6-2.0	2.5-3.0	13	20	–	17	14	4.2	32
	3.0-3.5	14	16	–	–	–	1.7	12
	(3.5-4.0)	2	2	–	–	–	0.2	(10)

Table A.18: Signal yields extracted with different methods for the $\bar{\Lambda}$ LL case and their systematic uncertainties Δ_S. The bins that are not used for a measurement are quoted in parentheses.

$p_{\mathrm{T}}[\mathrm{GeV}/c]$	y	CL	CQ	FQ	FLG	FQG	Δ_S	$\frac{\Delta_S}{|\mathrm{CL}|}[\%]$
0.4-0.8	2.5-3.0	26	23	24	24	24	0.9	4
	3.0-3.5	21	19	18	21	22	1.6	8
	(3.5-4.0)	1	−1	−	−	−	1.4	(146)
0.8-1.2	2.5-3.0	11	11	10	−	−	0.6	5
	3.0-3.5	23	24	16	23	23	3.1	13
	3.5-4.0	2	1	−	−	−	0.5	28
1.2-1.6	2.5-3.0	3	3	−	−	−	0.0	0
	3.0-3.5	11	7	8	−	−	2.8	25
	3.5-4.0	6	4	−	−	−	0.6	10

Table A.19: Signal yields extracted with different methods for the $\bar{\Lambda}$ DD case and their systematic uncertainties Δ_S. The bins that are not used for a measurement are quoted in parentheses.

$p_{\mathrm{T}}[\mathrm{GeV}/c]$	y	CL	CQ	FQ	FLG	FQG	Δ_S	$\frac{\Delta_S}{|\mathrm{CL}|}[\%]$
0.4-0.8	2.5-3.0	31	41	34	27	27	5.6	18
	3.0-3.5	86	70	86	76	76	9.6	11
	3.5-4.0	42	32	35	38	42	5.9	14
0.8-1.2	2.5-3.0	41	37	42	37	37	2.6	6
	3.0-3.5	82	94	79	81	81	5.6	7
	3.5-4.0	35	19	36	36	36	6.8	20
1.2-1.6	2.5-3.0	32	40	36	29	29	4.7	15
	3.0-3.5	29	26	29	29	29	1.3	5
	3.5-4.0	14	8	−	−	−	4.0	28
1.6-2.0	2.5-3.0	8	8	−	−	−	0.2	3
	3.0-3.5	8	8	−	−	−	0.0	0
	(3.5-4.0)	1	1	−	−	−	0.2	(24)

A.4.4   Trigger efficiency systematics

Table A.20: K_{S} trigger efficiencies in percents obtained in the reweighted Monte Carlo ϵ_{trig} and in the data $\epsilon_{\mathrm{trig,DATA}}$ with the TIS-TOS method, in bands of p_{T} or y.

$p_{\mathrm{T}}[\mathrm{GeV}/c]$ or y	ϵ_{trig} (LL)	$\epsilon_{\mathrm{trig,DATA}}$ (LL)	ϵ_{trig} (DD)	$\epsilon_{\mathrm{trig,DATA}}$ (DD)
$0.0 < p_{\mathrm{T}} < 0.2$	97.1 ± 0.4	89.0 ± 5.9	97.2 ± 0.3	99.7 ± 0.7
$0.2 < p_{\mathrm{T}} < 0.4$	97.3 ± 0.3	97.5 ± 1.8	97.9 ± 0.2	98.0 ± 1.1
$0.4 < p_{\mathrm{T}} < 0.6$	97.7 ± 0.2	97.1 ± 1.2	98.1 ± 0.1	98.6 ± 0.6
$0.6 < p_{\mathrm{T}} < 0.8$	97.8 ± 0.2	98.4 ± 0.7	98.2 ± 0.1	98.6 ± 0.5
$0.8 < p_{\mathrm{T}} < 1.0$	97.9 ± 0.2	98.2 ± 1.0	98.5 ± 0.1	98.1 ± 0.5
$1.0 < p_{\mathrm{T}} < 1.2$	98.6 ± 0.3	99.1 ± 0.9	98.9 ± 0.1	98.8 ± 0.4
$1.2 < p_{\mathrm{T}} < 1.4$	98.8 ± 0.4	98.5 ± 1.2	99.0 ± 0.2	98.5 ± 0.6
$1.4 < p_{\mathrm{T}} < 1.6$	96.8 ± 0.7	96.3 ± 2.9	99.2 ± 0.2	99.2 ± 0.5
$1.6 < p_{\mathrm{T}} < 1.8$	98.7 ± 0.6	100.0 ± 0.0	99.3 ± 0.2	99.7 ± 0.4
$1.8 < p_{\mathrm{T}} < 2.0$	99.6 ± 0.4	100.0 ± 0.0	99.8 ± 0.1	97.3 ± 1.5
$2.5 < y < 3.0$	97.3 ± 0.2	96.9 ± 1.4	98.4 ± 0.1	98.3 ± 0.6
$3.0 < y < 3.5$	97.9 ± 0.1	98.2 ± 0.5	98.2 ± 0.1	98.4 ± 0.4
$3.5 < y < 4.0$	98.3 ± 0.2	98.6 ± 0.7	98.3 ± 0.1	99.1 ± 0.3

Table A.21: Λ trigger efficiencies in percents obtained in the reweighted Monte Carlo ϵ_{trig} and in the data $\epsilon_{\mathrm{trig,DATA}}$ with the TIS-TOS method, in bands of p_{T} or y.

$p_{\mathrm{T}}[\mathrm{GeV}/c]$ or y	ϵ_{trig} (LL)	$\epsilon_{\mathrm{trig,DATA}}$ (LL)	ϵ_{trig} (DD)	$\epsilon_{\mathrm{trig,DATA}}$ (DD)
$0.4 < p_{\mathrm{T}} < 0.8$	97.5 ± 0.6	97.5 ± 3.0	98.3 ± 0.3	98.1 ± 1.1
$0.8 < p_{\mathrm{T}} < 1.2$	98.6 ± 0.5	98.2 ± 1.5	98.3 ± 0.3	100.0 ± 0.0
$1.2 < p_{\mathrm{T}} < 1.6$	98.7 ± 0.9	100.0 ± 0.0	99.1 ± 0.3	97.3 ± 1.4
$1.6 < p_{\mathrm{T}} < 2.0$	98.2 ± 2.5	100.0 ± 0.0	100.0 ± 0.0	100.0 ± 0.0
$2.5 < y < 3.0$	97.4 ± 0.6	95.6 ± 3.7	98.5 ± 0.4	99.0 ± 1.0
$3.0 < y < 3.5$	98.5 ± 0.4	99.3 ± 0.8	98.6 ± 0.3	98.5 ± 0.7
$3.5 < y < 4.0$	99.3 ± 1.0	100.0 ± 0.0	98.3 ± 0.4	99.7 ± 0.4

Table A.22: $\bar{\Lambda}$ trigger efficiencies in percents obtained in the reweighted Monte Carlo ϵ_{trig} and in the data $\epsilon_{\text{trig,DATA}}$ with the TIS-TOS method, in bands of p_{T} or y.

$p_{\text{T}}[\text{GeV}/c]$ or y	ϵ_{trig} (LL)	$\epsilon_{\text{trig,DATA}}$ (LL)	ϵ_{trig} (DD)	$\epsilon_{\text{trig,DATA}}$ (DD)
$0.4 < p_{\text{T}} < 0.8$	97.8 ± 0.6	96.9 ± 3.0	98.0 ± 0.3	98.8 ± 1.4
$0.8 < p_{\text{T}} < 1.2$	98.2 ± 0.6	97.9 ± 2.4	98.8 ± 0.3	98.8 ± 0.9
$1.2 < p_{\text{T}} < 1.6$	98.5 ± 1.0	100.0 ± 0.0	99.2 ± 0.5	99.4 ± 0.6
$1.6 < p_{\text{T}} < 2.0$	100.0 ± 0.0	100.0 ± 0.0	98.1 ± 0.8	100.0 ± 0.0
$2.5 < y < 3.0$	97.8 ± 0.6	94.6 ± 4.2	97.8 ± 0.5	98.2 ± 1.4
$3.0 < y < 3.5$	98.4 ± 0.5	99.3 ± 1.2	98.3 ± 0.3	99.2 ± 0.8
$3.5 < y < 4.0$	97.8 ± 1.5	100.0 ± 0.0	99.1 ± 0.4	99.5 ± 0.8

A.4.5   MC production spectra systematics

Table A.23: K_S LL: Signal yields S_i, total efficiencies ϵ_i in percents, and efficiency-corrected signal yields S_i/ϵ_i in four sub-bins of 0.1 GeV/c in p_T and 0.25 in y, in units of 10^3 events. Index 1 is lower p_T/lower y, index 2 is lower p_T/higher y, index 3 is higher p_T/lower y, and 4 is higher p_T/higher y. We quote also the sum of the four corrected yields ($\sum_i S_i/\epsilon_i$), the nominal corrected yield (S/ϵ), and the relative systematic error Δ_bin in percent.

p_T[GeV/c]	y	$S_1/\epsilon_1/\frac{S_1}{\epsilon_1}$	$S_2/\epsilon_2/\frac{S_2}{\epsilon_2}$	$S_3/\epsilon_3/\frac{S_3}{\epsilon_3}$	$S_4/\epsilon_4/\frac{S_4}{\epsilon_4}$	$\sum_i \frac{S_i}{\epsilon_i}$	S/ϵ	Δ_bin
0.0-0.2	2.5-3.0	3/0.55/0.50	4/1.32/0.32	3/0.49/0.67	6/1.11/0.57	2.06	2.00	3
	3.0-3.5	14/2.56/0.57	3/2.17/0.14	8/1.97/0.40	9/1.73/0.52	1.63	1.73	6
	3.5-4.0	—	—	—	—	—	—	—
0.2-0.4	2.5-3.0	9/0.42/2.19	8/1.00/0.77	5/0.35/1.51	9/1.07/0.80	5.28	4.41	20
	3.0-3.5	12/1.80/0.64	18/1.38/1.34	20/2.39/0.81	25/2.30/1.09	3.89	3.77	3
	3.5-4.0	—	—	—	—	—	—	—
0.4-0.6	2.5-3.0	10/0.68/1.42	23/1.41/1.61	12/1.07/1.10	19/1.72/1.09	5.23	5.28	1
	3.0-3.5	33/3.08/1.07	29/3.69/0.78	22/3.46/0.64	37/4.66/0.79	3.28	3.29	0.5
	3.5-4.0	15/1.65/0.88	0/0.27/0.08	23/2.80/0.81	3/0.66/0.49	2.27	3.02	25
0.6-0.8	2.5-3.0	12/1.50/0.82	25/1.91/1.32	9/1.76/0.50	17/2.71/0.64	3.27	3.31	1
	3.0-3.5	37/4.11/0.89	43/5.69/0.76	23/4.24/0.54	31/5.86/0.53	2.73	2.72	0
	3.5-4.0	27/3.82/0.70	6/1.14/0.51	21/4.74/0.45	11/1.75/0.61	2.27	2.24	1
0.8-1.0	2.5-3.0	12/2.40/0.48	19/2.56/0.72	9/2.65/0.34	11/2.98/0.37	1.91	1.91	0
	3.0-3.5	21/4.53/0.47	30/6.70/0.45	15/3.90/0.39	24/7.92/0.30	1.61	1.60	0.5
	3.5-4.0	19/5.61/0.34	10/1.80/0.54	17/5.84/0.29	7/2.70/0.27	1.44	1.29	11
1.0-1.2	2.5-3.0	10/2.45/0.40	6/2.89/0.20	6/2.97/0.19	9/3.15/0.27	1.06	1.05	1
	3.0-3.5	5/4.21/0.13	15/8.12/0.18	6/4.63/0.13	14/8.05/0.17	0.61	0.66	7
	3.5-4.0	13/6.21/0.21	4/1.48/0.27	18/6.48/0.28	1/2.45/0.02	0.78	0.82	5
1.2-1.4	2.5-3.0	6/2.53/0.22	2/2.61/0.09	4/2.56/0.15	4/3.22/0.12	0.57	0.58	1
	3.0-3.5	4/3.52/0.11	14/7.64/0.18	6/4.96/0.11	10/7.75/0.12	0.53	0.57	8
	3.5-4.0	14/6.06/0.23	3/2.91/0.09	11/6.60/0.16	−1/4.54/0.00	0.47	0.52	10
1.4-1.6	2.5-3.0	3/2.64/0.09	2/2.99/0.06	1/2.87/0.03	3/2.60/0.11	0.29	0.29	3
	3.0-3.5	7/5.09/0.13	7/8.10/0.09	3/2.97/0.09	3/6.42/0.05	0.35	0.34	4
	3.5-4.0	5/5.86/0.09	2/2.58/0.06	5/7.75/0.06	3/5.18/0.05	0.26	0.26	1
1.6-1.8	2.5-3.0	3/2.21/0.11	1/1.66/0.03	2/2.63/0.08	4/4.06/0.10	0.32	0.35	9
	3.0-3.5	1/4.07/0.02	1/9.10/0.01	0/3.80/0.00	4/5.13/0.08	0.11	0.11	3
	3.5-4.0	1/6.91/0.01	1/1.44/0.07	4/9.32/0.04	0/3.87/0.00	0.12	0.10	22
1.8-2.0	2.5-3.0	2/2.42/0.08	3/3.24/0.09	−1/2.99/0.00	1/5.56/0.02	0.19	0.17	15
	3.0-3.5	0/3.71/0.00	2/5.94/0.03	2/2.60/0.08	1/9.33/0.01	0.12	0.09	26
	3.5-4.0	1/6.19/0.01	0/0.49/0.00	2/5.37/0.03	0/2.90/0.00	0.04	0.06	29

Table A.24: K_S DD: Signal yields S_i, total efficiencies ϵ_i in percents, and efficiency-corrected signal yields S_i/ϵ_i in four sub-bins of 0.1 GeV/c in p_T and 0.25 in y, in units of 10^3 events. Index 1 is lower p_T/lower y, index 2 is lower p_T/higher y, index 3 is higher p_T/lower y, and 4 is higher p_T/higher y. We quote also the sum of the four corrected yields ($\sum_i S_i/\epsilon_i$), the nominal corrected yield (S/ϵ), and the relative systematic error Δ_{bin} in percent.

p_T[GeV/c]	y	$S_1/\epsilon_1/\frac{S_1}{\epsilon_1}$	$S_2/\epsilon_2/\frac{S_2}{\epsilon_2}$	$S_3/\epsilon_3/\frac{S_3}{\epsilon_3}$	$S_4/\epsilon_4/\frac{S_4}{\epsilon_4}$	$\sum_i \frac{S_i}{\epsilon_i}$	S/ϵ	Δ_{bin}
0.0-0.2	2.5-3.0	—	—	—	—	—	—	—
	3.0-3.5	—	—	—	—	—	—	—
	3.5-4.0	16/5.40/0.30	3/3.64/0.08	43/5.00/0.86	23/3.53/0.65	1.89	1.95	3
0.2-0.4	2.5-3.0	—	—	—	—	—	—	—
	3.0-3.5	—	—	—	—	—	—	—
	3.5-4.0	47/5.11/0.92	34/3.95/0.85	71/6.16/1.16	57/5.67/1.01	3.94	3.98	1
0.4-0.6	2.5-3.0	19/1.09/1.74	38/2.82/1.36	19/2.18/0.87	44/4.47/0.99	4.96	4.75	4
	3.0-3.5	55/4.51/1.23	68/6.60/1.02	65/6.25/1.04	75/7.81/0.96	4.25	4.26	0
	3.5-4.0	71/7.74/0.92	60/8.11/0.74	53/9.16/0.58	91/10.16/0.90	3.13	3.17	1
0.6-0.8	2.5-3.0	27/3.39/0.80	45/6.31/0.72	36/5.08/0.71	56/8.39/0.66	2.89	2.94	2
	3.0-3.5	54/7.76/0.69	61/9.06/0.67	71/9.85/0.72	65/11.02/0.59	2.67	2.71	1
	3.5-4.0	82/11.03/0.74	75/11.72/0.64	83/13.91/0.60	65/12.81/0.51	2.49	2.50	2
0.8-1.0	2.5-3.0	28/7.01/0.40	49/9.75/0.51	30/7.17/0.42	45/12.12/0.37	1.70	1.73	2
	3.0-3.5	49/11.30/0.43	59/12.86/0.46	45/12.44/0.36	32/14.17/0.23	1.48	1.48	0
	3.5-4.0	58/14.88/0.39	47/14.14/0.34	59/15.71/0.38	42/13.90/0.30	1.40	1.41	0
1.0-1.2	2.5-3.0	27/9.72/0.27	23/13.83/0.17	18/10.68/0.17	22/13.23/0.17	0.78	0.76	2
	3.0-3.5	39/13.93/0.28	41/14.79/0.28	34/16.03/0.21	38/16.75/0.22	1.00	1.00	0.5
	3.5-4.0	34/15.27/0.22	36/14.50/0.25	31/15.03/0.20	15/13.13/0.11	0.79	0.79	0
1.2-1.4	2.5-3.0	27/12.49/0.22	23/15.32/0.15	24/12.13/0.20	21/17.08/0.12	0.69	0.68	2
	3.0-3.5	18/16.45/0.11	34/18.25/0.19	22/13.62/0.16	16/20.46/0.08	0.53	0.53	1
	3.5-4.0	16/13.90/0.12	11/13.76/0.08	6/15.03/0.04	15/14.83/0.10	0.34	0.35	0
1.4-1.6	2.5-3.0	19/14.62/0.13	17/19.30/0.09	10/17.34/0.06	19/18.84/0.10	0.38	0.37	1
	3.0-3.5	23/17.71/0.13	12/17.55/0.07	15/18.23/0.08	11/15.53/0.07	0.35	0.35	0
	3.5-4.0	15/13.96/0.11	9/10.56/0.08	4/14.29/0.03	10/15.52/0.06	0.28	0.28	1
1.6-1.8	2.5-3.0	10/20.65/0.05	10/22.82/0.05	13/13.68/0.10	4/18.36/0.02	0.21	0.20	8
	3.0-3.5	8/21.62/0.04	10/17.49/0.06	11/23.74/0.05	3/15.11/0.02	0.17	0.17	0
	3.5-4.0	6/13.92/0.04	4/13.33/0.03	5/16.76/0.03	−1/12.55/0.00	0.11	0.11	1
1.8-2.0	2.5-3.0	9/16.41/0.06	6/18.72/0.03	7/17.96/0.04	9/22.81/0.04	0.17	0.17	1
	3.0-3.5	8/23.52/0.03	9/14.37/0.06	4/20.50/0.02	2/14.49/0.02	0.13	0.12	6
	3.5-4.0	2/11.93/0.02	0/13.17/0.00	6/11.38/0.05	2/11.18/0.02	0.09	0.09	6

A.4.6 Diffraction modelling

Table A.25: Relative sytematic uncertainties in percent due to the diffraction modelling for the K_S LL and DD cases.

$p_T[\text{GeV}/c]$	y	Δ_{Diff} LL	Δ_{Diff} DD
0.0-0.2	2.5-3.0	3.0	–
	3.0-3.5	3.9	–
	3.5-4.0	–	2.4
0.2-0.4	2.5-3.0	2.9	–
	3.0-3.5	3.0	–
	3.5-4.0	–	2.9
0.4-0.6	2.5-3.0	2.5	1.5
	3.0-3.5	3.3	2.0
	3.5-4.0	2.6	3.1
0.6-0.8	2.5-3.0	2.0	0.7
	3.0-3.5	2.6	1.4
	3.5-4.0	2.7	2.0
0.8-1.0	2.5-3.0	1.3	0.5
	3.0-3.5	1.8	1.3
	3.5-4.0	2.1	1.4
1.0-1.2	2.5-3.0	0.7	0.7
	3.0-3.5	1.0	0.5
	3.5-4.0	1.2	1.4
1.2-1.4	2.5-3.0	2.5	0.6
	3.0-3.5	0.3	0.4
	3.5-4.0	2.9	0.6
1.4-1.6	2.5-3.0	1.1	0.9
	3.0-3.5	0.8	1.1
	3.5-4.0	0.3	1.1
1.6-1.8	2.5-3.0	1.2	1.1
	3.0-3.5	2.0	0.2
	3.5-4.0	2.1	1.4
1.8-2.0	2.5-3.0	1.2	0.0
	3.0-3.5	3.3	0.4
	3.5-4.0	1.3	2.3

A.4.7 Final results

Table A.26: Signal yield S (in events), total efficiency ϵ_{tot} (in percents) and efficiency-corrected yield S/ϵ_{tot} (in units of 10^3 events) for the K_{S} LL case, with statistical, uncorrelated systematic, correlated systematic errors (evaluated bin by bin) and correlated systematic errors (common to all bins).

$p_{\text{T}}[\text{GeV}/c]$	y	$S\pm$stat.$+$syst.	$\epsilon_{\text{tot}}\pm$syst$_u\pm$syst$_c$	$S/\epsilon_{\text{tot}}\pm$stat.$\pm$syst$_u\pm$syst$_c\pm$syst$_{c2}$
0.0-0.2	2.5-3.0	$17 \pm 4.5 \pm 1.9$	$0.83 \pm 0.04 \pm 0.17$	$2.00 \pm 0.55 \pm 0.26 \pm 0.53 \pm 0.10$
	3.0-3.5	$34 \pm 7.0 \pm 2.9$	$1.99 \pm 0.13 \pm 0.40$	$1.73 \pm 0.35 \pm 0.18 \pm 0.44 \pm 0.09$
	3.5-4.0	$-$	$-$	$-$
0.2-0.4	2.5-3.0	$31 \pm 6.3 \pm 1.9$	$0.70 \pm 0.14 \pm 0.13$	$4.41 \pm 0.90 \pm 0.92 \pm 1.05 \pm 0.22$
	3.0-3.5	$75 \pm 9.4 \pm 3.8$	$1.98 \pm 0.07 \pm 0.34$	$3.77 \pm 0.47 \pm 0.23 \pm 0.79 \pm 0.19$
	3.5-4.0	$-$	$-$	$-$
0.4-0.6	2.5-3.0	$63 \pm 8.2 \pm 5.6$	$1.19 \pm 0.03 \pm 0.19$	$5.28 \pm 0.68 \pm 0.49 \pm 1.00 \pm 0.26$
	3.0-3.5	$121 \pm 12.0 \pm 2.5$	$3.67 \pm 0.06 \pm 0.54$	$3.30 \pm 0.33 \pm 0.09 \pm 0.57 \pm 0.16$
	3.5-4.0	$41 \pm 7.2 \pm 1.2$	$1.35 \pm 0.34 \pm 0.19$	$3.02 \pm 0.53 \pm 0.77 \pm 0.50 \pm 0.15$
0.6-0.8	2.5-3.0	$64 \pm 8.2 \pm 2.1$	$1.92 \pm 0.06 \pm 0.24$	$3.31 \pm 0.43 \pm 0.15 \pm 0.48 \pm 0.17$
	3.0-3.5	$134 \pm 12.1 \pm 2.5$	$4.92 \pm 0.09 \pm 0.55$	$2.72 \pm 0.25 \pm 0.07 \pm 0.35 \pm 0.14$
	3.5-4.0	$65 \pm 8.7 \pm 5.0$	$2.88 \pm 0.09 \pm 0.34$	$2.24 \pm 0.30 \pm 0.19 \pm 0.30 \pm 0.11$
0.8-1.0	2.5-3.0	$50 \pm 7.4 \pm 1.6$	$2.62 \pm 0.09 \pm 0.27$	$1.91 \pm 0.28 \pm 0.09 \pm 0.22 \pm 0.10$
	3.0-3.5	$91 \pm 10.1 \pm 2.2$	$5.64 \pm 0.15 \pm 0.58$	$1.61 \pm 0.18 \pm 0.06 \pm 0.19 \pm 0.08$
	3.5-4.0	$53 \pm 7.7 \pm 3.8$	$4.09 \pm 0.48 \pm 0.41$	$1.29 \pm 0.19 \pm 0.18 \pm 0.15 \pm 0.06$
1.0-1.2	2.5-3.0	$30 \pm 5.6 \pm 0.6$	$2.83 \pm 0.13 \pm 0.27$	$1.05 \pm 0.20 \pm 0.05 \pm 0.11 \pm 0.05$
	3.0-3.5	$40 \pm 6.7 \pm 5.0$	$6.08 \pm 0.48 \pm 0.57$	$0.66 \pm 0.11 \pm 0.10 \pm 0.07 \pm 0.03$
	3.5-4.0	$35 \pm 6.6 \pm 2.2$	$4.30 \pm 0.31 \pm 0.36$	$0.82 \pm 0.15 \pm 0.08 \pm 0.08 \pm 0.04$
1.2-1.4	2.5-3.0	$16 \pm 4.2 \pm 0.2$	$2.68 \pm 0.17 \pm 0.13$	$0.58 \pm 0.16 \pm 0.04 \pm 0.03 \pm 0.03$
	3.0-3.5	$33 \pm 6.0 \pm 4.8$	$5.71 \pm 0.54 \pm 0.45$	$0.57 \pm 0.11 \pm 0.10 \pm 0.05 \pm 0.03$
	3.5-4.0	$27 \pm 5.4 \pm 5.7$	$5.05 \pm 0.60 \pm 0.54$	$0.52 \pm 0.11 \pm 0.13 \pm 0.06 \pm 0.03$
1.4-1.6	2.5-3.0	$8 \pm 3.0 \pm 0.0$	$2.79 \pm 0.26 \pm 0.19$	$0.29 \pm 0.11 \pm 0.03 \pm 0.02 \pm 0.01$
	3.0-3.5	$19 \pm 4.8 \pm 2.9$	$5.65 \pm 0.45 \pm 0.36$	$0.34 \pm 0.08 \pm 0.06 \pm 0.02 \pm 0.02$
	3.5-4.0	$14 \pm 4.1 \pm 1.5$	$5.39 \pm 0.50 \pm 0.47$	$0.26 \pm 0.08 \pm 0.04 \pm 0.02 \pm 0.01$
1.6-1.8	2.5-3.0	$9 \pm 3.2 \pm 0.5$	$2.58 \pm 0.38 \pm 0.20$	$0.35 \pm 0.13 \pm 0.05 \pm 0.03 \pm 0.02$
	3.0-3.5	$6 \pm 2.7 \pm 0.9$	$5.53 \pm 0.54 \pm 0.39$	$0.11 \pm 0.05 \pm 0.02 \pm 0.01 \pm 0.01$
	3.5-4.0	$6 \pm 2.5 \pm 0.1$	$5.56 \pm 1.39 \pm 0.49$	$0.10 \pm 0.04 \pm 0.02 \pm 0.01 \pm 0.00$
1.8-2.0	2.5-3.0	$6 \pm 2.5 \pm 0.9$	$3.41 \pm 0.66 \pm 0.18$	$0.17 \pm 0.07 \pm 0.04 \pm 0.01 \pm 0.01$
	3.0-3.5	$5 \pm 2.2 \pm 0.9$	$5.13 \pm 1.48 \pm 0.22$	$0.09 \pm 0.04 \pm 0.03 \pm 0.00 \pm 0.00$
	3.5-4.0	$2 \pm 1.7 \pm 0.3$	$4.00 \pm 1.38 \pm 0.13$	$0.06 \pm 0.04 \pm 0.02 \pm 0.00 \pm 0.00$

Table A.27: Signal yield S (in events), total efficiency ϵ_{tot} (in percents) and efficiency-corrected yield S/ϵ_{tot} (in units of 10^3 events) for the K_{S} DD case, with statistical, uncorrelated systematic, correlated systematic errors (evaluated bin by bin) and correlated systematic errors (common to all bins).

$p_{\text{T}}[\text{GeV}/c]$	y	$S\pm$stat.$+$syst.	$\epsilon_{\text{tot}}\pm$syst$_u\pm$syst$_c$	$S/\epsilon_{\text{tot}}\pm$stat.$\pm$syst$_u\pm$syst$_c\pm$syst$_{c2}$
0.0-0.2	2.5-3.0	–	–	–
	3.0-3.5	–	–	–
	3.5-4.0	$85 \pm 16.1 \pm 19.8$	$4.37 \pm 0.18 \pm 0.41$	$1.95 \pm 0.37 \pm 0.46 \pm 0.20 \pm 0.10$
0.2-0.4	2.5-3.0	–	–	–
	3.0-3.5	–	–	–
	3.5-4.0	$209 \pm 23.5 \pm 17.9$	$5.26 \pm 0.10 \pm 0.54$	$3.98 \pm 0.45 \pm 0.35 \pm 0.45 \pm 0.20$
0.4-0.6	2.5-3.0	$121 \pm 17.6 \pm 24.6$	$2.54 \pm 0.13 \pm 0.26$	$4.75 \pm 0.69 \pm 1.00 \pm 0.55 \pm 0.24$
	3.0-3.5	$263 \pm 22.1 \pm 6.4$	$6.17 \pm 0.09 \pm 0.44$	$4.26 \pm 0.36 \pm 0.12 \pm 0.33 \pm 0.21$
	3.5-4.0	$275 \pm 21.9 \pm 20.8$	$8.68 \pm 0.16 \pm 0.72$	$3.17 \pm 0.25 \pm 0.25 \pm 0.29 \pm 0.16$
0.6-0.8	2.5-3.0	$164 \pm 16.0 \pm 16.1$	$5.59 \pm 0.13 \pm 0.32$	$2.94 \pm 0.29 \pm 0.30 \pm 0.18 \pm 0.15$
	3.0-3.5	$250 \pm 19.5 \pm 6.9$	$9.23 \pm 0.19 \pm 0.53$	$2.71 \pm 0.21 \pm 0.09 \pm 0.16 \pm 0.14$
	3.5-4.0	$305 \pm 20.8 \pm 35.4$	$12.19 \pm 0.19 \pm 0.86$	$2.51 \pm 0.17 \pm 0.29 \pm 0.19 \pm 0.13$
0.8-1.0	2.5-3.0	$153 \pm 13.8 \pm 5.6$	$8.80 \pm 0.23 \pm 0.21$	$1.73 \pm 0.16 \pm 0.08 \pm 0.04 \pm 0.09$
	3.0-3.5	$185 \pm 16.0 \pm 19.6$	$12.52 \pm 0.22 \pm 0.65$	$1.48 \pm 0.13 \pm 0.16 \pm 0.08 \pm 0.07$
	3.5-4.0	$207 \pm 16.9 \pm 38.4$	$14.67 \pm 0.28 \pm 0.83$	$1.41 \pm 0.12 \pm 0.26 \pm 0.08 \pm 0.07$
1.0-1.2	2.5-3.0	$90 \pm 10.7 \pm 3.7$	$11.78 \pm 0.32 \pm 0.02$	$0.76 \pm 0.09 \pm 0.04 \pm 0.00 \pm 0.04$
	3.0-3.5	$152 \pm 14.0 \pm 13.5$	$15.17 \pm 0.35 \pm 0.55$	$1.00 \pm 0.09 \pm 0.09 \pm 0.04 \pm 0.05$
	3.5-4.0	$116 \pm 12.4 \pm 13.3$	$14.61 \pm 0.40 \pm 0.73$	$0.79 \pm 0.08 \pm 0.09 \pm 0.04 \pm 0.04$
1.2-1.4	2.5-3.0	$96 \pm 11.0 \pm 8.3$	$14.05 \pm 0.44 \pm 0.10$	$0.68 \pm 0.08 \pm 0.06 \pm 0.01 \pm 0.03$
	3.0-3.5	$90 \pm 10.7 \pm 8.2$	$17.00 \pm 0.53 \pm 0.52$	$0.53 \pm 0.06 \pm 0.05 \pm 0.02 \pm 0.03$
	3.5-4.0	$49 \pm 8.2 \pm 8.1$	$14.27 \pm 0.57 \pm 0.67$	$0.35 \pm 0.06 \pm 0.06 \pm 0.02 \pm 0.02$
1.4-1.6	2.5-3.0	$65 \pm 8.6 \pm 8.6$	$17.39 \pm 0.57 \pm 0.14$	$0.37 \pm 0.05 \pm 0.05 \pm 0.00 \pm 0.02$
	3.0-3.5	$61 \pm 8.7 \pm 4.8$	$17.33 \pm 0.69 \pm 0.52$	$0.35 \pm 0.05 \pm 0.03 \pm 0.01 \pm 0.02$
	3.5-4.0	$37 \pm 6.4 \pm 2.5$	$13.51 \pm 0.78 \pm 0.57$	$0.28 \pm 0.05 \pm 0.02 \pm 0.01 \pm 0.01$
1.6-1.8	2.5-3.0	$38 \pm 6.5 \pm 6.4$	$19.11 \pm 1.66 \pm 0.18$	$0.20 \pm 0.03 \pm 0.04 \pm 0.00 \pm 0.01$
	3.0-3.5	$33 \pm 7.1 \pm 2.7$	$19.79 \pm 0.96 \pm 0.18$	$0.17 \pm 0.04 \pm 0.02 \pm 0.00 \pm 0.01$
	3.5-4.0	$15 \pm 4.7 \pm 2.0$	$14.21 \pm 1.00 \pm 0.47$	$0.11 \pm 0.03 \pm 0.02 \pm 0.00 \pm 0.01$
1.8-2.0	2.5-3.0	$31 \pm 6.0 \pm 3.8$	$18.59 \pm 1.01 \pm 0.21$	$0.17 \pm 0.03 \pm 0.02 \pm 0.00 \pm 0.01$
	3.0-3.5	$23 \pm 5.1 \pm 2.3$	$18.66 \pm 1.57 \pm 0.42$	$0.12 \pm 0.03 \pm 0.02 \pm 0.00 \pm 0.01$
	3.5-4.0	$10 \pm 3.4 \pm 1.8$	$11.95 \pm 1.33 \pm 0.20$	$0.09 \pm 0.03 \pm 0.02 \pm 0.00 \pm 0.00$

Table A.28: Signal yield S (in events), total efficiency $\epsilon_{\rm tot}$ (in percents) and efficiency-corrected yield $S/\epsilon_{\rm tot}$ (in units of 10^3 events) for the Λ LL case, with statistical, uncorrelated systematic, correlated systematic errors (evaluated bin by bin) and correlated systematic errors (common to all bins).

$p_{\rm T}[{\rm GeV}/c]$	y	$S\pm{\rm stat.}+{\rm syst.}$	$\epsilon_{\rm tot}\pm{\rm syst}_u\pm{\rm syst}_c$	$S/\epsilon_{\rm tot}\pm{\rm stat.}\pm{\rm syst}_u\pm{\rm syst}_c\pm{\rm syst}_{c2}$
0.4-0.8	2.5-3.0	$30 \pm 5.9 \pm 0.8$	$1.48 \pm 0.07 \pm 0.25$	$2.02 \pm 0.40 \pm 0.11 \pm 0.41 \pm 0.12$
	3.0-3.5	$23 \pm 5.1 \pm 2.7$	$1.06 \pm 0.07 \pm 0.15$	$2.14 \pm 0.48 \pm 0.29 \pm 0.34 \pm 0.13$
	3.5-4.0	$-$	$-$	$-$
0.8-1.2	2.5-3.0	$19 \pm 4.9 \pm 1.6$	$1.63 \pm 0.12 \pm 0.19$	$1.15 \pm 0.30 \pm 0.13 \pm 0.15 \pm 0.07$
	3.0-3.5	$55 \pm 7.6 \pm 2.5$	$4.08 \pm 0.21 \pm 0.55$	$1.34 \pm 0.19 \pm 0.09 \pm 0.21 \pm 0.08$
	3.5-4.0	$6 \pm 3.2 \pm 1.8$	$0.83 \pm 0.11 \pm 0.07$	$0.71 \pm 0.38 \pm 0.23 \pm 0.07 \pm 0.04$
1.2-1.6	2.5-3.0	$7 \pm 2.8 \pm 1.4$	$1.24 \pm 0.19 \pm 0.00$	$0.58 \pm 0.23 \pm 0.14 \pm 0.00 \pm 0.03$
	3.0-3.5	$17 \pm 4.6 \pm 1.5$	$3.13 \pm 0.34 \pm 0.24$	$0.54 \pm 0.15 \pm 0.07 \pm 0.04 \pm 0.03$
	3.5-4.0	$8 \pm 2.8 \pm 2.0$	$1.79 \pm 0.32 \pm 0.20$	$0.43 \pm 0.16 \pm 0.14 \pm 0.06 \pm 0.03$

Table A.29: Signal yield S (in events), total efficiency $\epsilon_{\rm tot}$ (in percents) and efficiency-corrected yield $S/\epsilon_{\rm tot}$ (in units of 10^3 events) for the Λ DD case, with statistical, uncorrelated systematic, correlated systematic errors (evaluated bin by bin) and correlated systematic errors (common to all bins).

$p_{\rm T}[{\rm GeV}/c]$	y	$S\pm{\rm stat.}+{\rm syst.}$	$\epsilon_{\rm tot}\pm{\rm syst}_u\pm{\rm syst}_c$	$S/\epsilon_{\rm tot}\pm{\rm stat.}\pm{\rm syst}_u\pm{\rm syst}_c\pm{\rm syst}_{c2}$
0.4-0.8	2.5-3.0	$47 \pm 10.1 \pm 11.1$	$2.05 \pm 0.11 \pm 0.27$	$2.31 \pm 0.49 \pm 0.55 \pm 0.36 \pm 0.18$
	3.0-3.5	$112 \pm 14.7 \pm 13.8$	$6.15 \pm 0.18 \pm 0.79$	$1.82 \pm 0.24 \pm 0.23 \pm 0.27 \pm 0.15$
	3.5-4.0	$45 \pm 9.3 \pm 7.5$	$3.03 \pm 0.14 \pm 0.40$	$1.48 \pm 0.31 \pm 0.26 \pm 0.22 \pm 0.12$
0.8-1.2	2.5-3.0	$51 \pm 8.7 \pm 1.7$	$3.88 \pm 0.20 \pm 0.25$	$1.32 \pm 0.22 \pm 0.08 \pm 0.09 \pm 0.11$
	3.0-3.5	$97 \pm 11.7 \pm 7.4$	$9.13 \pm 0.34 \pm 0.94$	$1.06 \pm 0.13 \pm 0.09 \pm 0.12 \pm 0.08$
	3.5-4.0	$67 \pm 9.0 \pm 3.5$	$7.31 \pm 0.35 \pm 0.70$	$0.92 \pm 0.12 \pm 0.07 \pm 0.10 \pm 0.07$
1.2-1.6	2.5-3.0	$38 \pm 7.0 \pm 6.9$	$6.38 \pm 0.46 \pm 0.15$	$0.60 \pm 0.11 \pm 0.12 \pm 0.01 \pm 0.05$
	3.0-3.5	$44 \pm 7.3 \pm 5.0$	$9.39 \pm 0.63 \pm 0.56$	$0.47 \pm 0.08 \pm 0.06 \pm 0.03 \pm 0.04$
	3.5-4.0	$20 \pm 5.0 \pm 4.8$	$7.41 \pm 0.70 \pm 0.35$	$0.27 \pm 0.07 \pm 0.07 \pm 0.01 \pm 0.02$
1.6-2.0	2.5-3.0	$13 \pm 4.3 \pm 4.2$	$8.29 \pm 0.89 \pm 0.35$	$0.16 \pm 0.05 \pm 0.05 \pm 0.01 \pm 0.01$
	3.0-3.5	$14 \pm 4.1 \pm 1.7$	$10.17 \pm 1.24 \pm 0.00$	$0.14 \pm 0.04 \pm 0.02 \pm 0.00 \pm 0.01$
	3.5-4.0	$-$	$-$	$-$

Table A.30: Signal yield S (in events), total efficiency ϵ_{tot} (in percents) and efficiency-corrected yield S/ϵ_{tot} (in units of 10^3 events) for the $\bar{\Lambda}$ LL case, with statistical, uncorrelated systematic, correlated systematic errors (evaluated bin by bin) and correlated systematic errors (common to all bins).

$p_{\text{T}}[\text{GeV}/c]$	y	$S\pm$stat.$+$syst.	$\epsilon_{\text{tot}}\pm$syst$_u\pm$syst$_c$	$S/\epsilon_{\text{tot}}\pm$stat.$\pm$syst$_u\pm$syst$_c\pm$syst$_{c2}$
0.4-0.8	2.5-3.0	$26 \pm 5.5 \pm 0.9$	$1.44 \pm 0.07 \pm 0.21$	$1.77 \pm 0.38 \pm 0.11 \pm 0.29 \pm 0.11$
	3.0-3.5	$21 \pm 5.3 \pm 1.6$	$1.40 \pm 0.08 \pm 0.22$	$1.46 \pm 0.38 \pm 0.14 \pm 0.27 \pm 0.09$
	3.5-4.0	—	—	—
0.8-1.2	2.5-3.0	$11 \pm 3.9 \pm 0.6$	$1.63 \pm 0.12 \pm 0.21$	$0.70 \pm 0.24 \pm 0.07 \pm 0.11 \pm 0.04$
	3.0-3.5	$23 \pm 5.3 \pm 3.1$	$3.52 \pm 0.22 \pm 0.46$	$0.66 \pm 0.15 \pm 0.10 \pm 0.10 \pm 0.04$
	3.5-4.0	$2 \pm 1.4 \pm 0.5$	$0.84 \pm 0.13 \pm 0.00$	$0.21 \pm 0.17 \pm 0.07 \pm 0.00 \pm 0.01$
1.2-1.6	2.5-3.0	$3 \pm 1.7 \pm 0.0$	$1.37 \pm 0.21 \pm 0.00$	$0.22 \pm 0.13 \pm 0.03 \pm 0.00 \pm 0.01$
	3.0-3.5	$11 \pm 3.7 \pm 2.8$	$4.20 \pm 0.46 \pm 0.26$	$0.27 \pm 0.09 \pm 0.07 \pm 0.02 \pm 0.02$
	3.5-4.0	$6 \pm 2.5 \pm 0.6$	$1.76 \pm 0.40 \pm 0.00$	$0.33 \pm 0.14 \pm 0.08 \pm 0.00 \pm 0.02$

Table A.31: Signal yield S (in events), total efficiency ϵ_{tot} (in percents) and efficiency-corrected yield S/ϵ_{tot} (in units of 10^3 events) for the $\bar{\Lambda}$ DD case, with statistical, uncorrelated systematic, correlated systematic errors (evaluated bin by bin) and correlated systematic errors (common to all bins).

$p_{\text{T}}[\text{GeV}/c]$	y	$S\pm$stat.$+$syst.	$\epsilon_{\text{tot}}\pm$syst$_u\pm$syst$_c$	$S/\epsilon_{\text{tot}}\pm$stat.$\pm$syst$_u\pm$syst$_c\pm$syst$_{c2}$
0.4-0.8	2.5-3.0	$31 \pm 9.1 \pm 5.6$	$1.80 \pm 0.11 \pm 0.26$	$1.72 \pm 0.50 \pm 0.33 \pm 0.29 \pm 0.14$
	3.0-3.5	$86 \pm 12.8 \pm 9.6$	$6.11 \pm 0.19 \pm 0.88$	$1.41 \pm 0.21 \pm 0.16 \pm 0.24 \pm 0.11$
	3.5-4.0	$42 \pm 9.0 \pm 5.9$	$3.40 \pm 0.17 \pm 0.48$	$1.25 \pm 0.26 \pm 0.18 \pm 0.21 \pm 0.10$
0.8-1.2	2.5-3.0	$41 \pm 7.0 \pm 2.6$	$3.66 \pm 0.20 \pm 0.34$	$1.11 \pm 0.19 \pm 0.09 \pm 0.11 \pm 0.09$
	3.0-3.5	$82 \pm 10.3 \pm 5.6$	$8.94 \pm 0.36 \pm 0.76$	$0.92 \pm 0.12 \pm 0.07 \pm 0.09 \pm 0.07$
	3.5-4.0	$35 \pm 7.4 \pm 6.8$	$6.84 \pm 0.40 \pm 0.75$	$0.51 \pm 0.11 \pm 0.10 \pm 0.06 \pm 0.04$
1.2-1.6	2.5-3.0	$32 \pm 6.3 \pm 4.7$	$5.81 \pm 0.45 \pm 0.18$	$0.55 \pm 0.11 \pm 0.09 \pm 0.02 \pm 0.04$
	3.0-3.5	$29 \pm 5.8 \pm 1.3$	$9.79 \pm 0.68 \pm 0.64$	$0.29 \pm 0.06 \pm 0.02 \pm 0.02 \pm 0.02$
	3.5-4.0	$14 \pm 4.4 \pm 4.0$	$6.54 \pm 0.89 \pm 0.43$	$0.22 \pm 0.07 \pm 0.07 \pm 0.02 \pm 0.02$
1.6-2.0	2.5-3.0	$8 \pm 3.4 \pm 0.2$	$9.28 \pm 0.94 \pm 0.00$	$0.09 \pm 0.04 \pm 0.01 \pm 0.00 \pm 0.01$
	3.0-3.5	$8 \pm 2.8 \pm 0.0$	$9.76 \pm 1.28 \pm 0.00$	$0.08 \pm 0.03 \pm 0.01 \pm 0.00 \pm 0.01$
	3.5-4.0	—	—	—

Table A.32: Final K_{S} results obtained as the weighted average of the LL and DD measurements. The units are 10^3 events for the combined efficiency-corrected yields and mb/(GeV/c) for the double differential cross-section.

$p_{\mathrm{T}}[\mathrm{GeV}/c]$	y	Yields+stat.+syst$_u$+syst$_c$	$d^2\sigma/dydp_{\mathrm{T}}$
0.0-0.2	2.5-3.0	$2.00 \pm 0.55 \pm 0.26 \pm 0.54$	2.94 ± 1.26
	3.0-3.5	$1.73 \pm 0.35 \pm 0.18 \pm 0.45$	2.55 ± 0.95
	3.5-4.0	$1.95 \pm 0.37 \pm 0.46 \pm 0.20$	2.87 ± 1.01
0.2-0.4	2.5-3.0	$4.41 \pm 0.90 \pm 0.92 \pm 1.06$	6.49 ± 2.63
	3.0-3.5	$3.77 \pm 0.47 \pm 0.23 \pm 0.79$	5.55 ± 1.62
	3.5-4.0	$3.98 \pm 0.45 \pm 0.35 \pm 0.45$	5.85 ± 1.37
0.4-0.6	2.5-3.0	$5.02 \pm 0.49 \pm 0.49 \pm 0.86$	7.39 ± 1.96
	3.0-3.5	$4.07 \pm 0.24 \pm 0.07 \pm 0.47$	5.98 ± 1.18
	3.5-4.0	$3.16 \pm 0.23 \pm 0.24 \pm 0.35$	4.65 ± 0.98
0.6-0.8	2.5-3.0	$3.02 \pm 0.24 \pm 0.19 \pm 0.33$	4.45 ± 0.93
	3.0-3.5	$2.71 \pm 0.16 \pm 0.06 \pm 0.26$	3.99 ± 0.74
	3.5-4.0	$2.41 \pm 0.15 \pm 0.20 \pm 0.27$	3.54 ± 0.75
0.8-1.0	2.5-3.0	$1.75 \pm 0.14 \pm 0.06 \pm 0.12$	2.58 ± 0.48
	3.0-3.5	$1.52 \pm 0.10 \pm 0.09 \pm 0.15$	2.24 ± 0.45
	3.5-4.0	$1.35 \pm 0.10 \pm 0.17 \pm 0.14$	1.99 ± 0.45
1.0-1.2	2.5-3.0	$0.80 \pm 0.08 \pm 0.03 \pm 0.05$	1.17 ± 0.23
	3.0-3.5	$0.86 \pm 0.07 \pm 0.07 \pm 0.07$	1.27 ± 0.26
	3.5-4.0	$0.80 \pm 0.07 \pm 0.07 \pm 0.07$	1.18 ± 0.25
1.2-1.4	2.5-3.0	$0.65 \pm 0.07 \pm 0.05 \pm 0.04$	0.96 ± 0.20
	3.0-3.5	$0.54 \pm 0.05 \pm 0.05 \pm 0.04$	0.79 ± 0.17
	3.5-4.0	$0.37 \pm 0.05 \pm 0.05 \pm 0.03$	0.55 ± 0.14
1.4-1.6	2.5-3.0	$0.35 \pm 0.04 \pm 0.04 \pm 0.02$	0.51 ± 0.12
	3.0-3.5	$0.35 \pm 0.04 \pm 0.03 \pm 0.02$	0.51 ± 0.11
	3.5-4.0	$0.27 \pm 0.04 \pm 0.02 \pm 0.02$	0.40 ± 0.09
1.6-1.8	2.5-3.0	$0.21 \pm 0.03 \pm 0.04 \pm 0.01$	0.31 ± 0.09
	3.0-3.5	$0.14 \pm 0.03 \pm 0.01 \pm 0.01$	0.21 ± 0.06
	3.5-4.0	$0.10 \pm 0.03 \pm 0.01 \pm 0.01$	0.15 ± 0.05
1.8-2.0	2.5-3.0	$0.17 \pm 0.03 \pm 0.02 \pm 0.01$	0.25 ± 0.06
	3.0-3.5	$0.12 \pm 0.02 \pm 0.01 \pm 0.01$	0.17 ± 0.05
	3.5-4.0	$0.08 \pm 0.02 \pm 0.01 \pm 0.00$	0.11 ± 0.04

Table A.33: Final Λ results obtained as the weighted average of the LL and DD measurements. The units are 10^3 events for the combined efficiency-corrected yields and mb/(GeV/c) for the double differential cross-section.

p_{T}[GeV/c]	y	Yields+stat.+syst$_u$+syst$_c$	$d^2\sigma/dydp_{\mathrm{T}}$
0.4-0.8	2.5-3.0	$2.09 \pm 0.31 \pm 0.19 \pm 0.42$	1.54 ± 0.47
	3.0-3.5	$1.89 \pm 0.21 \pm 0.19 \pm 0.32$	1.39 ± 0.38
	3.5-4.0	$1.48 \pm 0.31 \pm 0.26 \pm 0.22$	1.09 ± 0.37
0.8-1.2	2.5-3.0	$1.26 \pm 0.18 \pm 0.07 \pm 0.15$	0.93 ± 0.23
	3.0-3.5	$1.11 \pm 0.10 \pm 0.07 \pm 0.17$	0.82 ± 0.20
	3.5-4.0	$0.90 \pm 0.12 \pm 0.06 \pm 0.12$	0.66 ± 0.16
1.2-1.6	2.5-3.0	$0.60 \pm 0.10 \pm 0.10 \pm 0.05$	0.44 ± 0.12
	3.0-3.5	$0.48 \pm 0.07 \pm 0.05 \pm 0.05$	0.36 ± 0.09
	3.5-4.0	$0.30 \pm 0.06 \pm 0.06 \pm 0.03$	0.22 ± 0.08
1.6-2.0	2.5-3.0	$0.16 \pm 0.05 \pm 0.05 \pm 0.01$	0.12 ± 0.06
	3.0-3.5	$0.14 \pm 0.04 \pm 0.02 \pm 0.00$	0.10 ± 0.04
	3.5-4.0	−	−

Table A.34: Final $\bar{\Lambda}$ results obtained as the weighted average of the LL and DD measurements. The units are 10^3 events for the combined efficiency-corrected yields and mb/(GeV/c) for the double differential cross-section.

p_{T}[GeV/c]	y	Yields+stat.+syst$_u$+syst$_c$	$d^2\sigma/dydp_{\mathrm{T}}$
0.4-0.8	2.5-3.0	$1.75 \pm 0.30 \pm 0.13 \pm 0.32$	1.29 ± 0.39
	3.0-3.5	$1.43 \pm 0.18 \pm 0.12 \pm 0.27$	1.05 ± 0.30
	3.5-4.0	$1.25 \pm 0.26 \pm 0.18 \pm 0.21$	0.92 ± 0.31
0.8-1.2	2.5-3.0	$0.92 \pm 0.15 \pm 0.06 \pm 0.13$	0.67 ± 0.18
	3.0-3.5	$0.82 \pm 0.09 \pm 0.06 \pm 0.11$	0.60 ± 0.14
	3.5-4.0	$0.37 \pm 0.09 \pm 0.07 \pm 0.05$	0.27 ± 0.10
1.2-1.6	2.5-3.0	$0.36 \pm 0.08 \pm 0.05 \pm 0.03$	0.27 ± 0.08
	3.0-3.5	$0.29 \pm 0.05 \pm 0.03 \pm 0.03$	0.21 ± 0.06
	3.5-4.0	$0.25 \pm 0.06 \pm 0.06 \pm 0.02$	0.18 ± 0.07
1.6-2.0	2.5-3.0	$0.09 \pm 0.04 \pm 0.01 \pm 0.00$	0.06 ± 0.03
	3.0-3.5	$0.08 \pm 0.03 \pm 0.01 \pm 0.00$	0.06 ± 0.02
	3.5-4.0	−	−

Bibliography

[1] A. Einstein, *Uber das Relativitaetsprinzip und die aus demselben gezogene Folgerungen*, Jahrbuch der Radioaktivitaet und Elektronik 4 (1907) 411

[2] A. Einstein, *Die Feldgleichungen der Gravitation*, Sitzungsberichte der Preussischen Akademie der Wissenschaften zu Berlin (1915) 844

[3] A. Einstein, *Fundamental ideas and problems of the theory of relativity*, lecture delivered to the Nordic Assembly of Naturalists at Gothenburg (1923)
http://nobelprize.org/nobel_prizes/physics/laureates/1921/einstein-lecture.pdf

[4] E. Hubble and M. L. Humason, *The velocity-distance relation among extra-galactic nebulae*, Astrophysical Journal 74 (1931) 43

[5] R. Aaij *et al.*, [The LHCb collaboration], *Prompt K_S^0 production in pp collisions at $\sqrt{s} = 0.9$ TeV*, Phys. Lett. 693 (2010) 69

[6] W. Heisenberg, *Uber den anschaulichen Inhalt der quantentheoretischen Kinematik und Mechanik*, Zeitschrift fur Physik 43 (1927) 172

[7] P. Curie, M. Curie and H. Becquerel, Nobel speech and Nobel lectures:
http://nobelprize.org/nobel_prizes/physics/laureates/1903/

[8] P. Koppenburg, *Contribution to the development of the LHCb Vertex Locator and study of rare semileptonic decays*, Ph.D. thesis, Université de Lausanne (2002)

[9] See, for instance: http://lepewwg.web.cern.ch/LEPEWWG/

[10] P. Higgs, *Broken symmetries and the masses of gauge bosons*, Phys. Rev. Lett. 13 (1964) 508

[11] L. Susskind, *Dynamics of spontaneous symmetry breaking in the Weinberg-Salam theory*, Phys. Rev. D 20 (1979) 2619

[12] G. Ross, *Grand Unified Theories*, Westview Press (1984)

[13] S. P. Martin, *A Supersymmetric Primer*, (1997) arXiv:hep-ph/9709356v5

[14] E. Noether, *Invariante Variationsprobleme*, Nachr. D. Konig. Gesellsch. D. Wiss. Zu Gottingen, Math-phys. Klasse (1918) 235

[15] M. Knecht, *Aspects théoriques de la désintégration $B \rightarrow K\gamma\gamma$ et implications pour sa simulation dans le cadre de l'expérience BELLE*, Master Thesis, EPFL, Lausanne (2004)
http://lphe.epfl.ch/publications/2004/lphe_2004_14.pdf

[16] M. Knecht and T. Schietinger, *Probing photon helicity in radiative B decays via charmonium resonance interference*, Phys. Lett. B 634 (2006) 403

[17] G. Hiller, M. Knecht, F. Legger and T. Schietinger, *Photon polarization form helicity suppression in radiative decays of Λ_b to spin-2/3 baryons*, Phys. Lett. B 649 (2007) 152

[18] CERN Document Server (CDS), `http://weblib.cern.ch`

[19] L. Evans and P. Bryant (Eds), *LHC Machine*, JINST 3 (2008) S08001

[20] G. Aad *et al.* [The ATLAS collaboration], *The ATLAS Experiment at the LHC*, JINST 3 (2008) S08003

[21] R. Adolphi *et al.* [The CMS collaboration], *The CMS Experiment at the LHC*, JINST 3 (2008) S08004

[22] K. Aamodt *et al.* [The ALICE collaboration], *The ALICE Experiment at the LHC*, JINST 3 (2008) S08002

[23] A.A. Alves *et al.* [The LHCb collaboration], *The LHCb Detector at the LHC*, JINST 3 (2008) S08005

[24] O. Adriani *et al.* [The LHCf collaboration], *The LHCf Detector at the LHC*, JINST 3 (2008) S08006

[25] G. Anelli *et al.* [The TOTEM collaboration], *The TOTEM Experiment at the LHC*, JINST 3 (2008) S08007

[26] The MoEDAL collaboration, *MoEDAL Technical Design Report*, CERN-LHC-2009-006 (2009) `http://web.me.com/jamespinfold/MoEDAL_site/TDR_files/tdr-v6.pdf`

[27] J. Borel, *The analog readout of the LHCb vertex detector and study of the measurement of the B_s oscillation frequency*, Ph.D. thesis, EPFL, Lausanne (2008)

[28] R. Antunes Nobrega *et al.* [The LHCb collaboration], *LHCb Trigger System: Technical Design Report*, CERN Report LHCC-2003-31 (2003)

[29] G. Barrand *et al.*, *GAUDI - A Software Architecture and Framework for Building HEP Data Processing Applications*, Comput. Phys. Commun. 140 (2001) 45
See also: `http://proj-gaudi.web.cern.ch/proj-gaudi/`

[30] I. Belyaev *et al.*, *Simulation Application for the LHCb Experiment* (2003) [physics/0306035]
See also: `http://lhcb-release-area.web.cern.ch/LHCb-release-area/DOC/gauss/`

[31] T. Sjöstrand *et al.*, *PYTHIA 6.4 Physics and manual*, JHEP 0605 (2006) 026

[32] D. J. Lange, *The EVTGEN Particle Decay Simulation Package*, Nucl. Instrum. Meth. A 462 (2001) 152;
A. Ryd *et al.EvtGen: A Monte Carlo Generator for B-Physics*, EVTGEN-V00-11-07 (2005)
See also: `http://www.slac.stanford.edu/ lange/EvtGen/`

[33] Z. Was *et al. PHOTOS Monte Carlo and its theoretical accuracy*, Nucl. Phys. Proc. Suppl. 181-182 (2008) 269

[34] S. Agostinelli *et al.* [The GEANT4 collaboration], *GEANT4: A simulation toolkit*, Nucl. Instrum. Meth. A 506 (2003) 250 See also: `http://geant4.web.cern.ch/geant4/`

[35] The LHCb collaboration, *The BOOLE project*,
`http://lhcb-release-area.web.cern.ch/LHCb-release-area/DOC/boole/`

[36] The LHCb collaboration, *The BRUNEL project*,
http://lhcb-release-area.web.cern.ch/LHCb-release-area/DOC/brunel/

[37] The LHCb collaboration, *The DAVINCI project*,
http://lhcb-release-area.web.cern.ch/LHCb-release-area/DOC/davinci/

[38] S. Loschner and M. Schmelling, *The Beetle reference manual*, CERN-LHCb-2005-105 (2005)

[39] R. Jacobsson and B. Jost, *Timing and fast control*, CERN-LHCb-2001-0016 (2001)

[40] G. Haefeli *et al.*, *The LHCb DAQ interface board TELL1*, Nucl. Instr. Meth. A 560 (2006) 494

[41] M. Knecht, *Cooling pipes gluing tests*, Silicon Tracker meeting, LHCb week, May 30, 2006,
http://indico.cern.ch/
getFile.py/access?contribId=3&resId=0&materialId=slides&confId=3122

[42] M. Knecht, *6 months and 1 week of search and speculation*, LPHE Monday Seminar, October 30, 2006, http://lphe.epfl.ch/seminar/intern/2006/knecht_30Oct2006.pdf

[43] G. Haefeli and A. Gong, *VELO and ST non-zero suppressed bank data format*
https://edms.cern.ch/file/692431/2/velo_st_non_zerosuppressed.pdf

[44] G. Haefeli and A. Gong, *ST zero suppressed bank data format*,
https://edms.cern.ch/file/690583/3/st_zs_data_format.pdf

[45] G. Haefeli and A. Gong, *VELO and ST pedestal bank data format*,
https://edms.cern.ch/file/695007/1/velo_st_pedestal.pdf

[46] G. Haefeli and A. Gong, *VELO and ST error bank data format*,
https://edms.cern.ch/file/694818/2/velo_st_error_bank.pdf

[47] P. Somogyi, *Novel monitoring methods for diagnostic purposes in experimental medical and physical measurements*, Ph.D. thesis, Budapest (2010)
http://www.omikk.bme.hu/
collections/phd/Villamosmernoki_es_Informatikai_Kar/2010/Somogyi_Peter/ertekezes.pdf

[48] B. Andersson *et al.*, *A semi-classical model for quark jet fragmentation*, Z. Phys. C 1 (1979) 105

[49] B. Andersson and G. Gustafson, *Semi-classical models for gluon jets and leptoproduction based on the massless relativistic string*, Z. Phys. C 3 (1979) 223

[50] B. Andersson *et al.*, *A three-dimensional model for quark and gluon jets*, Z. Phys. C 6 (1980) 235

[51] B. Andersson, *et al.*, *A model for baryon production in quark and gluon jets*, Nucl. Phys. B 197 (1982) 45

[52] B. Andersson, *et al.*, *Baryon production in jet fragmentation and γ decay*, Physica Scripta 32 (1985) 574

[53] P. Edén and G. Gustafson, *Baryon production in the string fragmentation picture*, Z. Phys. C75 (1997) 41;
P. Edén, *A program for baryon generation and its applications to baryon fragmentation in DIS*, LU TP 96-29 arXiv:hep-ph/9610246v1

[54] D. Acosta *et al.* [The CDF collaboration], K_S^0 *and* Λ^0 *production studies in* $p\bar{p}$ *collisions at* $\sqrt{s}$=*1800 GeV and 630 GeV*, Phys. Rev. D 72 (2005) 052001

[55] P. Skands, `http://home.fnal.gov/~skands/leshouches-plots/`

[56] C. Amsler *et al.*, [Particle Data Group], *Review of particle physics*, Phys. Lett. B 667 (2008) 1

[57] Extensive documentation on the LHCb tracking can be found here: `https://twiki.cern.ch/` `twiki/bin/view/LHCb/LHCbTracking#Release_notes_and_Performance_Do`

[58] M. Krasowski *et al.*, *Primary Vertex Reconstruction*, CERN-LHCb-2007-011 (2007)

[59] J. Podolanski, R. Armenteros, *Analysis of V-events*, Phil. Mag. 7 45 (1954) 13

[60] S. Hansmann-Menzemer *et al.*, *Measurement of yield of* K_S *reconstructed with downstream tracks in 2009 data*, CERN-LHCb-ANA-2010-001 (2010)

[61] E. Lopez Asamar *et al.*, *Measurement of trigger efficiencies and biases*, CERN-LHCb-2008-073 (2008)

[62] B. Storaci, *Tracking efficiency*, Tracking and Alignment workshop, June 4, 2010, `http://indico.cern.ch/` `getFile.py/access?contribId=9&resId=0&materialId=slides&confId=93325`

[63] M. Knecht *et al.*, *Measurement of* V^0-*particle production at LHCb with 2009 data*, CERN-LHCb-ANA-2010-002 (2010)

[64] S. Navin, *Diffraction in PYTHIA*, LU TP 09-23 (2010) arXiv:1005.3894v1 [hep-ph]

[65] I. Belyaev *et al.*, *Handling of the generation of primary events in Gauss, the LHCb simulation framework*, CERN-LHCb-PROC-2010-056 (2010)

[66] P. Z. Skands, *The Perugia Tunes*, CERN-PH-TH-2010-113 (2010) arXiv:1005.3457v4 [hep-ph]

[67] G. Bocquet *et al.* [The UA1 collaboration], *Inclusive production of strange particles in* $p\bar{p}$ *collisions at* $\sqrt{s} = 630$ *GeV with UA1*, Phys. Lett. B 366 (1996) 441

[68] F. Abe *et al.* [The CDF collaboration], K_S^0 *production in* $p\bar{p}$ *interactions at* $\sqrt{s} = 630$ *and 1800 GeV*, Phys. Rev. D 40 (1989) 3791

[69] G.J. Alner *et al.* [The UA5 collaboration], *Kaon production in* $p\bar{p}$ *reactions at a centre-of-mass energy of 540 GeV*, Nucl. Phys. B 258 (1985) 505

[70] K. Aamodt *et al.* [The ALICE collaboration], *Strange particle production in proton-proton collisions at* $\sqrt{s}$=*0.9 TeV with ALICE at the LHC*, CERN-PH-EP-2010-065 (2010) arXiv:1012.3257v2 [hep-ex]

[71] The CMS collaboration, *Strange particle production in pp collisions at* $\sqrt{s} = 0.9$ *and 7 TeV*, CERN-PH-EP-2010-094 (2010) arXiv:1102.4282v1 [hep-ex]

CURRICULUM VITAE

Mathias KNECHT
Av. J.-J. Rousseau 22
1815 Clarens, Switzerland
+41 79 380 15 45
mathias.knecht@epfl.ch

8 January 1981
Single
Dual nationality : Swiss and French

WORK EXPERIENCE

April 2010-present	Teacher at the Collège de Montreux in mathematics and physics for secondary school students.
April 2006-March 2010	Doctoral Assistant at the Laboratoire de Physique des Hautes Energies (LPHE) of Ecole Polytechnique Fédérale de Lausanne (EPFL), in collaboration with CERN (Geneva) for the LHCb experiment.
April 2005-March 2006	Teacher at the Collège de Montreux in mathematics and physics for secondary school students.

PUBLICATIONS AS ONE OF THE MAIN AUTHORS

August 2010 (4)	"Prompt K_S production in pp collisions at sqrt(s)=0.9 TeV", the LHCb Collaboration, Physics Letters B, Volume 693, p. 69-80
July 2010 (3)	"Commissioning of the LHCb Silicon tracker using data from LHC injection tests", Proceedings of the RD09 conference, published under PoS(RD09)010
May 2007 (2)	"Photon polarization from helicity suppression in radiative decays of polarized Lambda_b to spin-3/2 baryons", G. Hiller, M. Knecht, F. Legger and T. Schietinger, Physics Letters B, Volume 649, p. 152-158
March 2006 (1)	"Probing photon helicity in radiative B decays via charmonium resonance interference", Mathias Knecht, Thomas Schietinger, Physics Letters B, Volume 634, p. 403-407

PRESENTATIONS GIVEN AT INTERNATIONAL CONFERENCES

March 2010	"Prompt K_S production in pp collisions at sqrt(s)=0.9 TeV" at Rencontres de Moriond, La Thuile, Italy, in the session titled QCD and High Energy Interactions.
October 2009	"Commissioning of the LHCb Silicon tracker using data from LHC injection tests", at 9th Intl. Conference on Large Scale Applications and Radiation Damage of Semiconductor Detectors (RD09), Florence, Italy. The proceedings were published; see (3) above.

| September 2009 | "V^0 production studies at LHCb" at Joint Annual meeting of SPS-OPG-OGAA, Innsbruck, Austria. |
| July 2009 | Poster on "V^0 production studies at LHCb" at EPS HEP 2009, Krakow, Poland. |

TEACHING ACTIVITIES

April 2006-June 2009	Teaching assistant for the following courses :
	- Physique Nucléaire et Corpusculaire I, by Prof. Olivier Schneider, 60 students
	- Physique Nucléaire et Corpusculaire II, by Prof. Olivier Schneider, 30 students
	- Physique Générale, by Prof. Olivier Schneider, 80 students

EDUCATION

2006-2010	PhD student in particle physics at EPFL (LHCb experiment)
1999-2004	Master of Physics degree at EPFL, Lausanne, Grade 6/6
1996-1999	Maturité type A (latin-greek), Gymnase de Burier
	Prize in mathematics

LANGUAGES

French	Mother tongue
English	Working language, good oral and written skills
German	Good oral and written skills
Italian	Basic knowledge

COMPUTER SCIENCES

Excellent PC, MAC, LINUX knowledge, C++ programming, LateX
Microsoft Office : Word, Excel, PowerPoint

HOBBIES

Classical violin, classical orchestra, chamber music
Travelling, learning foreign cultures